

# University of St Andrews



Full metadata for this thesis is available in  
St Andrews Research Repository  
at:

<http://research-repository.st-andrews.ac.uk/>

This thesis is protected by original copyright

# Thermal, Structural and Electrical Characterisation of Novel Proton Conducting Oxides for Solid Oxide Fuel Cell Applications

A thesis submitted for the title of Ph. D.

by

**Derek J.D. Corcoran B. Sc. (hons)**

University of St. Andrews

Supervised by Prof. John T.S. Irvine



Project Sponsors:



**Submitted September 2001**



TL  
D916



2000

## Declaration

I, Derek J.D. Corcoran, hereby certify that this thesis, which is approximately 34,000 words in length, has been written by me, that it is the record of work carried out by me and that it has not been submitted in any previous application for a higher degree.

Date 20/9/01 Signature of Candidate

I was admitted as a research student in September 1998 and as a candidate for the degree of Doctor of Philosophy in September 1999, the higher study for which this is a record was carried out in the University of St. Andrews between 1998 and 2001.

Date 20/9/01 Signature of Candidate

I hereby certify that the candidate has fulfilled the conditions of the Resolution and Regulations appropriate for the degree of Doctor of Philosophy in the University of St. Andrews and that the candidate is qualified to submit this thesis in application for that degree.

Date 20/9/01 Signature of Supervisor

In submitting this thesis to the University of St. Andrews I understand that I am giving permission for it to be made available for use in accordance with the regulations of the University Library for the time being in force, subject to any copyright vested in the work not being affected thereby. I also understand that the title and abstract will be published, and that a copy of the work may be made and supplied by any *bona fide* library or research worker.

Date 20/9/01 Signature of Candidate

## Acknowledgements

This work is dedicated to my parents back in Cork, whose everyday love and belief in me has helped me through to its completion, and to my brother Gary, for his support and of course all the important latest news in the games machine world. Special thanks to Francesca Visintin, you are wonderful.

A big thank you goes to my supervisor, John Irvine, who has given me the opportunity to work for him, and to travel to international conferences, his help and encouragement was unwavering. Gratitude also to the team at DERA Haslar (now QinietiQ), Darren Browning and Barry Lakeman who funded my PhD studentship and tested my materials in a working fuel cell. To the technical staff for their dedicated help and advice: Sylvia Williamson, Bobby Cathcart, Jim Rennie, Colin Smith, Brian Walker and Marjorie Parker in the stores.

To *all* of the JTSI Group, past and present, especially Alan “feck” Feighery and John “jcb” Bradley for help with impedance; Jesus “de nada” Canales for his dedicated TEM work; Cristian “the prophet” Savaniu who continues to work on my materials and gives great barbecues; Julian “jools” Tolchard and Jeremy “jez” Dobson for their computer wizardry; Shanwen “ni hao” Tao and Tom “cool man” McColm for their wisdom and hilarity respectively. I also would like to acknowledge Paul “the kiwi” Connor for some proof reading and useful advice with all the wonderful software we are slaves to.

To the members of staff here who worked with me to write some papers: John Walton (EPR), Jaya Kartha and David Tunstall (NMR). To Ron Smith and Richard Ibberson at Rutherford Appleton Laboratories during the neutron experiments and with the niggles of data refinement later. Thanks also to E.Post at Netzsch for performing the TG-MS experiments.

Without all the wonderful golf, and my golfing partner Brad MacKay, St. Andrews may have gotten the better of me. It was nice to get “oot ‘n about”.

Salutes also to my best friend Barry Healy back home in Cork, and the guys: Paul Costello and Fergus Ryan, we’ll always remember Cape Cod. Shouts out to the big man too, Eamonn Mulvee, still hungry for academic acronymic suffixes.

E&OE, because the waters of Lethe flow sometimes.

## ABSTRACT

This research has concentrated on the complex perovskite systems generally ascribed the formula  $AB_{1/3}B''_{2/3}O_3$  and their doped or stoichiometrically adjusted phases. The phase  $Sr_3Ca_{1.18}Nb_{1.82}O_{8.73}$  (SCN18) has been shown in the literature to be a proton conductor when hydrated and held at intermediate temperatures (300 to 600 °C) in a moist hydrogen-containing atmosphere. This arises as a result of  $H_2O$  incorporation as O-H groups at oxygen ion vacancy positions. Proton conduction is assumed to occur by the Grotthuss or "hopping mechanism" between adjacent oxygen ions. These materials have good potential for application as solid electrolytes in intermediate temperature SOFCs.

The synthesis, characterisation, structure and conductivity of a new series of complex perovskite oxides,  $Sr_3Ca_{1+x}Zr_{(1-y)-x/2}Ta_{(1+y)-x/2}O_{8.5-[(5x-2y)/4]}$  has been investigated as potential proton conducting ceramics for use in intermediate temperature (400 to 600 °C) Solid Oxide Fuel Cells using a wide range of techniques. Detailed structural characterisation of the  $Sr_3Ca_{1+x}Nb_{2-x}O_{9-(3x/2)}$  system as a function of temperature (water loss) served as a basis for the new  $Sr_3Ca_{1+x}Zr_{(1-y)-x/2}Ta_{(1+y)-x/2}O_{8.5-[(5x-2y)/4]}$  system and comparisons are drawn. It was determined that distortions on the  $[111]_p$  oxygen planes due to the filling of oxygen ion vacancies (in the dry state) causes a loss of symmetry at low temperatures. Unit cell symmetry was found to increase in both  $Sr_3Ca_{1+x}Nb_{2-x}O_{9-(3x/2)}$  and  $Sr_3Ca_{1+x}Zr_{(1-y)-x/2}Ta_{(1+y)-x/2}O_{8.5-[(5x-2y)/4]}$  phases with increasing temperature. A corresponding decrease in conductivity becomes evident as the material dehydrates.

Specifically, the phases  $\text{Sr}_3\text{CaZr}_{0.5}\text{Ta}_{1.5}\text{O}_{8.75}$  and  $\text{Sr}_3\text{CaZrTaO}_{8.5}$  were highlighted. The detailed crystallographic structure of hydrated  $\text{Sr}_3\text{CaZr}_{0.5}\text{Ta}_{1.5}\text{O}_{8.75}$  was investigated by means of variable temperature X-ray and high-resolution neutron diffraction experiments. Electrical characterisation of this phase was carried out under both hydrating and drying conditions using 2-terminal a.c. impedance spectroscopy. Thermogravimetric analysis and differential thermal analysis in dry and wet atmospheres were used to monitor water loss/uptake events in both phases.

High-pressure steam (2.5 MPa) treatments of  $\text{Sr}_3\text{CaZrTaO}_{8.5}$  resulted in significant  $\text{H}_2\text{O}$  uptake (lost by heating to 600 °C), along with a small amount of  $\text{CO}_2$  (lost over 700 °C), quantitatively determined by combined TGA-Mass Spectroscopy techniques.

Very high pressure and temperature (up to 340 GPa and 700 to 1000 °C) treatments of  $\text{Sr}_3\text{CaZrTaO}_{8.5}$  with  $\text{KClO}_4$  were performed to investigate  $\text{CO}_2$  and possible  $\text{O}_2$  uptake. The presence of unpaired electrons associated with possible  $\text{O}_2^-$  species giving rise to an ESR signal was investigated. It appears that the Zr dopant is associated with these defects.

Hydrogen titanate,  $\text{H}_2\text{Ti}_3\text{O}_7$  was produced by aqueous acid proton exchange from  $\text{Li}_2\text{Ti}_3\text{O}_7$  and both structures investigated by X-ray diffraction. The (protonic) conductivity of hydrogen titanate was also investigated by a.c. impedance spectroscopy.

All in all, these new perovskite proton conducting phases show promise as potential electrolytes for SOFCs as they have been shown to exhibit bulk conductivities on a par with the best of similar complex perovskites such as SCN18 and BCN18. They also have been shown to exhibit good stability under reducing gas atmospheres. An advantage to these phases is that all the cations are resistant to reduction under

realisable conditions, thereby minimising contributions from electronic conduction. Furthermore, the stability of these Sr based perovskites under CO<sub>2</sub> is much better compared to those that are Ba based.

# TABLE OF CONTENTS

1	Background and literature survey.....	1
1.1	Fuel Cells.....	1
1.2	Why a proton conducting electrolyte? .....	7
1.2.1	<i>SOFCS: The Status Today</i> .....	8
1.3	Ion-conducting solids.....	11
1.4	Proton Conducting Oxides:.....	15
1.5	Protonic Conduction in Solid Oxide Fuel Cell Electrolytes .....	21
1.6	Review of doped Barium Cerate, $X:\text{BaCeO}_{3-\alpha}$ .....	23
1.7	Review of the proton conductor $\text{Ba}_3\text{Ca}_{1.18}\text{Nb}_{1.82}\text{O}_{9-\delta}$ (BCN18):.....	27
1.8	Aims of this work .....	29
1.9	References.....	32
2	Experimental.....	35
2.1	Overview .....	35
2.2	Solid State Synthesis.....	35
2.2.1	<i>Sample Densities - The number of molecules in a unit cell, Z</i> .....	36
2.3	Hydrothermal Treatments .....	37
2.4	Thermogravimetric Analysis.....	37
2.5	Differential Thermal Analysis (DTA).....	38
2.6	The Alternating Current Impedance Spectroscopy Technique .....	39
2.6.1	<i>The Experiment</i> .....	39
2.6.2	<i>Theory</i> .....	40
2.7	2-terminal A.c. Impedance Experimental Set-up/Equipment .....	46
2.7.1	<i>Principle of Operation</i> .....	47
2.7.2	<i>Electrodes</i> .....	47
2.7.3	<i>Furnace/Jig Arrangement</i> .....	48
2.8	4-terminal Conductivity as a function of $\text{pO}_2$ .....	50
2.9	The use of Equivalent Circuits to model the electrochemical responses of polycrystalline materials .....	52
2.10	Electrode-Electrolyte Interface: Interfacial Electrochemistry .....	56
2.11	X- Ray Diffraction.....	59
2.11.1	<i>Background</i> .....	59
2.11.2	<i>Diffraction of X-rays</i> .....	60
2.11.3	<i>Miller Indices</i> .....	62
2.11.4	<i>The recording of a powder diffraction pattern</i> .....	62
2.11.5	<i>Systematic Absences</i> .....	64
2.11.6	<i>Peak Intensities</i> .....	65
2.11.7	<i>Rietveld Refinement of Crystal Structures</i> .....	68
2.12	Neutron Diffraction.....	71
2.12.1	<i>Theory of Neutron Diffraction</i> .....	71
2.12.2	<i>Instrumentation</i> .....	72
2.13	Electron Paramagnetic (Spin) Resonance (EPR/ESR) .....	73
2.13.1	<i>Introduction</i> .....	73
2.13.2	<i>The Experiment</i> .....	75

2.13.3 Theory .....	76
2.14 High Pressure Sample Treatment .....	77
2.14.1 The Equipment/Experimental .....	77
2.15 References.....	78
3 The Proton Conducting $Sr_3Ca_{1+x}Nb_{2-x}O_{9-\delta}$ system.....	79
3.1 Introduction.....	79
3.2 Results and Discussion .....	81
3.2.1 Thermogravimetric Analysis of the related composition	
$Sr_3Ca_{1.1}Nb_{1.9}O_{8.85-x}(OH)_{2x}$ .....	81
3.2.2 X-Ray diffraction studies of $Sr_3Ca_{1.18}Nb_{1.82}O_{8.73}$ .....	83
3.2.3 Neutron diffraction studies of $Sr_3Ca_{1+x}Nb_{2-x}O_{9-\delta}$ .....	84
3.2.4 TEM Studies of SCN18.....	89
3.3 Summary.....	91
3.4 References.....	92
4 Synthesis and Characterisation of the	
$Sr_3Ca_{1+x}Zr_{(1-y)-x/2}Ta_{(1+y)-x/2}O_{8.5-[(5x-2y)/4]}$ system .....	93
4.1 The system .....	93
4.2 Phase Characterisation.....	94
4.3 Initial TGA measurements.....	95
4.3.1 Thermogravimetric studies of $Sr_3CaZr_{0.5}Ta_{1.5}O_{8.75}$ .....	95
4.4 Other selected water loss measurements .....	99
4.5 Colour .....	102
4.6 Combined Thermogravimetric/Differential Scanning Calorimetric-Mass	
Spectrometric Analysis (TG/DSC-MS) of $Sr_3CaZrTaO_{8.5-x}(OH)_{2x}$ .....	103
4.6.2 The experiment.....	103
4.6.3 Results and discussion .....	105
4.7 The high temperature and pressure incorporation of molecular species .....	111
4.7.1 Introduction.....	111
4.7.2 Sample Preparation/Analysis.....	114
4.7.3 Results and Discussion.....	114
4.7.4 Spin concentrations.....	121
4.8 Summary.....	123
4.9 References.....	124
5 Structural Studies of the Complex Perovskite Proton Conductors	
$Sr_3Ca_{1+x}Zr_{(1-y)-x/2}Ta_{(1+y)-x/2}O_{8.5-\delta}$ [ $\delta = (5x - 2y)/4$ ].....	125
5.1 Introduction.....	125
5.2 Different Perovskite Unit Cells.....	126
5.3 Structural Results for $Sr_3CaZr_{0.5}Ta_{1.5}O_{8.75}$ .....	128
5.3.1 X-Ray diffraction studies of $Sr_3CaZr_{0.5}Ta_{1.5}O_{8.75}$ .....	128
5.3.2 High Temperature XRD Studies of $Sr_3CaZr_{0.5}Ta_{1.5}O_{8.75} + H_2O$ .....	129
5.3.3 Neutron diffraction studies of $Sr_3CaZr_{0.5}Ta_{1.5}O_{8.75}$ .....	134

5.3.4	<i>The change in structure with temperature for <math>Sr_3CaZr_{0.5}Ta_{1.5}O_{8.75} + D_2O</math></i>	142
5.3.5	<i>Structure modelling and proton positions</i>	146
5.3.6	<i>Structural data for <math>Sr_3CaZr_{0.5}TaO_{8.75-y}(OD)_{2y}</math> (<math>y \approx 0.1375</math>)</i>	151
5.3.7	<i>Multiple temperature neutron diffraction for <math>Sr_3CaZrTaO_{8.5-y}(OD)_{2y}</math></i>	152
5.3.8	<i>High Resolution TEM Studies of (vacuum treated) phase, <math>Sr_3CaZr_{0.5}Ta_{1.5}O_{8.75}</math></i>	155
5.4	Summary:	156
5.5	References:	157
6	Electrical Characterisation of $Sr_3CaZr_{0.5}Ta_{1.5}O_{8.75}$ and $Sr_3CaZrTaO_{8.5}$ .....	158
6.1	2-Terminal (A.C. Impedance) Conductivity Studies	158
6.1.1	<i>Introduction</i>	158
6.1.2	<i>Equivalent circuit fitting</i>	159
6.1.3	<i>Nyquist (<math>Z''</math> versus <math>Z'</math>) plots for <math>Sr_3CaZr_{0.5}Ta_{1.5}O_{8.75}</math></i>	163
6.1.4	<i>The total conductivity of <math>Sr_3CaZr_{0.5}Ta_{1.5}O_{8.75}</math></i>	167
6.1.5	<i>The bulk and grain boundary conductivities of <math>Sr_3CaZr_{0.5}Ta_{1.5}O_{8.75}</math></i>	169
6.1.6	<i>The influence of wet and dry atmospheres over time</i>	172
6.1.7	<i>Discussion</i>	174
6.2	D.c. 4-terminal conductivity versus $pO_2$ for $Sr_3CaZrTaO_{8.5}$	175
6.2.1	<i>Results and discussion</i>	175
6.3	Summary	177
6.4	References	178
7	Hydrogen Titanates as Potential Proton Conducting Fuel Cell Electrolytes	179
7.1	Introduction	179
7.2	Experimental	181
7.3	Results	183
7.3.1	<i>X-Ray Diffraction studies</i>	183
7.4	Solid-State Magic Angle Spinning NMR studies	184
7.5	Thermogravimetric analysis of ramsdellite $H_2Ti_3O_7$	186
7.6	A.c. impedance spectroscopy studies of the conductivity	187
7.7	Discussion	191
7.8	Summary	192
7.9	References	193
8	Conclusion	194

# Chapter One

## Background and Literature Survey

“Hydrogen is a colourless, odourless gas which, given enough time, turns into people.”

---*Henry Hiebert*

# 1 Background and literature survey

## 1.1 Fuel Cells

Fuel cells, like batteries, are electrochemical devices that convert the chemical energy of a reaction directly into electrical energy. The basic building block of a fuel cell consists of an ionically conducting dense electrolyte sandwiched between a porous anode (fuel electrode) and porous cathode (air electrode). Figure 1-1 below shows the principle of fuel cell operation.

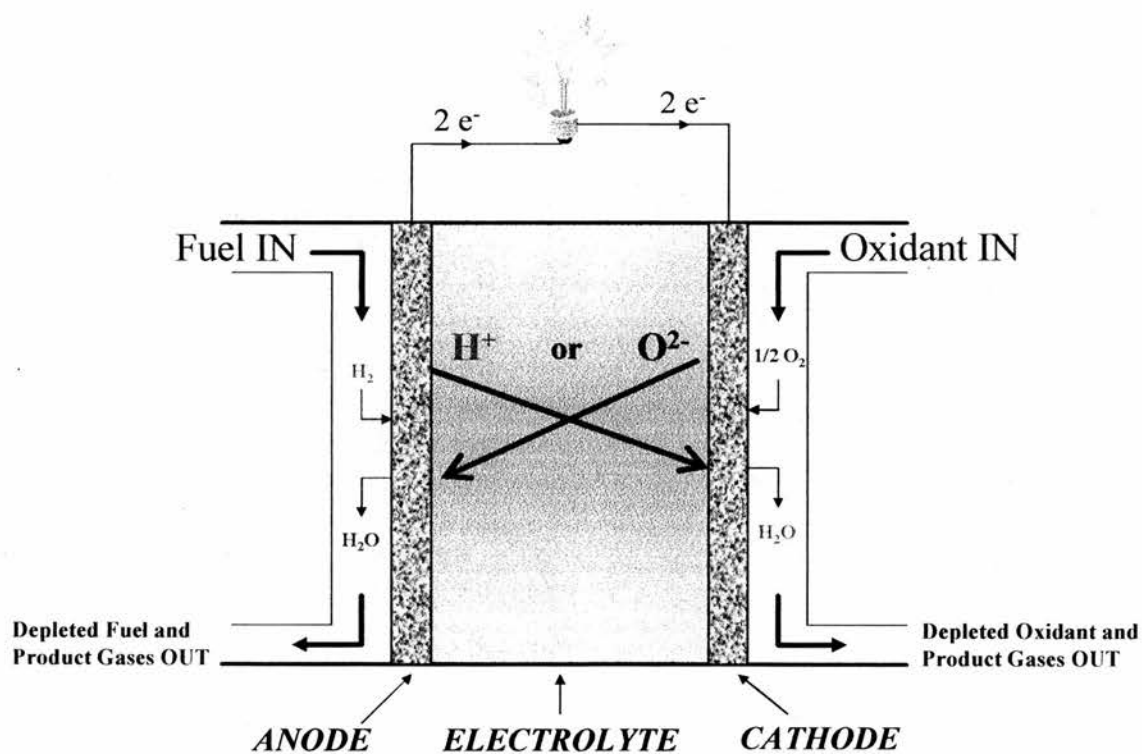


Figure 1-1: Principle of a Fuel Cell

A fuel cell differs in many respects from a conventional secondary (rechargeable) battery, in that, as long as the fuel and oxidant are supplied to the electrodes, the cell will continue to produce an electric current flowing from anode (the negative electrode) to cathode (positive electrode), as opposed to using stored chemical energy like a battery. Some problems arise however, such as corrosion and material degradation that limit the operating life of fuel cells [1]. The electrolyte can either be dominantly oxide ion conducting ( $O^{2-}$ ) where the fuel is oxidised to  $H_2O$  on the anode, or proton conducting ( $H^+$ ) whereby the oxidant (usually  $O_2$ ) is reduced at the cathode to also form water. It is often claimed that gaseous hydrogen is the fuel of choice for most applications, whether terrestrial or for space use, as it can be produced from the internal or external reforming of methane with steam ( $CH_4 + H_2O = 3H_2 + CO$ ), and the water gas shift reaction ( $CO + H_2O = CO_2 + H_2$ ). To avoid carbon altogether, this hydrogen would ideally come from a clean renewable source, such as the electrolysis of water using solar energy. Problems arise with hydrogen when considering how it is to be stored, because large heavy tanks would be needed, until the development of metal-hydride hydrogen storage or carbon-nanotube technology improves. However, there is a move towards the idea of “internal reforming”, utilising a suitable anti-coking (no residue of impure carbon after reaction) catalyst, so methane can be used directly. Methanol, although toxic and corrosive, could be a cheaper, viable option for low temperature, compact fuel cells for use in portable equipment. In the region of the porous electrode, a three-phase interface (*triple phase boundary*) is established between catalyst, electrode and electrolyte. The optimisation of this interface, in terms of thickness, porosity, structure and compatibility/mixing with the electrolyte is of crucial importance in improving the electrochemical performance and reducing the cost of the cell. The electrolyte must have good ionic conductivity to conduct the “dissolved”

reactants to the electrodes, and yet, must serve as a dense electronic insulator to prevent fuel and oxidant mixing and short-circuiting.

The functions of porous electrodes in fuel cells are at least threefold: 1) they provide a *surface site* where the charge transfer reactions between gases and liquids can take place, 2) they *conduct* ions to and from the triple phase boundary, as well as the electrons as a result of fuel oxidation or enabling oxidant reduction; and 3) to serve as a physical *barrier* between gases and the electrolyte. Because ionisation rates generally increase with temperature, the catalytic nature of the electrode becomes less important for higher temperature fuel cells (Solid Oxide). The various types of fuel cells comprise the following:

*Alkaline Fuel Cell (AFC)*: Limited to specialised applications, and used in the Apollo Missions in the 1960's, this cell consisted of a concentrated KOH electrolyte in an abbestos matrix and could be operated between 100 and 250°C depending on the concentration of KOH. A wide range of electrocatalysts can be used (Ni, Ag, metal oxides, etc.). The main drawback as far as cost and fabrication is concerned is the sensitivity of KOH to CO and CO<sub>2</sub>, forming carbonates and therefore requiring high-purity hydrogen as the fuel.

*Polymer Electrolyte Fuel Cell (PEFC)*: The proton-conducting electrolyte is a solid ion-exchange membrane (fluorinated sulfonic acid polymer or related), the development of which was instigated by the original idea of Grubbs in 1959 [2]. The upper operational limit is 120°C in order to maintain the cell in a hydrated state. Pt is usually used for the electrodes/catalyst, which is made hydrophobic by coating with Teflon<sup>®</sup>. The electrochemical reactions are the same as for the PAFC (described below), whereby

protons are formed from the fuel on the anode side, and conduct through the electrolyte membrane in solvated form, having given up electrons which travel through the external circuit to the cathode. These electrons combine with oxygen ions (from the oxidant gas, oxygen), and the solvated protons, to produce water at the cathode side. This water is in fact produced in the liquid state, so high water content (saturation) in the electrolyte is important. At high current densities, water drag becomes a problem, due to sluggish osmosis in the electrolyte, where between 1 and 2.5 molecules of water are dragged with each proton, giving  $\text{H}(\text{H}_2\text{O})_n^+$  [3].

Due to its lightweight construction [4], low temperature of operation ( $80^\circ\text{C}$ ), and compactness, it is suitable for transport applications, where the most likely fuel would be methanol [5]. The use of reformed hydrocarbons are also a real possibility. An example of a successful operation of a PEFC, is that by Ballard Power Systems, with validated PEFC operation at ambient pressure for over 25,000 hours with a six cell stack without forced air flow, without humidification, and without active cooling [6]. The typical proton conducting electrolyte in a PEFC is Nafion, the generic brand name for the Teflon-based polymer electrolyte developed by DuPont [7]. It consists of a fluoropolymer backbone, like Teflon, with chemically bonded sulfonic acid groups [8].

*Phosphoric Acid Fuel Cell (PAFC):* In this cell, the electrolyte is concentrated  $\text{H}_3\text{PO}_4$  in a SiC matrix, with Pt electrodes. It can operate at temperatures from  $150\text{-}220^\circ\text{C}$ , because of the relative stability of phosphoric acid compared to other acids. The high (up to 100%) concentration also means that the water vapour pressure is low, thereby enabling easier water management.  $\text{CO}_2$  does not react with the electrolyte of the PAFC, but merely dilutes the fuel. CO is a poison to the Pt catalyst, and external reforming is

necessary to obtain high-purity hydrogen. Some steam and rejected heat is available for co-generation and other uses.

*Molten Carbonate Fuel Cell (MCFC):*  $\text{CO}_3^{2-}$  is the conducting species. Operating at higher temperatures (600-700°C), this cell does not require noble metals, so Ni/NiO is sufficient at the anode/cathode to promote reaction. Usually, the electrolyte consists of Na/K carbonates as a highly conductive molten salt in a  $\text{LiAlO}_2$  ceramic matrix. Because of the high temperature of operation, internal reforming is possible and CO is directly usable as fuel, however  $\text{CO}_2$  is required at the cathode (can be recycled from anode exhaust). Stainless steel can be used for cell fabrication.

*Solid Oxide Fuel Cell (SOFC):* Solid, non-porous  $\text{Y}_2\text{O}_3$ -stabilised  $\text{ZrO}_2$  (usually 8 to 9 mol %) is the most commonly used electrolyte, conducting  $\text{O}^{2-}$  ions in the temperature range 650-1000°C. The typical anode is a Co or Ni- $\text{ZrO}_2$  cermet (*ceramic-metal* composite), and a typical cathode material is Sr-doped  $\text{LaMnO}_3$ .

An alternate mode of operation for an SOFC would be to use a proton conducting electrolyte, whereby the fuel would be oxidised to protons at the anode to form protons ( $\text{H}^+$ ) which would then be transported through the electrolyte to react with oxygen at the cathode. A lot of research has focussed on acceptor doped  $\text{BaCeO}_3$  (usually with 5-10 %  $\text{Y}^{3+}$ ) as the material of choice as a proton conducting electrolyte, but it presents some drawbacks regarding stability, and will be discussed later. Thus the search for more stable (and better conducting) proton conducting oxides is at the forefront of research today.

The SOFC has the longest development period, from the 1950's. The ceramic components are easily shaped into tubes or plates, and the solid electrolyte is impervious to gas crossover. Like the MCFC, CO is directly usable as fuel, and internal reforming is certainly achieved at 1000°C. There are restrictions on materials selection for these high temperatures, and fabrication can be difficult. Owing to the nature of the electrolyte (solid oxide ceramic), there can be relatively high ohmic polarisation (internal resistivity) losses, which increases with lower temperatures.

A Table of the comparisons between the major fuel cell types is shown below:

	PEFC	PAFC	MCFC	SOFC
Electrolyte	Ion Exchange Membrane	Immobilised Liquid H <sub>3</sub> PO <sub>4</sub>	Immobilised Liquid Molten Carbonate	Ceramic
Operating Temperature	80°C	205°C	650°C	(600 – 1000°C)
Charge Carrier	H <sup>+</sup>	H <sup>+</sup>	CO <sub>3</sub> <sup>2-</sup>	O <sup>2-</sup> (H <sup>+</sup> )
Catalyst	Pt	Pt	Ni	Perovskites
Main Cell Components	C-based	Graphite-based	Stainless Steel	Ceramic

**Table 1-1: Comparisons between Fuel Cell Types.**

## 1.2 Why a proton conducting electrolyte?

When incorporated into an electrochemical device, a proton conducting ceramic solid electrolyte has three fundamental functions: electromotive function, preferential ionic transport and discrimination of ions (as in gas purification/separation techniques). Electrolytes that conduct protons instead of negative oxide ions could provide a novel basis for cost-effective, low temperature Solid Oxide Fuel Cells. A proton conductor SOFC would essentially operate in “reverse”, with positive charged hydrogen ions

flowing from anode to cathode. Because of this difference in the mode of operation, water production would be shifted from the anode to the cathode, diluting the air instead of the fuel. When a protonic conductor is used instead of an oxygen ion conductor, fuel circulation is unnecessary in the case of a hydrogen fuel cell, because no water molecules are generated at the anode. Also, the efficiency should be higher, because in SOFCs air is typically supplied in excess of stoichiometric needs for cooling, whereas the fuel is limited. Proton conducting electrolytes would operate at lower temperatures (650-800°C), with several advantages over the conventional materials, including better compatibility with hydrocarbons. There is however, always a trade-off between conductivity due to protons and that due to oxygen ions (possibly at high temperatures), as well as optimisation of the transport number of the proton. Although solid-electrolyte proton conductors have long been laboratory curiosities, little is known about their properties and use in SOFCs. Greater compatibility with hydrocarbon fuels is another advantage, since it is the reformed and reacted fuel (in the form of protons at the electrode/electrolyte reaction interface), which is conducted through the electrolyte as a result of a concentration gradient. No known ceramic oxide ion conductor, for example, can conduct ions at such temperatures of operation as low as 500°C, as an improved proton conducting solid oxide can. This can be explained in terms of the relative sizes, mobilities and diffusion coefficients of the ions ( $O^{2-}$  versus  $H^+$ ).

### 1.2.1 SOFCs: The Status Today

Christian Friedrich Schoenbein discovered the fuel cell effect in 1838 [9,10] and William R. Grove invented the fuel cell in 1845 [11,12,13]. Between 1838 and 1845 Schoenbein studied and interpreted the phenomenon, whereas Grove turned his research into a practical reality [14]. Investigations into "galvanic cells with solid oxide

electrolytes" began in the 1940s in Germany and were themselves followed by experiments with ceramic zirconia in the 1950s. The development of modern SOFCs was chiefly pioneered in the USA in the 1960s. Research efforts have followed two separate pathways and resulted in two distinct designs: tubular SOFCs and planar SOFCs. The tubular technology was pioneered in the USA by Siemens Westinghouse Corporation (with some Japanese involvement), and has been funded almost entirely by the US Department of Energy. The planar technology has roused even more interest, with several international collaborative programmes emerging over the last decade.

Both tubular (mainly) and planar SOFCs are targeting stationary power applications, albeit at different power levels. Tubular SOFCs are envisaged at ratings from 100s of kW to tens of MW and as such are best suited to centralised generation or industrial power applications. A power range from 1kW to 100s of kW renders the planar SOFC suitable for higher volume small- and medium-scale "distributed" power generation, and it may also find a market in the transportation sector, particularly where there may be both an electrical and thermal load. Planar SOFC developers have cited commercial and residential cogeneration as a target market, and possibly an entry point. The tubular SOFC is a near commercial product having celebrated its first field trial demonstration of 100kW earlier in 1998. Pending the success of larger demonstrations, commercially available units rated at over 1MW are likely to emerge in the 2001 to 2003 timeframe.

In commercial terms, planar SOFCs have been somewhat behind their sister technology. However, now this technology is progressing much faster, with effective commercial units in production by SulzerInnotec in Switzerland. Typically, the SOFC employs a solid ceramic yttria stabilised zirconia electrolyte, conducting the charge-carrying oxide ( $O^{2-}$ ) ions at between 800°C and 1000°C. Tubular designs operate at the upper end of

the temperature range, whereas development efforts for planar SOFCs are focused on the lower temperatures. Commercial operation at around 800°C now enables the use of cheaper materials (such as stainless steel for the interconnects or glass-type rings for sealing) compared to expensive gold-ring seals, and doped lanthanum chromite for interconnects. Operation at lower temperatures, 700°C or even 400°C (sufficient for methanol reformation), allowing the use of cheaper ceramics is one of the expected directions for future research.

The conventional (oxide ion conducting electrolyte) SOFC's elevated operating temperatures allow for internal reforming of just about any chosen fuel. In trials, the tubular technology has been operated on diesel and jet fuel as well as natural gas. Furthermore, high operating temperatures mean that process steam is available in abundance for cogeneration applications or to drive a steam turbine. Operation on natural gas yields an overall efficiency of well over 50% (Lower Heating Value, LHV). Integrating a gas turbine or microturbine into the cycle conceivably increases efficiency beyond 70% LHV [15]. In this configuration, the fuel cell replaces the combustion chamber of the gas turbine (which may itself be used to pressurise the SOFC), and feeds the power turbine stage with exhaust emissions from the fuel cell, thus contributing perhaps 20-25% of the total electrical output. This approach is also expected to have lower specific cost than a conventional SOFC.

One advantage of SOFCs is that the use of a ceramic solid electrolyte dramatically reduces the corrosion problems associated with liquid electrolytes such as the very mobile alkali carbonates ( $K_2CO_3$ ) in MCFCs. The SOFC also has a fairly high power density. The tubular SOFC may be regarded as a near commercial product, and has performed successfully as a prototype demonstrator. It is a highly efficient generator as

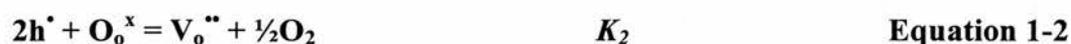
a stand-alone device, but is especially so in the SOFC-GT (gas turbine linked) configuration. One of the limitations of tubular SOFC is said to be its restricted power range (although this is as wide as that of the molten carbonate fuel cell or MCFC, its principal rival). The planar SOFC is behind the tubular design in terms of maturity, but benefits from wider support and private investment. It has advantages of size, cost and efficiency over tubular technology, although there is only limited overlap between the two designs in terms of currently available power range. Even if there are doubts as to the durability of the planar SOFC, it has now been demonstrated to prove itself outside the laboratory (SulzerInnotec). Cost is most definitely the major issue, and the planar SOFC is becoming cheaper.

### **1.3 Ion-conducting solids**

Ionic materials that are doped or inherently exhibit non-stoichiometry may have considerable concentrations of ionic defects, such as anion or cation vacancies and interstitials. Such defects will facilitate the diffusion of ions as extrinsic defects and give rise to ionic conductivity. Materials with dominant ionic conductivity may be used as solid electrolytes. These can be used for fuel cells (e.g. solid oxide fuel cells, SOFC), electrolysers (e.g. for water vapour electrolysis) and sensors [e.g. lambda (fuel/air ratio) in cars or for sensing gases in molten metals].

The systematic investigation of proton conducting perovskite type oxides of the formula  $ABO_3$  was instigated by the work of Takahashi and Iwahara in 1980 [16]. This paper reported protonic conductivity in a series of indium doped strontium zirconates ( $In:SrZrO_3$ ), which was later been developed as a separator material in high temperature potentiometric hydrogen sensors [17]. Proton conducting perovskite-type oxide

ceramics typically exhibit *p*-type electronic (hole) conduction in an oxidising atmosphere free from hydrogen or water vapour [18]. On introduction of hydrogen or water vapour into the atmosphere surrounding the specimen at high temperature, electronic conductivity decreases, and protonic ( $H^+$ ) conduction tends to appear. Positively charged (protonic) defects ( $OH_o^\bullet$ ) on oxygen lattice sites of the doped perovskite oxide compete with other positively charged defects such as electronic holes ( $h^\bullet$ ) and Schottky defects as oxide ion vacancies ( $V_o^{''}$ ). Negatively charged defects such as the presence of a lower valence (dopant) cation on the B-site metal sub-lattice provide charge compensation. The defect equations can be written as:



(charge neutrality condition)

where  $C_B$  is a dopant (lower valency) cation in place of an original B cation and is considered to be a negatively charged defect. See Table 1-2 below as a key to the Kröger-Vink notation used above:

Site Description	Notation
$B^{4+}$ on $B^{4+}$ site	$B^x_B$
Vacancy on B site	$V^{///}_B$
Interstitial B ion	$B^{''''}_i$
$C^{4+}$ on $B^{4+}$ site	$C_B$
$C^{3+}$ on $B^{4+}$ site	$C'_B$
$O^{2-}$ on $O^{2-}$ site	$O^x_o$
Vacancy on $O^{2-}$ site	$V^{''}_o$
Interstitial $O^{2-}$	$O^{//}_i$
free hole	$h^{\bullet}$
free electron	$e'$

**Table 1-2: Kröger-Vink Notation for doped Perovskite  $AB_{1-x}C_xO_{3-\alpha}$**

$^x$  = neutral charge,  $^{\bullet}$  = positive charge,  $'$  = negative charge [19]

Table 1-3 below shows the various applications open to solid oxide proton conducting electrolytes, with the fuel cell being perhaps the most technologically and economically important. It will be discussed in the following section.

<b>Function</b>	<b>Phenomena applicable</b>	<b>Application</b>
	Power	Fuel-cell
Electrochemical permeation of hydrogen	Separation	Hydrogen extractor
		Hydrogen pump
		Hydrogen gas controller
	Electrolysis	Steam electrolyser for H <sub>2</sub> production
		H <sub>2</sub> S electrolyser for desulphurisation HCl electrolyser for Cl <sub>2</sub> recovery
Reaction	Hydrogenation of organic compounds Dehydrogenation of organic compounds	
E.m.f.	Signal	Hydrogen gas sensor Hydrogen activity (in fused metal) sensor Steam sensor

**Table 1-3: Applications of solid oxide proton conductors [20].**

## 1.4 Proton Conducting Oxides:

There are a number of classes of oxides that conduct protons. Precipitated materials (from aqueous solution) include the heteropoly-acid hydrates such as polycrystalline  $\text{H}_3\text{PW}_{12}\text{O}_{40}\cdot 29\text{H}_2\text{O}$  [21], with a room temperature protonic conductivity on the order of  $0.1 \text{ S cm}^{-1}$  [22] at room temperature. The layered hydrogen uranyl phosphates, HUPs ( $\text{H}_3\text{OUO}_2\text{PO}_4\cdot 3\text{H}_2\text{O}$ ) and arsenates HUAs [23] are unstable above  $\text{pH} = 3$  and lose water (and hence conductivity) above  $50^\circ\text{C}$ , with formation of  $\text{H}_2\text{UO}_2\text{PO}_4$  at  $157^\circ\text{C}$  [24]. NMR studies confirm that  $\text{H}^+$  (and not  $\text{H}_3\text{O}^+$ ) is the conducting (mobile) species [25]. Antimonic acid,  $\text{HSbO}_3\cdot n\text{H}_2\text{O}$  has a number of origins, one example is the hydrolysis of  $\text{SbCl}_3$  [26], giving a defect pyrochlore structure with room temperature conductivity ranging from  $10^{-3} \text{ S cm}^{-1}$  ( $n = 1.5$ ) to  $10^{-7} \text{ S cm}^{-1}$  ( $n = 0.25$ ), with activation energies below  $0.15 \text{ eV}$  [26]. The deposition of hydrous  $\text{SnO}_2$  inside mordenite (a zeolite) has also been studied, and such a material exhibited a conductivity of  $2.5 \times 10^{-2} \text{ S cm}^{-1}$  at  $100^\circ\text{C}$  and 100 % relative humidity [27].  $\text{HTaO}_3$  and  $\text{HNbO}_3$  are similar materials and also show protonic conductivity [28]. Layered structures such as  $\text{Zr}(\text{HPO}_4)_2\cdot \text{H}_2\text{O}$  have also been investigated [29,30,31] with conductivities around  $3 \times 10^{-4} \text{ S cm}^{-1}$  at room temperature, along with a polyhydrated form called  $\alpha\text{-ZrP}$  which approaches  $10^{-3} \text{ S cm}^{-1}$  due to aligned crystallites and high hydration level [32].

Those that require cation exchange (sodium cations,  $\text{Na}^+$  exchanged with ammonium,  $\text{NH}_4^+$  or hydroxonium,  $\text{H}_3\text{O}^+$ ) belong to the first class, and include  $\beta$ -alumina [33,34,35], hydrated NASICON (sodium super-ionic conductor) phases [36,37,38,39] of the formula  $(\text{H}_3\text{O})_{2.5}\text{Zr}_2\text{Si}_{1.5}\text{P}_{1.5}\text{O}_{12}$  and zeolites such as ammonium-zeolite-A approximated by  $(\text{NH}_4)_4\text{Ca}_3\text{Si}_{14}\text{Al}_{10}\text{O}_{48}\cdot 200\text{-}300\text{H}_2\text{O}$  [40,41]. In these materials, proton

conduction occurs in the range 25-200/300°C, beyond which water (and therefore protons) are lost and the protonic conductivity degrades.

The most successful “solid” protonic membrane for fuel cell use is the Nafion membranes used in kW-sized fuel cells in the US Gemini Space Programme. Nafion is a perfluorinated polysulphonic acid polymer [42]. It is one such example of a poly(tetrafluoroethylene) based ionomer. From its development by DuPont [43] in the 1960s, it has found applications in liquid and gas separations, fuel cells, and the chlor-alkali industries. It possesses good thermal and chemical resistance, ion-exchange properties, selectivity, mechanical strength, and insolubility in water. However, as the membrane is around 30% water, the term “solid electrolyte” may be misleading. The limiting operating temperature is around 150°C, but 90°C is more usual.

Materials however, that exhibit protonic conduction in the temperature range 600-1000°C have great technological interest today, as they can be incorporated into devices such as fuel cells, hydrogen gas sensors, gas separators and steam electrolyzers. The majority of these materials are perovskites. The fact that certain doped perovskites exhibit protonic conduction in wet hydrogen containing atmospheres, instigated by the work of Iwahara [16], has led to vigorous research in this area since the early eighties. Important early examples are the strontium and barium cerates, but they have their limitations in that, they are stable only in certain atmospheres, exhibit some electronic conductivity, and tend to have oxide ion conductivity at high temperatures. New and interesting materials that fit the criterion of stable protonic conduction without the problems outlined above comprise the complex perovskites, introduced by Nowick [44,45,46,47].

The high temperature protonic conductors among the perovskite related oxide compounds ( $ABO_3$ ) have received considerable interest (Figure 1-2) over the last 3 to 4 years [48].

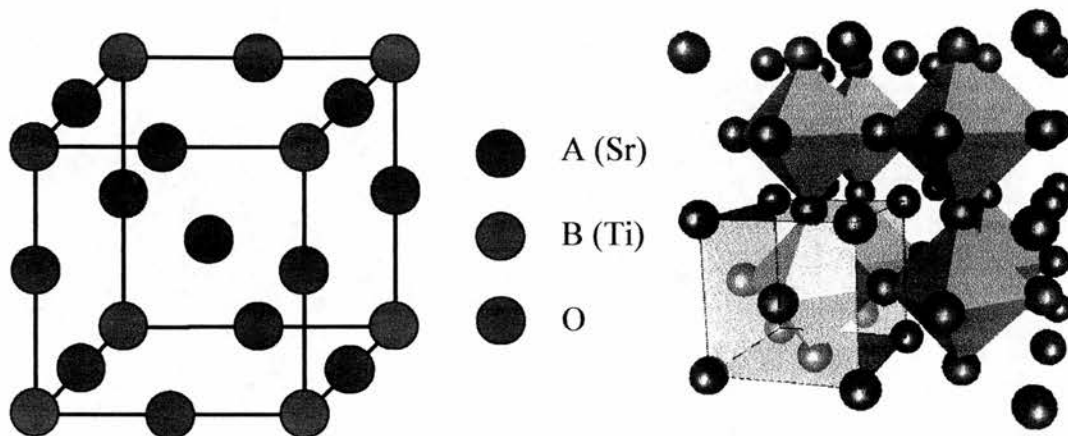


**Figure 1-2 : The perovskite structure for  $ABO_3$  compounds (e.g.  $SrTiO_3$ )**

**The  $BO_6$  octahedral framework (unit cell is shaded) is shown on the right**

The simple perovskite structure consists of a cubic unit cell, with a 12-coordinate A-cation at the body centre, 6-coordinated B-cations at the corners of the cube, and O-anions at the midpoints of the edges. It can also be viewed (in Figure 1-2) as four corner-sharing  $BO_6$  octahedra surrounding a central A-cation. It can also be thought of as a *ccp* (cubic-close packed) array of A and O ions with the B cations occupying the octahedral holes. The perovskite octahedral framework is the same as that of  $ReO_3$  (no A cation). Compounds with this structure include  $SrTiO_3$ ,  $SrZrO_3$ ,  $SrHfO_3$ ,  $SrSnO_3$  and  $BaSnO_3$  [49].

In order to introduce defects into the normal perovskite ( $ABO_3$ ), acceptor dopants of lower valence (X) are introduced on the B-site, to produce oxygen ion vacancies on the

lattice to give  $AB_{1-x}X_xO_{3-\delta}$  [50,51,52,53,54]. Proton conduction in such perovskite oxides, doped on the B-site, has been the subject of extensive work; ever since Iwahara and his co-workers demonstrated the utility of such materials in hydrogen sensors, steam electrolyzers and other such solid-state devices [50]. Comparison of a proton conductor with an oxide ion conductor as the electrolyte in (a) ethane fuelled and (b) hydrogen fuelled cells is made in Figure 1-3 below:

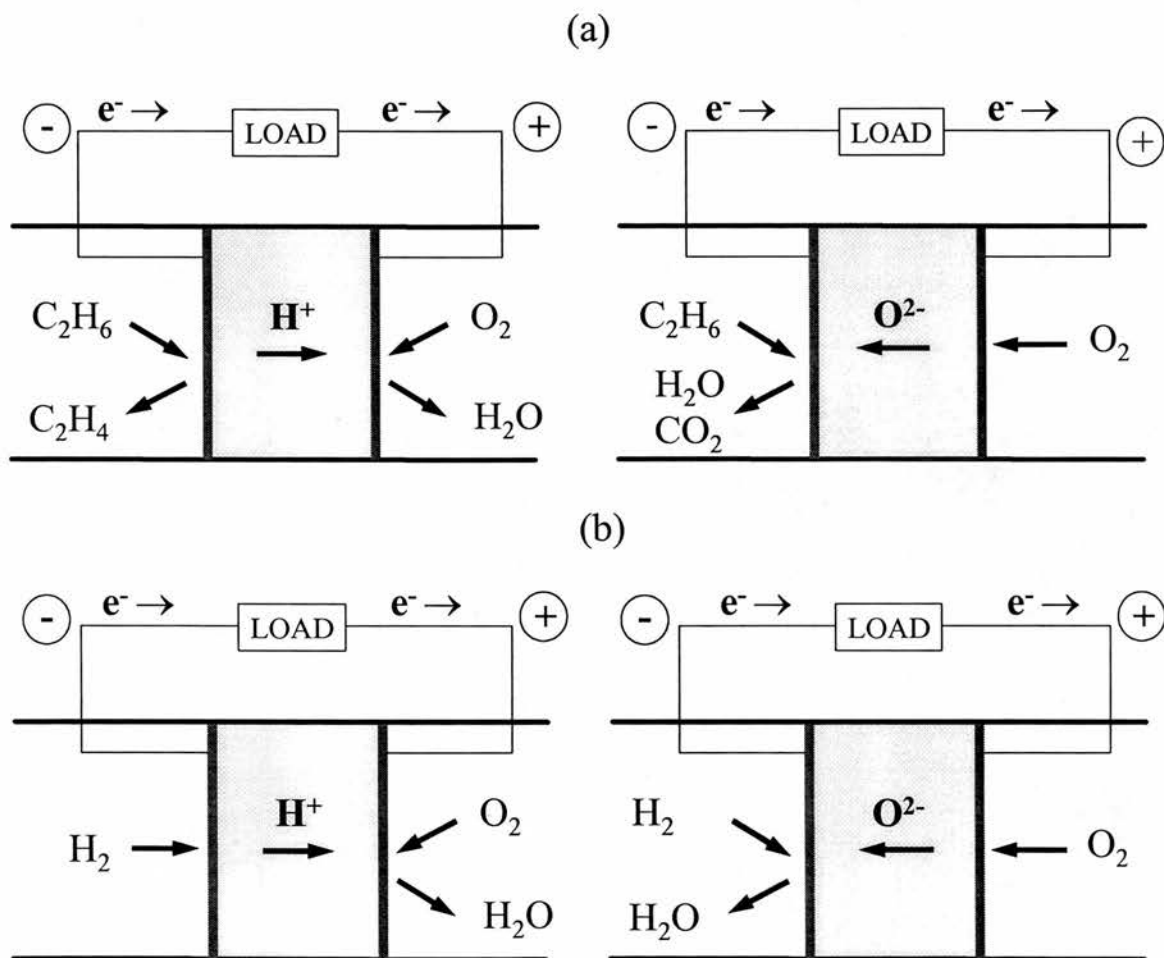


**Figure 1-3: Comparative schematics of proton and oxide ion conducting electrolytes using (a) ethane or (b) hydrogen as fuel, after Ref. [55]**

Under investigation in this project are the so-called “1/3-2/3” perovskite-type oxides of the formula  $A(B'_{1/3}B''_{2/3})O_3$  or more clearly written as  $A_3(B'B_2)O_9$ , where A is a divalent cation ( $Sr^{2+}$  or  $Ba^{2+}$  for example),  $B'$  and  $B''$  are divalent and pentavalent cations, respectively ( $B' = Ca^{2+}$ ,  $B'' = Nb^{5+}$ , for example). These types of compounds may show ordering on the B sites in the perovskite lattice.

$O^{2-}$  ion vacancies in the lattice can be created in these materials without the need for additional dopants on the B-site. A shift in stoichiometry is employed to reduce the overall ionic charge on the B-sites so that it will be compensated for by the creation of oxide ion vacancies in the oxide ion lattice. The new molecular formula will then be represented by  $A_3B'_{1+x}B''_{2-x}O_{9-\delta}$  e.g.  $B' = Ca^{2+}$ ,  $B'' = Nb^{5+}$  ( $\delta = 3x/2$ ,  $x = 0.18$ ), where the deficiency of oxygen ions in the lattice is caused as a result of the now decreased overall positive charge on the B-sites (+4 in the parent formula unit, and now +3.82 per stoichiometrically shifted formula unit). Subsequent exposure to humid atmospheres is presumed to lead to the incorporation of protons and in Kröger-Vink notation, (see Table 1-2) this can be denoted by:



The protons introduced according to Equation 1-6 are not bound to any particular oxygen ion, but are rather free to migrate from one ion to the next. This easy migration results in the high proton conductivity observed in these stoichiometrically shifted (doped) perovskite oxides. They can be considered as being “doped” because more  $B'$

cations are being introduced into B'' cation sites, i.e. the number of B'' cations has been reduced, and the number of B' cations increased.

Previous work, investigating various types of fuel cells using ceramics based on SrCeO<sub>3</sub> or BaCeO<sub>3</sub> as a solid electrolyte, has shown that when the cell was operated at 800°C, water vapour was detected in the exhaust gas from the cathode at a rate governed by Faraday's Law, indicating that the conduction in the electrolyte was protonic [20]. However, with increasing temperature, the predominant charge carrier in the electrolyte changed from protons to oxygen ions. The measurement of water evolution from anode and cathode enabled the respective contributions of protons and oxygen ions to the conduction to be determined. Thermal cracking of hydrocarbons on the anode surface in a fuel cell with a proton conducting electrolyte has also been investigated, especially in the case of ethane as the fuel [56]. H<sub>2</sub>, C<sub>2</sub>H<sub>4</sub> and residual C<sub>2</sub>H<sub>6</sub> were detected in the exhaust gas from the anode. Water vapour, the product of the cell reaction, was observed at the cathode.

## 1.5 Protonic Conduction in Solid Oxide Fuel Cell Electrolytes

Protonic conduction can be considered as a particular case of ionic conduction; however there are some similarities with electronic conduction because of the proton size (radius is approximately  $1.5 \times 10^{-3}$  pm). In both cases, defects play an important role.

A problem arises in finding out whether the conductivity of the material is due to mainly electronic mobility (*n* or *p* type) or mainly ionic conductivity (electrolytic domain), respectively [57].

The ionic transport number  $t_i$  is represented by the following equation:

$$t_i = 1 - [\sigma_e / (\sigma_e + \sigma_i)] \quad \text{Equation 1-8}$$

where  $\sigma_e$  is electronic and  $\sigma_i$  ionic conductivity respectively. The ionic transport number is directly related to the utilisation of the material as electrolyte or insertion electrode. The  $\sigma_e / (\sigma_e + \sigma_i)$  ratio is usually of the order of  $10^{-5}$  or  $10^{-6}$  if the material is supposed to be used as an electrolyte. Its measurement is not straightforward and has rarely been made for protonic conductors.

Clearly, the requirements for a typical High Temperature Proton Conductor (HTPC) for use in SOFCs must include high proton conductivity, along with low conductivity of other species [58]. The expression for the protonic conductivity can be expressed as the Nernst-Einstein relation:

$$\sigma = \frac{F^2}{RTV_m} [\text{OH}^*] D_{H^*}^{eff} \quad \text{Equation 1-9}$$

where  $F$  is the Faraday constant,  $V_m$  the molar volume and  $D_{H^*}^{eff}$  the effective diffusivity of the protons, with activation energy  $E_{H^*}^{eff}$ . The maximum hydrogen concentration can be given by  $[\text{OH}^*] \approx 2\delta$ , where  $\delta$  is the deviation from a full oxygen compliment, i.e.  $\text{AB}_{1-x}\text{C}_x\text{O}_{3-\delta}$  due to doping on the  $\text{B}^{4+}$  site by  $\text{C}^{3+}$ , rather than  $\text{ABO}_3$  for a non-doped system. The diffusivity of the proton, is written as:

$$D_{H^*}^{eff} = x_f D_0 \exp(-H_H^m/kT) \quad \text{Equation 1-10}$$

where  $x_f$  is the fraction of protons which are not trapped and are thus free to participate in the conduction process.  $H_H^m$  is the migration energy of the proton.  $D_0$  is usually described as:

$$D_0 = \frac{z d^2 N v_0}{6} \quad \text{Equation 1-11}$$

where  $z$  is the number of jump directions,  $d$  the jump distance,  $N$  the fraction of vacant jump destinations and  $v_0$  the attempt frequency.

The proton transport number must also be optimised. It is represented by:

$$t_H = \frac{\sigma_H}{\sigma_{H^+} + \sigma_{O^{2-}} + \sigma_{e^-} + \sigma_{h^*}} \quad \text{Equation 1-12}$$

Ideally, for a good proton conductor suitable for SOFC purposes, one needs  $t_H \approx 1$ , with  $t_H > t_{O^{2-}}$  and  $t_H + t_{O^{2-}} \approx 1$ . Under fuel atmosphere, the proton conductor should only exhibit protonic ionic conductivity. Large electronic conduction is undesirable here.

Considering the proton transfer to be critical, it was recently discovered that the highest proton diffusivities are observed for perovskites with high lattice constants corresponding to large structural oxygen separations,  $Q_0$  [59]. For  $\text{BaCeO}_3$ ,  $Q_0 = 3.12 \text{ \AA}$  at room temperature, corresponding to a proton transfer barrier of about 1.8 eV, as revealed by a quantum chemical calculation for a fixed oxygen separation  $Q$  [60]. Contrary to the expectation that such a large oxygen separation would allow little hydrogen bond interaction (hindering a path for proton transfer), IR studies of hydroxide ions in some perovskite type oxides have revealed that large structural oxygen separations show a tremendous red shift of the OH stretching frequency. This softening of the fundamental vibration frequency for perovskite-type oxides with relatively large structural oxygen separations corresponds to those which exhibit the highest proton mobilities [61].

## 1.6 Review of doped Barium Cerate, $\text{X}:\text{BaCeO}_{3-\alpha}$

The most widely studied perovskite proton conductors are  $\text{SrCeO}_3$ ,  $\text{BaCeO}_3$  and  $\text{SrZrO}_3$ , doped on the B-cation site with trivalent ions such as  $\text{Y}^{3+}$  and  $\text{Yb}^{3+}$  [50,51,52,53,54,62,63]. Both  $\text{BaCe}_{0.9}\text{Y}_{0.1}\text{O}_{2.95}$  and  $\text{SrCe}_{0.9}\text{Y}_{0.1}\text{O}_{2.95}$  are orthorhombic (space group  $Pnma$ ) at room temperature, and have the following lattice parameters, as determined by X-Ray Diffraction:

Lattice Parameter (Å)	BaCe <sub>0.9</sub> Y <sub>0.1</sub> O <sub>2.95</sub>	SrCe <sub>0.9</sub> Y <sub>0.1</sub> O <sub>2.95</sub>
a	6.2610 (3)	6.1420(1)
b	8.7897(6)	8.5889(1)
c	6.2185(2)	6.0031(1)
V (Å <sup>3</sup> )	342.22	316.68

**Table 1-4 : Lattice parameters for doped Strontium and Barium Cerates [64]**

The introduction of trivalent ions (e.g. Gd<sup>3+</sup>) to the B-site of the stoichiometric compound BaCeO<sub>3</sub> creates vacant oxygen sites, or, when in oxidizing atmospheres, creates electronic holes [65]. It has been proposed [66], based on optical spectra that the electron holes localised on the Ce<sup>4+</sup> sub-lattice of BaCeO<sub>3</sub> in an oxygen atmosphere form small radius polarons (quasi-particles) which determine the mechanism of electronic conduction. The exposure of the material to H<sub>2</sub>O or H<sub>2</sub> containing atmospheres leads to the occupation of previously vacant oxygen sites by hydroxyl groups and the uptake of the remaining protons at other oxygen sites or the exchange of electronic holes with protons. Such rare earth doped strontium and barium cerates exhibit a typical protonic conductivity of 1 x 10<sup>-3</sup> S cm<sup>-1</sup> at 600°C [72]. They have been shown to exhibit appreciable hole (h<sup>•</sup>) conduction in oxidising atmospheres [67], and suffer from decomposition into ACO<sub>3</sub> and CeO<sub>2</sub> species when there is CO<sub>2</sub> present in the surrounding atmosphere [62].

Recently, the dependence of current in SrCe<sub>0.95</sub>Yb<sub>0.05</sub>O<sub>3-α</sub> in a DC hydrogen pump (Figure 1-4) has been investigated with regards to changing the atmosphere from dry Ar to wet H<sub>2</sub> [68]. An increase in current in wet hydrogen atmospheres was attributed to an

increase in potential difference between the anode and cathode due to the appreciable difference in hydrogen activity between the two electrodes. The authors also determined the mobilities of  $H^+$  and  $D^+$  (deuterons) to be  $3 \times 10^{-4}$  and  $2 \times 10^{-4} \text{ cm}^2 \text{ s}^{-1} \text{ V}^{-1}$  respectively at  $900^\circ\text{C}$ .

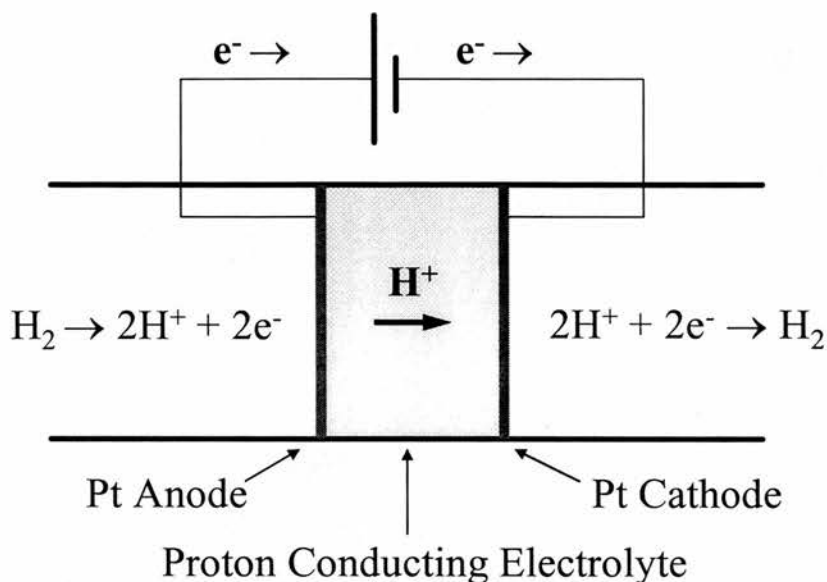


**Figure 1-4 : Principle of the hydrogen pump**

It has been proposed that the grain boundaries in barium cerate, in particular, are responsible for the overall high conductivity of this material. However, with the discovery that [65] even if grain boundaries were to present a relatively easy pathway for ion transport, the area presented by grain boundaries in parallel to the grains is small, and ions consequently would utilise the larger pathway offered by the grain interiors (see Figure 1-5. below):

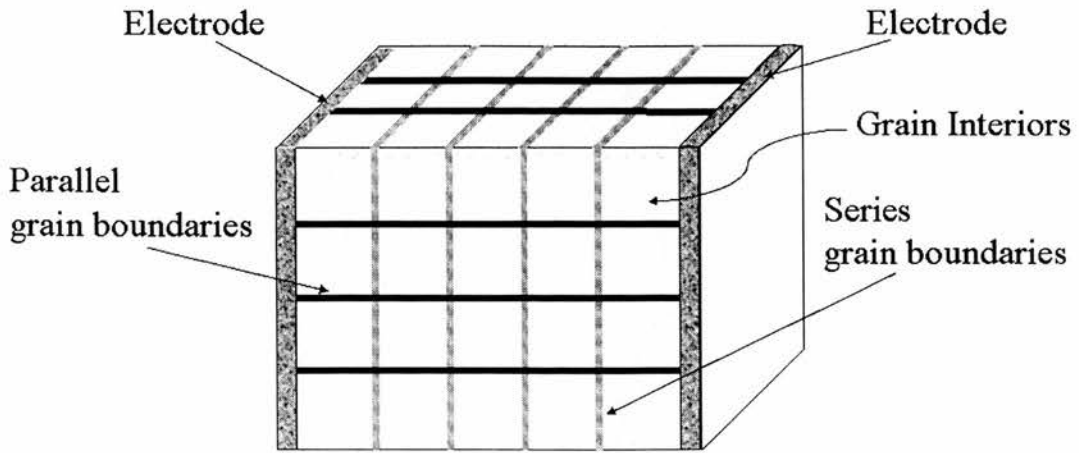


**Figure 1-5: “Brick layer” model of a polycrystalline material. Grains are assumed to be cube-shaped, and grain boundaries to exist as flat layers between grains.**

**Adapted from Ref. [65].**

A lot of work has been done to conclude that changes in the microstructure of Gd doped barium cerate are of lesser importance compared to differences in composition, when considering the conductivity of such a material [18]. It was found that the specific grain boundary conductivity exhibits an activation energy of about 0.7 eV and is independent of grain size, even with a number of different processing routes used. Experimental observations have shown [65] that, for an impedance spectrum that shows two arcs (technique to be described later), the grain boundaries are considerably more resistive than the bulk, regardless of the relative magnitudes of the resistances associated with these arcs. This of course, depends on the stoichiometry of the composition, and it may be possible that excess BaO may precipitate at the grain boundaries. Work by Nafe [69] in the eighties, in analysing the conductivity of several materials and the change from bulk to grain boundary conduction mechanisms as a function of temperature, has justified the efficacy of the brick layer model [70]. However, even now, there are

unresolved questions with respect to the chemical and electrical properties of the grain boundary in these materials.

### 1.7 Review of the proton conductor $\text{Ba}_3\text{Ca}_{1.18}\text{Nb}_{1.82}\text{O}_{9-\delta}$ (BCN18):

$\text{Ba}_3\text{Ca}_{1+x}\text{Nb}_{2-x}\text{O}_{9-\delta}$  with  $x = 0.18$  is more commonly known as BCN18 [71,72,73] and belongs to the mixed perovskites, where the creation of oxygen vacancies is achieved by varying the Ca/Nb ratio, and essentially can be seen as a “doped” system, with increased Ca and less Nb on the B-sites. Reported literature values for the conductivity values of BCN18 [58] are  $1 \times 10^{-4} \text{ S cm}^{-1}$  at  $200^\circ\text{C}$ , and an extrapolated value of  $7 \times 10^{-2} \text{ S cm}^{-1}$  at  $700^\circ\text{C}$ . As the value at  $200^\circ\text{C}$  corresponds to a “frozen-in” situation, and not an equilibrium state (where water vapour is provided in continuous supply, at temperatures above  $270^\circ\text{C}$ ), the extrapolated value may be somewhat unreliable.

It has been shown [48] by electron diffraction for BCN18 that, for values of  $x$  close to zero and those near 0.18, there is a change of ordering among the B-sites, from a 1-2 ordering for the stoichiometric phase where there is one B' plane to two B'' planes in the structure, to a 1-1 ordering in the shifted phases ( $x = 0.15$  to  $0.18$ ), where B' and B'' planes alternate. The same work has also found that the saturation value of  $[\text{H}^{\bullet}_i]$  was approximately  $x/3$  rather than  $x$ , indicating that  $1/3$  of the oxygen-ion vacancies are filled as a result of water vapour treatment (10 hours at  $600^\circ\text{C}$ ). IR measurements on  $\text{H}_2\text{O}$  vapour treated SCN18 (the strontium analogue of BCN18), show a clear OH stretch occurring at  $3300 \text{ cm}^{-1}$ , while the parent (stoichiometric) phase, SCN, shows a very weak or insignificant response [48].

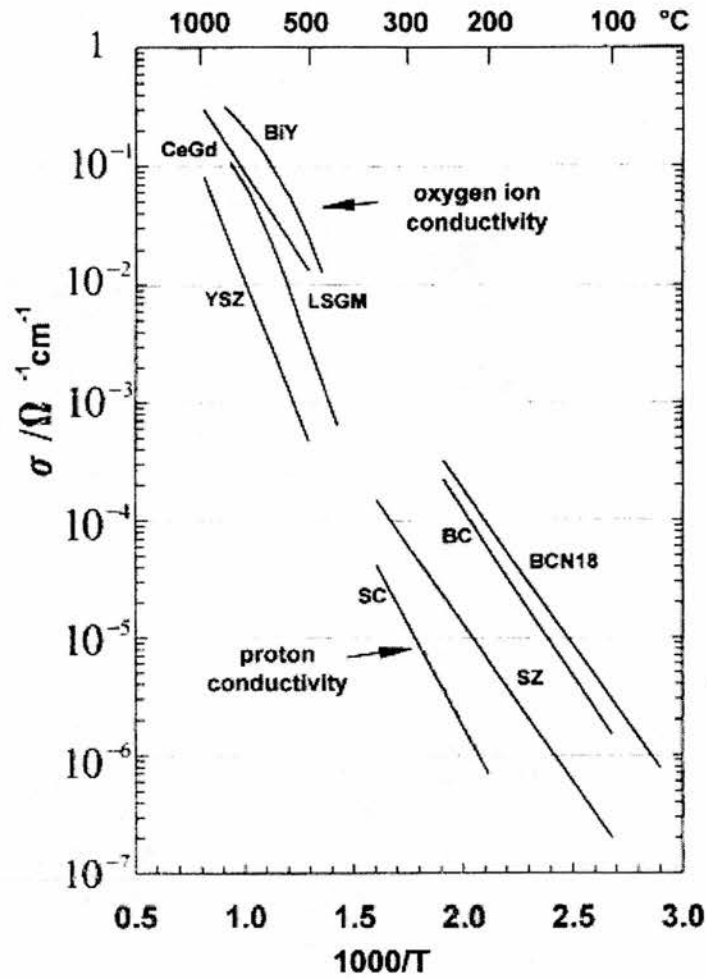


Figure 1-6 : Comparison of the conductivities of some important proton and oxygen ion conductors [58]. BC = 5%Nd:BaCeO<sub>3</sub> [48], SZ = SrZrO<sub>3</sub> [74], SC = 5%Yb:SrCeO<sub>3</sub> [75], BiY = Y<sub>2</sub>O<sub>3</sub> stabilised Bi<sub>2</sub>O<sub>3</sub>, YSZ = Y<sub>2</sub>O<sub>3</sub> stabilised ZrO<sub>2</sub> [76], LSGM = La<sub>0.9</sub>Sr<sub>0.1</sub>Ga<sub>0.8</sub>Mg<sub>0.2</sub>O<sub>2.85</sub> [77], CeGd = Gd doped CeO<sub>2</sub> [78].

A wet chemical route to the synthesis of BCN18 [79] has been successful also, starting with a solution of Ca and Ba acetates, and Nb as a dispersed hydroxide precipitate. A viscous paste was then made by concentrating the original solution, freeze drying, decomposition of the acetates by decalcination, and sintering of pellets. The change in

lattice parameter of BCN18 following exposure to water vapour has also been investigated [80]. This is to be expected, when the oxygen-ion vacancies are filled by molecular H<sub>2</sub>O in the unit cell, and the disappearance of the vacancy. There also seems to be an effect due to the insertion of a proton into the electron cloud of the O-atom with the accompanying change of charge [81]. Schober and Mono report that BCN in the dry state is face centred cubic with a  $\approx 8.4 \text{ \AA}$ , with an increase in a by  $0.203 \text{ \AA}$  when one water molecule is introduced in a unit cell [80]. This doubled primitive unit cell of side  $2a_p$  contains 2.666 formula units of A<sub>3</sub>B<sub>3</sub>O<sub>9</sub> per unit cell (A<sub>8</sub>B<sub>8</sub>O<sub>24</sub>).

Recently, work carried out by Glöckner et al. [82] have investigated the defect structure and transport properties of complex perovskites of the formula Sr<sub>3</sub>(Sr<sub>1-x</sub>Nb<sub>2-x</sub>)O<sub>9-3x/2</sub> through the use of thermogravimetric, conductivity and transport number measurements. They reported values for the enthalpy ( $\Delta H$ ) and entropy ( $\Delta S$ ) of the reaction below (the incorporation of water into vacant oxygen sites to form hydroxyl groups):



as  $-166 \pm 5 \text{ kJ mol}^{-1}$  and  $-160 \pm 5 \text{ J K}^{-1} \text{ mol}^{-1}$  respectively, for the stoichiometry Sr<sub>3</sub>(Sr<sub>1.4</sub>Nb<sub>1.6</sub>)O<sub>8.4</sub>. At 450°C, they report a proton conductivity of between  $1 \times 10^{-5}$  and  $1 \times 10^{-6} \text{ S cm}^{-1}$  at p<sub>H<sub>2</sub>O</sub> values of between  $1.8 \times 10^{-2}$  and  $1.8 \times 10^{-4} \text{ atm}$  respectively.

## 1.8 Aims of this work

An improved level of proton conduction and greater stability of oxides, which may have potential as proton conducting ceramics in electrolytes for SOFCs, is an important issue

in solid state research today. The proton conductor fuel cell or PCFC, can offer advantages over the conventional oxide ion conducting SOFC in that a lower temperature of operation is possible, along with high ionic conduction in the electrolyte, thereby allowing the use of cheaper metallic interconnects in the cell. Established materials such as doped BaCeO<sub>3</sub> exhibit problems of degradation and instability in the presence of CO<sub>2</sub> and little water uptake at intermediate temperatures (350 to 500 °C), with some formation of BaCO<sub>3</sub> and precipitation of Ba(OH)<sub>2</sub>. Even though complex perovskite oxides such as BCN18 offer good protonic conductivity and reasonable stability under reducing atmospheres, the problem of significant electronic conduction may be a possibility due to the reducibility of Nb. The use of Ba is also not desirable, with issues such as high toxicity and sensitivity to CO<sub>2</sub>. New materials must be found without these disadvantages.

The aims of this project were to devise, synthesise and characterise new proton conducting perovskite oxides with potential as electrolytes for the next generation of SOFCs. The search for novel proton conducting oxides therefore involves finding a material without these disadvantages, and yet exhibits a high level of proton conductivity at lower temperatures ( $\approx 10^{-3}$  S cm<sup>-1</sup> at 300 °C). The issues involved include:

1. Hydrothermal treatments to try to incorporate significant amounts of water into the vacancies of this new complex perovskite system and perform variable atmosphere thermogravimetric studies to determine the temperature ranges over which water is incorporated or lost from the structure. (Chapters 3 and 4)

2. Detailed structural characterisation of such a novel perovskite system, in order that structural changes with temperature and water loss be investigated. Further insight into the symmetry changes in these materials with temperature may help in understanding more about how the protonic conductivity may be affected by unit cell distortion.

(Chapter 5)

3. Electrical characterisation of a new potential proton conducting oxide to show that proton conduction is dominant due to the significant increase in conductivity as the sample is hydrated. The change in conductivity with oxygen partial pressure should also be investigated, to examine the material's behaviour in strong reducing conditions or under air.

(Chapter 6)

4. To investigate any other possible structures that might be amenable to appreciable low temperature proton conduction. (Chapter 7)

## 1.9 References

- [1] J.H. Hirshenhofer, D.B. Stauffer, R.R. Engelman, M.G. Klett, "Fuel Cell Handbook – Fourth Edition", Business Technology Books 2000
- [2] W.T. Grubbs, Proceedings of the 11<sup>th</sup> Annual Battery Research and Development Conference, PSC Publications Committee, Red Bank, NJ, p.5 (1957); US Patent No. 2,913,511 (1959)
- [3] T.A. Zawodinski et al., Journal of Electrochemical Society, **1042** (1993) 138
- [4] J.C. Amphlett, M. Farahani, R.F. Mann, B.A. Peppley, P.R. Roberge, in Proceedings of the 26<sup>th</sup> Intersociety Energy Conversion Engineering Conference, August 4-9 (1991), Volume 3, Conversion Technologies/Electrochemical Conversion, American Nuclear Society, La Grange, Illinois, p. 624 (1991)
- [5] S. Gottesfeld, "Polymer Electrolyte Fuel Cells: Potential Transport and Stationary Applications", No. 10, An EPRI/GRI Fuel Cell Workshop on Technology Research and Development, Stonehart Associates, Madison, Connecticut (1993)
- [6] D. Wilkinson, A. Steck, "General Progress in the Research of Solid Polymer Fuel Cell Technology at Ballard", Proceedings of the Second International Symposium on New Materials for Fuel Cell and Modern Battery Systems, Montreal, Quebec, Canada, July 6-10 (1997)
- [7] Ballard, J. of Power Sources **29** (1990) 239
- [8] T. Ralph, Platinum Metals Review, **41** (1997) 102-113
- [9] C.F. Schoenbein, "Ueber die Ursache der Farbenveraenderung, welche manche Koerper unter dem Einflusse der Waerme erleiden", Ann. Phys. Chem. **45** (1838) 263
- [10] C.F. Schoenbein, "Sur la cause du changement de couleur qu'éprouvent certains corps sous l'influence de la chaleur", Bibl. Univ. (NS) **22** (1839) 126
- [11] W.R. Grove, "On a gaseous voltaic battery", Phil. Mag. (III) **21** (1842) 417
- [12] W.R. Grove, "On the gas voltaic battery – Experiments made with a view of ascertaining the rationale of its action and its application to Eudiometry", Phil. Transactions (I) (1843) 91
- [13] W.R. Grove, "On a gas voltaic battery – Voltaic action of phosphorus, sulphur and hydrocarbons", Phil. Transactions (I) (1845) 351
- [14] U. Bossel, "The Birth of the Fuel Cell", Published by the European Fuel Cell Forum (2001), ISBN 3-905592-06-1
- [15] J.H. Hirshenhofer, D.B. Stauffer, R.R. Engelman, M.G. Klett, "Fuel Cell Handbook – Fourth Edition", Business Technology Books 2000, Section 1-9
- [16] T. Takahashi, H. Iwahara, Rev. Chim. Miner. **17** (1980) 610.
- [17] T. Yashima, K. Koide, N. Fukatsu, T. Ohashi, H. Iwahara, Sensors Actuators B **13/14** (1993) 697
- [18] D. Shima and S. Haile, Solid State Ionics **97** (1997) 443
- [19] F. A. Kröger, H.J. Vink, "Relations between the concentrations of imperfections in crystalline solids", in *Solid State Physics*, vol. 3, F. Seitz and D. Turnbull (eds.), Academic Press Inc, New York (1956)
- [20] H. Iwahara, Solid State Ionics, **77** (1995) 289
- [21] O. Nakamura, T. Yodama, I. Ogino, Y. Miyake, Chem. Lett. (Chem. Soc. Japan) **1** (1979) 17
- [22] K.D. Kreuer, M. Hampele, K. Dolde, A. Rabenau, Solid State Ionics **27/28** (1988) 589
- [23] M.G. Shilton, A.T. Howe, Mat. Res. Bull., **12** (1977) 701
- [24] F. Weigel, G. Hoffmann, J. Less-Common Metals, **44** (1976) 99

- [25] K. Metcalfe, T.K. Halstead, *Solid State Ionics*, **26** (1988) 209
- [26] C. Forano, J.P. Besse, J.P. Battut, J. Dupuis, A. Hajjimoahamad, *Solid State Ionics* **34 (1-2)** (1988) 7
- [27] N. Knudsen, E. Krogh Andersen, I.G. Krogh Andersen, E. Skou, *Solid State Ionics* **27/28** (1988) 627
- [28] P.G. Dickens, M.T. Weller, *Solid State Comm.*, **59** (1986) 569
- [29] G. Alberti, M. Casciola, U. Costantino, M. Leonardi, *Solid State Ionics* **14** (1984) 289
- [30] M. Casciola, U. Costantino, *Solid State Ionics* **20** (1986) 69
- [31] M. Casciola, U. Costantino, S. D'Amico, *Solid State Ionics* **22** (1986) 127
- [32] G. Alberti, M. Casciola, U. Costantino, F. Di Gregorio, *Solid State Ionics* **27/28** (1988)
- [33] K.G. Frase, G.C. Farrington, J.O. Thomas, *Ann. Rev. Mater. Sci.* **14** (1984) 279
- [34] J.O. Thomas, G.J. McIntyre, J. DeNuzzio, *Solid State Ionics*, **18,19** (1986) 642
- [35] G.C. Farrington, J.L. Briant, *Mat. Res. Bull.* **13** (1978) 763
- [36] H.H. Hofer, M.F. Bell, A. Rabenau, *Ger. Offen. DE.*, 3013677 (1981)
- [37] A. Rabenau, H.H. Hofer, M.F. Bell, *Ger. Offen. DE.*, 3110571 (1982)
- [38] J. Gulens, T.H. Longhurst, A.K. Kuriakose, J.D. Canaday, "Proceedings of the 6<sup>th</sup> International Conference on Solid State Ionics, 1987, Garmisch-Partenkirchen, Germany", *Solid State Ionics* **27/28** (1988)
- [39] J.D. Canaday, A.K. Kuriakose, A. Ahmad, T.A. Wheat, *J. Can. Ceram. Soc.*, **55** (1986) 34
- [40] E. K. Andersen, I.G. Krogh Andersen, E. Skou, S. Yde-Andersen, *Solid State Ionics* **18/19** (1986) 1170
- [41] K.D. Kreuer, W. Weppner, A. Rabenau, *Mat. Res. Bull.*, **17** (1982) 501
- [42] P.C. Rieke, N.E. Vanderborgh, *J. Electrochem. Soc.*, **134** (1987) 1099
- [43] Nafion<sup>®</sup> is a registered trademark of E.I. DuPont de Nemours & Co.
- [44] K.C. Liang, A.S. Nowick, *Solid State Ionics* **61** (1993) 77
- [45] K.C. Liang, Y. Du, A.S. Nowick, *Solid State Ionics* **69** (1994) 17
- [46] Y. Du, A.S. Nowick, *Mater. Res. Soc. Proc.* **369** (1995) 289
- [47] Y. Du, A.S. Nowick, *J. Am. Ceram. Soc.* **78** (1995) 3033
- [48] A.S. Nowick, Y. Du, *Solid State Ionics* **77** (1995) 137-146
- [49] L. Smart, E. Moore, "Solid State Chemistry – An Introduction", 2<sup>nd</sup> Ed. Chapman and Hall (1995)
- [50] H. Iwahara, T. Esaka, H. Uchida, N. Maeda, *Solid State Ionics* **3/4** (1981) 359
- [51] H. Uchida, N. Maeda, H. Iwahara, *J. Appl. Electrochem.* **12** (1982) 645
- [52] A. Mitsui, M. Migayama, N. Yanagida, *Solid State Ionics* **22** (1987) 213
- [53] N. Bonanos, B. Ellis, M.H. Mahmood, *Solid State Ionics*, **28-30** (1988) 579
- [54] T. Scherban, W.K. Lee, A.S. Nowick, *Solid State Ionics*, **28-30** (1988) 585
- [55] Ph. Colomban, ed., in *Proton Conductors* (Cambridge Univ. Press, Cambridge, 1992) p. 122
- [56] H. Iwahara, H. Uchida, S. Tanaka, *J. Appl. Electrochem.*, **16** (1986) 663
- [57] B.C.H. Steele, R.W. Shaw, Thermodynamic measurements with solid electrolytes, in *Solid Electrolytes*, P. Hagenmuller and W. Van Gool (eds), Ch. 28. *Mat. Sci. Ser.* (Academic Press, New York (1978)).
- [58] T. Schober, F. Krug, W. Schilling, *Solid State Ionics* **97** (1997) 369-373
- [59] K.D. Kreuer, *Solid State Ionics*, **97** (1997) 1-15
- [60] W. Münch, G. Seifert, K.D. Kreuer, J. Maier, *Solid State Ionics*, **97** (1997) 497
- [61] T. Scherban, Yu.M. Baikov, E.K. Sharkova, *Solid State Ionics*, **66** (1993) 159

- [62] T. Yajima, H. Suzuki, T. Yogo, H. Iwahara, *Solid State Ionics*, **51** (1992) 101
- [63] K.C. Liang, I.Y. Lee, A.S. Nowick, *Mater. Res. Soc. Symp.* **293** (1993) 355
- [64] W. Munch, K.D. Kreuer, St. Adams, G. Seifert, J. Maier, *Phase Transitions* **68** (1999) 567-586
- [65] S.M. Haile, D.L. West, J. Campbell, *J. Mater. Res.*, **13** 6 (1998) 1576-1595
- [66] T. He, P. Ehrhart, *Solid State Ionics*, **86-88** (1996) 633
- [67] N. Bonanos, *Solid State Ionics*, **53/56** (1992) 967
- [68] H. Matsumoto, F. Asakura, K. Takeuchi, H. Iwahara, *Solid State Ionics* **129** (2000) 209-218
- [69] H. Nafe, *Solid State Ionics* **13** (1984) 255
- [70] T. van Dijk and A.J. Burggraaf, *Phys. Stat. Sol. (a)* **63** (1981) 229-240
- [71] K.C. Liang, Yang Du, A.S. Nowick, *Solid State Ionics* **69** (1994) 117
- [72] Yang Du, A.S. Nowick, *Mat. Res. Soc. Symp.* **369** (1995) 289
- [73] Yang Du, A.S. Nowick, *J. Amer. Cer. Soc.* **78** (1995) 3033
- [74] T. Yajima, H. Suzuki, T. Yogo, H. Iwahara, *Solid State Ionics* **51** (1992) 101
- [75] Th. Matzke, U. Stimming, R. Hempelmann, C. Karmonik, *Solid State Ionics* **86-88** (1996) 621
- [76] K. R. Kendall, C. Navas, J.K. Thomas, H.C. zur Loye, *Solid State Ionics* **82** (1995) 215
- [77] Man Feng, J.B. Goodenough, *Mat. Res. Soc. Symp. Proc.* **369** (1995) 333
- [78] H. Inaba, T. Tagawa, *Solid State Ionics* **83** (1996) 1
- [79] E. Zimmer, K. Scharf, T. Mono, J. Friedrich, T. Schober, *Solid State Ionics* **97** (1997) 505-509
- [80] T. Mono, T. Schober, *Solid State Ionics* **91** (1996) 155-159
- [81] F.M. Ernsberger, *J. Amer. Cer. Soc.* **66** (1983) 747
- [82] R. Glöckner, A. Neiman, Y. Larring, T. Norby, *Solid State Ionics* **125** (1999) 369

## Chapter Two

### Experimental

"What happens if a big asteroid hits Earth? Judging from realistic simulations involving a sledge hammer and a common laboratory frog, we can assume it will be pretty bad."

*---Dave Barry.*

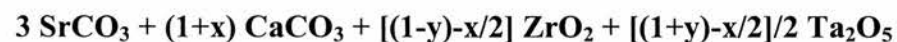
## 2 Experimental

### 2.1 Overview

The procedures and techniques involved in the synthesis and characterisation of a ceramic oxide for potential use as an electrolyte for SOFCs are outlined in the following sections. An outline of 2- and 4-terminal conductivity measurements is given, as well as a description of the apparatus designed to hold the sample. Hydration treatments as well as in-situ treatments during conductivity measurements are described. Structural characterisation by X-ray and neutron diffraction and electron paramagnetic resonance is also discussed.

### 2.2 Solid State Synthesis

Stoichiometric amounts of SrCO<sub>3</sub>, CaCO<sub>3</sub>, ZrO<sub>2</sub> and Ta<sub>2</sub>O<sub>5</sub> (Alfa Aesar, or Aldrich Chemicals, purity >99%) were mixed in the appropriate ratios according to the equation:



where  $\delta = (5x-2y)/4$ .

The starting materials were ground together in acetone in a pestle and mortar for 20 minutes, and also some samples were ground in a planetary ball mill (ZrO<sub>2</sub> mills) for the

same length of time. The mixture was then set in an oven at 170°C to ensure evaporation of the acetone. The mixture was then put in a furnace at 1000°C for 24 hours to achieve decarbonation of the reactants. This was followed by further grinding and/or ball-milling of the mixture for 20 min. The powder was then uniaxially pressed into pellets under 2.5 tons of pressure. The material was then heated to 1400°C in an alumina crucible and left for 2 days, with intermediate grinding for 20 minutes and re-pelletising of the product again after each day. Sintered pellets were also made at 1400°C. An identical procedure was carried out for the  $\text{Sr}_3\text{Ca}_{1+x}\text{Nb}_{2-x}\text{O}_{9-(3x/2)}$  system. Sample densities achievable were approximately 90 % of theoretical.

### 2.2.1 Sample Densities - The number of molecules in a unit cell, Z

The actual density of a sintered pellet of a powder sample can be calculated as follows, with accurate measurements made using a micrometer screw gauge:

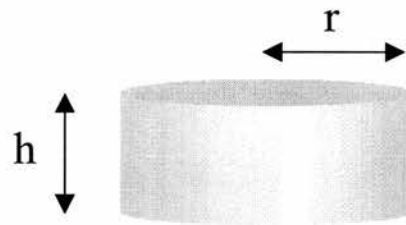


**Figure 2-1: Illustration of a sample compact (sintered pellet) of a powdered ceramic oxide**

$$\rho = \frac{\text{mass}}{\text{Volume}} = \frac{m}{\pi r^2 h} \text{ (g cm}^{-3}\text{)} \quad \text{Equation 2-2}$$

The theoretical density of the unit cell, requires a knowledge of the unit cell parameters, a, b and c (if different) as determined by a solution of the structure by Rietveld Refinement of X-Ray (or neutron) data, and the molecular mass of the material. So:

$$\rho_{\text{theoretical}} = \frac{\text{unit cell mass} \times Z}{\text{unit cell volume}} = \frac{M_r (6.0223 \times 10^{23}) Z}{a \times b \times c (10^{-24})} \text{ (g cm}^{-3}\text{)} \quad \text{Equation 2-3}$$

where the relative molecular mass,  $M_r$  is in  $\text{g mol}^{-1}$  and the unit cell parameters are inserted in Å ( $10^{-10}$  m).  $Z$  is the number of molecules (formula units) per unit cell, and is generally an integer value between 1 and 4.

### 2.3 Hydrothermal Treatments

Hydrothermal treatments involved putting the product as reacted powder, vacuum treated sample or sintered pellet (1-2 g) in a Teflon bomb along with 10 ml of water, sealing the bomb, and heating at 220°C for 24 hours in an oven. Water incorporation was also achieved in the conductivity jig, by treatment with wet 5%  $\text{H}_2/\text{Ar}$  flow at 900°C for 24 hours. Dry reference samples were prepared by vacuum treatment at a pressure of  $2.4 \times 10^{-5}$  bar at 1000°C for 12 hours in a TORVAC variable pressure furnace.

### 2.4 Thermogravimetric Analysis

Thermogravimetric analysis (TGA) involves the study of the change in mass of a sample as the temperature is varied. The instrumentation involves a sensitive balance

with a sample pan inside a furnace whose temperature can be accurately controlled and programmed to change. There are also facilities for controlling the atmosphere ( $O_2/N_2/Ar/H_2$ ) around the sample, as well as a display/manipulation program for integration and derivative curve analysis.

TGA can be used for the qualitative and/or quantitative analysis of a wide range of materials, particularly for inorganics and polymers [1]. A kinetic study, where a weight change accompanies a reaction, is also possible. The weight changes can be used for quantitative analysis of such thermal events as oxidation/reduction and loss of water. Derivatives can easily be obtained, where the weight change is subtle. The balance used in this work was a Rheotherm TG 1000M Thermogravimetric analyser (vertically hanging Pt sample pan) with Rheometric Scientific Plus V v.5.44 Software. The furnace was capable of temperatures up to 1000 °C, with 2 different gas inputs (5 %  $H_2/Ar$  or  $Ar$ ) at flows of 15-20 ml/min. Provisions can also be made for drying/wetting (with soaked cotton wool) the gas streams before entry to the furnace.

## **2.5 Differential Thermal Analysis (DTA)**

The principle of DTA involves the monitoring of the temperature difference between a sample and an inert reference (calcined  $Al_2O_3$ ) as they are uniformly heated (in separate alumina pans). Endothermic or exothermic changes in the sample lead to characteristic deviations in temperature, which can be used for qualitative and quantitative analysis. The instrumentation comprises a programmable electric furnace containing sample and reference, sensitive thermocouples and recorders to give a  $\Delta T/T$  plot, and the facility to

control the atmosphere/gas flow rate surrounding the sample. The equipment used in this work TA Instruments SDT 2960 Simultaneous TGA/DTA, with O<sub>2</sub> or N<sub>2</sub> inputs and PC Software control/data analysis (TA Instruments Universal Analysis). Temperatures from 25°C to 1200°C are possible.

## **2.6 The Alternating Current Impedance Spectroscopy Technique**

### **2.6.1 The Experiment**

The general approach to a basic impedance experiment to ascertain the electrochemical behaviour of an electrolyte or electrode is to apply an alternating electrical stimulus (voltage or current) and observe the materials response in terms of resultant current or voltage. The sample is usually prepared in the shape of a dense cylinder or bar (in the case of a ceramic), and electrodes of Pt or Au are coated on opposing faces. A reducing, oxidising, neutral or vacuum atmosphere can be used in the sample environment to examine the dependencies of the material on the partial pressures of oxygen. The response of the material as a function of temperature, water vapour pressure, and current/voltage bias can all be investigated.

Virtually every liquid and solid is able to pass current when a voltage is applied to it. If a variable (a.c.) voltage is applied to the material, the ratio voltage to current ( $V/I$ ) is known as the impedance. In many materials, especially those which are not generally regarded as conductors of electricity, the impedance varies with the frequency of the applied voltage changes, in a way that is related to the properties of the liquid or solid. This may be due to the physical structure of the material, to chemical processes within it, or to a combination of both. Thus, if a measurement of impedance over a suitable

frequency range is made, and the results plotted on suitable axes, it is possible to relate the results to the physical and chemical properties of the material. Since impedance measurement is repeatable and non-destructive, it can provide valuable insights into the behaviour of a huge variety of substances, components and systems.

A.c. impedance spectroscopy [6] is a very useful technique for studying the conductivity of ionic conductors, not only because the need for non-blocking electrodes is eliminated, but also because the resistances due to grain interiors and that due to grain boundaries can, in many cases be measured independently. Measurements are made over a wide frequency range, and different regions of the material can be characterised according to their electrical relaxation times or *time constants* [2]. From the data obtained and from knowledge of the sample dimensions, the bulk (or grain interior) conductivity can be extracted in a rather straightforward manner.

### 2.6.2 Theory

The term “alternating current” comes from the phasor concept of sinusoidally alternating currents, where along with the associated voltages, they can be thought of as rotating vectors, depicted in the complex plane or Argand diagram. A sinusoidal voltage can be represented by:

$$E = \Delta E \sin \omega t \qquad \text{Equation 2-4}$$

where  $\omega$  is the angular frequency ( $= 2\pi f$ , where  $f$  is the frequency of the signal in Hz),  $E$  is the instantaneous voltage value, and  $\Delta E$  is the maximum amplitude of the signal. Note that  $i$  and  $E$  are *vector* quantities.

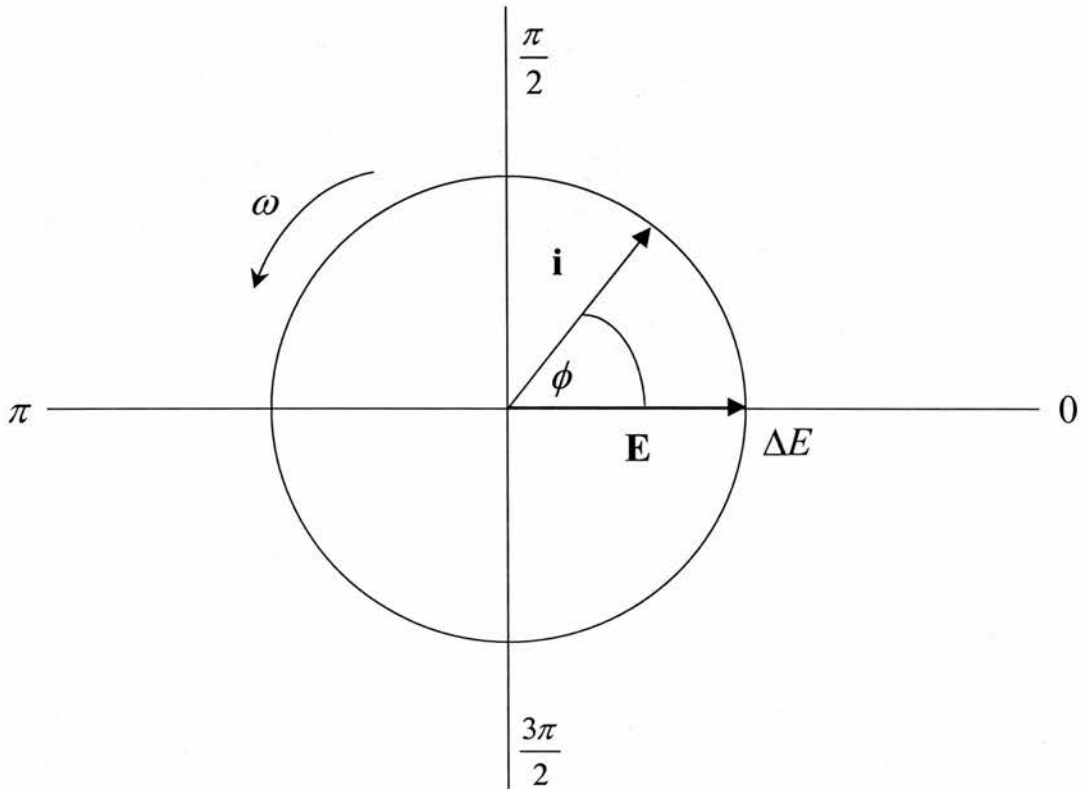


**Figure 2-2: Phasor diagram for an alternating voltage  $E = \Delta E \sin\omega t$ .  $\Delta E$  is the maximum amplitude. The phasor is the rotating vector  $E$ .**

Ordinarily, the current is also sinusoidal with frequency  $\omega$ , and will differ in amplitude. However, there will be a (lagging or leading) phase difference,  $\phi$ , between the current and voltage:

$$i = \Delta i \sin(\omega t + \phi) \qquad \text{Equation 2-5}$$

For a pure resistor,  $R$ , the current response obeys Ohm's Law:

$$i = E/R \qquad \text{Equation 2-6}$$

and the phase angle,  $\phi$  is zero.

The definition of capacitance is the relationship between the potential ( $E$ ) between two plates and the charge ( $q$ ) on the plates:

$$C = \frac{q}{E} \qquad \text{Equation 2-7}$$

On differentiation:

$$i = \frac{dq}{dt} = C \frac{dE}{dt} \qquad \text{Equation 2-8}$$

And from Equation 2-5:

$$i = \omega C \Delta E \cos \omega t \qquad \text{Equation 2-9}$$

The “reactance” of a capacitor,  $1/\omega C$  is denoted by  $X_c$ , and therefore:

$$i = \frac{\Delta E}{X_c} \sin \left( \omega t + \frac{\pi}{2} \right) \qquad \text{Equation 2-10}$$

The phase angle here is positive, so the current “leads” the voltage. Other expressions for  $E$  for a capacitor include:

$$E = E \sin \omega t \quad \text{or} \quad E = -jX_c I \qquad \text{Equation 2-11}$$

For the case of a resistor and capacitor in series, the sum of the potential drops across each element must equal the total potential drop, so:

$$E = E_R + E_c = i(R - jX_c) \quad \text{or} \quad \text{Equation 2-12}$$

$$E = iZ \quad \text{Equation 2-13}$$

where  $Z = (R - jX_c)$  is termed the *impedance*.

The phase angle can now be obtained from the Argand diagram (x-axis = Real Component, y-axis = Imaginary Component to Impedance), as:

$$\tan \phi = \frac{X_c}{R} = \frac{1}{\omega RC} \quad \text{Equation 2-14}$$

A simple circuit comprising a resistor and capacitor in series can be used to describe the properties of an “ideal solid electrolyte”.

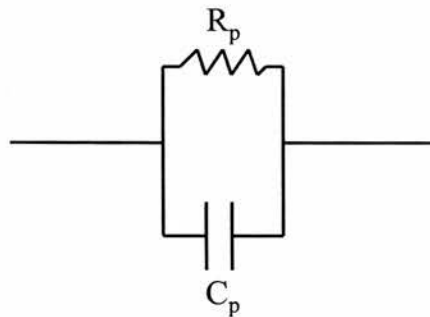


**Figure 2-3: The equivalent circuit for an “ideal solid electrolyte”**

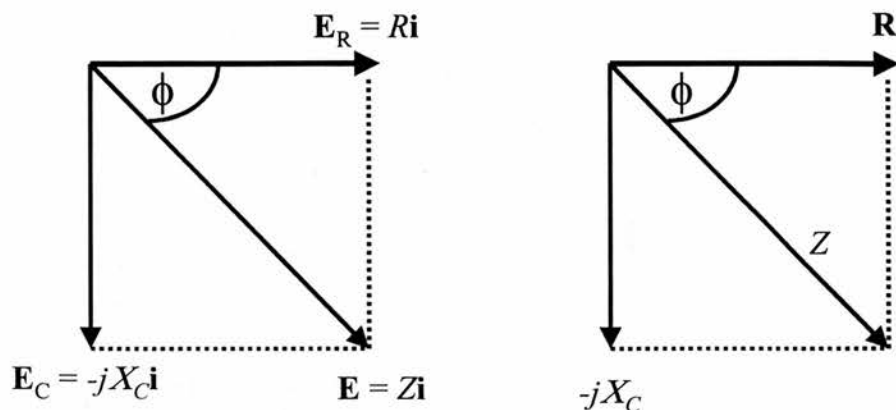


**Figure 2-4: Phasor diagrams for a series resistor and capacitor**

A Nyquist ( $-Z_I$  vs.  $Z_R$ ) plot (e.g. scan from 6 MHz to 0.1 Hz) as a representation of the impedance data of many polycrystalline materials, typically exhibits an arc at high frequency (e.g. 1 MHz to 4 kHz), a second arc at intermediate frequencies (e.g. 4 kHz to 25 Hz), and a linear portion at the lower frequencies (e.g. 25 Hz to 0.1 Hz). Depending on the capacitance values associated with each of the arcs, these three regimes can correspond to the bulk, grain boundary and electrode response, respectively. On investigation of the conductivity regimes of the perovskite oxides examined in this thesis, the following scheme (Table 2-1) has been suggested for the capacitance values of the components of the various responses possible:

Capacitance value (F)	Conductivity Phenomenon
$10^{-12}$	Bulk
$10^{-11}$	Minor second phase
$10^{-11} - 10^{-8}$	Grain boundary
$10^{-10} - 10^{-9}$	Bulk Ferroelectric
$10^{-9} - 10^{-7}$	Surface layer
$10^{-7} - 10^{-5}$	Sample-electrode interface
$10^{-4}$	Electrochemical reactions

**Table 2-1: Corresponding conductivity responses at various capacitance values in AC Impedance [2]**

Figure 2-5 illustrates the typical impedance response for an electroceramic (in this case a perovskite proton conductor). It illustrates how the complex versus real impedance plot can help distinguish between the various resistive components in a ceramic oxide, showing two distinct features attributable to the intra-grain (bulk) and grain boundary regions. The data shown is for 13 mm diameter pellet sample of  $\text{Sr}_3\text{CaZr}_{0.5}\text{Ta}_{1.5}\text{O}_{8.75}$  at 199°C in wet 5 %  $\text{H}_2/\text{Ar}$ .

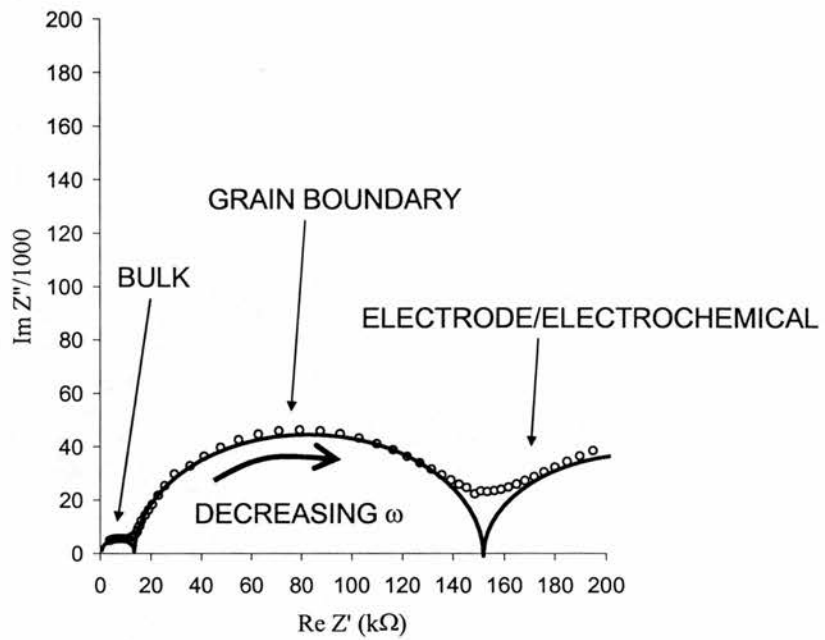


**Figure 2-5: A typical Nyquist plot for a proton conducting solid oxide. The real and imaginary components of impedance are plotted as the frequency of the applied signal is scanned from left to right.**

## 2.7 2-terminal A.c. Impedance Experimental Set-up/Equipment

In this work a Solartron 1260 digital Impedance/Gain-phase Analyser (Frequency Response Analyser, FRA) is used to apply an a.c. current at fixed potential (typically 100 mV) to a ceramic oxide disc, using the two-terminal technique. The ratio of applied potential to current is termed the *impedance*,  $Z$ . A wide current frequency range is possible (0.01 Hz to 32 MHz) with this instrument. It has capacitance, impedance and inductance ranges of 1 pF to 10 mF, 10 mΩ - 100 MΩ, 100 nH to 1000 H, respectively. The instrument is connected to a PC loaded with Z-Plot/Z-View (Scribner and Associates) software via a GPIB (General Purpose Interface Bus) connection, which

enables instrument control/parameter modification as well as real-time plotting of results and post-measurement data analysis.

### 2.7.1 Principle of Operation

The FRA generates a sinusoidal voltage, typically with amplitude of 100 mV, which is applied to the faces (electrodes) of the sample under investigation. The in-phase, and 90° out-of-phase components of the applied voltage are measured at inputs “X” and “Y” on the instrument, expressed as two complex voltages  $V_x = V'_x + jV''_x$  and  $V_y = V'_y + jV''_y$ . These values, as well as the measurement frequency,  $f$ , are recorded by the PC.

### 2.7.2 Electrodes

In most cases, to apply electrodes to a sample, Pt ink (Engelhard-Clal) is carefully painted on each of the faces of a sintered cylinder (disc) of the ceramic material. A well-defined cross-section is thus ensured. A suitable organic solvent such as  $\alpha$ -pinene helps to distribute the platinum evenly. Sometimes Au paste can be used. The pellet with electrodes is then heated to 90°C to evaporate some of the excess solvent. Subsequent heating at 300°C, 600°C, and 900°C in 30 minute stages, with slow cooling to room temperature results in firmly fixed electrodes, without the “islanding”/blistering of platinum or low adhesion.

### 2.7.3 Furnace/Jig Arrangement

The impedance jig used was of a new type, whereby the sample disc is held by the compressive forces of a “split-end” 4-bore alumina tube (Coors Ceramics). The electrode wires were run through thinner single bore alumina tubes slotted through two of the bores of the main alumina tube. The remaining two holes were used for the thermocouple wires. When the split is widened to allow a pellet to be inserted, the compressive forces along the split alumina tube can hold a pellet in place and keep tight and reliable contacts with the electrodes. The set-up is shown below in Figure 2-6 and Figure 2-7. A quartz tube (approx 3 cm internal diameter) of about 25 cm in length was used to sheath the sample environment

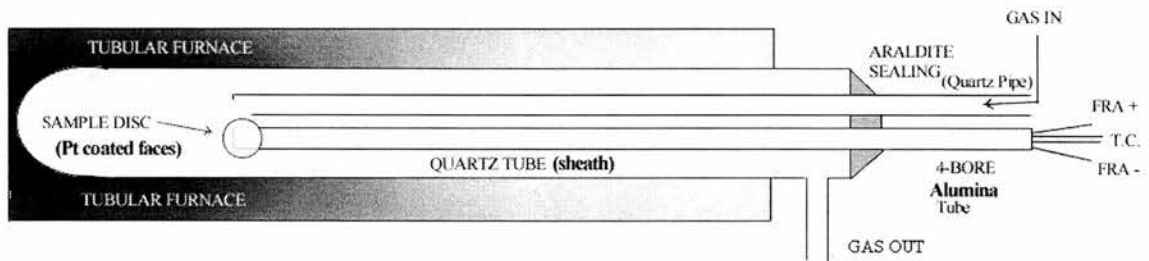


**Figure 2-6: Two-terminal conductivity jig set-up (FRA = Frequency Response Analyser, Solartron)**

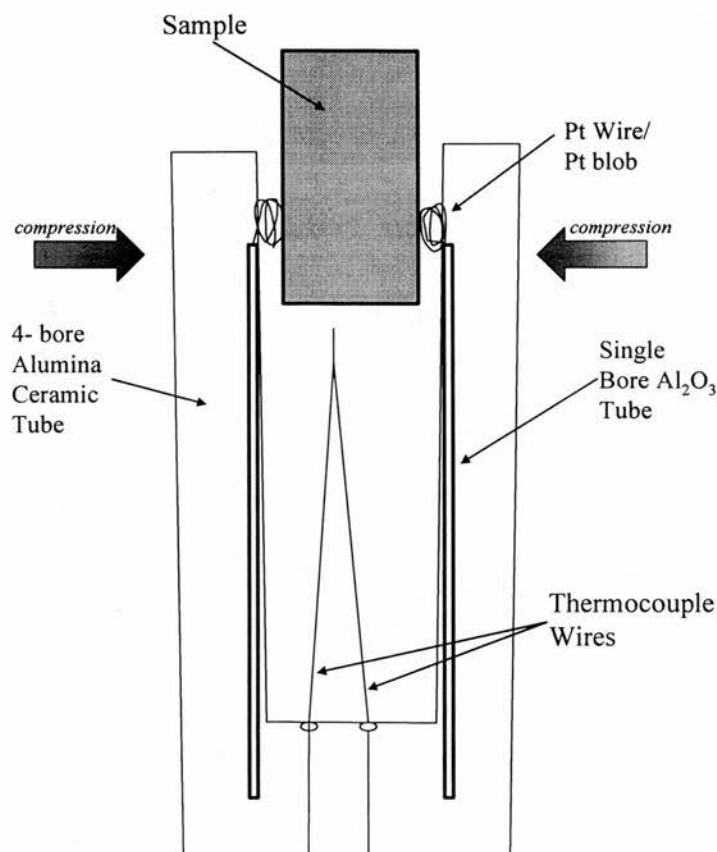


**Figure 2-7: Side-on view of sample pellet in jig held by split-end alumina tube**

In order to elucidate the differences in the electrochemical responses of samples under hydrating and dehydrating atmospheres, gas pre-treatment stages were set up prior to the jig gas inlet. The jig could be set up with a flowing wet gas atmosphere, with distilled water bubblers before and after the gas inlet/outlet. The gas composition then approximates to [4% H<sub>2</sub>O, 4% H<sub>2</sub>, 92% Ar]. Achieving a dry gas input involved changing the first water bubbler for one containing concentrated H<sub>2</sub>SO<sub>4</sub>, a well-known water scavenger, resulting in < 0.01 % H<sub>2</sub>O vapour in the gas inlet stream. . A second bubbler after the output from the conductivity jig ensures a sealed throughput of 5% H<sub>2</sub>/Ar, prevented back-flow from the outlet.

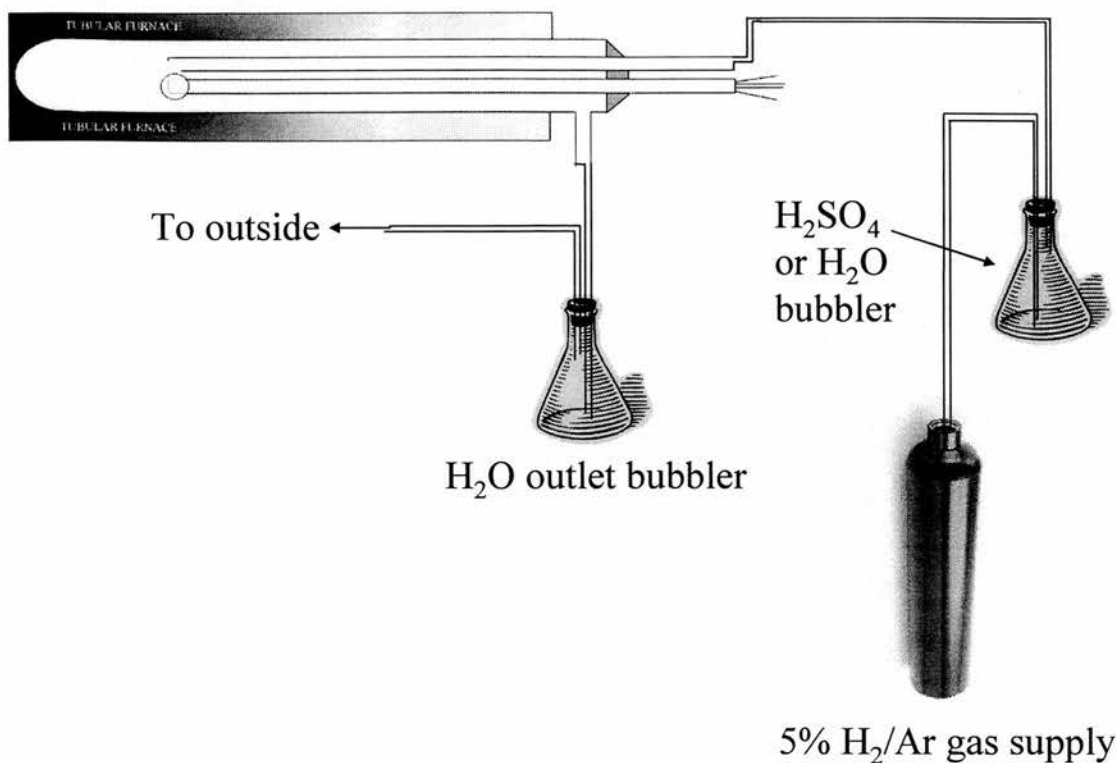


**Figure 2-8: In-situ hydration/dehydration set-up for 2-terminal AC Impedance studies**

## 2.8 4-terminal Conductivity as a function of $pO_2$

Four equally spaced 1 mm thick platinum strips were applied with Pt paste (pinene solvent) to one of the faces of a sintered sample disc. The electrodes were dried of the organic solvent at 900°C for 1 hour. The sample was then placed in the jig assembly with the sample electrodes face down, (see Figure 2-10) to contact the raised Pt wires in the base of the flat ended pyrophyllite tube. A movable cylindrical weight inside the tube helps to keep the sample firmly in place when inserting the jig into the furnace. The furnace was then sealed, heated to the required measuring temperature, and purged with 5 % H<sub>2</sub>/Ar gas to attain the lowest oxygen partial pressure. This reduction

procedure takes a few hours, and oxidation of the sample then involves, shutting off the gas supply and closing both valves. The entire set-up is shown below in Figure 2-9:

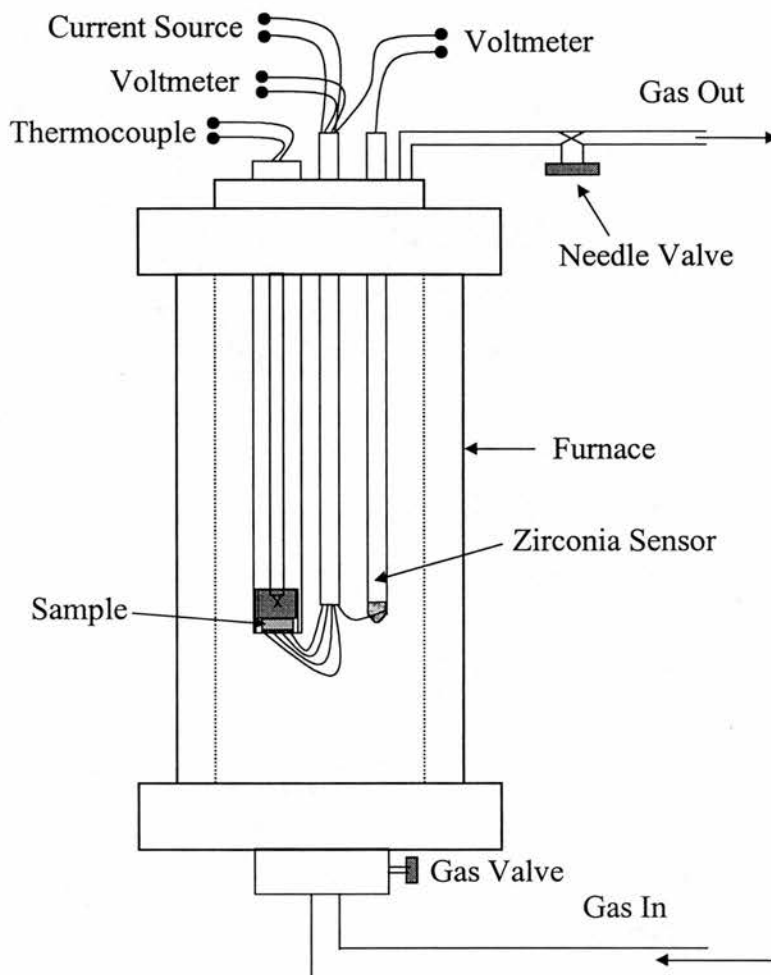


**Figure 2-9: 4-terminal conductivity jig and furnace**

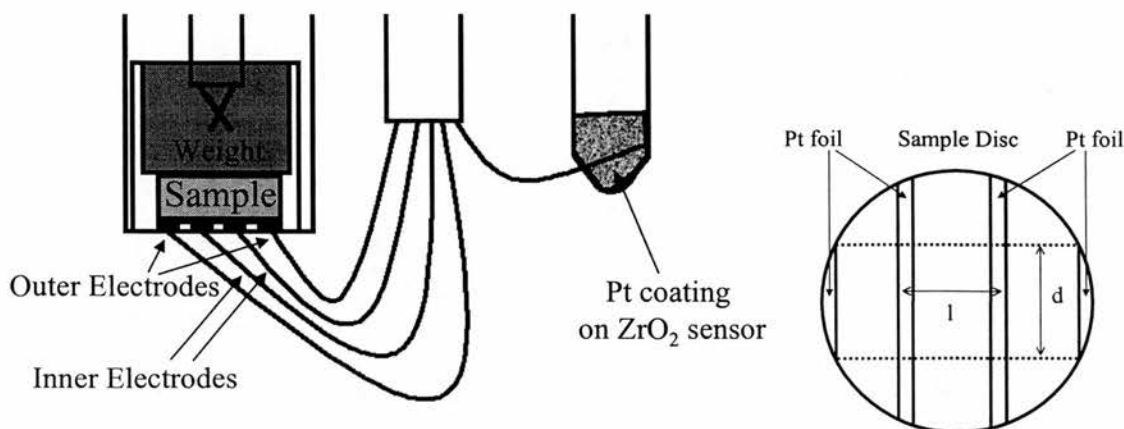


**Figure 2-10: Close up of sample environment and connections**

The reoxidation usually requires waiting overnight for equilibrium to be reached. The resistivity of the sample is calculated from  $\rho = AR/l$ , where  $A (= l \times d)$  is the cross-sectional area of the rectangle outlined by the two centre electrodes (see Figure 2-10 above).  $R$  is the resistance calculated from the input current value applied across the outer electrodes and the voltage measured between the two inner electrodes. The current is applied using a Keithley 220 Programmable Current Source, and the potential difference across the inner electrodes is measured using a Solartron 7065 Voltmeter. The oxygen partial pressure is measured by monitoring the voltage of the  $ZrO_2$  sensor with a Solartron 7150 Digital Voltmeter.

## **2.9 The use of Equivalent Circuits to model the electrochemical responses of polycrystalline materials**

An “Equivalent Circuit” model can be constructed to fit an impedance response, and is indicative of the connection that can exist between the behaviour of a “real” system (e.g. ceramic material), and that composed of ideal discrete electrical components (resistors,

capacitors, inductors, etc.). It is essentially an attempt at fitting the behaviour (with respect to charge and potential) of an ionically conducting solid (conduction in the bulk and grain boundary regions) to that of an idealised electrical circuit. These fits and models however, can only be considered as approximate at best, due to the supposition of linear behaviour in a non-linear system. However, because small-amplitude signals are used, the voltage dependence of the electrochemical parameters can be slow, therefore the a.c. current can be considered linear. Limitations on the correspondence between equivalent circuits and real electrochemical systems include the effect of geometry on current distribution, and the anomalous dependence of conductivity and interface capacitance on frequency. Conductivity is undoubtedly related to the diffusion of ions in a concentration gradient, thus a.c. impedance spectroscopy is useful for the determination of diffusion coefficients (e.g. in thin oxide films).

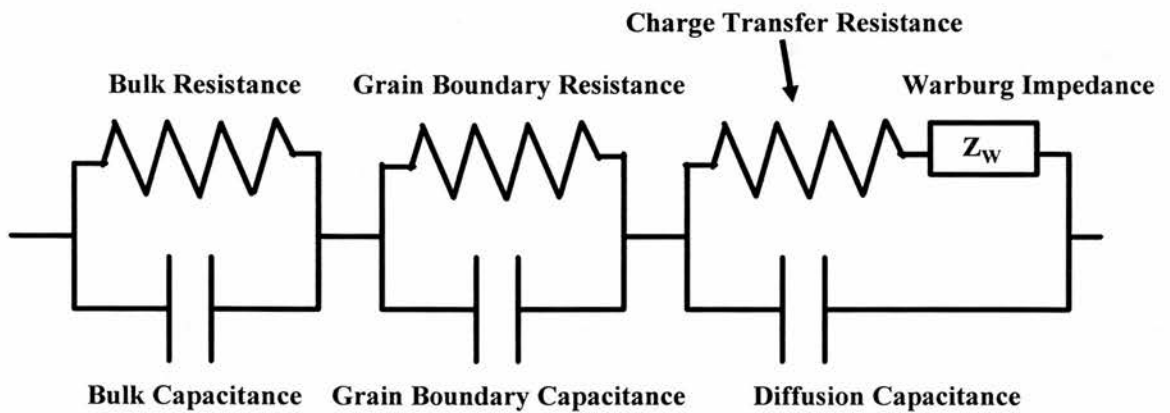


**Figure 2-11: An equivalent circuit for a typical crystalline solid electrolyte.**

In such a circuit as in Figure 2-11, the resistance represents a conductive path, and a given resistor in the circuit would account for the bulk conductivity of a material or perhaps the chemical step associated with an electrode reaction [3]. In a similar fashion, space charge polarisation regions, specific adsorption, and electrocrystallisation

processes at an electrode can be associated with capacitances and inductances. A fact that cannot be avoided is the distinction between ideal resistors and “real” resistors, which would ordinarily be “distributed in space” and therefore possess some residual inductive, capacitive, and time-delay characteristics. However, over wide frequency ranges, these properties are small enough to discard, and it may be possible to model the real physical resistor by a pure, ideal resistance, which does not exhibit any time-delay properties when subjected to an electrical stimulus. It is usually necessary to add a series resistor before the elements in Figure 2-11 above to account for the resistance of the connecting wires from the Frequency Response Analyser to the sample assembly. It may also be insufficient to simply use pure capacitors to describe the capacitive component to the response because of its dependence on frequency as outlined below.

So called “Distributed Elements” can serve as an improvement over a pure capacitor, when used in an equivalent circuit model, especially when attempting to fit a depressed arc. This occurs because the capacitive component has *some* resistance characteristics associated with it. One type of distribution is associated with non-local processes such as diffusion, occurring even in a homogeneous material. With diffusion, charge mobilities are the same all through the material. Another type of distribution is that of the microscopic properties of a material, exemplified by the Constant Phase Element (CPE). This is characterised by the fact that solid electrolyte-solid electrode interfaces are never smooth or uniform, and often exhibit variations in composition and stoichiometry. The overall impedance, therefore, has contributions from the various reaction rates across the interface, and is measured as an average. A distributed phase element such as the CPE, is more suitable a model for this physically real case in

materials, although it exhibits a more complicated frequency response than simple *undistributed* RC time constant processes [4].

The classic example of such property distributions is the relaxation of dipoles in a pseudo-viscous liquid. This was the first distribution involving the CPE and is called the Cole-Cole distribution [5], whereby the normalised complex dielectric constant can be represented as:

$$(\varepsilon - \varepsilon_\infty) / (\varepsilon_s - \varepsilon_\infty) = [1 + (j\omega\tau_0)^{1-\alpha}]^{-1} \quad \text{Equation 2-15}$$

where  $\varepsilon$  is the dielectric constant,  $\varepsilon_s$  and  $\varepsilon_\infty$  are the static and high-frequency limiting dielectric constants,  $\tau_0$  the mean relaxation time, and  $\alpha$  a parameter describing the width of the material property distribution (in the case of Cole and Cole above, it is the distribution of dielectric relaxation times in frequency space).

The most common diffusion circuit is the so-called "Warburg Impedance" diffusion element. This element can be used to model semi-infinite linear diffusion, that is, unrestricted diffusion to a large planar electrode. This is the simplest diffusion situation because it is only the linear distance from the electrode that matters. The Warburg impedance is an example of a constant phase element for which the phase angle is a constant  $45^\circ$  and independent of frequency. The magnitude of the Warburg impedance is inversely proportional to the square root of the frequency ( $1/\omega^{1/2}$ ). The ideal Warburg is unique among CPEs because the real and imaginary components are equal at all frequencies and both depend upon  $1/\omega^{1/2}$ .

## 2.10 Electrode-Electrolyte Interface: Interfacial Electrochemistry

Interfaces across which charged species tend to equilibrate (once contact has been made between the bulk phases), are called *non-blocking* interfaces, and those where there is no intermediate equilibration of charged species are called *blocking* interfaces.

If extreme positive and negative potential differences are avoided, a real blocking electrode can then be considered to be effectively blocking. When the exchange current is very low at a non-blocking interface ( $< 10^{-10} \text{ A cm}^{-2}$ ) it will tend to behave like a blocking interface, so that the distinction between the two types of interfaces is blurred.

Electrical measurements that are made on interfaces generally involve changing the potential difference between two points in the different phases. The potential difference is changed in a sinusoidal manner with time, with an amplitude  $< 10 \text{ mV}$  ( $\Delta E = \Delta E_0 \sin(\omega t)$ ). In this case, the current response is also sinusoidal, but in general is out of phase with the exciting potential by an angle  $\theta$  so that  $\Delta i = \Delta i_0 \sin(\omega t + \phi)$ . This response is expressed as an impedance ( $Z$ ), which is a vector quantity, the magnitude of which is the ratio of the amplitude of the potential to the current, i.e.

$$|Z| = \frac{\Delta E_0}{\Delta i_0} \quad \text{Equation 2-16}$$

whilst the two components of the vector  $Z$  are  $Z' = |Z| \sin \theta$ . Impedance diagrams are produced by representing in the complex (imaginary versus real) a series of  $Z$  values,

corresponding to a range of frequencies. Where an interface behaves electrically like a capacitance ( $C_{dl}$ ), which is generally the case for a blocking interface, then

$$Z = \frac{1}{j\omega C_{dl}} \text{ where } j = \sqrt{-1}. \quad \text{Equation 2-17}$$

In this case the impedance plane display consists of a series of points on the  $Z''$  axis each a distance of  $\frac{1}{\omega C_{dl}}$  from the axis.

In practice, experimental a.c. impedance data are rarely found to exhibit arcs that have their origin on the x-axis, the real impedance axis on the complex plane [6]. The centres of these semicircles are often shifted by an angle  $\theta$  below the real axis. This is attributed to a distribution in the relaxation times within the bulk of the material, or other relaxations within 2 orders of magnitude of the bulk. As mentioned above, these relaxation times can be combined within one element called a CPE or *constant phase element*, which can account for the frequency dependence of the conductivity, when there is a deviation from the ideal resistor and capacitor combination response. This requires the introduction of a frequency independent parameter,  $\phi$  ( $0 < \phi < 1$ ), to the inductive response:

Figure 2-12 below illustrates the relationships between the various depression angles.

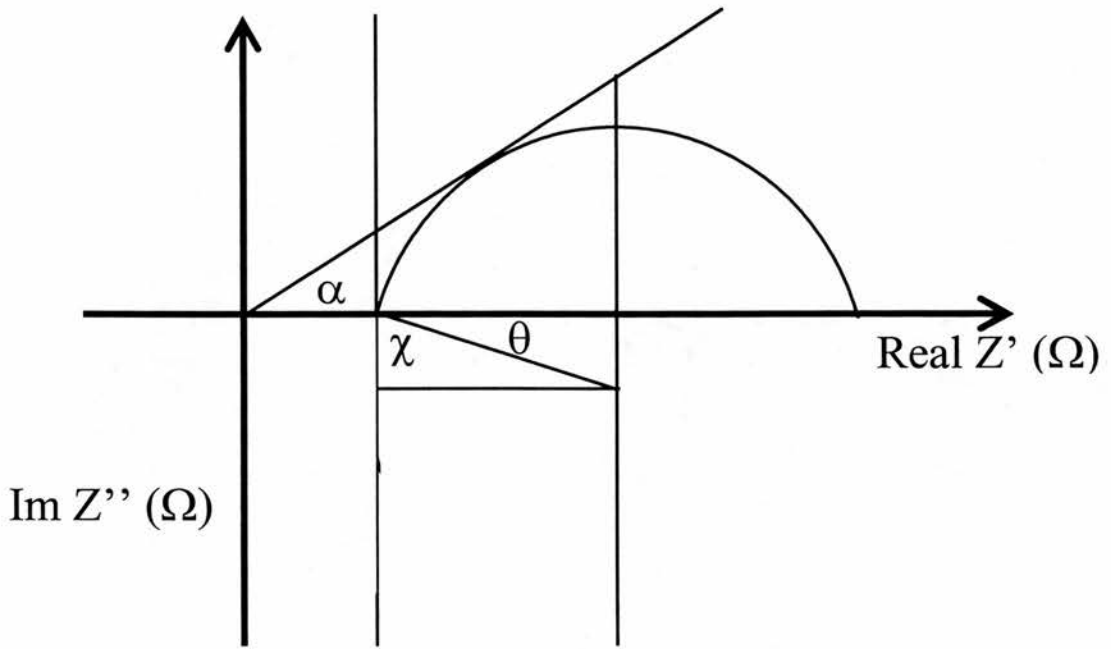


**Figure 2-12 : Nyquist Impedance plot for a depressed circular arc showing angle definitions**

The impedance of a CPE is given by

$$1/Z = Y = Q^\circ (j\omega)^\phi$$

where Y is the admittance,  $1/|Z|$  and  $Q^\circ$  is its value at  $\omega=1$  rad/s.

A consequence of this equation is that the phase angle  $\alpha$  of the CPE impedance is independent of the frequency and has a value of  $[\phi(\pi/2)]$  degrees. This gives the CPE its name. When  $n = 1$ , this is the same equation as that for the impedance of a capacitor, where  $Q^\circ = C$ .

$$1/Z = Y = j \omega Q^\circ = j \omega C$$

The angle relationships can be summarised as follows:

**If**  $\phi = (2/\pi)\chi$                       **and**                       $\chi = (\pi/2) - \theta$                       **Equation 2-18**

**then**  $\theta = (\pi/2)(1-\phi)$                       **or**                       $\phi = 1 - (2\theta/\pi)$                       **Equation 2-19**

and  $\chi = \alpha$

Where  $\phi$  is sometimes used by impedance measurement software to describe the depression angle. Again, because of the presence of distributed phase elements in the material-electrode system, the centre of the arc of an impedance response can lie below the x-axis. In this case, the relaxation time  $\tau$  becomes distributed around a mean,  $\tau_m = \omega_m^{-1}$ . The depression angle  $\theta$  is related to the width of the relaxation time distribution.

## 2.11 X-Ray Diffraction

### 2.11.1 Background

Röntgen made the discovery of X-rays, in 1895. To produce X-rays, an electrically heated tungsten filament is heated (glowing hot) emitting electrons that are then accelerated by a high potential difference (20-50 kV). These electrons then bombard a (Cu or Mo) metal target (anode), which emits a continuous spectrum of “white” X-radiation, superimposed with sharp, intense  $K_\alpha$  and  $K_\beta$  X-Ray peaks. The frequencies of the  $K_\alpha$  ( $\lambda = 1.5418 \text{ \AA}$  for Cu) and  $K_\beta$  lines are characteristic of the anode metal, where the energy of the impacting electrons is sufficient to “knock out” electrons from its innermost K ( $n = 1$ ) shell. Electrons from the shells above fill the resultant holes, and the decrease in energy appears as radiation. Electrons from the L shell ( $n = 2$ ) give rise to the  $K_\alpha$  lines and those from the M shell ( $n = 3$ ) give rise to the  $K_\beta$  lines. These lines

are each actually composed of two very closely spaced lines ( $K_{\alpha 1}$ ,  $K_{\alpha 2}$  and  $K_{\beta 1}$ ,  $K_{\beta 2}$ ). A Ni filter can be used to remove the  $K_{\beta}$  line from the Cu emission, and, using a primary monochromator to separate the  $\alpha 1$  and  $\alpha 2$  lines, one can obtain a monochromatic beam of  $\text{CuK}_{\alpha 1}$  radiation. Software wavelength subtraction techniques can also filter out the  $K_{\alpha 2}$  line, which can complicate the diffraction pattern, by causing doublets to appear.

Synchrotron sources (particle accelerators) also produce X-rays. Synchrotron radiation is the electromagnetic radiation emitted by high-speed electrons spiraling along the lines of force of a magnetic field. Depending on the electron's energy and the strength of the magnetic field, the maximum intensity will occur as radio waves, visible light, or X-rays.

### 2.11.2 Diffraction of X-rays

For the diffraction of X-rays to take place, the wavelength of the incident radiation must be of the same order of magnitude as the interplanar spacing of atomic arrays within the crystal. The three-dimensional crystal structure of a crystalline material acts like a diffraction grating to light of a suitable wavelength ( $\text{CuK}_{\alpha 1}$  radiation). W.H. and W.L. Bragg (1913) first discovered that X-Ray diffraction can be thought of as a “reflection” from the atomic planes within a crystal, but only occurring when the conditions for *constructive interference* are fulfilled. This led to the derivation of the “Bragg equation” and is outlined as follows (refer to Figure 2-13).

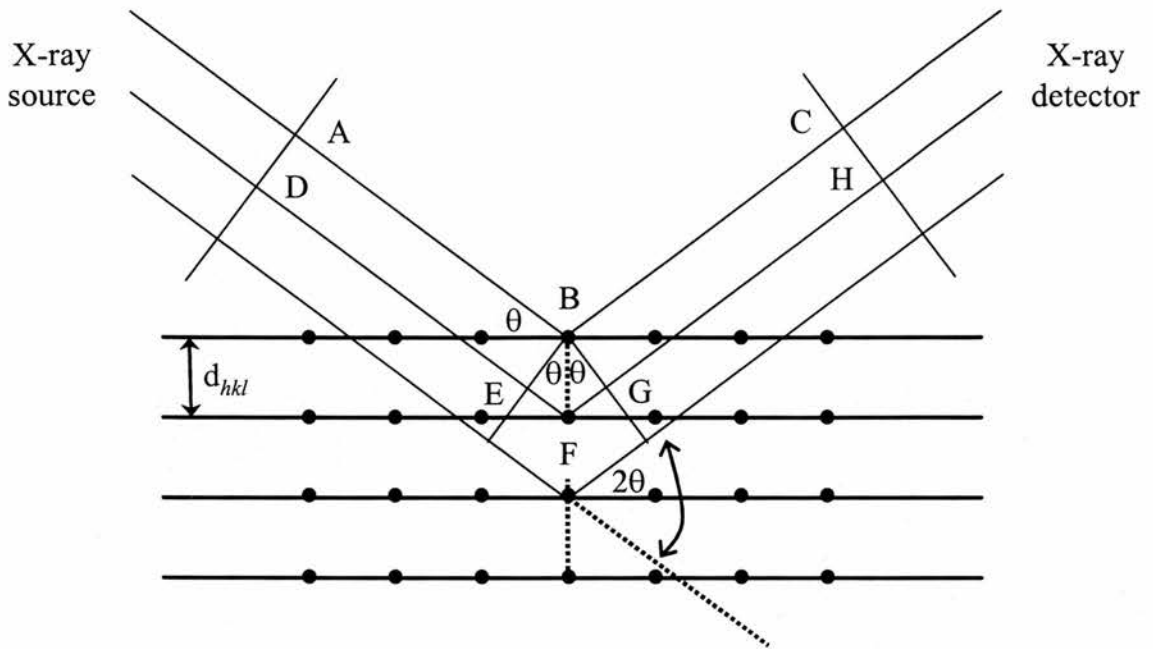


**Figure 2-13 : Illustration of Bragg's Law for the Diffraction of X-rays [7]**

The black lines in Figure 2-13 above represent an array of atomic planes, of Miller index  $hkl$  with interplanar spacing of  $d_{hkl}$  (in Angstroms). A parallel beam of monochromatic X-rays (AD) is incident to the planes at angle  $\theta_{hkl}$ . The ray A is scattered by the atom at B and the ray D is scattered by the atom at F. For constructive interference to occur, the path lengths of the two rays must differ by an integral number of wavelengths. With regard to the two beams ABC and DFH:

$$\text{Path length difference} = (DF + FH) - (AB + BC),$$

However since  $AB = DE$  and  $BC = GH$ ,

$$\text{Path length difference} = EF + FG.$$

From the Figure, it is evident that  $EF = FG = d_{hkl} \sin\theta_{hkl}$

So the total difference in path length is  $2 d_{hkl} \sin\theta_{hkl}$ ,

And, as this must be equal to an integral number,  $n$ , times the wavelength of the radiation,  $\lambda$ , the result is the *Bragg equation*:

$$\mathbf{n\lambda = 2 d_{hkl} \sin\theta_{hkl}}$$

### 2.11.3 Miller Indices

The Miller index notation,  $hkl$ , defines a set of parallel crystallographic planes which intersect the a, b and c axes at  $a/h$ ,  $b/k$  and  $c/l$  respectively.

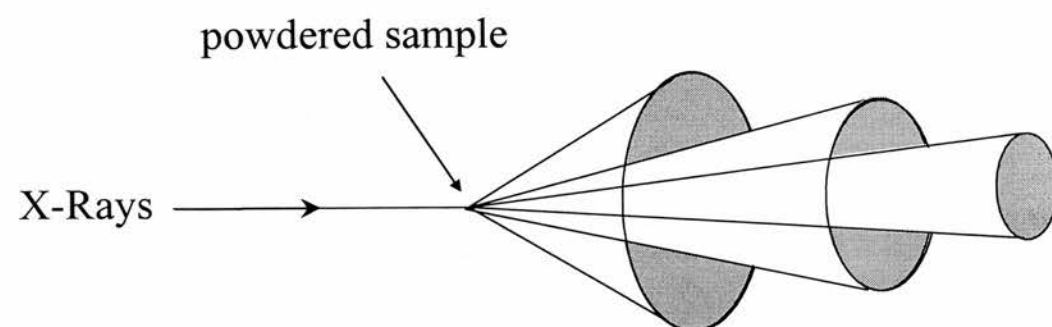
### 2.11.4 The recording of a powder diffraction pattern

When a crystalline ceramic material is finely ground and milled to a powder, the numerous *crystallites* are oriented randomly to one another. On placing such a powdered sample in the path of a monochromatic X-Ray beam, diffraction will occur from the planes in those crystallites that are oriented at the correct angle so as to fulfil the *Bragg condition*. The diffracted beams can be visualised as “cones” of radiation, which make a half-angle of  $2\theta$  with respect to the incident beam (Figure 2-14a). (The full apex angle is  $4\theta$ ). A photographic plate placed perpendicular to the diffracted beams would record a series of concentric rings, Figure 2-14b. In order to expand the maximum  $2\theta$  value that this method could achieve, the *Debye-Scherrer* method employs a strip of film that surrounds the sample, with two holes at the diameter ends for the incoming and exiting beams. The sample is kept rotating at the centre of the film loop, to ensure a maximum in the number of diffracting planes. The  $d_{hkl}$  spacing for each reflection (seen on the uncoiled film loop) can be calculated (via Bragg’s Law) from:

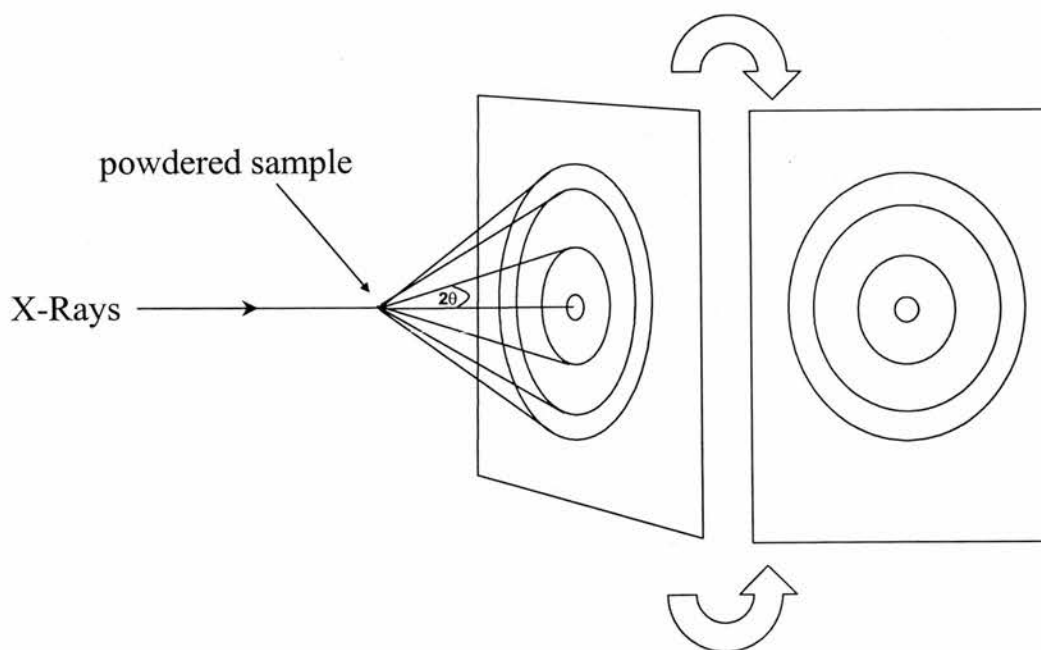
$$\frac{y}{2\pi R} = \frac{4\theta}{360}$$

**Equation 2-20**

where  $y$  is the distance between 2 arcs of the same circle (base of cone) and  $R$  is the camera radius. Modern diffractometers employ the *Debye-Scherrer* method, but make use of an electronic position-sensitive detector (PSD), which scans a wide (typically  $5^\circ$  to  $90^\circ$ )  $2\theta$  range, and records the intensities of the diffracted beams. Assigning the correct  $hkl$  index to each “peak” in the diffraction pattern incorporates the “solving” of the crystal structure, determining its symmetry and unit cell dimensions.



(a)



(b)

**Figure 2-14: (a) Cones produced by a powder diffraction experiment (b)**

**Production of a powder photograph, the angle shown is  $2\theta$ .**

### 2.11.5 Systematic Absences

For a cubic unit cell of side  $a$ , the inter-planar spacing is given by:

$$d_{hkl} = \frac{a}{\sqrt{h^2 + k^2 + l^2}} \quad \text{Equation 2-21}$$

And using the Bragg equation, the following equation can be derived:

$$\lambda = \frac{2a \sin \theta_{hkl}}{\sqrt{h^2 + k^2 + l^2}} \quad \text{Equation 2-22}$$

Rearranged to give,

$$\sin^2 \theta_{hkl} = \frac{\lambda^2}{4a^2} (h^2 + k^2 + l^2) \quad \text{Equation 2-23}$$

For the *primitive* cubic system, all integral values of  $h$ ,  $k$  and  $l$  are possible; however, some values of  $(h^2 + k^2 + l^2)$  are mathematically disallowed with integer values, such as 7, 15, 23, 28.... and so on. With the *body-centred* (I) and *face-centred* (F) classes, even more reflections called *systematic absences* can be absent due to the centring and destructive interference. Upon examination of the reflections from an F-centred system, it is the case that the values of  $h$ ,  $k$  and  $l$  must be *all odd* or *all even*. For an I-centred cell, the total of  $(h + k + l)$  must be *even*. The presence of screw axes or glide planes, can also lead to further systematic absences. For example, a twofold screw axis along  $a$  imposes the restriction that for  $h00$ ,  $h$  must be divisible by 2 (even). Similarly, for a threefold screw axis along  $c$ , the restriction is that  $00l$  must have  $l$  divisible by 3. For an  $a$ -glide plane (translation of  $a/2$ ) perpendicular to  $b$ ,  $h$  must be even. Correspondingly, for a  $c$ -glide,  $l$  must be even for a  $h0l$  Miller Index. The effect of a screw axis is to introduce a plane of atoms between the  $001$  planes, thereby destructively interfering

with them; a glide plane will halve the unit cell length in the direction of the glide. For lower symmetry systems (orthorhombic, monoclinic), there will be a tendency for lines to overlap, due to the greater number of reflecting planes possible. To solve these more complicated structures (and even the higher symmetry ones), a method called *Rietveld* analysis takes into account the intensities of the reflections as well as the peak profiles in order to build up a good theoretical match to the observed data. This will be discussed in a later section.

#### 2.11.6 Peak Intensities

The detector device in a modern X-Ray diffractometer is called a *scintillation counter* and the intensity of each reflection is recorded electronically. Because the intensity of the diffracted wave is proportional to the square of its amplitude, the phase information of the wave is lost, a key piece of information related to the atomic positions in the crystal structure. X-rays are scattered from the electron cloud surrounding the atoms (not the nucleus as neutrons do), and the extent to which this occurs is called the *scattering factor*,  $f_0$  of the particular atom. In general,  $f_0$  depends on the atomic number (the heavier the atom, the more electrons, the greater the scattering), however the presence of a set of atomic planes in between another set of planes may destructively interfere with one another, significantly reducing the expected intensity if considering the mere number of electrons present. This could also result in the reflection appearing absent. For any  $hkl$  reflection, the resultant scattered wave from the contents of the unit cell is called the *structure factor*,  $F_{hkl}$ . It depends on the atomic positions within the unit cell, and their scattering factors. For  $n$  atoms in a unit cell:

$$F_{hkl} = \sum_n f_n e^{2\pi i(hx_n + ky_n + lz_n)} \quad \text{Equation 2-24}$$

where  $f_n$  is the scattering factor of the  $n$ th atom and  $x_n, y_n, z_n$  are its coordinates in the unit cell. Because the diffracted wave is obviously periodic in nature, the above expression can be simplified as a *Fourier series*. A crystal structure consists of a basic motif that is repeated in 3-D space by the symmetry operators of the crystallographic space group. One can determine the coordinates of the atoms in this basic motif, called the *asymmetric unit*. It is the smallest part of a crystal structure from which the complete structure can be built using space group symmetry. The asymmetric unit may consist of only one molecule or ion, part of a molecule, or several molecules that are not related by crystallographic symmetry. So for a unit cell with  $n$  atoms per asymmetric unit:

$$F_{hkl} = 2 \sum_n f_n \cos 2\pi (hx_n + ky_n + lz_n) \quad \text{Equation 2-25}$$

Similarly, a three-dimensional Fourier series can be constructed, to account for the crystal's electron density distribution, with  $\rho(x,y,z)$  representing the electron density at a point  $x,y,z$  in the unit cell:

$$\rho(x,y,z) = \frac{1}{V} \sum_h \sum_k \sum_l F_{hkl} e^{-2\pi i(hx+ky+lz)} \quad \text{Equation 2-26}$$

This is in fact a *Fourier transform* of the structure factors, and the structure factors are a Fourier transform of the electron density. The *Fourier transform*, in essence, decomposes or separates a waveform or function into sinusoids of different frequency which sum to the original waveform. It identifies or distinguishes the different frequency sinusoids and their respective amplitudes. If one knows the structure factors, the electron density distribution can be calculated, leading to a determination of the

atomic positions. The intensity of a hkl reflection is proportional to its structure factor, however some corrections are necessary. These are the *Lorentz correction*,  $L$ , related to the collection mode geometry, and the *polarization correction*,  $p$ , due to the polarization of the diffracted X-Ray beam by the sample:

$$|F_{hkl}| = \sqrt{\frac{KI_{hkl}}{Lp}} \quad \text{Equation 2-27}$$

where  $K$  is a scaling factor.

Because most crystals are not spherical, absorption due to heavy atoms can affect some reflections due to differences in the path length of the reflections, so an *absorption correction* can also be made. Friedel's empirical law [8] claims that diffraction from crystals is symmetric with respect to an inversion of the crystal, even if the elementary cell of the crystal possesses no symmetry. In fact, this rule holds for most crystals which were investigated at that time. Particularly, the rule is true for all purely refractive crystals. Nevertheless, later it was shown that Friedel's law is generally broken in the presence of "anomalous" (absorptive) scatterers. At certain X-ray energies, the incident electromagnetic wave will have a frequency that interferes with the oscillation of bound core electrons of a particular element. This effect, the so-called *anomalous dispersion*, influences the atomic scattering factor,  $f$ , for that particular element:

$$f = \frac{\omega}{\omega - \omega_r^2 - ik\omega} \quad \text{Equation 2-28}$$

where  $\omega$  is the frequency of the incoming wave,  $\omega_r$  is the resonance frequency, and  $k$  is a damping factor.

Not knowing the sign or *phase* of the structure factor creates some difficulties, but some methods have been employed to eventually deduce the atomic positions, among them, Fourier difference maps. When some atoms have been located within the structure, the set of structure factors,  $F_{\text{calc}}$  can be calculated. A difference Fourier calculation compares the values of  $F_{\text{obs}}$  and  $F_{\text{calc}}$  and computes a function with coefficients  $\Delta F = |F_o| - |F_c|$ . The result is a three-dimensional map that reveals the missing electron density within the structure. It is then possible to locate the positions of any missing atoms. With good data, it may be possible to locate hydrogen or deuterium atoms.

### 2.11.7 *Rietveld* Refinement of Crystal Structures

This involves the use of a *least squares method* to *refine* the rough atomic positions, thermal parameters, site occupancies, unit cell parameters, and peak profile (shape) parameters. The work in this thesis was performed using the General Structure Analysis System program, GSAS [9]. The process is continued until the best agreement between the calculated and observed structure factors is achieved. The higher the temperature the sample is subjected to, the greater the volume-spread of electron density around each atom, and thus the scattering factor may need to be corrected for this:

$$f = f_0 e^{\frac{-U \sin 2\theta}{\lambda^2}}$$

**Equation 2-29**

$U$  is the *isotropic temperature factor*, and serves to confine the electron density to a sphere around each atomic nucleus. A further step can be taken to refine the electron density to an ellipsoid shape, using 6 adjustable parameters called the *anisotropic temperature factors*.

The  $R$ -factor or residual index gives a numerical value to the “goodness of fit” of the observed versus the calculated data. These are known as agreement indices or R-values [10]. The weighted-profile R-value,  $R_{wp}$ , is defined as:

$$R_{wp} = \sqrt{\frac{\sum_i w_i [y_i(obs) - y_i(calc)]^2}{\sum_i w_i [y_i(obs)]^2}} \quad \text{Equation 2-30}$$

where  $y_i(obs)$  is the observed intensity at step  $i$ ,  $y_i(calc)$  is the calculated intensity, and  $w_i$  is the weight. The aim is to minimise the numerator over the course of the refinement. If the background is also refined, then the observed and calculated values will also include a background contribution. When the background is included, the R-factor will tend to be lower, as is generally the case for neutron data (below 6% R-factor is the target). X-Ray diffraction data refinements generally result in an optimum value around 10%. The statistically expected R-value,  $R_{exp}$  is the number that  $R_p$  should tend to approach:

$$R_{exp} = \sqrt{\frac{(N - P)}{\sum_i w_i y_i(obs)^2}} \quad \text{Equation 2-31}$$

where  $N$  is the number of observations, and  $P$  is the number of parameters. Thus, the “goodness of fit”, the ratio between the observed and calculated R-factors is defined as:

$$\chi^2 = \frac{R_{wp}}{R_{exp}}$$

**Equation 2-32**

The value of  $\chi^2$  should approach 1 with each successive cycle of least-squares refinement. Other important considerations in the process of data refinement are the *peak profile parameters*, which are a function of the sample microstructure as well as the instrument geometries and type of radiation source. These parameters will generally vary with  $2\theta$  and may also depend on the hkl indices. An analytical *peak shape function* is generally chosen to describe the peak shapes of a diffraction pattern, whereby the coefficients are allowed to vary and refine during the Rietveld analysis.

A typical peak-shape function used for X-Ray and neutron data is the *pseudo-Voigt* [11] approximation of the Voigt function, which combines Lorentzian and Gaussian components in the ratio  $\eta/(1-\eta)$ , where  $\eta$  is the pseudo-Voigt mixing parameter. However, this does not account for peak asymmetry due to the divergence of the diffracted beam at low angles. For instance, Time-Of-Flight (TOF) neutron data tends to exhibit some peak asymmetry, due to the broadening effect of the neutron-pulse structure. In general, the “by eye” quality of the observed, calculated and difference plots of the result of a Rietveld refinement, are generally more informative (to follow and guide the refinement in a sensible way) as to the quality of the fit compared to the reliability factors or R-values.

## 2.12 Neutron Diffraction

### 2.12.1 Theory of Neutron Diffraction

The wavelength of a neutron can be described by the following equation:

$$\lambda = \left( \frac{h^2}{2mE} \right)^{1/2} = \frac{9.04}{E^{1/2}} \quad \text{Equation 2-33}$$

where  $\lambda$  is in Å, the energy  $E$  of the neutron is in meV, and  $h$  is Planck's constant ( $4.136 \times 10^{-12}$  meV s). The neutron mass,  $m$ , is  $1.675 \times 10^{-27}$  kg.

At a pulsed source, the universally applied method of determining  $\lambda$  is to measure the time of flight,  $T$ , of the neutron over a known flight path,  $L$ , from the source ( $T = 0$ ) to sample and subsequently over the scattering path to the detector.

From this, the magnitude of neutron velocity,  $v$ , may be calculated and substituted in Equation 2-33 to yield:

$$\lambda = 0.3955 / v = 0.003955 T / L \quad \text{Equation 2-34}$$

where  $\lambda$  is in Å,  $v$  is in  $\text{m s}^{-1}$ ,  $T$  is in  $\mu\text{s}$  and  $L$  in m. The neutron wavelength and its time of flight have a linear relationship. The neutron beam at a pulsed source is polychromatic and using the TOF method the wavelengths are discriminated by their time of arrival at the detector facilitating the measurement of different  $d$ -spacing at a fixed scattering angle. Bragg's Law may therefore be written as:

$$\lambda_{hkl} = 2 d_{hkl} \sin \theta_0$$

**Equation 2-35**

The combination of Equations 2-34 and 2-35 gives the relation in convenient units of time in  $\mu\text{s}$  and  $d$ -spacing in  $\text{\AA}$ :

$$t_{hkl} = 505.55685(40) L d_{hkl} \sin \theta_0$$

**Equation 2-36**

It should be emphasised that diffractometers, such as HRPD, at pulsed neutron sources operate in a fundamentally different manner from their conventional reactor-based counterparts. Instead of measuring Bragg reflections by scanning a detector from low to high  $2\theta$  scattering angles, HRPD uses the pulsed white beam nature of ISIS to measure Bragg reflections at fixed scattering angles (HRPD backscattering C bank =  $168.33^\circ$ ), monitoring the time of arrival of the neutron after the initial neutron burst produced in the target.

### 2.12.2 Instrumentation

The High resolution Diffractometer (HRPD), offers an unparalleled high resolution and allows subtle effects and complex structures to be studied with great accuracy and precision, and the Polaris Diffractometer which offers rapid data collection, in situ and time-dependent studies; are both located at ISIS, Rutherford Appleton Laboratories [12], a spallation neutron source. Neutrons are produced at ISIS by the spallation process. A heavy metal target is bombarded with pulses of highly energetic protons from an accelerator ring, driving neutrons from the nuclei of the target atoms. This results in an extremely intense neutron pulse, delivered with only modest heat production in the neutron target.

HRPD is the highest resolution neutron diffractometer in the world, located at the ISIS pulsed neutron and muon source in Didcot, Oxfordshire. It is situated approx. 100m from the tantalum target and offers a  $\Delta d/d$  resolution of  $\sim 4 \times 10^{-4}$  from the main backscattering bank, with an effective d-spacing range of 0.3 to  $\sim 5$  Å. This is ideal for the study of phase transitions, or slight changes in unit cell symmetry where the splitting of key peaks can be resolved.

The sample environment is typically a vanadium can on a “candlestick” fitted with a thermocouple. The backscattering bank possesses a ZnS scintillator detector arrangement at a fixed scattering angle (intersecting the entire Debye-Scherrer rings) of  $160^\circ \leq 2\theta \leq 176^\circ$  (solid angle,  $\Omega$ , of 0.41 steradians).

## **2.13 Electron Paramagnetic (Spin) Resonance (EPR/ESR)**

### 2.13.1 Introduction

The great power of this technique lies in the fact that it can detect the presence of unpaired electrons down to very low concentrations, and thus characterise them very precisely in terms of their location and energy states, information which is directly related to the physical properties of the material. It thus has direct application to transition metal compounds, or those formed by irradiation processes, as well as free-radicals, metals and semi-conductors. This technique is undoubtedly spawned from the huge advances made in microwave engineering during World War II.

Electron resonance [13] can only be obtained from materials which possess unpaired electrons, which have an associated spin (angular momentum), and magnetic moment. When a net magnetic moment is present, the material may interact with externally applied magnetic fields. An applied magnetic field (H) will tend to align the magnetic moments of the unpaired electrons and they will be separated into 2 (parallel aligned and antiparallel aligned) groups (those with spin quantum number  $s = +1/2$  and  $s = -1/2$ ). These of course have different energies ( $= \mu H$ ).

The basic idea of a resonance experiment is to apply such an external magnetic field, to produce these two groups of electrons, and the energy separation between them is given by  $g\mu_B B_0$  (where B is the magnetic flux density). The electrons in the lower energy level will absorb quanta of radiation and move to the higher energy level, and this absorption of energy and g-values can be measured. The resonance frequency of absorption is typically in the microwave region (around 1-10 GHz), so a microwave source is used to provide the excitation energy. The fact that stimulated emission produced in both the ground and higher levels does not cancel the absorption of radiation in both levels can be explained by the fact that the ground level is more populated than the higher one. The sensitivity of the technique depends largely on this population difference, which is given by the Maxwell-Boltzmann distribution:

$$\frac{n_1}{n_2} = e^{-\frac{h\nu}{kT}}$$

**Equation 2-37**

therefore higher frequencies and lower temperatures are more desirable.

The single line absorption is the simplest spectrum that can be observed, however there are 5 important parameters associated with it. (1) The integrated intensity: This is

proportional to the number of unpaired electrons in the sample; (2) The width of the absorption line: This is determined by the interaction of the unpaired electron with its surroundings (other electrons, the lattice, or molecule on which it resides); (3) The resonance position of the line in the applied magnetic field: This leads to the determination of the  $g$ -value, and its difference compared to that of a free-electron (2.0023). Electronic intermolecular binding interactions involve spin-orbit interactions, and the resulting variation in the  $g$ -value can give valuable insight into the nature of the bonding involved; (4) The Hyperfine splitting: This arises from the interaction of the unpaired electron with the nuclear magnetic moment of an atom in close vicinity or of the atom itself around which the electron is moving.

If the nuclear spin in general has a value of  $I$ , then  $(2I + 1)$  equally spaced lines of equal intensity will result. Within a molecular system, the intensity distribution follows that of a binomial distribution; (5) Electronic splitting: This occurs when more than one unpaired electron is associated with a particular atom. This arises because of the different orientations and energies now possible, and this splitting is usually several orders of magnitude greater than the hyperfine splitting because electron spins and magnetic moments are involved.

### 2.13.2 The Experiment

Electron Paramagnetic Resonance (EPR) measurements were carried out using a Bruker EMX 10/12 EPR spectrometer operating at 9 GHz with 100 kHz modulation, connected to a PC with WinEPR software. 1-5 mg of sample was contained in a thin glass tube.

### 2.13.3 Theory

For an electron, the spin magnetic moment is proportional to the angular momentum, and the magnetic moment operator is given by:

$$\mu_e = -g_e \mu_B \mathbf{S} \quad \text{Equation 2-38}$$

where  $\mathbf{S}$  is the operator for the spin angular momentum. As the magnetic moment of the electron is *antiparallel* to its spin, a negative sign is introduced.  $g_e \mu_B$  is the magnetogyric ratio, and includes the Bohr magneton,  $\mu_B$ , described by:

$$\mu_B = \frac{e\hbar}{2m_e} = 9.2741 \text{ J T}^{-1} \quad \text{Equation 2-39}$$

where  $e$  and  $m_e$  are the electron charge and mass respectively, and  $g_e$  is the free electron  $g$ -factor equal to 2.0023. It can be viewed as the correction factor for the anomalous magnetic moment of the electron. However, when the electron is involved in atomic or molecular bonding, the  $g$ -value can differ considerably from that of the free electron, and a study of its magnitude and variation with angle can give precise information related to the nature of the bonding present. If either the number of protons or neutrons is odd, nuclei can also possess spin.  $\mathbf{I}$  is the nuclear angular momentum operator of magnitude  $\{I(I+1)\}^{1/2}$ , with  $M_I$  being its projection in a specified direction, and it ranges in integral values from  $+I$  to  $-I$ . Nuclear spins are either integral or half integral. Similarly, the nuclear magnetic moment operator can be written as:

$$\mu_N = \gamma_N \mathbf{I} \quad \text{Equation 2-40}$$

where  $\gamma_N (= g_N \mu_N)$  is the nuclear magnetogyric ratio which is isotope specific. The nuclear magneton can also be described in a similar way to the electron. Nuclear spin and magnetic moment are generally parallel, with some exceptions (e.g.  $^{15}\text{N}$ ).

The basic resonance condition for the free electron is given by the Bohr frequency condition:

$$\Delta E = h\nu = g_e\mu_B B_0$$

**Equation 2-41**

## **2.14 High Pressure Sample Treatment**

### 2.14.1 The Equipment/Experimental

High pressure/temperature oxidising treatments were performed using a piston-cylinder vessel designed by Rockland Research Corporation (New York), capable of hydrostatic pressures up to 34 GPa, and temperatures up to 2000 °C. Potassium perchlorate was used as an oxidising agent, and samples were encapsulated in gold foil. In general, a 20:1 ratio of sample to  $\text{KClO}_4$  was used to ensure oxygen excess, giving a typical total (sample + oxidant) sample weight of around 0.2 g.

NaCl granules were compressed to form a tube (3.5 cm long) which serves as the “pressure medium” used to surround the sample assembly. A thin graphite tube, served as a furnace heating element when electric current is passed through, and this slips inside the NaCl tube. The sample is then encapsulated in gold foil to prevent physical contact with the graphite. The sample is to be located in the centre of the graphite furnace, so rods of MgO (which has a high thermal conductivity and thus smoothes the thermal gradient) are placed above and below the sample capsule, snugly fitting in the graphite tube. The top MgO cylinder has a bore through it for the thermocouple (in alumina rod) assembly, where as the lower MgO cylinder is solid. All of these pieces are contained within the NaCl pressure medium, which is then tightly wrapped in lead foil, which acts as a lubricant. The entire sample assembly is then inserted into the

centre bore of the lower piston assembly, the top electrical contact is connected, the pressure is applied, water cooling turned on, and sample heated to the desired temperature. For reliability and high temperature resilience, an R-Type thermocouple was used [Pt-Pt(87%)/Rh(13%)]. Once the sample is removed after cooling and pressure release, TGA, EPR and XRD experiments were performed to examine water uptake/loss, O<sub>2</sub>/CO<sub>2</sub> loss/uptake, colour changes upon reduction, and phase character.

## 2.15 References

- [1] F.W. Fifield, D. Kealey, "Principles and Practice of Analytical Chemistry", 4<sup>th</sup> Edition, Chapman and Hall (1995) 475ff
- [2] J.T.S. Irvine, D.C. Sinclair and A.R. West, *Adv. Mater.*, **2** (1990) 132.
- [3] R.A. Armstrong, M.F. Bell and A.A. Metcalfe, *Electrochemistry (Chemical Society Specialist Periodical Reports* **6**, (1978) 98-127
- [4] J.F. McCann, S.P.S. Badwal, *J. Electrochem. Soc.* **129**, (1982) 551-559
- [5] K.S. Cole and R.H. Cole, *J. Chem. Phys.* **9**, (1941) 341-351
- [6] J.R. Macdonald, (ed.), "Impedance Spectroscopy", John Wiley and Sons, 1987
- [7] L. Smart and E. Moore, "Solid State Chemistry: An Introduction", Chapman and Hall (1995) 83
- [8] G Friedel, *Comptes Rendus Acad. Sci. Paris* **157** (1913) 1533-1536
- [9] A.C. Larson and R.B. Von Dreele, "General Structure Analysis System (GSAS)", Los Alamos National Laboratory Report LAUR 86-748 (1994).
- [10] L.B. McCusker, R.B. Von Dreele, D.E. Cox, D. Louer and P. Scardi, *J. Appl. Cryst.* **32** (1999) 36-50
- [11] P. Thompson, D.E. Cox and J.B. Hastings, *J. Appl. Cryst.*, **20** (1987) 79-83
- [12] R M Ibberson, W I F David and K S Knight, The High Resolution Neutron Powder Diffractometer (HRPD) at ISIS - A User Guide, Rutherford Appleton Laboratory Report RAL-92-031 (1992)
- [13] "The techniques of NMR and ESR", by R.A.Y. Jones et al., United Trade Press (1965)

## Chapter Three

### The Proton Conducting $\text{Sr}_3\text{Ca}_{1+x}\text{Nb}_{2-x}\text{O}_{9-\delta}$ system

“Learning research tells us that the time lag from experiment to feedback is critical ...”

---*Kent Beck*

### 3 The Proton Conducting $\text{Sr}_3\text{Ca}_{1+x}\text{Nb}_{2-x}\text{O}_{9-\delta}$ system

#### 3.1 Introduction

The perovskite systems  $\text{Ba}_3\text{Ca}_{1+x}\text{Nb}_{2-x}\text{O}_{9-3x/2}$  and  $\text{Sr}_3\text{Ca}_{1+x}\text{Nb}_{2-x}\text{O}_{9-3x/2}$ , that respectively exhibit protonic conductivities when hydrated of  $10^{-4}$  [1] and  $10^{-5}$   $\text{S cm}^{-1}$  [2] for  $x = 0.18$  at  $200^\circ\text{C}$  have been the subject of considerable investigation. On consideration of the chemical formula, the parent phase for these systems might be expected to be a trigonal 1:2 ordered perovskite ( $\text{B}'\text{:}2\text{B}''$ ) of the  $\text{Ba}_3\text{ZnTa}_2\text{O}_9$  type [3].

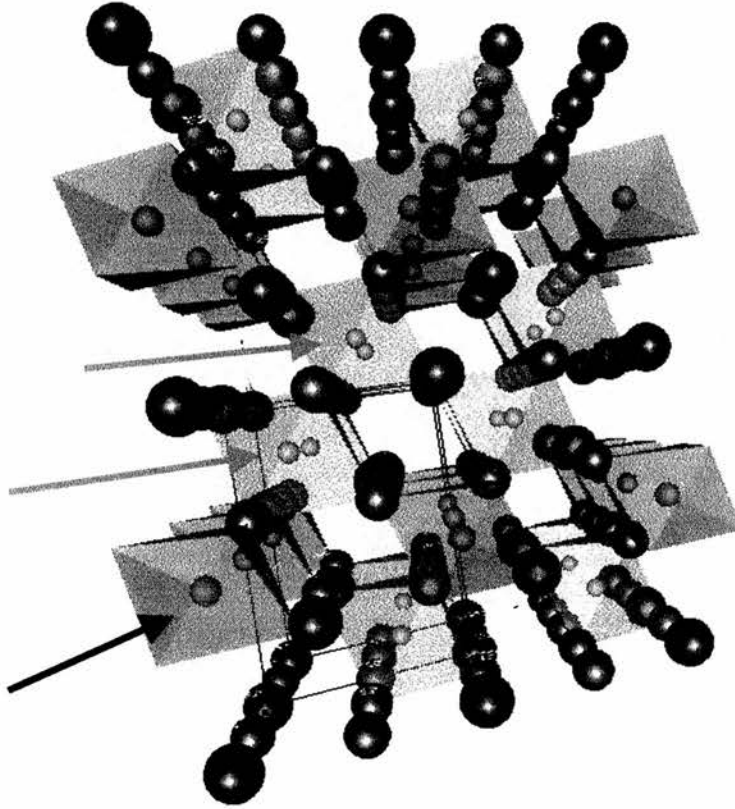


**Figure 3-1: Unit cell of 1:2 B-site ordered  $\text{Ba}_3\text{ZnTa}_2\text{O}_9$ . The arrows highlight the 1:2 alternations of Zn and Ta centred octahedra respectively. Key: Red = Oxygen (some are highlighted), Blue = Sr, Green = Zinc or Tantalum**

Indeed, there are some indications of such order [4]; however, a tetragonal 1:1 order [i.e.  $1B'':(0.66B''/0.33B')$ ], where one B-site alternates with a shared B-site in three dimensions throughout the structure in a “chessboard” type arrangement, is generally reported to be much more prevalent [2].

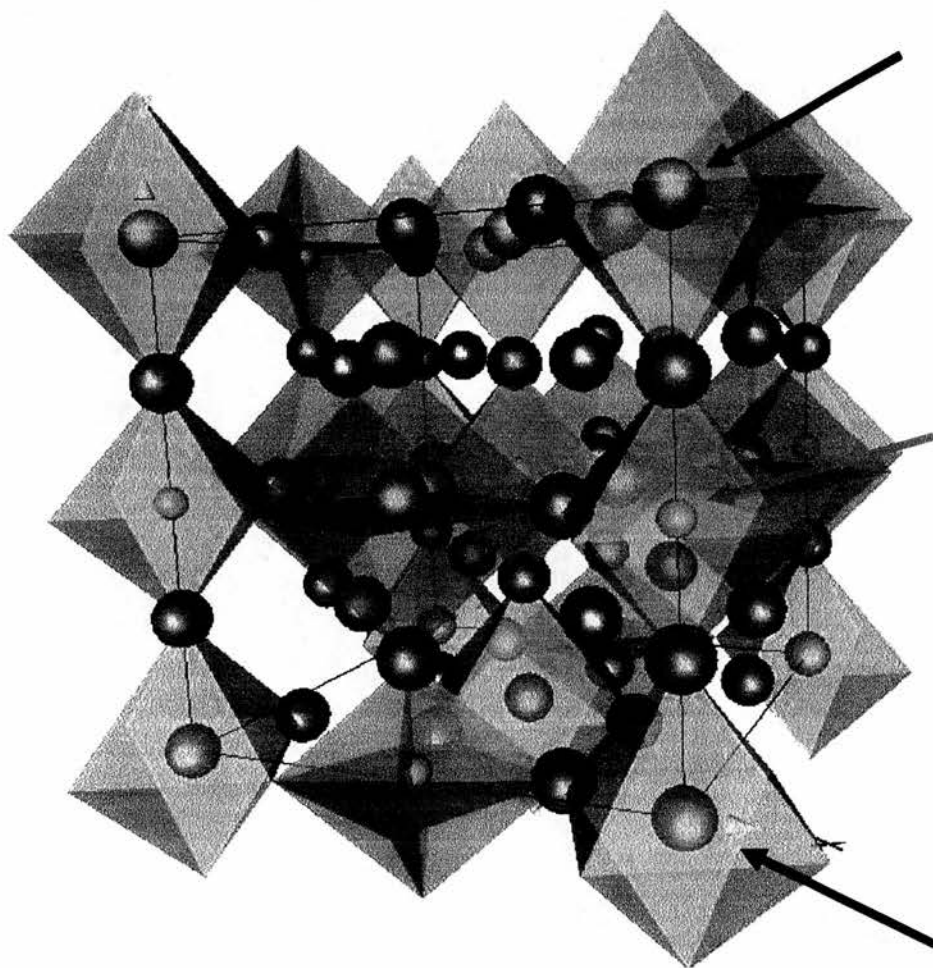


**Figure 3-2: Unit cell of  $Sr_3CaNb_2O_9$ , with arrows distinguishing the Nb and Ca/Nb centred octahedral, alternating in three dimensions.**

The simple cubic primitive perovskite formula,  $ABO_3$  of unit cell parameter  $a_p$  can be extended in the form of multiple complex systems such as  $A_2B'B''O_6$  and  $A_3B'B''_2O_9$  (e.g.  $Sr_3CaNb_2O_9$  [5]). These give rise to double ( $2a_p \times a_p \times a_p$ ), triple (rhombohedral), and quadruple perovskite ( $2a_p \times 2a_p \times 2a_p$  cubic *or*  $\sqrt{2}a_p \times \sqrt{2}a_p \times 2a_p$  tetragonal) unit cells compared to the simple primitive cubic cell. The triple perovskite unit cell is of trigonal (rhombohedral) symmetry, with 1:2 ordering of B-site cations. An archetypal example is  $Ba_3ZnTa_2O_9$  [6], with trigonal space group P-3m1 (No. 164) and lattice parameters  $a = 5.780(1) \text{ \AA}$  and  $c = 7.104(1) \text{ \AA}$  for the hexagonal setting. Most phases within the  $Sr_3Ca_{1+x}Nb_{2-x}O_{9-\delta}$  system exhibit 1:1 order however, and are better described as  $Sr_2Ca_{0.666+x}Nb_{1.333-x}O_{6-\delta}$ . The unit cell is reported to be of the tetragonal ( $2a_p \times 2a_p \times 2a_p$ ) type, with space group P-4 (No. 81) and lattice parameters of  $a = b = 8.190 \text{ \AA}$ ,  $c = 8.209 \text{ \AA}$ .

Here we report in more detail on the structural changes associated with extent of hydration and change in temperature of  $Sr_3Ca_{1.18}Nb_{1.82}O_{8.73}(H_2O)_y$ . In situ studies have been performed using both neutron and X-Ray techniques.

## 3.2 Results and Discussion

### 3.2.1 Thermogravimetric Analysis of the related composition



An as-prepared sample of  $Sr_3Ca_{1.1}Nb_{1.9}O_{8.85}$  (white powder) was first vacuum dried ( $10^{-4}$  mbar) at  $1000^\circ\text{C}$  for 6 hours resulting in a grey powder. The sample was then heated to  $1000^\circ\text{C}$  and cooled to room temperature in a flowing wet 5%  $H_2/Ar$  atmosphere (gas pre-bubbled through distilled  $H_2O$  at room temperature, 3 kPa vapour

pressure). The TGA experiment was run on this resultant hydrated sample under a dry 5% H<sub>2</sub>/Ar atmosphere (10-15 ml min<sup>-1</sup>). A buoyancy effect due to the continuous gas flow over the sample results in a gradual superimposed slope for small weight losses. The plot is shown in Figure 3-3:

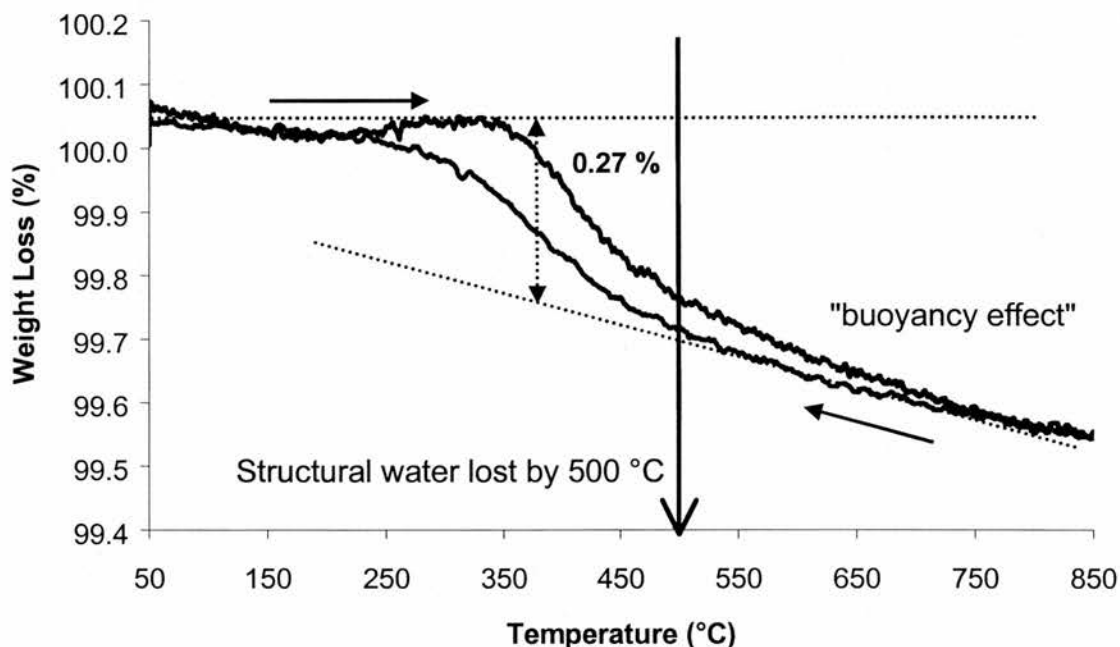


**Figure 3-3: TGA trace for hydrated Sr<sub>3</sub>Ca<sub>1.1</sub>Nb<sub>1.9</sub>O<sub>8.85</sub> under dry 5% H<sub>2</sub>/Ar flow.**

Any hydrated composition can be written as Sr<sub>3</sub>Ca<sub>1.1</sub>Nb<sub>1.9</sub>O<sub>8.85-x</sub>(OH)<sub>2x</sub>. The theoretical maximum water uptake (all oxygen vacancies filled) would result in a sample of composition Sr<sub>3</sub>Ca<sub>1.1</sub>Nb<sub>1.9</sub>O<sub>8.7</sub>(OH)<sub>0.3</sub>. The weight loss of 0.27 % would correspond to the filling of approx. 66 % of the oxygen-ion vacancies by O-H groups, giving the hydrated composition Sr<sub>3</sub>Ca<sub>1.1</sub>Nb<sub>1.9</sub>O<sub>8.75</sub>(OH)<sub>0.2</sub>. The average temperature for the maximum rate H<sub>2</sub>O loss/uptake rate was found to be 380°C. Very similar results were obtained for the hydrated Sr<sub>3</sub>Ca<sub>1.18</sub>Nb<sub>1.82</sub>O<sub>8.73</sub> phase.

### 3.2.2 X-Ray diffraction studies of $\text{Sr}_3\text{Ca}_{1.18}\text{Nb}_{1.82}\text{O}_{8.73}$

Refinement of XRD data of  $\text{Sr}_3\text{Ca}_{1.18}\text{Nb}_{1.82}\text{O}_{8.73}$  reveals a face-centred (doubled  $a_p$ ) cubic unit cell of side 8.2153(2) Å. All the major peaks are indexed in Figure 3-4 below.

The data were refined using the Fm-3m space group.

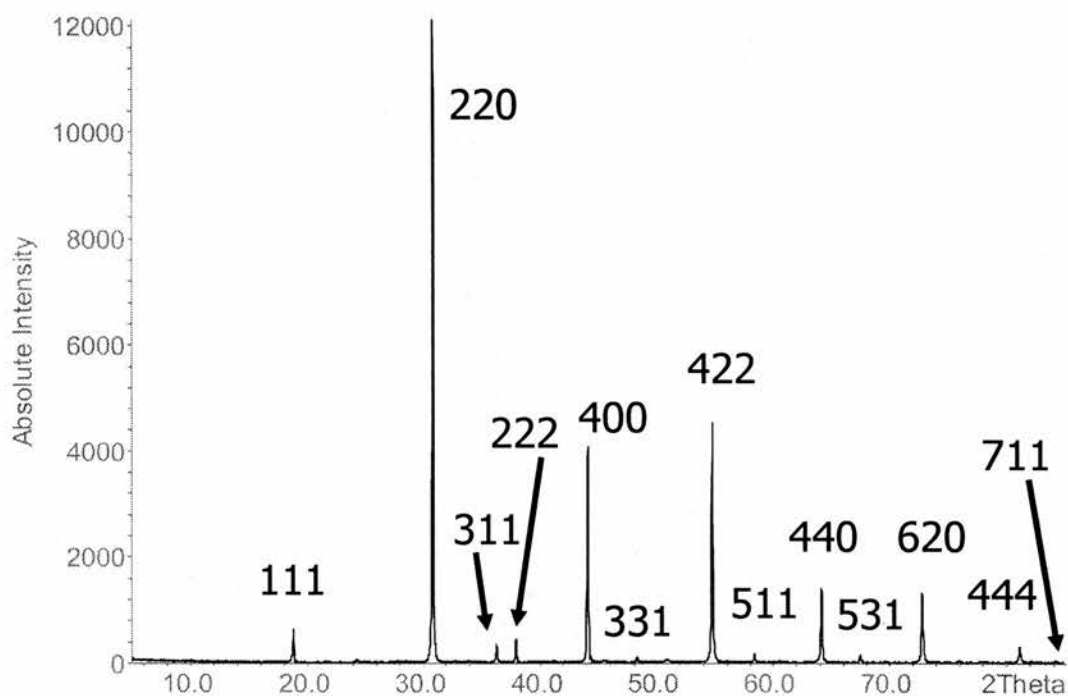


**Figure 3-4: X-Ray diffraction pattern for as prepared  $\text{Sr}_3\text{Ca}_{1.18}\text{Nb}_{1.82}\text{O}_{8.73}$**

### 3.2.3 Neutron diffraction studies of $\text{Sr}_3\text{Ca}_{1+x}\text{Nb}_{2-x}\text{O}_{9-\delta}$

The issue of B-cation ordering is important when considering changes in the structure, and therefore how it affects the  $\text{H}^+$  conductivity. The parent phase ( $\text{Sr}_3\text{CaNb}_2\text{O}_9$ ) is 1:2 ordered ( $1\text{B}' : 2\text{B}''$ ) and is trigonal, while 1:1 ordering is more usual i.e.  $\text{B}''_{1.5} : (\text{B}'_{1.5}\text{B}''_{0.5})$  giving a tetragonal system [7]. Water incorporation into the oxygen ion vacancy positions in the perovskite oxygen framework has been achieved by high pressure (2.5 MPa) steam treatment at  $220^\circ\text{C}$  in a Teflon bomb. On heating these fully hydrated samples, water is lost from the lattice, in two stages, typically at  $380$  and  $500^\circ\text{C}$  depending on atmosphere and composition. Through neutron and X-Ray diffraction studies, we have seen that  $\text{D}_2\text{O}$  (and  $\text{H}_2\text{O}$ ) incorporation changes the structure, affecting the dominant cation order. Some supercell peaks are also evident with some compositions, indicative of incommensurate order.

Neutron diffraction data were collected (at room temperature) at the Polaris instrument at Rutherford Appleton Laboratories for two deuterated and two vacuum degassed compositions in the series  $\text{Sr}_3\text{Ca}_{1+x}\text{Nb}_{2-x}\text{O}_{9-\delta}$ , namely  $\text{Sr}_3\text{Ca}_{1.1}\text{Nb}_{1.9}\text{O}_{8.85-y}(\text{OD})_{2y}$  (SCN10-D) and  $\text{Sr}_3\text{Ca}_{1.18}\text{Nb}_{1.82}\text{O}_{8.73-y}(\text{OD})_y$  (SCN18-D). Extra peaks (other than those for the cubic perovskite) were observed for the room temperature phases, indicating a slight tetragonal or orthorhombic distortion may in fact be present. Indeed, only in the dry (vacuum treated, undeuterated) state, will the  $\text{Sr}_3\text{Ca}_{1+x}\text{Nb}_{2-x}\text{O}_{9-\delta}$  tend towards exhibiting a cubic (no split peaks, no extra peaks) diffraction pattern. Further evidence for this was obtained by focussing on the peak at  $2.37 \text{ \AA}$ , corresponding to the cubic close packed  $\text{AO}_3$  layers in the doubled perovskite unit cell ( $111 a_p$ ). The corresponding

index for a tetragonal/orthorhombic  $\sqrt{2}a_p \times \sqrt{2}a_p \times 2a$  unit cell is (022). This peak is prone to significant splitting (022, 202) when the oxygen sublattice is distorted (at temperatures  $<500^\circ\text{C}$ ) due to the filling of oxygen vacancies on hydration.

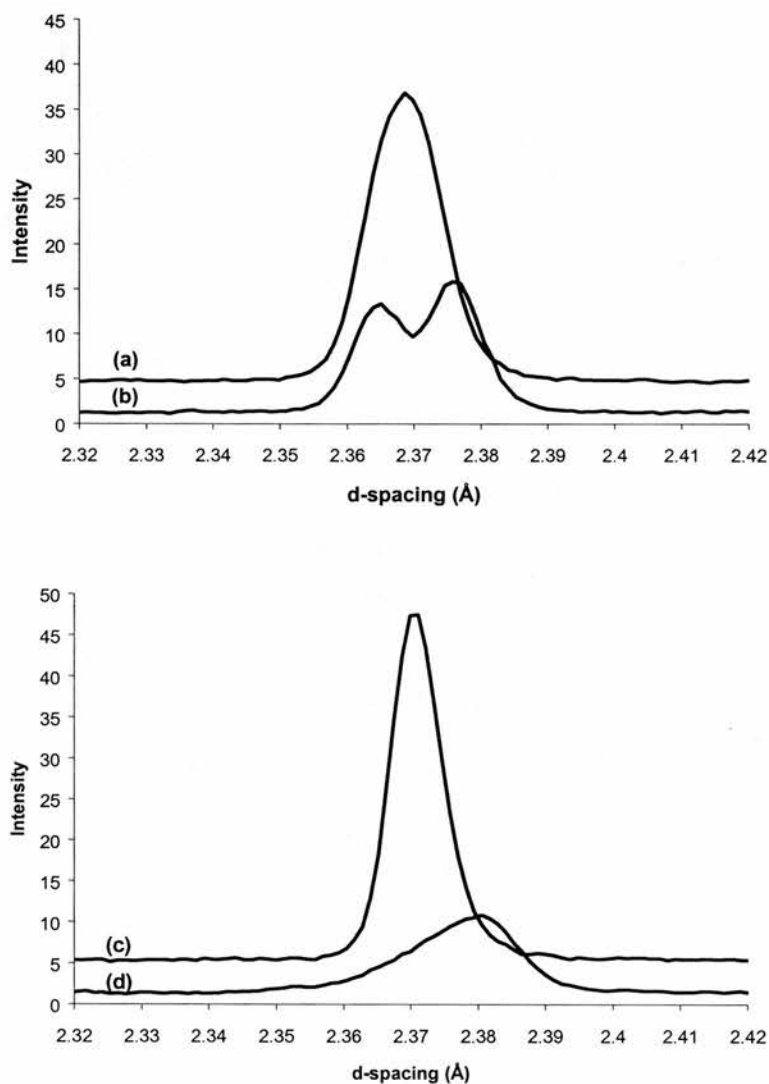


**Figure 3-5: Portions of the neutron powder diffraction patterns of various  $\text{Sr}_3\text{Ca}_{1+x}\text{Nb}_{2-x}\text{O}_{9-3x/2}$  samples: (a)  $x = 0.18$  dry, (b)  $x = 0.18$  deuterated, (c)  $x = 0.1$  dry, (d)  $x = 0.1$  deuterated.**

In Figure 3-5, a clear splitting is evident for the deuterated  $x = 0.18$  sample. The width of this peak for the deuterated  $x = 0.1$  sample also indicates a split, however it seems that there is little if any splitting of this peak for dry (vacuum degassed at  $1000^{\circ}\text{C}$  for 6 hours prior to experiment, then cooled to room temperature)  $x = 0.18$  and  $x = 0.1$  samples. The higher level water content possible for SCN18-D (due to the fact that there are more  $\text{O}^{2-}$  vacancies present in the dry state), clearly has an influence on the degree of splitting of the peak at  $2.37 \text{ \AA}$ , as the doublet is less clearly defined for SCN10-D.

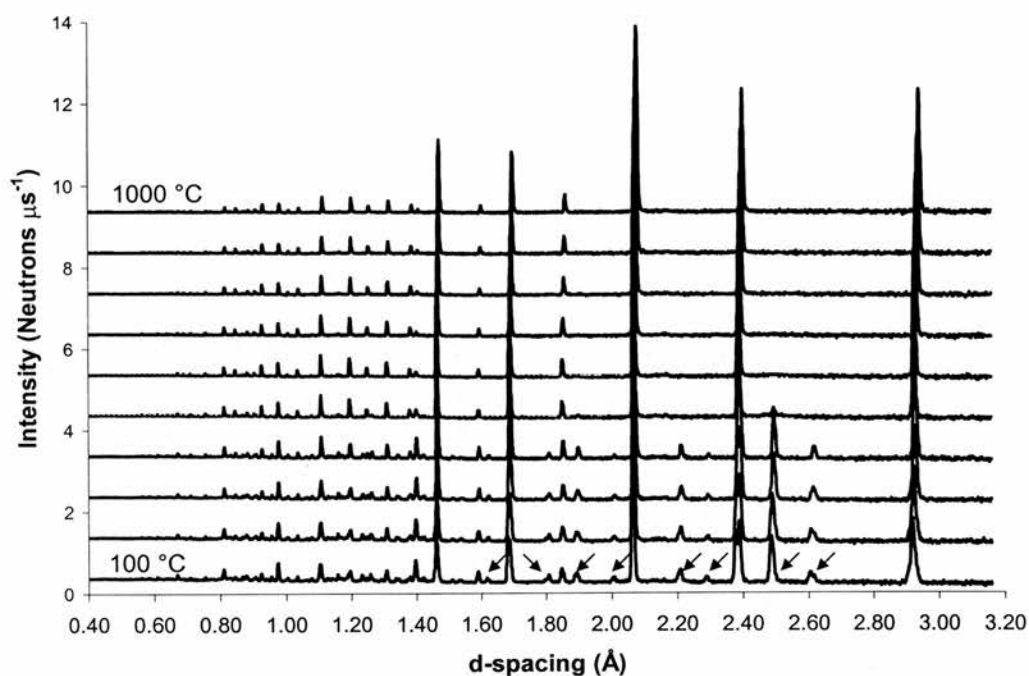


**Figure 3-6: Polaris Neutron Diffraction scans for  $\text{Sr}_3\text{Ca}_{1.18}\text{Nb}_{1.82}\text{O}_{8.73-y}(\text{OD})_{2y}$  ( $y \leq 0.16$ ) from  $100$  to  $1000^{\circ}\text{C}$  in  $100^{\circ}$  increments. The arrows point to the peaks that are lost by  $500^{\circ}\text{C}$  when the sample is fully dehydrated.**

Figure 3-6 shows that a clear increase in symmetry is evident as the temperature is raised from  $100^{\circ}\text{C}$  to  $1000^{\circ}\text{C}$ . The most significant peaks (from  $1.6$  to  $2.8 \text{ \AA}$ ) that are lost by  $500^{\circ}\text{C}$  are indicated by an arrow. It is therefore assumed that the symmetry of

this phase remains the same from 500 – 1000°C. Clearly, from Figure 3-7  $\text{SCN18} + \text{D}_2\text{O}$  cannot be cubic at room temperature (or even at 100 °C), because of the split peak centred at approximately 2.38 Å. Certainly by 500°C,  $\text{D}_2\text{O}$  (as O-D groups) has left the structure, and an increase in symmetry occurs with the loss of many split peaks. The peak(s) at approx 2.38 Å reveal that it is O-H (or O-D) group incorporation within the oxygen vacancy sites of the close packed  $\text{AO}_3(111)_p$  planes which are causing the unit cell distortion at temperatures <500°C.

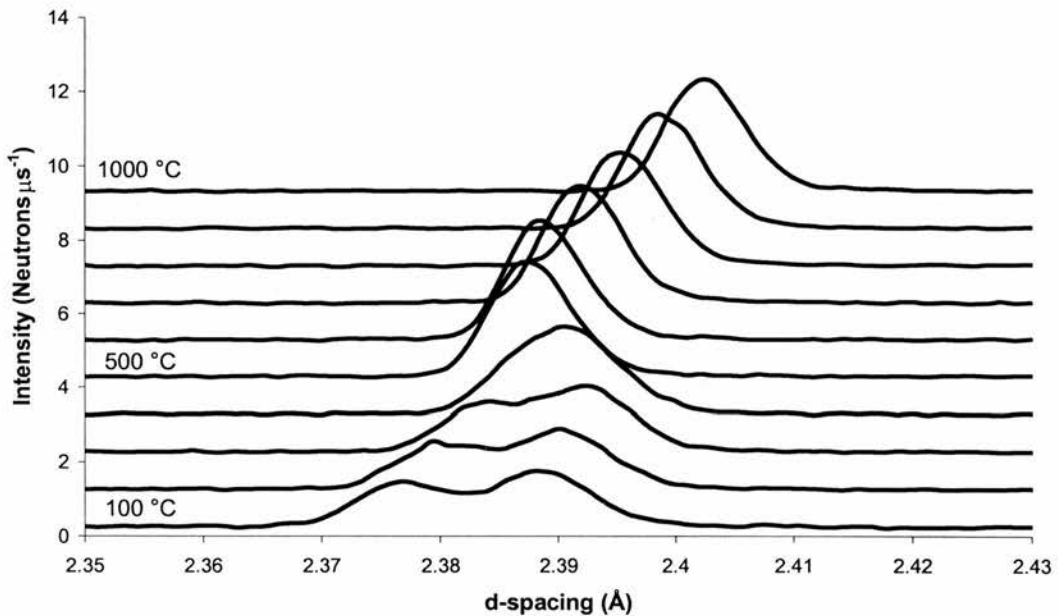


**Figure 3-7: Evolution of the  $(111)_p$  peak for  $\text{Sr}_3\text{Ca}_{1.18}\text{Nb}_{1.82}\text{O}_{8.73-y}(\text{OD})_{2y}$  with temperature.**

Structureless whole pattern fitting (LeBail) [8] was used in the GSAS program to elucidate the space group evolution with temperature. This routine extracts the intensities of each peak, and refines their position and shape to match the experimental data in the pattern. The unit cell and profile parameters can thus be accurately determined without a full structural model. The deuterated phase,

$\text{Sr}_3\text{Ca}_{1.18}\text{Nb}_{1.82}\text{O}_{8.73-y}(\text{OD})_{2y}$  ( $y = 0.162$  at room temperature) exists up to  $400^\circ\text{C}$ , but by  $500^\circ\text{C}$  the  $\text{H}_2\text{O}$  (as structural O-H groups) is lost giving rise to a single peak between 2.38 and 2.40 Å. From considerations of possible systematic absences and the goodness of fit of the LeBail refinements, the low temperature data were found to indicate orthorhombic Pmmm and the high temperature data cubic Fm-3m. Such an evolution of Space Group is entirely consistent with symmetry considerations. At  $500^\circ\text{C}$  and below the pattern was fitted using the Pmmm (No. 47) space group with a  $\sqrt{2}a_p \times \sqrt{2}a_p \times 2a_p$  unit cell which was necessary to accommodate the 022, 202 doublet. Above  $500^\circ\text{C}$  the sample is essentially dehydrated with a corresponding increase in unit cell symmetry from orthorhombic to cubic. The Fm-3m space group with a  $2a_p \times 2a_p \times 2a_p$  unit cell was used to fit the patterns at temperatures  $> 500^\circ\text{C}$ . The space group/unit cell parameter changes are illustrated in Figure 3-8. Judging by the changes in intensity the transition is fairly sharp and may well approach first order. The low temperature data did not appear to fit the higher symmetry space group P-4 as previously reported in the literature [5] due to the appearance of extra and split peaks.

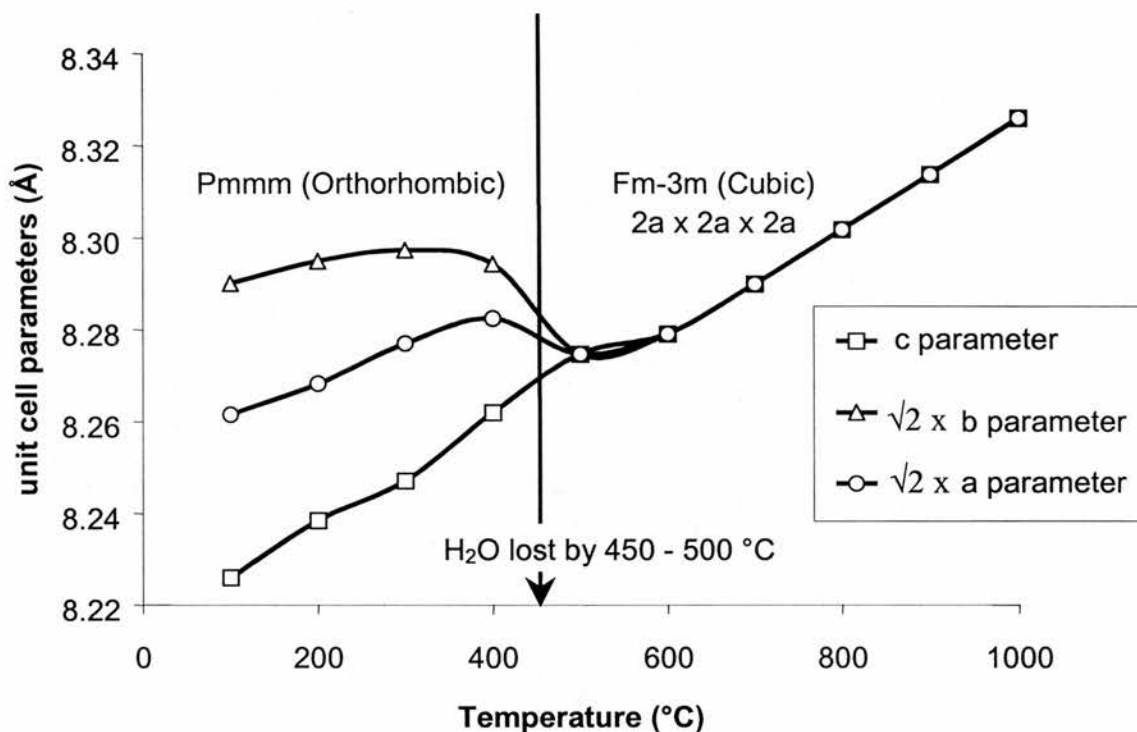


**Figure 3-8: Space Group and lattice parameter changes with temperature for**



### 3.2.4 TEM Studies of SCN18

Transmission Electron Microscopy (TEM) was used to check the homogeneity of the sample (Electron Dispersive Spectroscopy). High Resolution TEM (HRTEM) and Electron Diffraction were carried out in order to verify the  $2a_p \times 2a_p \times 2a_p$  structure. Figure 3-9 shows a view along the  $[111]_p$  axis of SCN18. This honeycomb-like image can be regarded as the A-cations and B-cations one behind the other (dark regions) surrounded by 6 oxygens (bright regions).

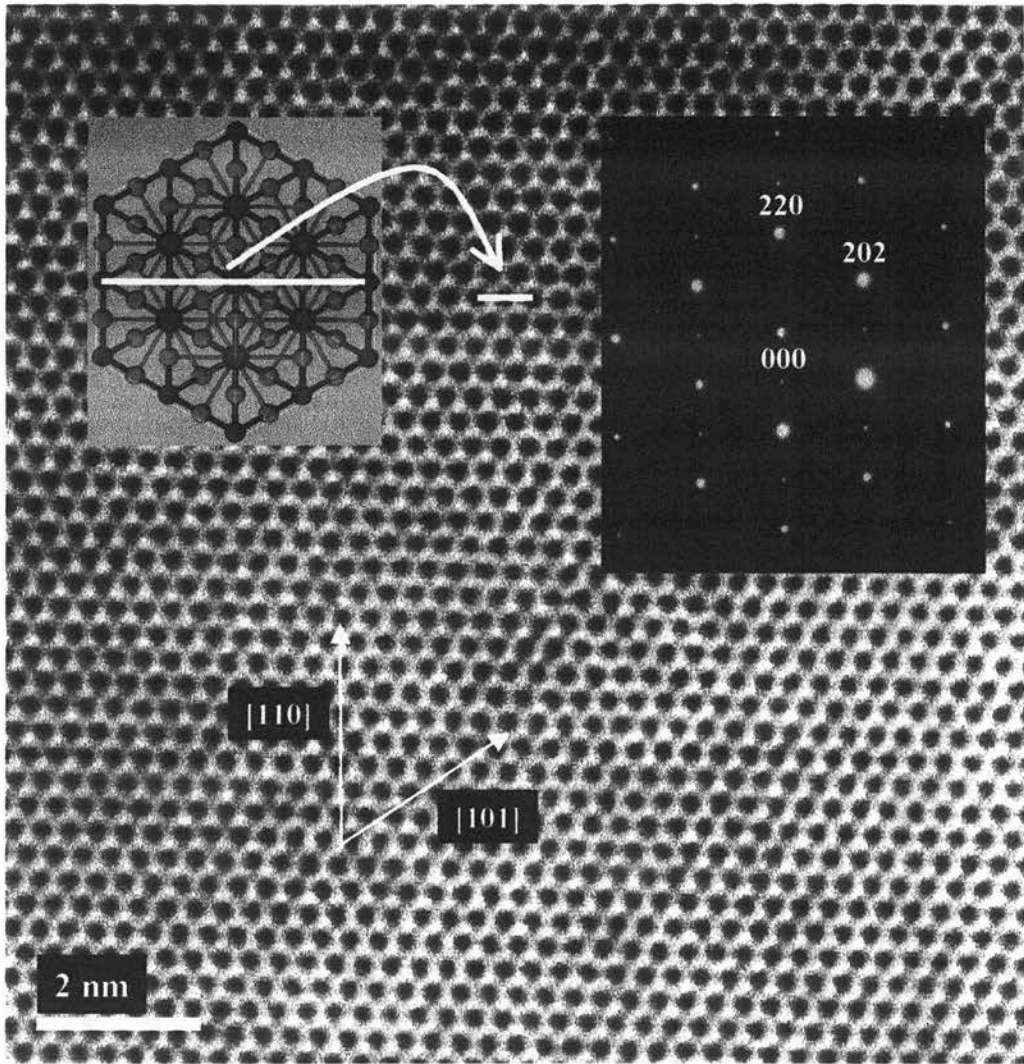


**Figure 3-9: HRTEM image of the [111] plane of vacuum dried  $\text{Sr}_3\text{Ca}_{1.18}\text{Nb}_{1.82}\text{O}_{8.73}$ . The top right inset shows the electron diffraction pattern with the  $2a_p$  (doubled unit cell) cubic indices. The [111] plane of a perovskite model is also shown (top left).**

This image is compared to the theoretical model of the perovskite structure, inset, showing the identical cation and oxygen arrangements. Yellow lines and a curved arrow denote equivalent distances in model and image ( $\approx 8 \text{ \AA}$ ). The perovskite model is enlarged for clarity. The most important features of the structure appear in the electron diffraction pattern shown in the top right corner. The strongest spots are the (220) reflections of the doubled cubic unit cell,  $2a_p$ .

Weak spots corresponding to the (110) reflections of the doubled cell are evident. The appearance of these spots confirms a reduction in symmetry from face-centred cubic, most probably to tetragonal or orthorhombic. In fact, the doubled unit cell is best viewed as  $\sqrt{2}a_p \times \sqrt{2}a_p \times 2a_p$  for tetragonal or orthorhombic, as was found from neutron and X-ray studies.

### 3.3 Summary

The family of perovskites  $\text{Sr}_3\text{Ca}_{1+x}\text{B}_{2-x}\text{O}_{9-\delta}$  offers considerable potential as proton conducting electrolytes that are relatively resistant to carbonation. In this study, we discuss the important structural features of these oxides and demonstrate that the structures of hydrated proton conducting oxides differ quite significantly from those of unhydrated samples. We aim here to highlight the fact that the structure determination of hydrated perovskites has generally been ignored in the literature. Subtle changes in unit cell symmetry due to octahedral tilting/distortion, oxygen vacancy filling/creation and cation displacements are all important features accompanying water uptake/loss and play an intrinsic role in the level of proton conduction and mechanism of proton transfer.

The established proton conducting phase  $\text{Sr}_3\text{Ca}_{1.18}\text{Nb}_{1.82}\text{O}_{8.73}$  has been shown to exhibit significant distortions from cubic/tetragonal symmetry when hydrated/deuterated at elevated temperatures and/or pressures. A distortion towards orthorhombic symmetry occurs due to the formation of O-H groups on filling the  $\text{O}^{2-}$  vacancies with  $\text{H}_2\text{O}$ . This distortion is intimately linked with the creation of proton carriers for conduction to occur at intermediate temperatures (350-500°C). These symmetry changes have

generally been overlooked in the related literature on these types of complex perovskite proton conductors, an important issue in relation to the operation of an electrochemical device such as a fuel cell. In systems such as  $\text{Sr}_3\text{Ca}_{1+x}\text{Nb}_{2-x}\text{O}_{9-\delta}$  or  $\text{Sr}_3\text{CaZrTaO}_{9-\delta}$  [9] this significant distortion is clearly visible due to the large concentration of protonic defects. In other systems with lower  $\text{H}_2\text{O}$  solubility, e.g. Y-doped  $\text{BaCeO}_3$ , similar distortions are likely to occur, but possibly on a more restricted length scale.

### 3.4 References

- [1] T. Schober, F.Krug and W. Schilling, *Solid State Ionics*, 1997, **97**, 369.
- [2] Y. Du and A.S. Nowick, *J. Am. Ceram. Soc.*, 1995, **78**, 3033.
- [3] A.J. Jacobson, B.M. Collins and B.E.F. Fender, *Acta Crystallogr. B*, 1982, **24**, 1968.
- [4] A.S. Nowick, Y. Du, *Solid State Ionics* **77** (1995) 137-146
- [5] M. Hervieu, B. Raveau, *Journal of Solid State Chemistry*, **28** (1979) 209-222
- [6] A.J. Jacobson, B.M. Collins, B.E.F. Fender, *Acta Crystallographica B* **32** (1976) 1083-1087
- [7] Y. Du, A.S. Nowick, *J. Am. Ceram. Soc.* **78** 11 (1995) 3033-3039
- [8] A. LeBail, in *Microstructure Analysis by Diffraction*, edited by H. Bunge, J. Fiala and R. L. Snyder, IUCr/Oxford University Press (1988)
- [9] D.J.D. Corcoran and J.T.S. Irvine, *Solid State Ionics*, in press (2001)

Chapter Four  
Synthesis and Characterisation of the  
 $\text{Sr}_3\text{Ca}_{1+x}\text{Zr}_{(1-y)-x/2}\text{Ta}_{(1+y)-x/2}\text{O}_{8.5-[(5x-2y)/4]}$  system

"Research is to see what everybody else has seen, and to think what nobody else has thought."

---Albert Szent-Gyorgi

## 4 Synthesis and Characterisation of the

### $\text{Sr}_3\text{Ca}_{1+x}\text{Zr}_{(1-y)-x/2}\text{Ta}_{(1+y)-x/2}\text{O}_{8.5-[(5x-2y)/4]}$ system

#### 4.1 The system

In a similar manner to the  $\text{Sr}_3\text{Ca}_{1+x}\text{Nb}_{2-x}\text{O}_{9(3x/2)}$  system outlined in Chapter Three, B-site substitution can be used to control oxygen stoichiometry. In this system,  $\text{Ta}^{5+}$  was used instead of  $\text{Nb}^{5+}$  and varying amounts of  $\text{Zr}^{4+}$  (typically between 0.25 and 1 per formula unit) were introduced to the B-site in order to introduce charge compensating oxygen ion vacancies into the lattice. The system was also amenable to increasing calcium content as well as adjustment of the Zr/Ta ratio, to obtain different phases with different oxygen contents. The general formula of this system can be written as

$\text{Sr}_3\text{Ca}_{1+x}\text{Zr}_{(1-y)-x/2}\text{Ta}_{(1+y)-x/2}\text{O}_{8.5-[(5x-2y)/4]}$ , and the introduction of oxygen ion vacancies by  $\text{Zr}^{4+}$  addition (by substitution with  $\text{Ta}^{5+}$ ) can be written in Kroger-Vink notation as:



so that, on average, one oxygen ion position is vacant for every eighteen oxygen ion positions, upon substitution of 1 Zr for every 1 Ta per formula unit, giving the parent phase composition  $\text{Sr}_3\text{CaZrTaO}_{8.5}$ . These phases were synthesised according to the solid state reaction of the metal oxides and carbonates as outlined in Chapter Two.

## 4.2 Phase Characterisation

The phases of the  $\text{Sr}_3\text{Ca}_{1+x}\text{Zr}_{(1-y)-x/2}\text{Ta}_{(1+y)-x/2}\text{O}_{8.5-[(5x-2y)/4]}$  system were initially characterised by X-Ray diffraction as outlined in Chapter Two. Starting points for unit cell parameter values were based on the findings that  $\text{Sr}_3\text{Ca}_{1.18}\text{Nb}_{1.82}\text{O}_{8.73}$  is cubic, with a cell side that of a doubled simple cubic perovskite ( $2a_p$ ).

After hydration treatments, the final structure (at least when considering the metal lattice) seems to change little. Table 4-1 below reveals that, on hydration, the units cell volume differs by about 0.23 %. Considering also that the lattice parameter,  $c$ , of the tetragonal unit cell is approximately  $2a$ , we can calculate that there is an decrease of about 0.085 % in “cubicity” considering a cubic unit cell of  $2a \times 2a \times 2a$ .

Lattice parameters (Å)	a	c	Tetragonality ( $\sqrt{2}a/c$ )	Unit Cell Volume (Å <sup>3</sup> )
Dry sample	5.8049(6)	8.220(1)	0.99872	276.99
Hydrothermally treated	5.8016(7)	8.222(3)	0.99787	276.76

**Table 4-1: Lattice parameter change of  $\text{Sr}_3\text{CaZr}_{0.5}\text{Ta}_{1.5}\text{O}_{8.75}$**

### 4.3 Initial TGA measurements

#### 4.3.1 Thermogravimetric studies of $\text{Sr}_3\text{CaZr}_{0.5}\text{Ta}_{1.5}\text{O}_{8.75}$

For a sample that was vacuum dried, and then thermogravimetrically analysed in a “hydrating” atmosphere it can be seen from Figure 4-1, that maximum water uptake occurs at 380°C, with loss of all water from the structure at 520°C. From there the composition is stable up to 800°C, and on cooling, down to 600°C, when water uptake from the wet gas atmosphere occurs until 240°C. Figure 4-1 illustrates how a vacuum dried sample uptakes water from a wet 5%  $\text{H}_2/\text{Ar}$  gas stream (gas is passed through wet cotton wool, at 15-20 ml min<sup>-1</sup>), with maximum structural uptake at 380°C. Bound structural protons are lost by 520°C and the phase is then stable up to 850°C. On cooling in the flowing wet gas stream, water is again incorporated into the oxygen-ion vacancies, resulting in a hydrated phase at room temperature.

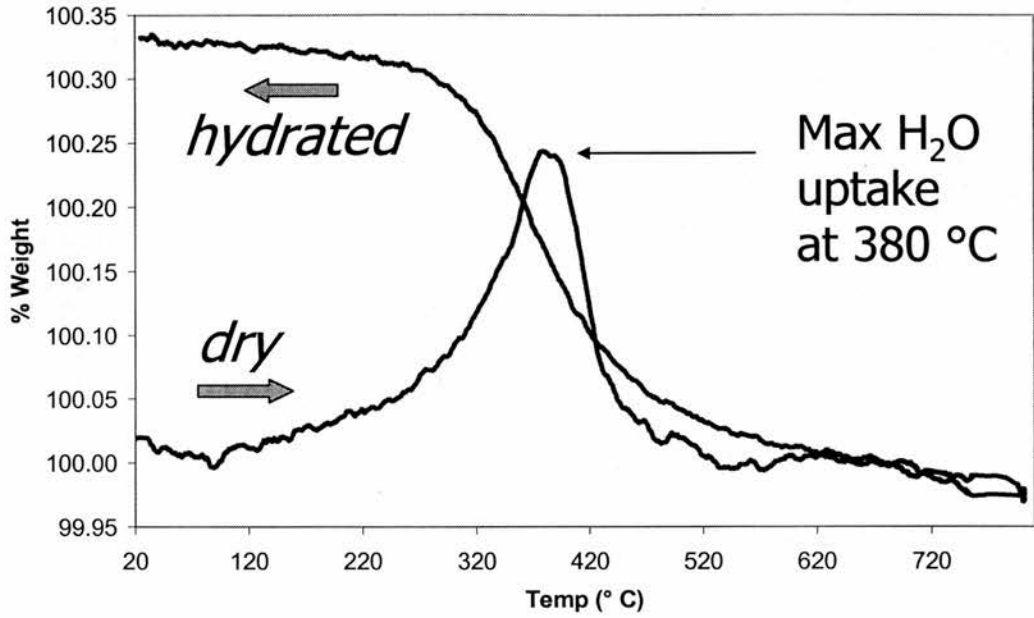


**Figure 4-1 :  $\text{Sr}_3\text{CaZr}_{0.5}\text{Ta}_{1.5}\text{O}_{8.75}$  Vacuum degassed at 1000°C (dry reference) for 5 hours (Run under wet 5% $\text{H}_2$ /Ar flow)**

With this weight increase on cooling of 0.33 %, it is calculated that approx. 55% of the oxygen ion vacancies are filled with water by this thermal treatment in the TGA furnace, giving a resultant room temperature hydrated phase stoichiometry of  $\text{Sr}_3\text{CaZr}_{0.5}\text{Ta}_{1.5}\text{O}_{8.6125}(\text{OH})_{0.275}$ . This can be tied in with the pre-treatment in the same type of atmosphere (wet 5%  $\text{H}_2$ /Ar), during conductivity measurements. Whether the “half-filled” state is the optimal for proton conduction is a maximised condition is still under consideration. Close to 100% filling of vacancies has been achieved with  $\text{Sr}_3\text{Ca}_{1.18}\text{Nb}_{1.82}\text{O}_{8.73}$ , but this may not be an optimised proton concentration.

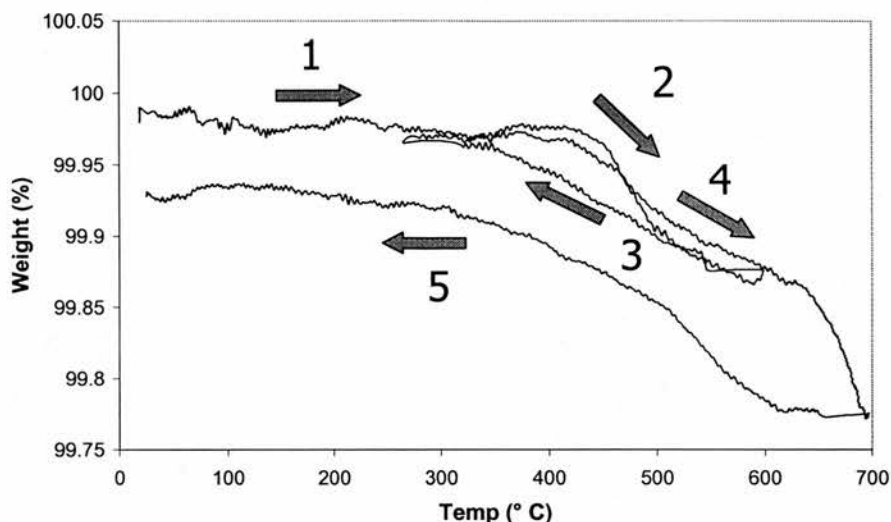


**Figure 4-2:  $\text{Sr}_3\text{CaZr}_{0.5}\text{Ta}_{1.5}\text{O}_{8.75}$  Vacuum degassed at  $1000^\circ\text{C}$  (5 hrs), then bomb deuterated at  $220^\circ\text{C}$  (24 hrs) in wet 5%  $\text{H}_2/\text{Ar}$  flow**

The weight loss response of a sample hydrated using alternative method was also investigated. An as prepared powdered sample of  $\text{Sr}_3\text{CaZr}_{0.5}\text{Ta}_{1.5}\text{O}_{8.75}$  was first vacuum treated ( $1 \times 10^{-4}$  mbar) at  $1000^\circ\text{C}$  for 5 hours, and then subjected to  $\text{D}_2\text{O}$  steam at  $220^\circ\text{C}$  in a Teflon bomb as outlined in Chapter Two. To observe the reversibility in  $\text{D}_2\text{O}$  loss, and  $\text{H}_2\text{O}$  uptake, the TGA program involved first heating in a wet 5%  $\text{H}_2/\text{Ar}$  stream to  $600^\circ\text{C}$  (Stages 1 and 2 in Figure 4-2) so that all the incorporated  $\text{D}_2\text{O}$  is lost. During cooling to  $280^\circ\text{C}$ , the sample is again hydrated due to the  $\text{H}_2\text{O}$  present in the flowing gas stream (Stage 3). This water is again lost on heating to  $600^\circ\text{C}$  again (Stage 4), with a response similar to that of the initial  $\text{D}_2\text{O}$  loss. As the temperature is raised up to  $700^\circ\text{C}$ , there seems to be a further weight loss which has not reached a plateau. The final cooled sample (some rehydration occurs, Stage 5) was therefore heated again in a separate experiment, and the result is shown in Figure 4-3. Only by  $900^\circ\text{C}$  has this second extra weight loss begun to reach a plateau.

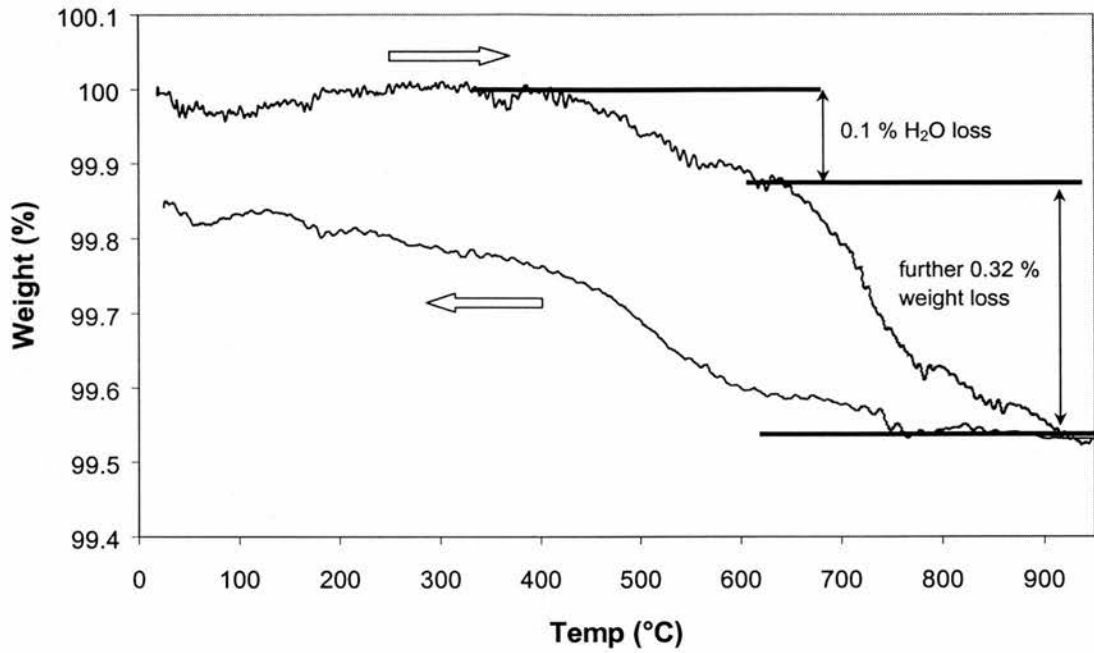


**Figure 4-3: Cooled sample of  $\text{Sr}_3\text{CaZr}_{0.5}\text{Ta}_{1.5}\text{O}_{8.75-x}(\text{OH})_{2x}$  from Figure 4-2. Run in wet 5%  $\text{H}_2/\text{Ar}$ .**

There is a significant difference in the TGA plots of samples which have been hydrated by treatment in a wet 5%  $\text{H}_2/\text{Ar}$  atmosphere (in TGA itself, Figure 4-1) or even after initial preparation, and those vacuum dried and then bomb hydrated/deuterated at 220°C for 24 hours. If all the oxygen ion vacancies in  $\text{Sr}_3\text{CaZr}_{0.5}\text{Ta}_{1.5}\text{O}_{8.75}$  were filled by  $\text{H}_2\text{O}$ , this would correspond to a theoretical decrease in weight loss on heating (from  $\text{Sr}_3\text{CaZr}_{0.5}\text{Ta}_{1.5}\text{O}_{8.5}(\text{OH})_{0.5}$ ) of 0.59 %. Initially, (in the cycled run, Figure 4-2) cooling back to 25°C from 600°C, there is a loss of about 0.125 % up to about 600°C, and the phase is stable at the 600°C mark. This corresponds to around 22 % of the oxygen ion vacancies having been filled as a result of  $\text{D}_2\text{O}$  treatment.

In the wet gas atmosphere, the sample picks up water again on cooling, and the original weight is restored at 300°C. On the next ramp up to 700°C, a further loss of 0.1 % occurs between 620°C and 700°C and is investigated by taking the final cooled sample

up to 950°C and back to room temperature (Figure 4-3). It can be seen from Figure 4-3 that there is a further loss of about 0.32 % in weight from 620 to 950°C after the previous cycled run in Figure 4-2. Adding these three losses together corresponds to a total weight loss (up to 950°C at least) of about 0.545 %, close to the theoretical 100% filling of vacancies with H<sub>2</sub>O. Water loss would not occur above 600°C, so another molecular species must be incorporated as a result of bomb hydration, and is lost above 600°C, so this weight loss probably does not correspond to 100% filling of vacancies.

If all the vacancies were filled with O<sub>2</sub> molecules rather than H<sub>2</sub>O, a weight loss of 1.04% would be expected. It is speculated that this second weight loss above 620°C (when the sample is hydrothermally pre-treated in H<sub>2</sub>O at 220°C) could be due to O<sub>2</sub> gas lost as a result of peroxide/superoxide formation in this perovskite. There is also the possibility of molecular CO<sub>2</sub> incorporation, and this will be discussed later. Since the total weight loss is so close to the theoretical maximum for H<sub>2</sub>O filling the vacancies, and the dry reference hydration experiment shows that a maximum of around 55% of oxide ion vacancies can be filled by H<sub>2</sub>O, it may be possible that a combination of H<sub>2</sub>O, CO<sub>2</sub> and possibly O<sub>2</sub> may be incorporated. Gas chromatography (as a TGA supplement), EPR (electron paramagnetic resonance) and mass spectroscopy could be needed to confirm this.

#### 4.4 Other selected water loss measurements

Table 4-2 below shows some other TGA results for compositions in the A<sub>3</sub>B<sub>3</sub>O<sub>9-δ</sub> system. Only the B<sub>3</sub> component is tabulated here, as A = Sr in all cases. B<sub>3</sub> is split up as B'<sub>1+x</sub>B''<sub>(1-y)-x/2</sub>B'''<sub>(1+y)-x/2</sub> (in the system Sr<sub>3</sub>Ca<sub>1+x</sub>Zr<sub>(1-y)-x/2</sub>Ta<sub>(1+y)-x/2</sub>O<sub>8.5-δ</sub>). Some

compositions have been charged in a Teflon bomb at 220°C for 24 hours with either water or heavy water, and some are tested as prepared. Various gases both dry and wet (achieved by having a throughput cylinder with wet cotton wool before the TGA gas inlet) were used.

Perovskite (B <sub>3</sub> )	Stage II % Weight Loss (%)	Maximum Theory Weight Loss (%)	O <sup>2-</sup> vacancies filled (%)
Ca <sub>1.1</sub> Zr <sub>0.85</sub> Ta <sub>1.05</sub> †	0.65	1.28	50.8
Ca <sub>1.2</sub> Zr <sub>0.9</sub> Ta <sub>0.9</sub> ‡	0.8	1.714	46.7
Ca <sub>1.2</sub> Zr <sub>0.9</sub> Ta <sub>0.9</sub> + H <sub>2</sub> O †	1.5	1.714	87.5

Key: † = Dry Ar gas flow; ‡ = Wet 5% H<sub>2</sub> in Ar flow

**Table 4-2 : Water Uptake/Loss of Selected Phases in the SrCa(Zr)Ta Oxide system**

The “Stage II” loss is considered here to be the loss of the most tightly bound water in the lattice, being the H<sub>2</sub>O that fills the vacancies according to the mechanism outlined in the introduction. Stage I water loss is considered to be water that is surface bound, and not associated with the filling of vacancies. These results show that the phase Sr<sub>3</sub>Ca<sub>1.2</sub>Zr<sub>0.9</sub>Ta<sub>0.9</sub>O<sub>8.25</sub> has the greatest capacity for water to fill the oxygen ion vacancies in the lattice, and it also has over twice as many oxygen ion vacancies available than the Sr<sub>3</sub>Ca<sub>1.18</sub>Nb<sub>1.82</sub>O<sub>8.73</sub> composition.

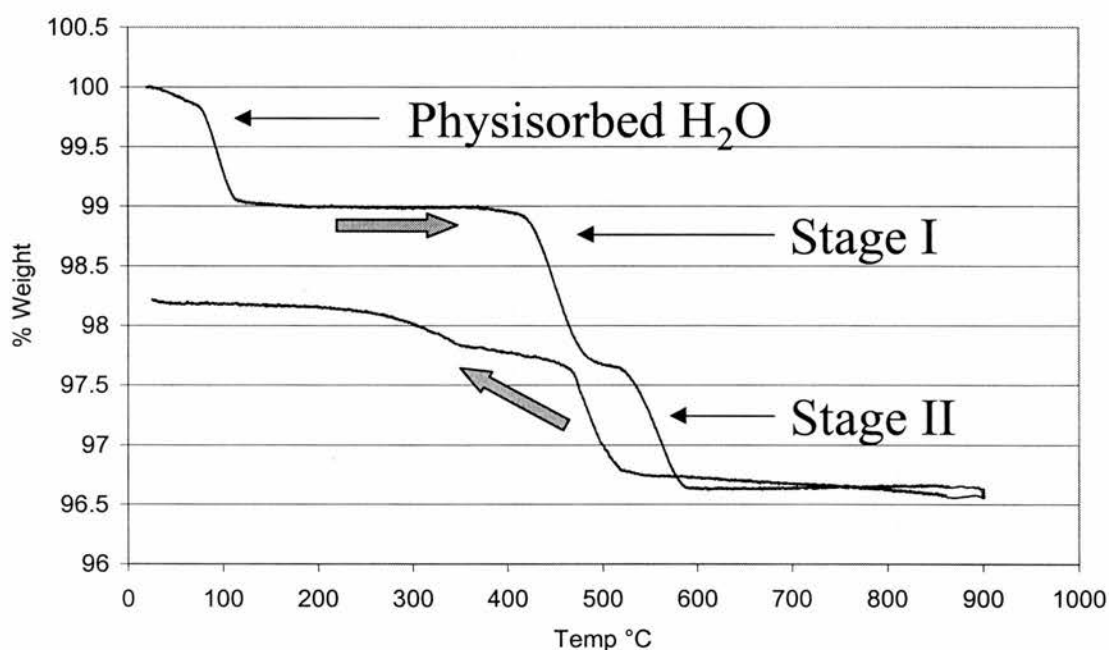


**Figure 4-4 : TGA trace of Sr<sub>3</sub>Ca<sub>1.1</sub>Zr<sub>0.95</sub>Ta<sub>0.95</sub>O<sub>8.375</sub> (as prepared, not hydrothermally treated) in wet 5% H<sub>2</sub>/Ar gas**

Figure 4-4 above shows the TGA trace for Sr<sub>3</sub>Ca<sub>1.1</sub>Zr<sub>0.95</sub>Ta<sub>0.95</sub>O<sub>8.375</sub>. The sample was run as prepared, and was not treated in a water saturated atmosphere. There are two water loss stages after the initial surface water loss up to 100°C. These occur at 383°C to 506°C and 510°C to 600°C. The percentage weight losses are 1.31 % and 1.04 %

respectively. All of this water seems to have been incorporated after synthesis, when the sample was air-quenched to room temperature from 1000°C. The two stages of water loss are distinct, and the second stage seems to be reversible in the wet gas. It is assumed that this Stage II loss, is the loss of water incorporated into the oxygen-ion vacancies according to the equation:



Stage I loss is here ascribed to resilient surface bound water. There is no noticeable weight loss above 600°C, and since this sample was not hydrothermally treated, there has been no extra CO<sub>2</sub> or O<sub>2</sub> incorporated. Upon water uptake, we assume that an O-H exists where an oxygen ion vacancy had been, and another proton has attached itself to a neighbouring oxygen ion. The theoretical maximum water loss (assuming all vacancies filled, 0.625 H<sub>2</sub>O per formula unit) is 1.58 %, therefore 65.7 % of the O<sup>2-</sup> vacancies are filled with H<sub>2</sub>O after preparation in this case.

Note that in Figure 4-1, for a vacuum treated sample of Sr<sub>3</sub>CaZr<sub>0.5</sub>Ta<sub>1.5</sub>O<sub>8.75</sub>, run in a wet 5% H<sub>2</sub>/Ar atmosphere, there was no water loss up to 400°C, only a gain, this being the uptake of H<sub>2</sub>O from the gas stream.

#### 4.5 Colour

There is also a notable change in colour from hydrated samples (they tend to be a light blue) and those vacuum-dried at 1000°C (off-white/brown-grey). As-prepared powdered samples (pelleted) and sintered pellets (at 1400°C) are light blue also. It is proposed that

the filled vacancies cause the sample to appear blue. However, after hydration treatments, the blue colour does not return. Under reducing conditions also, the sample will tend to lose its blue coloration, or remain brown-grey if vacuum dried beforehand. Only high pressure treatment with oxidant ( $\text{KClO}_4$ ) was successful in reverting the colour to blue from grey. The colour change on dehydration can be seen in Figure 4-5 below:

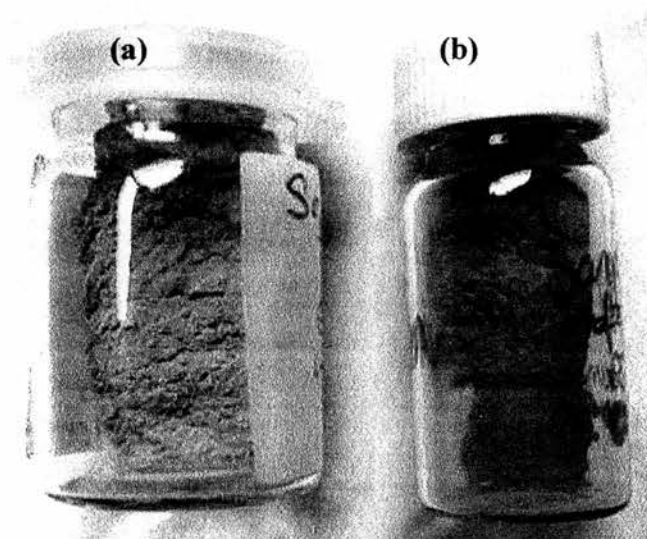


**Figure 4-5: (a) [on left]  $\text{Sr}_3\text{CaZr}_{0.5}\text{Ta}_{1.5}\text{O}_{8.75}$  as prepared (b) [on right]  $\text{Sr}_3\text{CaZr}_{0.5}\text{Ta}_{1.5}\text{O}_{8.75}$  after vacuum degassing**

#### **4.6 Combined Thermogravimetric/Differential Scanning Calorimetric-Mass Spectrometric Analysis (TG/DSC-MS) of $\text{Sr}_3\text{CaZrTaO}_{8.5-x}(\text{OH})_{2x}$**

##### **4.6.1 The experiment**

This study involved the characterisation of the mass loss, energetics and evolved gas analysis by mass spectrometry of a 2.5 MPa steam treated (at  $220^\circ\text{C}$ ) sample of (initially) vacuum-treated  $\text{Sr}_3\text{CaZrTaO}_{8.5}$ . The NETZSCH STA 449 C *Jupiter*

simultaneous thermal analyser, equipped with a Pt furnace (25 to 1500°C) was used to measure the mass change and energetics (DSC). The mass spectrometer data acquisition was carried out with a BALZERS Thermostar Mass Spectrometer, coupled by a heat capillary (230°C). Simultaneous start/stop of the STA and the Thermostar was enabled.

The working parameters are outlined in Table 4-3 below:

Temperature Program	<p>RT to 200°C at 10 K/min</p> <p>200°C isothermal for 30 mins</p> <p>200°C to 500°C at 10 K/min</p> <p>500°C isothermal for 30 min</p> <p>500°C to 1000°C at 10 K/min</p> <p>1000°C isothermal for 30 min</p>
Atmosphere	<p>(a) Ar (4.6 N grade)</p> <p>(b) Ar/H<sub>2</sub> (95:5 %)</p>
Flow Rates	50 ml/min
Crucibles	Pt/Rh with lids
Sample holder	TG/DSC type S
Sample weights	<p>86.50 mg (Ar)</p> <p>103.11 mg (Ar/H<sub>2</sub>)</p>

Mass Spectrometry data acquisition was set to detect the following mass numbers:

C (12), O (16), OH (17), H<sub>2</sub>O (18), CO (28), O<sub>2</sub> (32), CO<sub>2</sub> (44).

**Table 4-3: Working Parameters for TG-MS Experiments**

## 4.6.2 Results and discussion

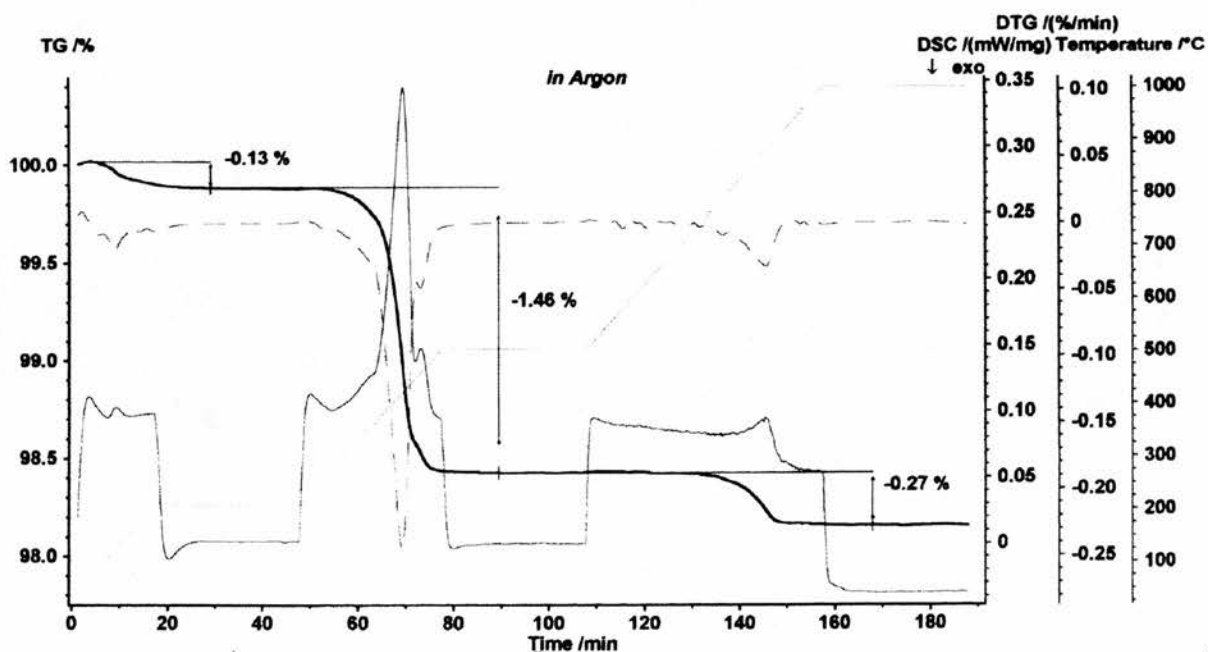


**Figure 4-6: TG (black), DTG (green) and DSC (blue) curves for hydrated  $\text{Sr}_3\text{CaZrTaO}_{8.5}$  in Argon atmosphere**

There are three weight losses evident from Figure 4-6 above (in the black TG curve), with the first loss of about 0.13 % attributable to surface adsorbed water on the sample due to storage in normal lab-air conditions. The second weight loss of 1.46 % is the loss of incorporated structural O-H groups as a result of the hydration treatment (2.5 MPa steam at 220°C). In theory, filling 0.5  $V_o^{**}$  per formula unit with  $\frac{1}{2}$   $\text{H}_2\text{O}$  ( $\text{O}_{0.5}\text{H}$ ), and losing it in a TG experiment, would appear as a 1.25 % mass loss for this composition. It appears then that more  $\text{H}_2\text{O}$  is forced into the structure by the high-pressure steam treatment, than expected from the hydrated formula. However, a closer zoom in on this region reveals two separable stages of water loss with a smooth transition between the two, the major part amounting to 1.30 %, a closer match to the theoretical  $\text{H}_2\text{O}$  loss

prediction. The third weight loss stage (above 600°C), always seems to be in the range  $0.25 \pm 0.03 \%$  when the sample is steam hydrated (Figure 4-6 above). The main purpose of these TG-MS experiments was to ascertain the nature of the species or gas released at high temperatures (above 600°C), and also to determine the energy released or gained during the losses by Differential Scanning Calorimetry. Two different gases were used (Ar and 5% $H_2$ /Ar), to understand the influence of the presence or absence of hydrogen, a reducing gas, on the temperatures of decomposition onset and nature of the gases evolved.

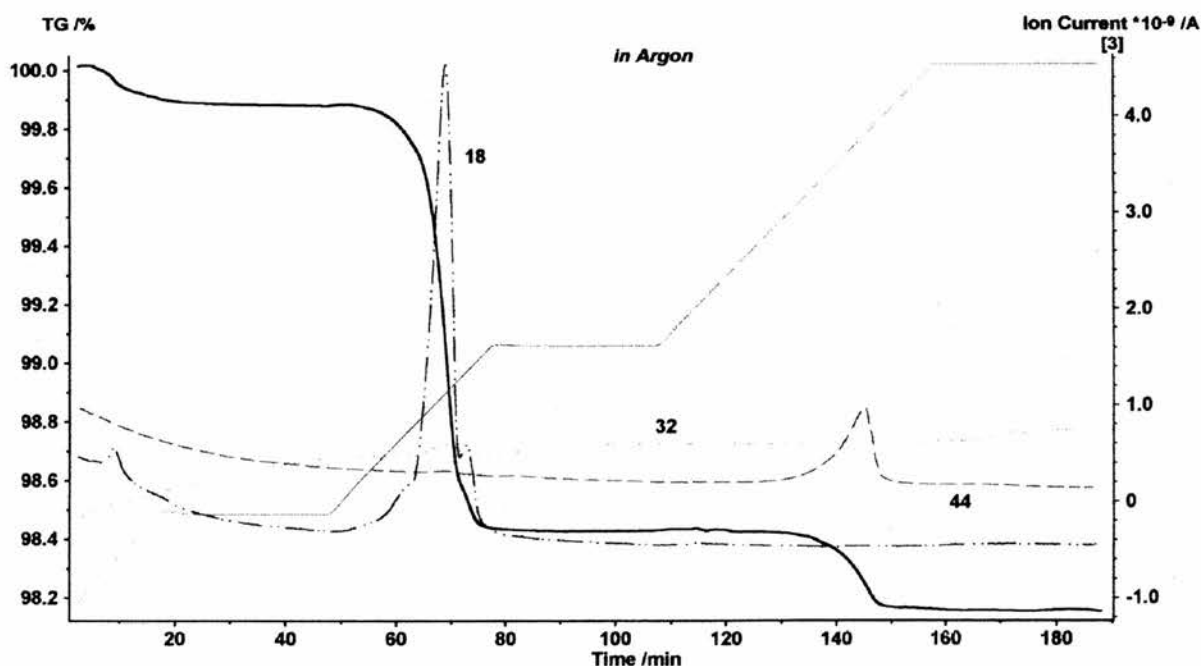


**Figure 4-7: TG trace (black), and MS detection for  $H_2O$  (18 amu, in blue),  $CO_2$  (44 amu, in dashed purple) and  $O_2$  (32 amu, in red). The ion-current axis is only valid for the  $H_2O$  response.**

In Figure 4-7 above, it is clear from the mass spectrometer detector (blue trace) that the first major weight loss (largest weight loss) is that due to crystallographic  $H_2O$ , and the second loss has been determined as  $CO_2$ . This could be attributed to structurally bound

CO<sub>2</sub> species (possibly CO<sub>3</sub><sup>2-</sup>) as a result of hydrothermal treatment in 2.5 MPa steam/air. It can also be seen that there is a second small H<sub>2</sub>O loss stage appearing as a shoulder to the right of the main water loss peak in the TG curve. This shows up as a second peak in the blue MS curve also. This may be due to the fact that a fraction of the O-H groups may be more strongly bound within the lattice, and hence more resistant to temperature increase. It could also be the case that, on the BO<sub>6</sub> octahedra, apical O-H groups might tend to leave the structure at a slightly different temperature compared to axial O-H groups.

According to the mass spectroscopic trace, there is no evidence for oxygen loss, which means that hydrothermal treatment in steam does not enable interstitial oxygen incorporation or uptake. Further investigations follow in the next section to determine if more forcing conditions with high pressures (>1500 psi) and elevated temperatures (>800°C) along with an appropriate oxidant (KClO<sub>4</sub>) can enable extra oxygen uptake. Table 4-4 below shows the energetics results for this sample under Ar gas:

Temp Range (°C)	Weight Loss (%)	DSC Maximum (°C)	DSC Endotherm Integral (J g <sup>-1</sup> )	DTG Minimum (°C)
85 - 160	0.09	127	0.8	124
280 - 500	1.30, 0.14	424, 460	81.2	421
700 - 910	0.27	878	6.5	877

**Table 4-4 : Event temperature ranges, weight loss and energetics results for hydrothermally treated Sr<sub>3</sub>CaZrTaO<sub>8.5</sub> in Argon (DTG = Differential Thermogravimetry)**

Again, Table 4-4 shows that the major weight loss from this hydrothermally treated occurs from 280 to 500°C and is attributed to crystallographic water loss. This event also is the largest endothermic weight loss with over 81 J g<sup>-1</sup> of heat absorbed from the surroundings. This energy would correspond to a “solution energy” for water in this material of around 58 kJ mol<sup>-1</sup> when heated under argon. Energy measurements were also carried out under a 5% H<sub>2</sub>/Ar gas flow, and the results are outlined below:

Temp Range (°C)	Weight Loss (%)	DSC Maximum (°C)	DSC Endotherm Integral (J g <sup>-1</sup> )	DTG Minimum (°C)
100 - 160	0.1	127	0.8	123
275 - 500	1.32, 0.13	427, 465	73.1	424
575 - 800	0.27	769	11.1	767

**Table 4-5 : Event temperature ranges, weight loss and energetics results for hydrothermally treated Sr<sub>3</sub>CaZrTaO<sub>8.5</sub> in 5% Hydrogen/ 95% Argon**

These results are virtually identical to those for the sample subjected to an argon only atmosphere up to 500°C. The corresponding solution energy for water under 5% H<sub>2</sub>/Ar is 52 kJ mol<sup>-1</sup>. There is however, a marked difference in the temperature range and energetics of the next weight loss stage, which was attributed to CO<sub>2</sub> loss under argon. Shown below is a comparison of the detected gasses evolved above 500°C under both Ar (Figure 4-8) and 5% H<sub>2</sub>/Ar (Figure 4-9) atmospheres.

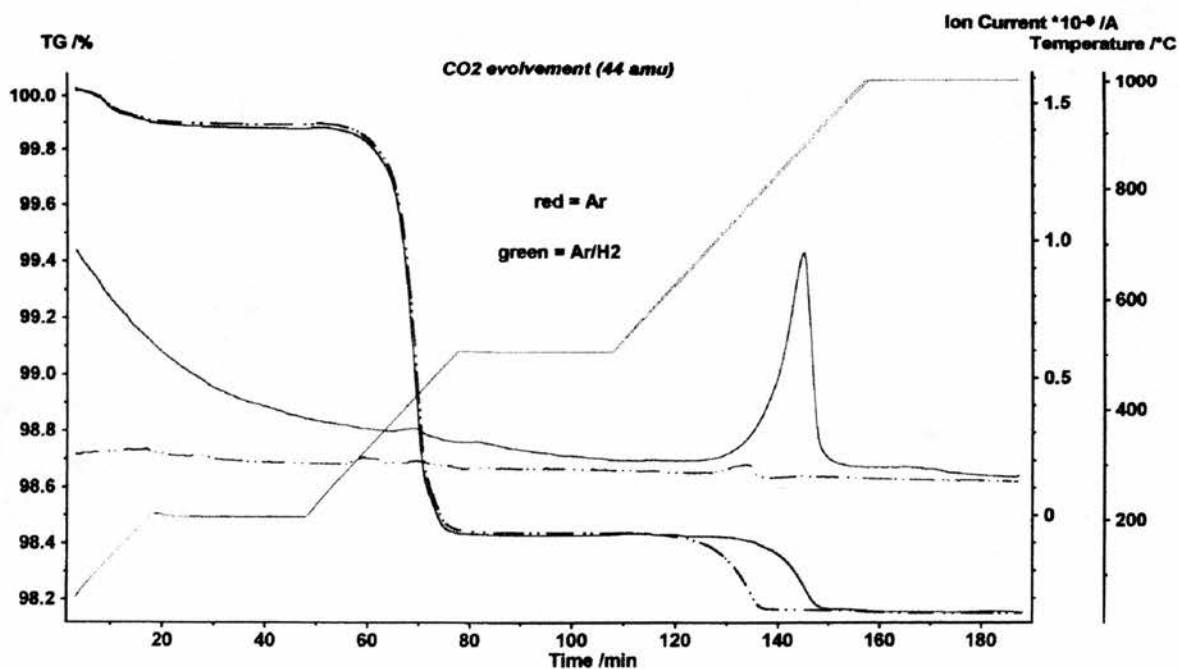


Figure 4-8: Detection results for CO<sub>2</sub> gas evolution above 500°C for hydrothermally treated Sr<sub>3</sub>CaZrTaO<sub>8.5</sub> under Ar (red trace) and 5% H<sub>2</sub>/Ar (green trace) atmospheres.

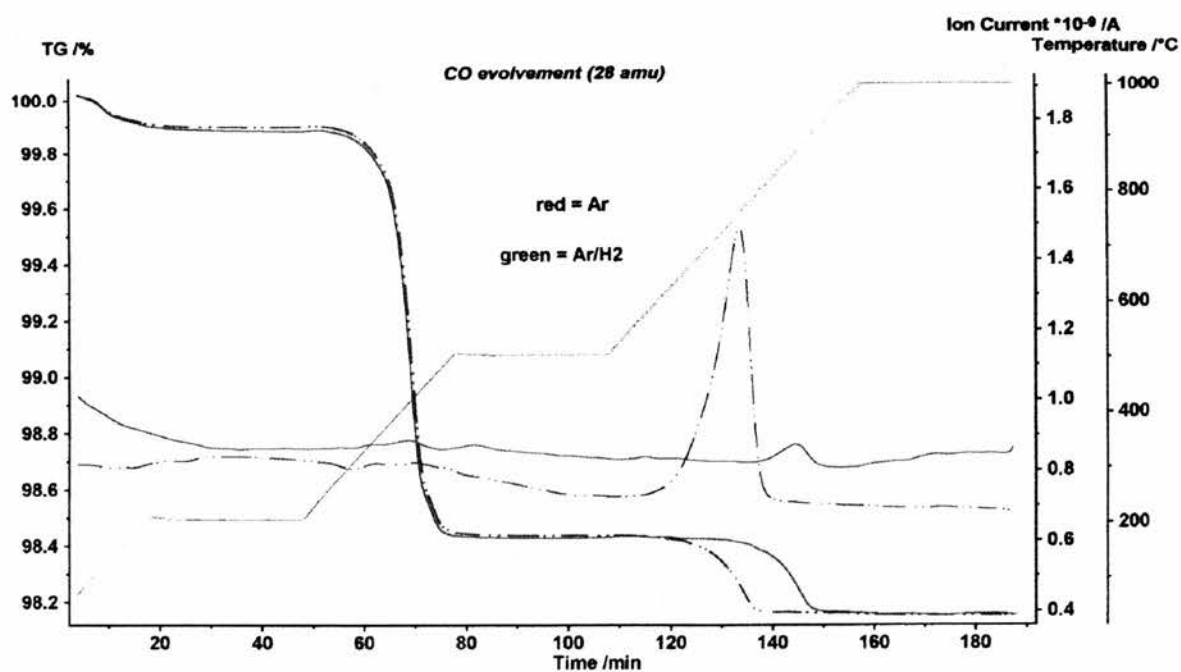


Figure 4-9: Detection results for CO gas evolution above 500°C for hydrothermally treated Sr<sub>3</sub>CaZrTaO<sub>8.5</sub> under Ar (red trace) and 5% H<sub>2</sub>/Ar (green trace) atmospheres.

These results reveal that CO is evolved above 500°C under 5% H<sub>2</sub>/Ar, whereas CO<sub>2</sub> is evolved under Ar atmosphere. The CO evolution occurs about 110°C lower than CO<sub>2</sub> evolution. The energy taken in from the environment (endothermic process) is also doubled (Table 4-5). It appears that the H<sub>2</sub> is reacting with the incorporated interstitial CO<sub>2</sub> according to the reverse water gas shift (RWGS) reaction:



This reaction seems to be occurring within the solid (i.e. a surface reaction), and not in the gas phase, as negligible CO<sub>2</sub> is released along with the CO release under 5% H<sub>2</sub>/Ar. This also implies that the reaction equilibrium is strongly tending to the right hand side of Equation 4-2. An interesting question arises as to whether Sr<sub>3</sub>CaZrTaO<sub>8.5</sub> is a catalyst for the almost 100 % reduction of CO<sub>2</sub> to CO in the presence of hydrogen gas (5% H<sub>2</sub>/Ar in this case). This issue is worthy of further work.

## 4.7 The high temperature and pressure incorporation of molecular species

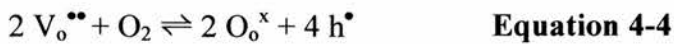
### 4.7.1 Introduction

Perovskite oxides containing large concentrations of oxygen vacancies are of widespread scientific and technological significance. Examples of such materials are the superconducting cuprate YBa<sub>2</sub>Cu<sub>3</sub>O<sub>7-δ</sub>, the oxide ion conductor La<sub>0.9</sub>Sr<sub>0.1</sub>Ga<sub>0.8</sub>Mg<sub>0.2</sub>O<sub>2.85</sub> and the proton conductor BaY<sub>0.1</sub>Ce<sub>0.9</sub>O<sub>2.95</sub>. These vacancies are a consequence of the cation stoichiometries and valence, although only some perovskite oxide compositions can accommodate significant oxygen deficiencies with

respect to the ideal  $ABO_3$  stoichiometry. The filling of these oxide vacancies by neutral water molecules (Equation 4-3) is generally thought to be the origins of protonic conductivity in oxides such as  $BaY_{0.1}Ce_{0.8}O_{2.95}$ , although the amount of water incorporated into the bulk cerate is barely detectable.



Oxygen vacancies may also be replaced by oxygen atoms (Equation 4-4) introducing electron holes into the lattice. In the cuprate superconductors this is the most powerful means of doping the cuprates to induce superconductivity, although there has been considerable debate as to whether the holes are oxygen holes or copper holes. In fact, the covalency of the CuO framework means that both types of hole must exist to some extent.

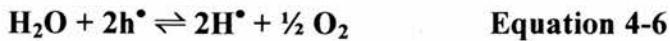


The introduction of trivalent ions ( $Gd^{3+}$ ) to the B-site of the stoichiometric compound  $BaCeO_3$  creates vacant oxygen sites, or, when in oxidizing atmospheres, creates electronic holes [1]. p-type conductivity in Y doped  $BaCeO_3$  is effected by the filling of the charge-compensating oxygen-ion vacancies by oxygen at high  $pO_2$  according to the equation:



However, in the presence of a  $H_2O$ -saturated atmosphere, molecular water will combine

with the holes to create protons according to:



Perovskites that have been found to exhibit a superconducting transition at low temperatures (up to 125 K) include Nb-doped SrTiO<sub>3</sub> (0.2 K), tungsten bronzes such as K<sub>x</sub>WO<sub>3</sub> (1-4 K), BaPb<sub>1-x</sub>Bi<sub>x</sub>O<sub>3</sub> for 0.05 ≤ x ≤ 0.3 (9-13 K), and La<sub>2-x</sub>Sr<sub>x</sub>(Ba<sub>x</sub>)CuO<sub>4</sub> phases with the K<sub>2</sub>NiF<sub>4</sub> structure [2]. YBa<sub>2</sub>Cu<sub>3</sub>O<sub>7</sub> exhibits superconductivity above the temperature of liquid N<sub>2</sub> [3], and has a perovskite-related orthorhombic structure with 2/3 of the Cu ions forming CuO<sub>4</sub> planar groups and Cu in a square pyramidal coordination, and 1/3 forming one dimensional chains of compressed CuO<sub>4</sub> planar groups. The presence of Cu<sup>3+</sup> in sample such as YBa<sub>2</sub>Cu<sub>3</sub>O<sub>7-δ</sub> may be expected, but there is no evidence for this, therefore species such as (Cu<sup>2+</sup> - O<sup>2-</sup>) and hole-species like (Cu<sup>2+</sup> - O<sup>-</sup>), or (Cu<sup>+</sup> - O<sup>-</sup>) may be present due to the highly covalent nature of Cu-O bonds in superconducting oxides. There is also possibility of O<sup>-</sup> dimerisation leading to peroxide species, O<sub>2</sub><sup>2-</sup>.

In ionic conductors such as La<sub>0.9</sub>Sr<sub>0.1</sub>Ga<sub>0.8</sub>Mg<sub>0.2</sub>O<sub>2.85</sub> or BaY<sub>0.1</sub>Ce<sub>0.9</sub>O<sub>2.95</sub>, decreases of the ionic transference number due to p-type contributions are frequently encountered in air or more oxidising conditions. Such p-type conduction in perovskites seems likely to arise from filling of oxygen vacancies by oxygen (Equation 4-4). The amount of oxygen taken up is generally too small to be detectable in these ionically conducting systems.

#### 4.7.2 Sample Preparation/Analysis

Samples of  $\text{Sr}_3\text{CaZrTaO}_{8.5}$  were prepared by the solid state method as outlined in Chapter Two. The high pressure and temperature treatments have also been outlined in Section 2.10. Water/carbonate/oxygen excess content was investigated by thermogravimetric analysis (TGA) and simultaneous differential thermal analysis (STA/DTA). Electron Paramagnetic Resonance (EPR) measurements were also carried out to detect species with unpaired electrons such as peroxide.

#### 4.7.3 Results and Discussion

In this study, we have investigated  $\text{Sr}_3\text{CaZrTaO}_{8.5}$  and related compositions in an effort to prepare oxygen deficient perovskites that can reversibly uptake large, determinable amounts of water, engendering significant proton conductivity. In this study we have not only demonstrated that this is the case, but have also shown that significant amounts of oxygen can also be taken up, with retention of the perovskite structure. Table 4-6 below outlines the different temperatures, pressures and times used for treatment of a number of samples of  $\text{Sr}_3\text{CaZrTaO}_{8.5}$ .

Sample phase number	High Pressure conditions
1	None, as prepared, then vacuum treated
2	1380 MPa @ 600°C for 1.5 hours + KClO <sub>4</sub>
3	1380 MPa @ 800°C for 1 hour + KClO <sub>4</sub>
4	1034 MPa @ 1000°C for 10 mins + KClO <sub>4</sub>
5	2068 MPa @ 800°C for 1 hour + KClO <sub>4</sub>

Table 4-6: Different high pressures and temperatures used to oxygenate the Sr<sub>3</sub>CaZrTaO<sub>8.5</sub> sample

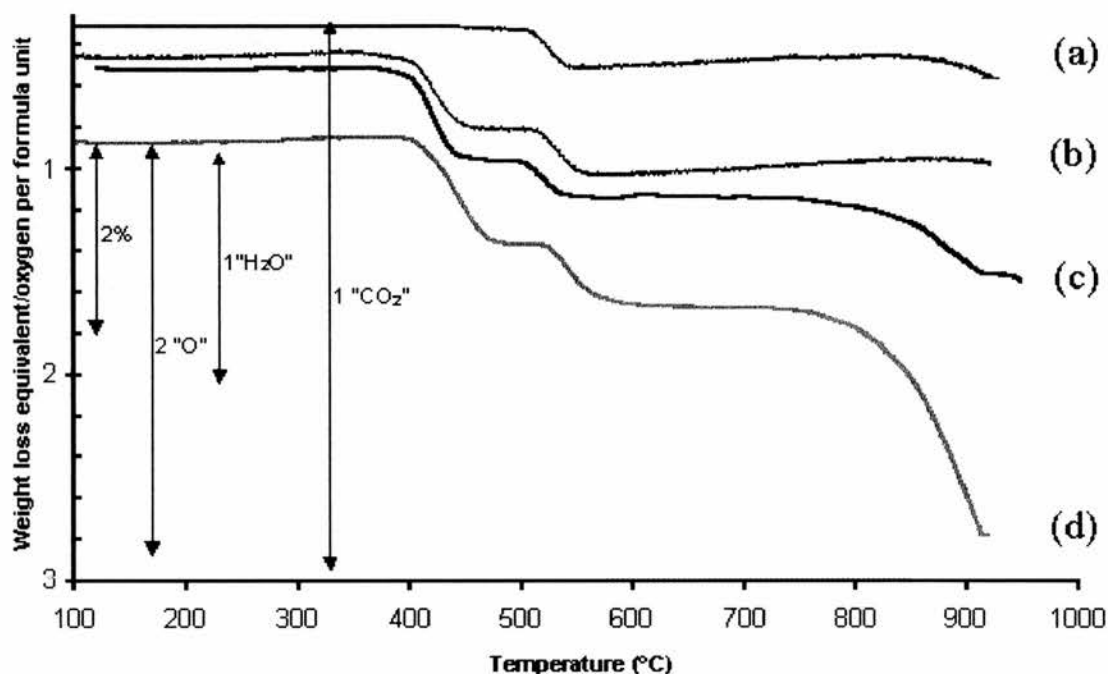
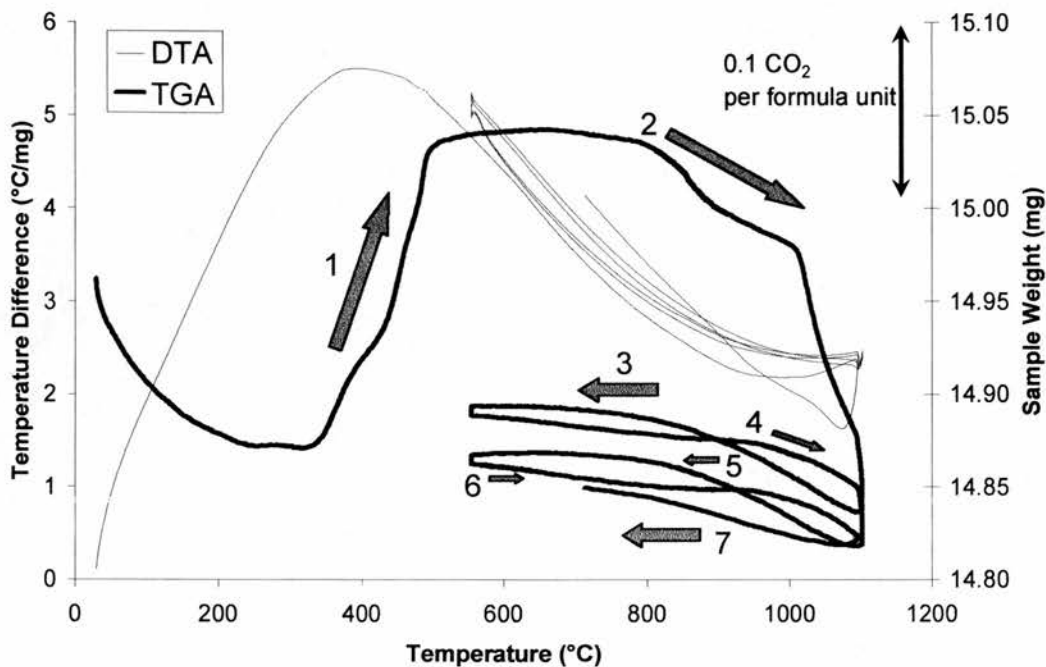


Figure 4-10: TG weight loss profiles for Sr<sub>3</sub>CaZrTaO<sub>8.5</sub>: (a) vacuum treated, (b) wet 5% H<sub>2</sub>/Ar treated, (c) hydrothermally treated, air/220°C, (d) stored at ambient before 1.3GPa O<sub>2</sub> @ 800°C for 1 hour. Measurements performed in wet 5%H<sub>2</sub>/Ar heating at 5° per minute and holding for 1 hour at maximum temperature.

Figure 4-10 shows the thermogravimetric traces performed in dry hydrogen for a range of dried, high pressure steam or oxygen treated samples. Two groups of features are apparent. First of all one or two weight losses at 400 - 500°C that are associated with water loss and secondly a weight loss at  $\approx 800^\circ\text{C}$  that is attributed largely to carbon dioxide loss. The fact that none of the cations present are either reducible or oxidisable under realisable conditions, implies that it is the oxygen that is being reduced at high temperatures. Similar weight changes also occur in wet or inert atmospheres.

As there is no evidence from X-Ray diffraction studies for either carbonate or hydroxide formation, we suggest that these molecular species are incorporated into the oxygen-ion vacancies present within the perovskite lattice as per the equations below. The changes in stoichiometry that occur on annealing in wet or oxidising atmospheres can be summarised in equations 4-7 and 4-8.





**Figure 4-11: TGA/DTA run under CO<sub>2</sub> gas for a high-pressure treated sample, Sr<sub>3</sub>CaZrTaO<sub>8.5-y</sub>(CO<sub>3</sub>)<sub>y-z</sub>(O)<sub>2z</sub>. Some CO<sub>2</sub> uptake is evident on cooling and heating cycles from 550-1100°C**

Vacuum treated and high pressure treated samples were run under flowing CO<sub>2</sub> gas in the simultaneous TGA/DTA furnace from room temperature to 1100°C. The temperature was also cycled from 550°C to 1100°C repeatedly to investigate CO<sub>2</sub> uptake or loss. Indeed, it can be seen from Figure 4-11 (high pressure treated sample) and Figure 4-12 (vacuum treated sample) that a significantly larger amount of CO<sub>2</sub> can reversibly be taken up and lost from the lattice of a vacuum treated sample. This is because a significant number of oxygen ion vacancies are available for filling with molecular CO<sub>2</sub>. In comparison, the oxygenated sample has very few oxygen ion vacancies left, as most have been filled by either H<sub>2</sub>O or CO<sub>2</sub> or O<sub>2</sub><sup>x-</sup> as a result of the high pressure treatment.

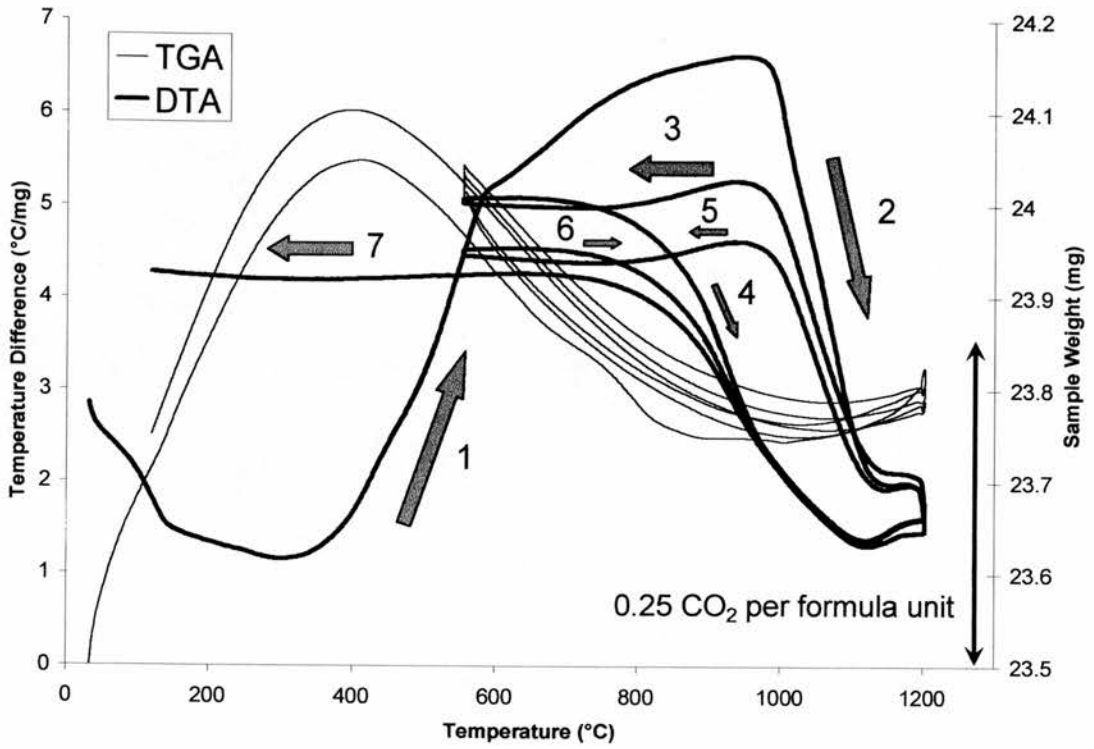


**Figure 4-12: TGA/DTA plot for vacuum treated (1000°C)  $\text{Sr}_3\text{CaZrTaO}_{8.5}$ , under  $\text{CO}_2$ . A higher percentage of  $\text{O}^{2-}$  vacancies are filled by  $\text{CO}_3^{2-}$  as more are available.**

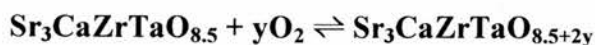
Table 4-7 below refers to the variables x and y as identified in Equations 4-7 and 4-8:

Sample Phase Number	Unit Cell Parameters	Colour after high pressure	Colour after TGA	x *	y **	8.5 + x + 2y
As Prepared	a = 5.808(8) c = 8.248(8)					
1	a = 5.798(7) b = 8.206(7)	n/a	brown/grey	0.156	0.052	8.708
2	a = 5.795(3) c = 8.213(7)	black/brown	brown/grey	0.144	0.449	9.542
3	a = 5.785(0) c = 8.162(4)	light blue	brown	≈ 0	0.485	9.47
4	a = 5.799(4) c = 8.188(5)	brown	brown/grey	0.164	0.214	9.091
5	a = 5.783(4) c = 8.182(1)	light blue	brown/grey	0.34	0.40	9.64

**Table 4-7: Unit cell parameters, colours, and water/oxygen contents of differently treated samples of Sr<sub>3</sub>CaZrTaO<sub>8.5</sub> (refer to Table 4-6)**

\* : If x = 0.5, vacancies are filled with H<sub>2</sub>O; \*\* : If y = 0.25, vacancies filled with O<sub>2</sub>

The weight losses are extensive and it is easy to see that the amount of water uptake can approach the amount needed to fill the vacancies,  $x \rightarrow 0.5$ , or more significantly that the oxygen uptake corresponds to the filling of the vacancies by molecular oxygen species, ie  $y \rightarrow 0.5$ . In addition, there is also evidence of oxygen incorporation, especially on high-pressure and high temperature oxygenation.



**Equation 4-9**

This indication of superoxide or peroxide formation is strongly supported by other techniques. First of all only samples that from TG seem to contain excess oxygen are blue and give an ESR signal. On heating these in reducing atmospheres or in vacuum, the blue coloration and EPR signal are lost.

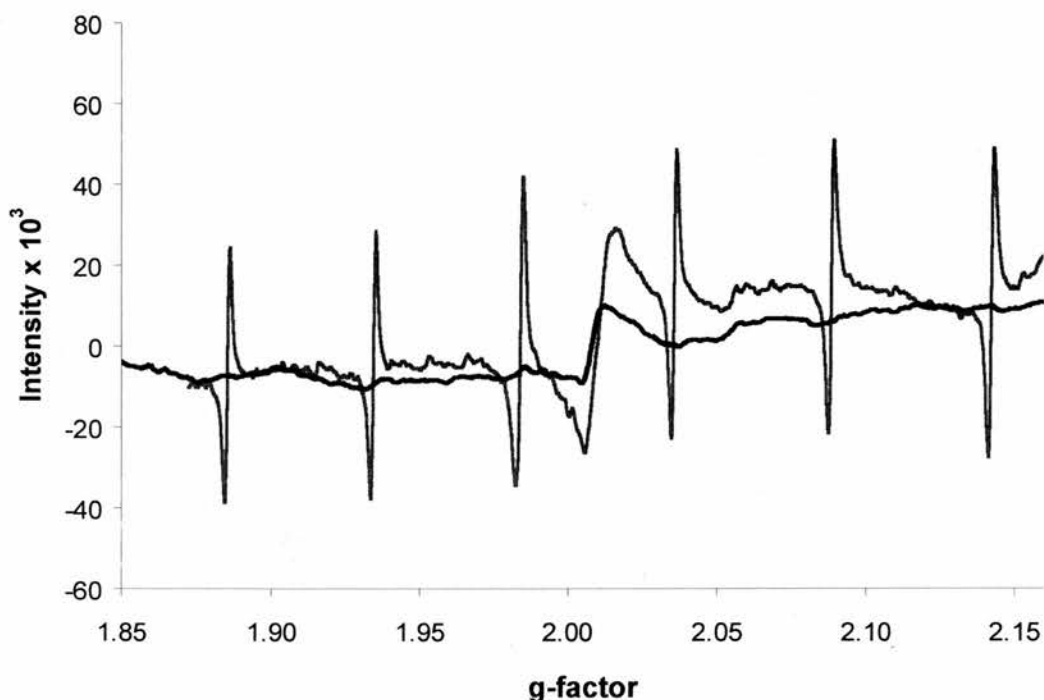


**Figure 4-13: Sextet EPR signal resulting from sample 5 (blue coloration) in Table 4-6. Also shown is the signal resulting from a reduced (treated under 5% H<sub>2</sub>/Ar at 1000°C, grey coloration) sample: only the central signal is present.**

The EPR signal of Sr<sub>3</sub>CaZrTaO<sub>8.5</sub> which has been treated at high pressure and temperature with KClO<sub>4</sub> [2068 MPa @ 800°C for 1 hour, (sample 5 in Table 4-6)] appears as a sextet of equal intensity lines surrounding a central singlet due to hyperfine coupling with <sup>91</sup>Zr. In turn, this shows that the peroxidic species is part of the bulk perovskite and not a created impurity phase. The appearance of a sextet can be ascribed to a *nuclear* coupling to one unpaired electron. The central signal, which is associated with the paramagnetic nature of a peroxide species, O<sub>2</sub><sup>2-</sup> occurs at a g-value of 2.011,

with the inter-peak spacings in the sextet of 82.6, 84.6, 87.7, 87.7, and 91.7 Gauss with increasing magnetic field.  $^{91}\text{Zr}$  is an isotope of zirconium with an 11.2 % natural abundance. This isotope has a nuclear spin of  $5/2$  hence spin-spin coupling of one unpaired electron to the  $^{91}\text{Zr}$  nucleus would produce six lines of equal intensity.  $^{181}\text{Ta}$ , with 99.98 % natural abundance also has a nuclear spin, but with  $I = 7/2$  that would give 8 lines. However, Ta also has a quadrupole moment, which might broaden these lines out of observation. Alternatively the one unpaired electron in the sample is at a site where there is no Ta close by. Recent neutron studies of samples containing both excess water and oxygen in the perovskite also suggest the presence a superoxide type entity and a hydroxyl entity that occupy different oxygen sites in the lattice.

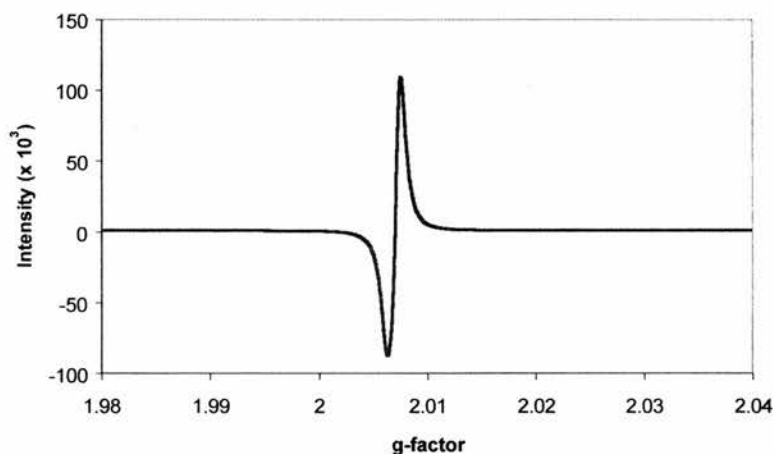


**Figure 4-14 : EPR signal from a DPPH standard (0.3 mg)**

#### 4.7.4 Spin concentrations

The concentration of spins  $[R^{\bullet}]$  associated with a species which has an electronic spin quantum number  $I$  of  $1/2, 3/2, 5/2, 7/2, \dots$  can be calculated using a known standard. One of the most widely used standards in conventional EPR spectroscopy is 2,2-diphenyl-1-

picrylhydrazyl (DPPH) [4]. This radical is well characterised at low fields and frequencies. The room temperature EPR spectrum of polycrystalline DPPH at X band consists of a single narrow line appearing at  $g = 2.0036 \pm 0.0002$  [5].

$$[R^{\bullet}] = [DPPH] \times \frac{d_i}{d_i[DPPH]} \times \frac{Gain_{DPPH}}{Gain_{R^{\bullet}}} \times \frac{(\Delta H_{R^{\bullet}})^2}{(\Delta H_{DPPH})^2} \times \frac{T_{R^{\bullet}}}{T_{DPPH}} \times F$$

**Equation 4-10**

Equation 4-10 above outlines the methodology for the calculation, where  $[R^{\bullet}]$  (here it represents the spin-active nucleus of  $^{91}\text{Zr}$ , with nuclear  $I = 5/2$ ) is the required spin concentration of the species which gives rise to the EPR signal under investigation and  $d_i$  is the double integral value (total of the 6 lines in the sample signal, Figure 4-13). The microwave amplifier *Gain* used was so chosen as to give optimum signal intensity for the DPPH and  $\text{Sr}_3\text{CaZrTaO}_{8.5}$  sample. The spin concentration of the sample is *inversely* proportional to the *Gain*.  $\Delta H$  is the *sweep field width* and was the same for both standard and sample (2990 to 3790 Gauss).  $T$  is the temperature in K, and both standard

and sample were run at room temperature.  $F$  is the factor  $\frac{2 \frac{y}{2} + 1}{x}$ , whereby a number of lines,  $x$ , at a time can be selected from a multiplet associated with a spin of  $y/2$  for the calculation.

Using Equation 2-10 above, and 0.3 mg DPPH standard, 4.6 mg  $\text{Sr}_3\text{CaZrTaO}_{8.5}$  (high pressure treated with  $\text{KClO}_4$ , sample 5 in Table 4-6), it was determined that there are  $7.4 \times 10^{13}$  spins (spin-active nuclei) for  $^{91}\text{Zr}$  present (from the sextet) and  $2.66 \times 10^{14}$  spins

associated with all other Zr isotopes (central singlet signal). From this, the ratio  $\frac{^{91}\text{Zr}}{\text{Zr}} =$

27.8 %, a significant deviation from the actual isotopic abundance ratio of 11.22 %. This can be rationalised in terms of the peroxy ( $O_2^{2-}$ ) radical actually being associated with 2 B-cations, which would give an impression of a doubled isotopic abundance percentage of 22.44 %. This value is comparable to the isotopic abundance ratio obtained from the ESR signal ratio (27.8 %)

#### 4.8 Summary

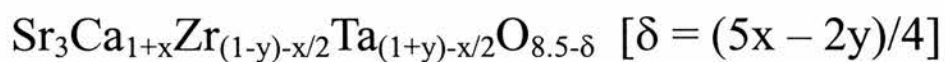
When treated with high pressure ( $> 2.5$  MPa) steam in air or solid oxidant at high pressure (689 to 2068 MPa), extra oxygen species may also exist as  $O_2^{2-}$  within the complex perovskite structure of  $Sr_3CaZrTaO_{8.5}$  and variant phases of the formula  $Sr_3Ca_{1-x}(Zr_{(1-y)-x/2}Ta_{(1+y)-x/2}O_{8.5-[(5x-2y)/4]}$ . Water is lost from hydrated samples between 300 and 450°C and loss of molecular oxygen-containing species ( $CO_3^{2-}$  and  $O_2^{x-}$ ) at temperatures in excess of 600°C occurs when high pressure pre-treated with an oxidising agent.

These samples are *very* sensitive to water uptake, tending to hydrate and fill the  $O^{2-}$  vacancies readily even at room temperature after synthesis or vacuum treatment. Thermogravimetric experiments on high-pressure oxygenated samples indicate that “oxygen excess” may be possible on the oxygen sublattice, or in “chemical book-keeping” terms, the B-site metal cations may be oxidised to  $Ca^{3+}$ ,  $Zr^{+5}$  or even  $Ta^{+6}$ . The unusually high oxygen contents could mean that a peroxide species may be covalently bound to the framework structure.

## 4.9 References

- [1] S.M. Haile, D.L. West, J. Campbell, *J. Mater. Res.*, **13** 6 (1998) 1576-1595
- [2] P. Ganguly, C.N.R. Rao, *J. Solid State Chem.* **53**, (1984) 193
- [3] M.K. Wu, J.R. Ashburn, C.J. Torng, P.H. Hor, R.L. Meng, L. Gao, Z.J. Wang, Y.Q. Chu, C.W. Chu, *Phys. Rev. Lett.*, **58**, (1987) 908
- [4] J. Krzystek, A. Sienkiewicz, L. Pardi, L.C. Brunel, *J. Mag. Res.*, **125**, (1997) 207-11
- [5] S. A. Al'tshuler, B.M. Kozyrev, in "Electron Paramagnetic Resonance" (C.P. Poole, Jr., Ed.) Academic Press, New York, 1964

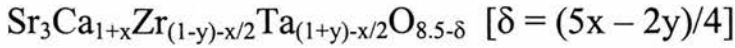
Chapter Five  
Structural Studies of the Complex  
Perovskite Proton Conductors



"Computers in the future may weigh no more than 1.5 tons."

---*Popular Mechanics*, 1949

## 5 Structural Studies of the Complex Perovskite Proton Conductors



### 5.1 Introduction

Here we report the structure of a new composition of multiple perovskite,  $\text{Sr}_3\text{CaZr}_{0.5}\text{Ta}_{1.5}\text{O}_{8.75}$ , as determined by X-Ray and Neutron refinement studies, including the deviations (lowering of symmetry) evident when the sample is hydrated compared to vacuum dried. The unit cell formula is written  $\text{Sr}_4\text{Ca}_{1.33}\text{Zr}_{0.66}\text{Ta}_2\text{O}_{11.66}$ , and compared with  $a_p$ , the simple cubic perovskite lattice parameter, this unit cell is tetragonal (as found by X-Rays) with cell  $\sqrt{2}a_p \times \sqrt{2}a_p \times 2a_p$ . In Chapter Four, TGA work on dry samples heated in wet 5%  $\text{H}_2/\text{Ar}$  atmospheres has revealed that approximately 55% of the oxygen-ion vacancies can be filled by water, according to the equation (in Kröger-Vink notation [1]):



The hydrating stage after vacuum treatment can be described by the following equation:



This present work focuses on the distortions induced by hydration of these proton conducting perovskites and on how the structure changes with temperature. Both high resolution and high-flux neutron diffraction were used to elucidate these differences.

## 5.2 Different Perovskite Unit Cells

Figure 5-1 below shows several of the unit cell distortions from the basic primitive cubic perovskite, that can occur. The simple primitive cubic perovskite (e.g.  $\text{SrTiO}_3$ ) has a cell side  $a$  of about  $4 \text{ \AA}$ , and is shown in blue. The bright red cell represents the distortion to tetragonal symmetry, with a  $\sqrt{2}a \times \sqrt{2}a \times 2a$  type unit cell. The largest cell ( $2a \times 2a \times 2a$ ) contains 8 primitive perovskite unit cells and is usually either cubic, or slightly orthorhombic. The trigonal/rhombohedral cell is shown in green. These other (enlarged) unit cell possibilities are more usual for doped systems, or those with a shift in stoichiometry on the B-site sublattice. These two modifications of the B-site sublattice induce the creation of oxygen ion vacancies as discussed before.

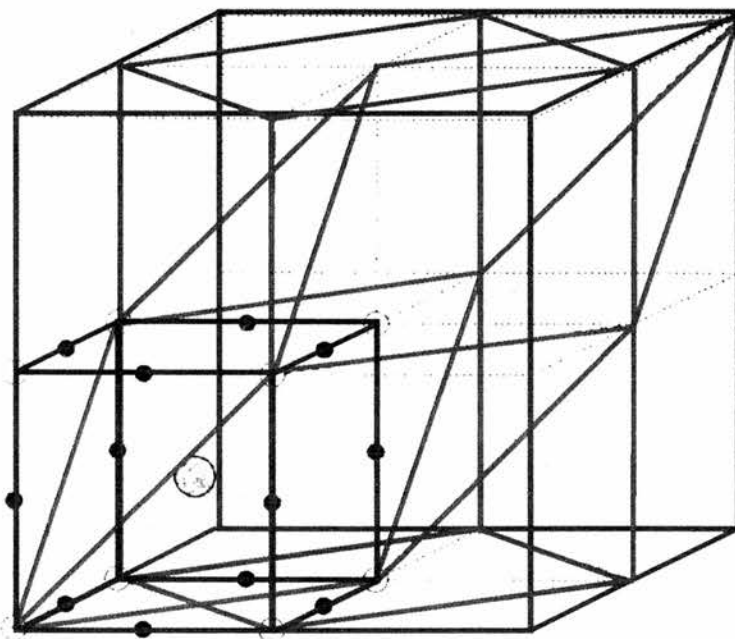


**Figure 5-1 : The primitive cubic perovskite unit cell is shown (in blue) as one octant of the  $2a \times 2a \times 2a$  doubled unit cell (purple). The tetragonal  $\sqrt{2}a \times \sqrt{2}a \times 2a$  unit cell is shown in red in the centre.**

An increased distortion to monoclinic symmetry in the tetragonal  $\sqrt{2}a \times \sqrt{2}a \times 2a$  unit cell would involve an angle deviation from  $90^\circ$  between any pair of axes. The simple primitive cubic unit cell contents can be represented by the formula  $ABO_3$ . The  $\sqrt{2}a \times \sqrt{2}a \times 2a$  unit cell however can be described as follows. 8 Sr cations are on the larger ( $\sqrt{2}a \times a$ ) faces of the tetragonal unit cell, which are each shared by 2 unit cells each ( $8 \times \frac{1}{2}$ ) giving rise to an equivalent of 4 Sr positions. 8 B cations are located at the corners of the tetragonal cell ( $8 \times \frac{1}{8}$ ), 4 at the centre points of the long ( $2a$ ) edges ( $4 \times \frac{1}{4}$ ), 2 at the centre of the smaller faces ( $2 \times \frac{1}{2}$ ) and one in the body centre of the cell, representing a total of 4 B cations. 8 O anions are located along the long edges (2 per edge) each shared by 4 unit cells ( $8 \times \frac{1}{4}$ ) equivalent to 2 positions. 8 O anions are located on the smaller faces of the cell (4 on each face), each shared by 2 unit cells, equivalent to 4 O positions. 6 more O anions are located in the centre of the cell surrounding the central B cation, forming an octahedron. This gives a total of 12 O positions. The unit cell formula of the  $\sqrt{2}a \times \sqrt{2}a \times 2a$  tetragonal unit cell is therefore  $A_4B_4O_{12}$  (assuming no oxygen or cation vacancies are present).

### 5.3 Structural Results for $Sr_3CaZr_{0.5}Ta_{1.5}O_{8.75}$

#### 5.3.1. X-Ray diffraction studies of $Sr_3CaZr_{0.5}Ta_{1.5}O_{8.75}$

The XRD pattern of as prepared  $Sr_3CaZr_{0.5}Ta_{1.5}O_{8.75}$  is shown in Figure 5-2. All the peaks found could be indexed to a unit cell of  $\sqrt{2}a_p \times \sqrt{2}a_p \times 2a_p$  tetragonal type symmetry. Both hydrated/deuterated phases, and vacuum treated phases were also examined by X-Ray diffraction.

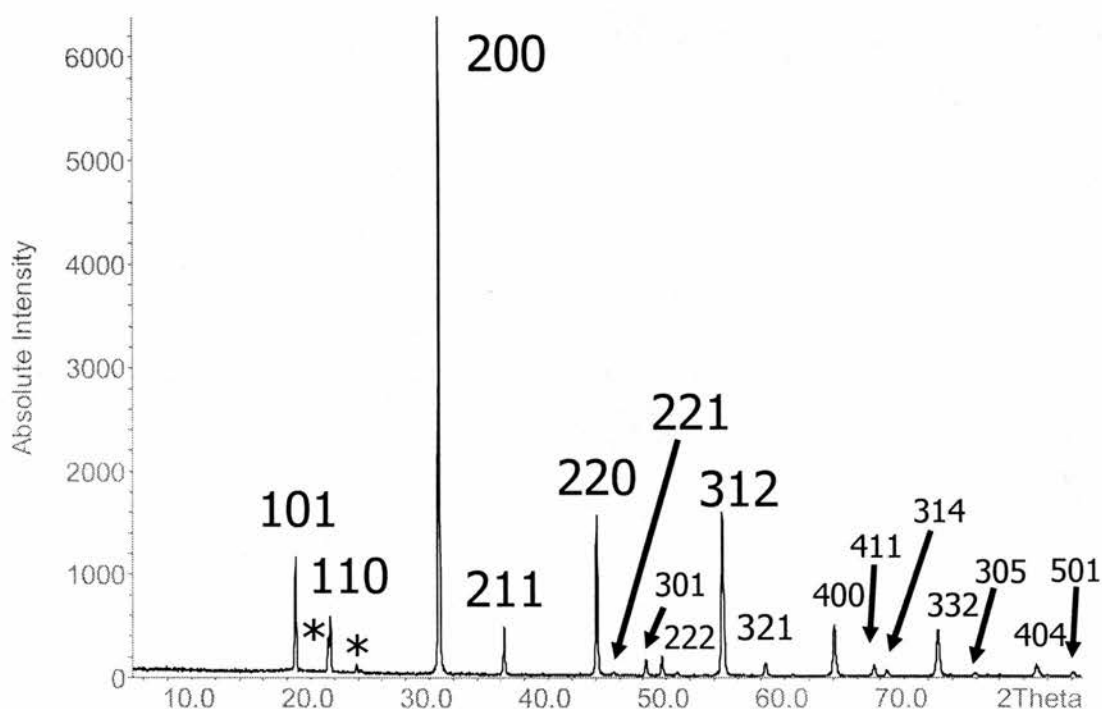


**Figure 5-2: XRD pattern for as prepared  $\text{Sr}_3\text{CaZr}_{0.5}\text{Ta}_{1.5}\text{O}_{8.75}$ . The indices are according to the tetragonal unit cell. Peaks marked with \* are due to Vaseline mounting jelly.**

Compositional Formula	Symmetry	a	c
$\text{Sr}_3\text{CaZr}_{0.5}\text{Ta}_{1.5}\text{O}_{8.75-y}(\text{OD})_{2y}$	Tetragonal	5.8112(6)	8.2213(5)
$\text{Sr}_3\text{CaZr}_{0.5}\text{Ta}_{1.5}\text{O}_{8.75}$	Tetragonal	5.8009(10)	8.2132(22)

**Table 5-1: Lattice parameters of hydrated and dry phases as determined by X-Ray diffraction ( $Z = 1.333$ )**

From Table 5-1, it is clear that at room temperature, the deuterated phase  $\text{Sr}_3\text{CaZr}_{0.5}\text{Ta}_{1.5}\text{O}_{8.75-y}(\text{OD})_{2y}$  exhibits a slightly expanded unit cell compared to the dry (vacuum treated) phase,  $\text{Sr}_3\text{CaZr}_{0.5}\text{Ta}_{1.5}\text{O}_{8.75}$ . The unit cell volumes are observed to expand by around 1% on deuteration using the Teflon bomb method. The number of

formula units, Z, per unit (tetragonal) cell is 1.333. The unit cell formula in the dry state can therefore be written as  $\text{Sr}_4\text{Ca}_{1.333}\text{Zr}_{0.666}\text{Ta}_2\text{O}_{11.666}$ .

### 5.3.2. High Temperature XRD Studies of $\text{Sr}_3\text{CaZr}_{0.5}\text{Ta}_{1.5}\text{O}_{8.75} + \text{H}_2\text{O}$

X-Ray diffraction was used to elucidate structural changes upon hydration/dehydration of the sample. The sample was first pre-treated in vacuum at 1000°C, and then hydrated in a Teflon bomb at 220°C with distilled H<sub>2</sub>O. Preliminary investigations by variable temperature X-Ray diffraction were carried out on a Stoe StadiP diffractometer, modified with a graphite furnace equipped with water and N<sub>2</sub> cooling. The sample was contained in a 0.5 mm quartz capillary and mounted in the furnace, and held for 3 hours at each temperature while a diffraction pattern was taken. For these runs, the sample was *not* rotating due to the surrounding furnace arrangement. Rotating the sample aids in minimising effects due to preferred orientation, in order to bring the greatest number of planes possible into the diffracting condition. A high amorphous background was present due to the contamination of the outer surface of the capillary with graphite. Up to 11 distinct peaks could be identified from the background for each run, and were used to refine the unit cell.

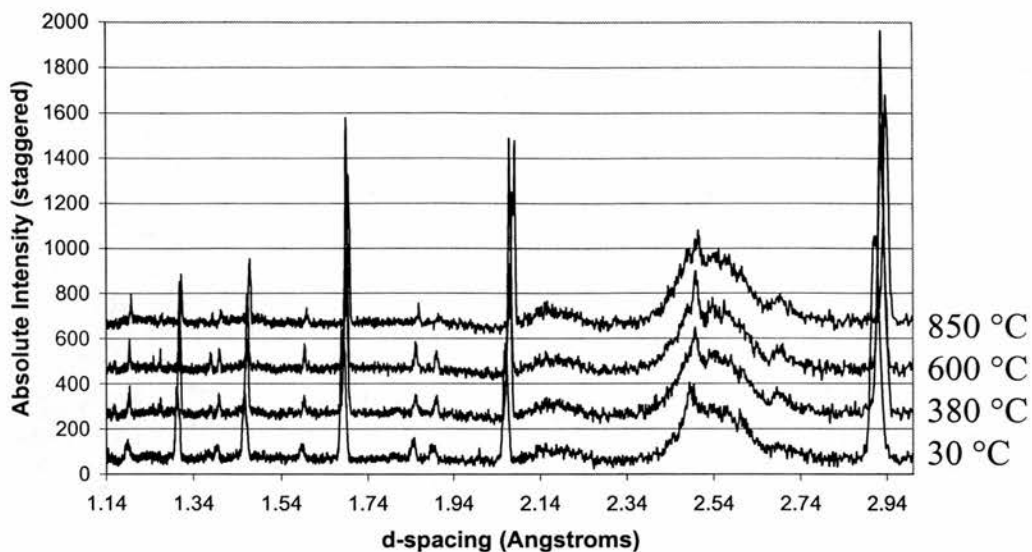


**Figure 5-3: Variable temperature XRD of  $\text{Sr}_3\text{CaZr}_{0.5}\text{Ta}_{1.5}\text{O}_{8.75} + \text{H}_2\text{O}$  over the entire d-spacing range measured**

Figure 5-3 shows the XRD patterns at 4 different temperatures corresponding to the hydrated state (30°C), the temperature at which the water loss/uptake rate reaches a maximum (380°C), the temperature at which all the water is lost from the structure (600°C), and the temperature at which  $\text{CO}_2$  is released (850°C). These temperatures were chosen in accordance with the results from the TGA-MS measurements under 5 %  $\text{H}_2/\text{Ar}$  as discussed in Chapter Four. The phases present at 30°C and 600°C are assumed to be stable, as represented by a flat portion in the TGA trace. These weight loss events are assumed to occur over similar temperature ranges in static air (no flow), the condition present in the capillary tube. The broad superimposed peak centred at 2.54 Å is due to the quartz  $\text{SiO}_2$  capillary tube.

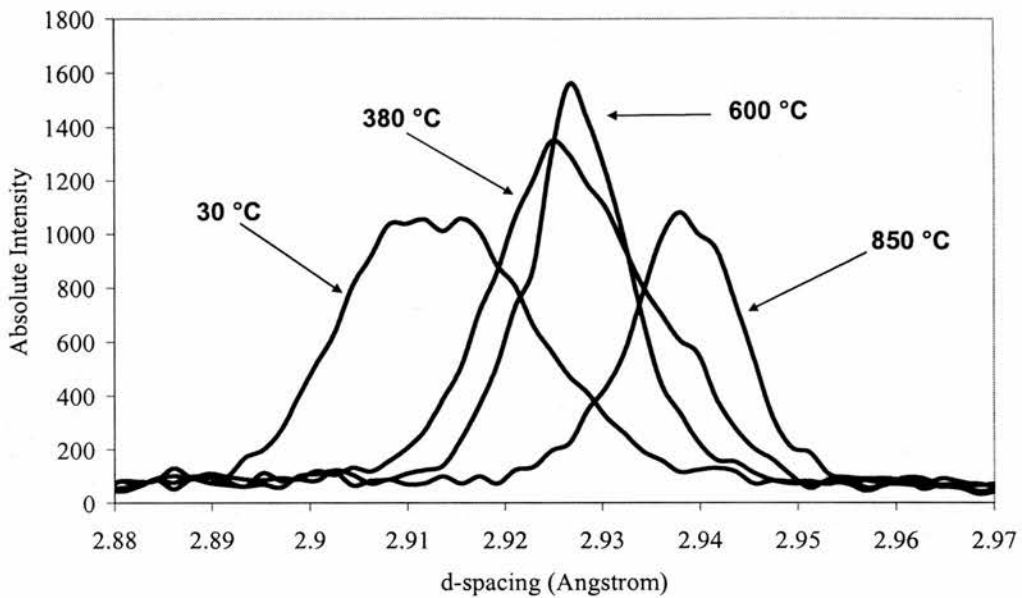


**Figure 5-4: Multi-temperature XRD of  $\text{Sr}_3\text{CaZr}_{0.5}\text{Ta}_{1.5}\text{O}_{8.75} + \text{H}_2\text{O}$  centred on most intense 200 peak at  $\sim 2.93 \text{ \AA}$**

From Figure 5-4 above, it is evident that from 30 to 380°C, there is an increase in d-spacing of the most intense (200) peak (by about 0.02 Å), with an implicit slight increase in the overall cell volume (Table 5-3). Little change occurs from 380 to 600°C (when H<sub>2</sub>O leaves the structure, and O<sup>2-</sup> vacancies return) as it is probable that cell shrinkage due to water loss is now superposed on cell expansion with temperature. At 850°C, there is a further increase in the d-spacing of this (200) peak (indexed on a tetragonal unit cell).

The unit cell volume has expanded by about 1.48 % between 600 and 850°C, according to a normal lattice expansion on heating. At this high temperature (850°C), close to the maximum number of oxygen ion vacancies would be present according to the compositional formula for the dry state,  $\text{Sr}_3\text{CaZr}_{0.5}\text{Ta}_{1.5}\text{O}_{8.75}$ . The inter-cation electrostatic forces would now be greater than in the room temperature hydrated phase as there are fewer anions surrounding them, thus causing the unit cell to expand. This

unit cell expansion with increasing temperature is also supported by the neutron diffraction results, discussed later. It is also possible that there is merely a change in the thermal expansion co-efficient with temperature, or even that this occurs in tandem with the increased inter-cation electrostatic forces. Estimated thermal expansion coefficients are shown below in Table 5-2. These values are calculated from the proportional difference in unit cell volume expansion at each temperature divided by the temperature range of interest.

Material	Thermal expansion coefficient, $\alpha$ ( $K^{-1}$ )	Temperature Range ( $^{\circ}C$ )
$Sr_3CaZr_{0.5}Ta_{1.5}O_{8.75}.xH_2O$	$4.3 \times 10^{-6}$	30-380
$Sr_3CaZr_{0.5}Ta_{1.5}O_{8.75}.xH_2O$	$19.6 \times 10^{-6}$	600-850
$ZrO_2$	$11.6 \times 10^{-6}$	30-850

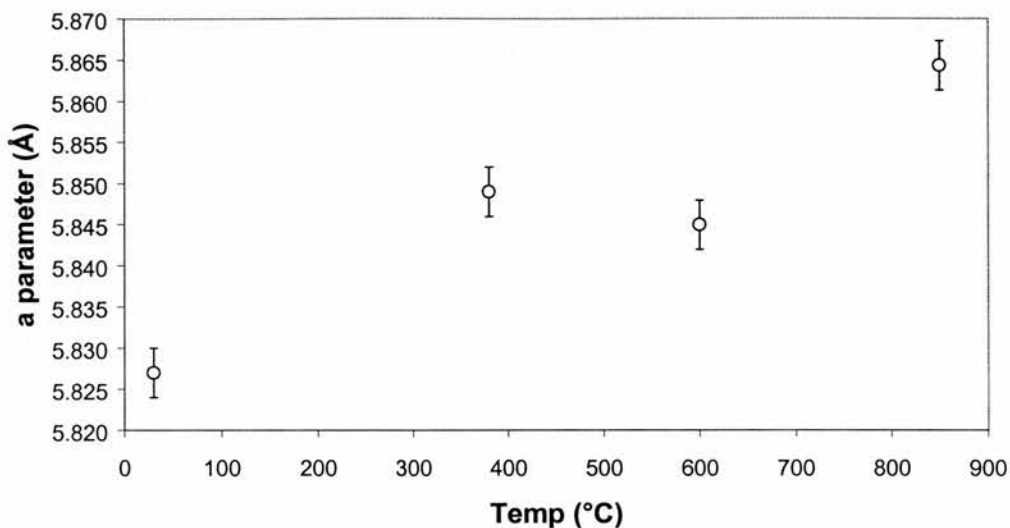
**Table 5-2: Estimated thermal expansion coefficients for hydrated  $Sr_3CaZr_{0.5}Ta_{1.5}O_{8.75}$  at room temperature from XRD data**

Temp	Symmetry	Lattice parameter ( $\text{\AA}$ )	UCV ( $\text{\AA}^3$ )	Tetragonality ( $\sqrt{2a/c}$ )
30 $^{\circ}C$	Tetragonal	a = 5.827(1) c = 8.248(3)	280.07(2)	0.999(1)
380 $^{\circ}C$	Tetragonal	a = 5.848(2) c = 8.263(2)	282.61(3)	1.001(1)
600 $^{\circ}C$	Tetragonal	a = 5.844(2) c = 8.250(1)	281.47(1)	1.002(1)
850 $^{\circ}C$	Tetragonal	a = 5.868(2) c = 8.303(3)	285.93(1)	1.000(1)

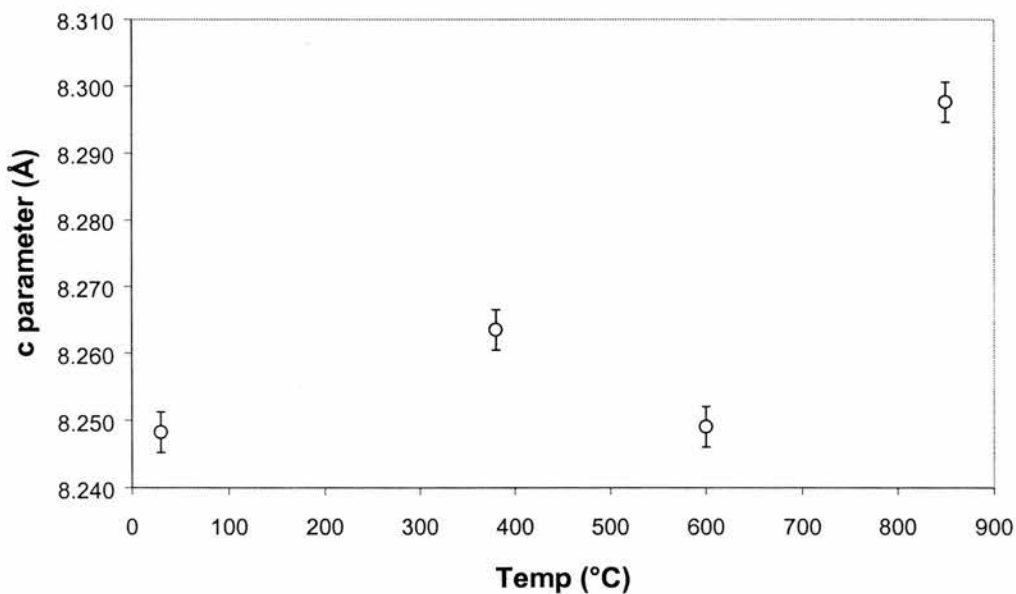
**Table 5-3: Unit cell parameters for various temperatures as determined by XRD for  $Sr_3CaZr_{0.5}Ta_{1.5}O_{8.75} + H_2O$**

It is evident from Table 5-3 that although an increase in unit cell volume with increasing temperature was picked up, any slight tetragonal distortion (lower symmetry

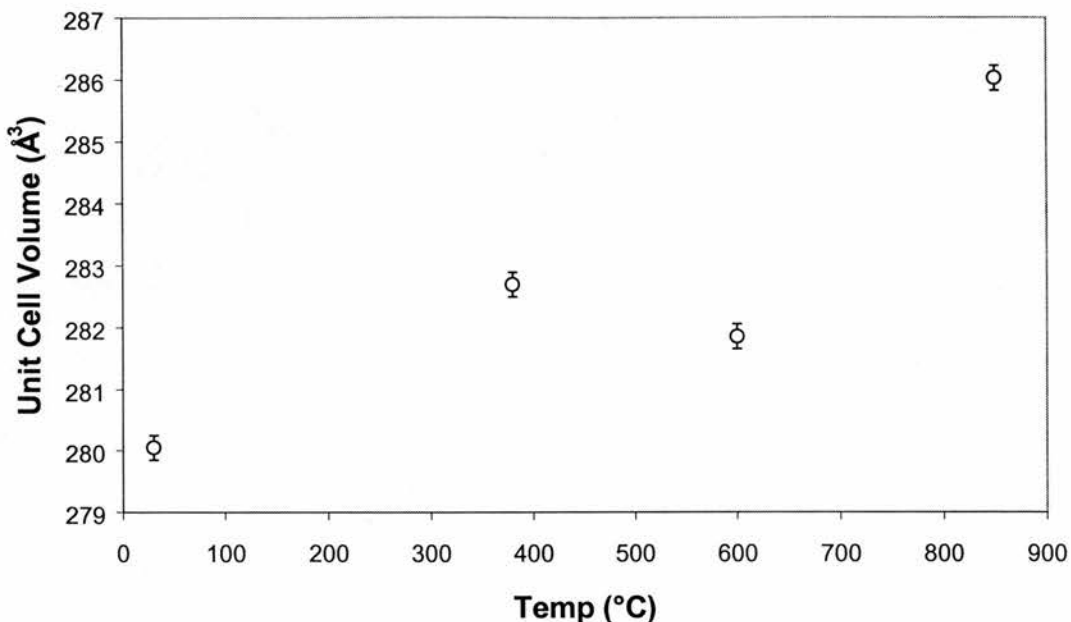
orthorhombic or increase in symmetry to cubic) is not really evident from the obtained unit cell parameters, although it is perceptible from the peak shapes seen in Figure 5-4.



**Figure 5-5: Unit Cell parameter a, for  $\text{Sr}_3\text{CaZr}_{0.5}\text{Ta}_{1.5}\text{O}_{8.75} + \text{H}_2\text{O}$  with increasing temperature. (XRD Results)**



**Figure 5-6: Unit Cell parameter c, for  $\text{Sr}_3\text{CaZr}_{0.5}\text{Ta}_{1.5}\text{O}_{8.75} + \text{H}_2\text{O}$  with increasing temperature. (XRD Results)**



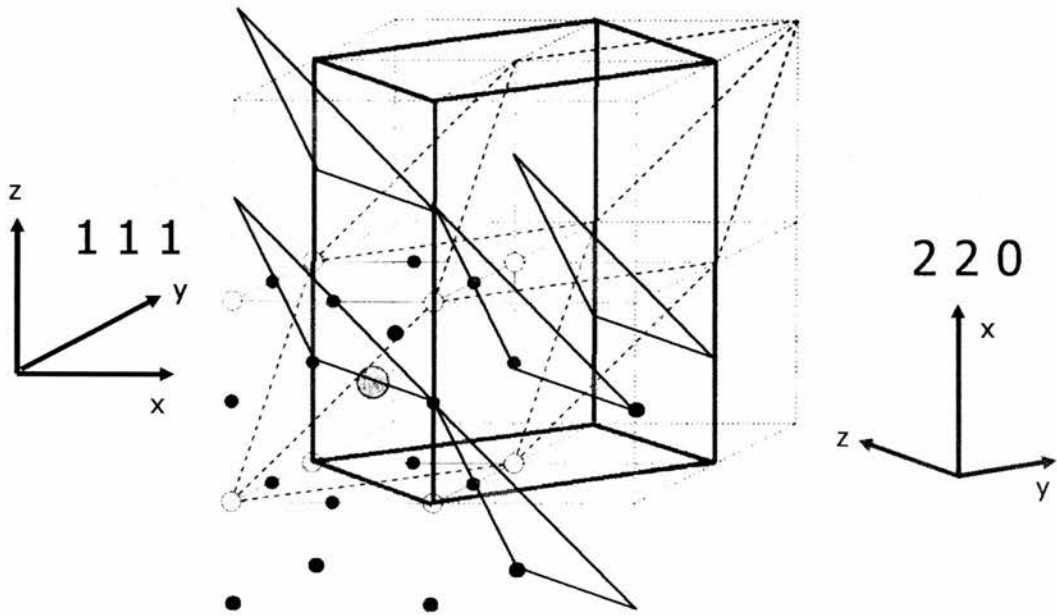
**Figure 5-7: Unit Cell volume, for  $\text{Sr}_3\text{CaZr}_{0.5}\text{Ta}_{1.5}\text{O}_{8.75} + \text{H}_2\text{O}$  with increasing temperature. (XRD Results)**

Figure 5-5, 5-6 and 5-7 illustrate the changes in lattice parameters and unit cell volume with temperature. A stable phase seems to be present at 600°C after the first water loss between 400 and 600°C, with little change in unit cell volume, and the TGA results on the sample up to 600°C support this well.

### 5.3.3. Neutron diffraction studies of $\text{Sr}_3\text{CaZr}_{0.5}\text{Ta}_{1.5}\text{O}_{8.75}$

The hydrated/deuterated phase of  $\text{Sr}_3\text{CaZr}_{0.5}\text{Ta}_{1.5}\text{O}_{8.75}$  was subsequently investigated by neutron powder diffraction, seeking to exploit the sensitivity of this technique to oxygen and the possibility of detecting protons or deuterons. The peaks at a d-spacing around 2.37Å originate from the primitive perovskite (111)<sub>p</sub> peak and would be anticipated to

be very sensitive to distortions away from cubic close packing of the  $\text{SrO}_3$  layers that are perpendicular to the  $[111]_p$  directions in the cubic perovskite.



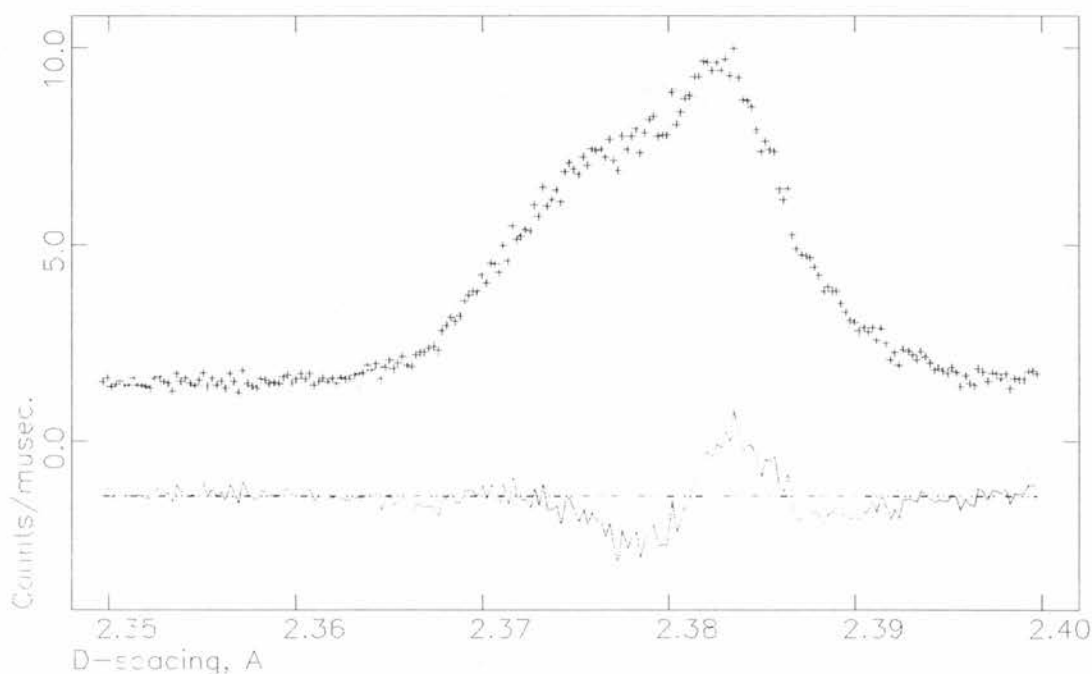
**Figure 5-8: The tetragonal  $\sqrt{2}a \times \sqrt{2}a \times 2a$  unit cell is depicted with the 220 planes of ccp  $\text{SrO}_3$  layers shown in grey. These are equivalent to the primitive  $(111)_p$  planes. The relative axes are shown.**

Figure 5-8 shows the equivalent planes in the tetragonal  $\sqrt{2}a \times \sqrt{2}a \times 2a$  unit cell to the  $(111)_p$  planes of the simple cubic  $a \times a \times a$  primitive cell, and can thus be indexed as the  $(220)$  planes with a suitable choice of origin. Oxygen displacements due to vacancy creation or filling (by O-H) groups will tend to result in a split peak at the interplanar d-spacing value associated with these  $(111)_p$  or  $(220)$  planes. This can be seen on examination of high resolution neutron diffraction data in the d-spacing region of 2.36 to 2.4 Å, according to the equation:

$$d_{111} = \frac{a}{\sqrt{h^2 + k^2 + l^2}} \quad \text{Equation 5-3}$$

when  $a \approx 4.11$ . The wider the splitting, the greater the distortion on the oxygen sublattice, and therefore, the lower the symmetry of the perovskite unit cell.

At the highest levels of hydration (at room temperature), these samples will tend to exhibit the highest level of unit cell deviation from cubic symmetry. In the dry state (at temperatures in excess of  $900^\circ\text{C}$ ), oxygen ion vacancies are present, and will tend to order, giving rise to higher symmetry.



**Figure 5-9: Orthorhombic space group (Pmnm) convergent LeBail extraction fitting of the (220),(202) doublet at 2.37-2.39 Å for  $\text{Sr}_3\text{CaZr}_{0.5}\text{Ta}_{1.5}\text{O}_{8.75} + \text{D}_2\text{O}$  (in-situ at  $200^\circ\text{C}$ ).**

Initial attempts at refinement with an orthorhombic unit cell, did not give satisfactory results. This failure is highlighted by the inability to achieve the necessary splitting of the (220),(202) doublet peak at 2.375 Å using Pmnm, Pmmm and P222<sub>1</sub> (used in

structural studies of  $\text{Sr}_{0.97}\text{NbO}_3$ ) [2]. Figure 5-9 above shows the refinement results with the LeBail extraction technique (observed, calculated and difference profiles) using the orthorhombic space group Pmmn. Similar results were obtained for other closely related orthorhombic space groups, and even poorer fitting was obtained using tetragonal space groups. All other peaks are adequately fitted using tetragonal/orthorhombic space groups, except the doublet between 2.36 and 2.4 Å, and a widened splitting fit (as in Figure 5-9) merely results in all other peaks being too strongly split. So even resorting to orthorhombic symmetry (the same sample was found to be tetragonal by X-Ray diffraction), the calculated splitting of the peak centred at 2.375 Å d-spacing is clearly not adequate, suggesting that a lower symmetry space group is required for improved refinement.

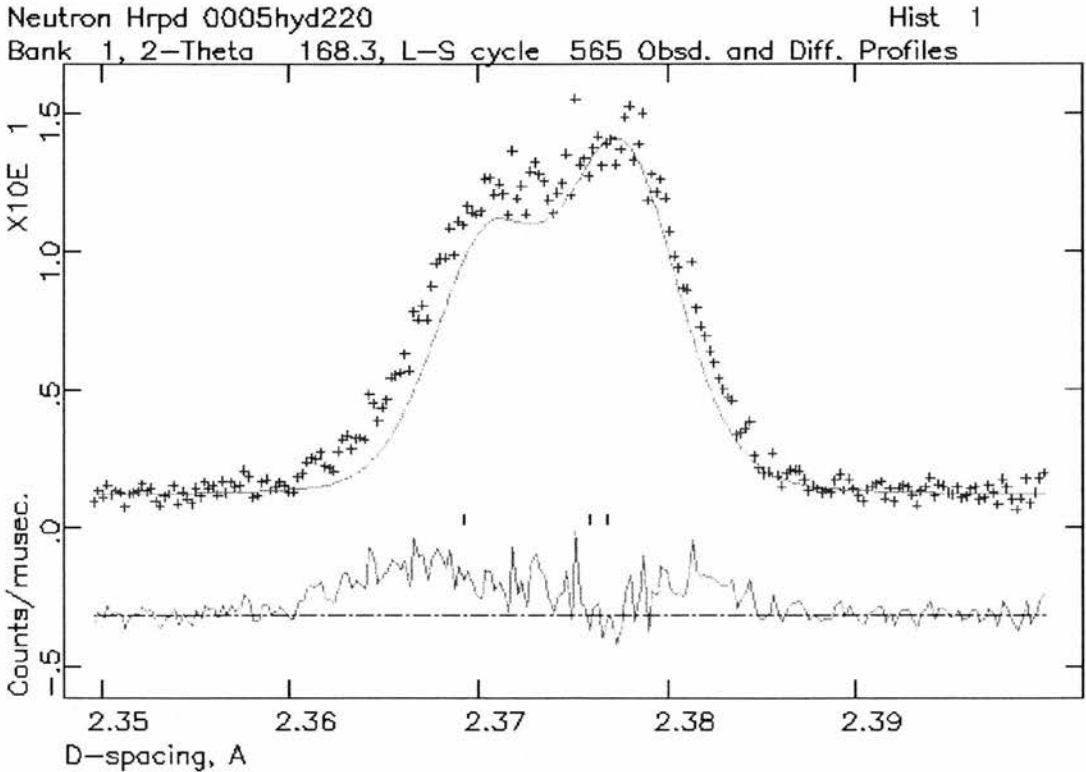


**Figure 5-10: Splitting obtained with the Monoclinic P1a1 space group. Both peaks are now accommodated.**

Figure 5-10 above, clearly shows the considerable improvement in fitting the 220,202,-202 splitting using a monoclinic space group. This result was obtained from Rietveld refinement and was identical to LeBail extraction results, indicating a more accurate structural solution has been obtained. The final determination of the unit cell dimensions of a hydrated  $\text{Sr}_3\text{CaZr}_{0.5}\text{Ta}_{1.5}\text{O}_{8.75}$  sample was obtained from a full Rietveld refinement of Neutron Diffraction data, collected on the HRPD instrument at Rutherford Appleton Laboratories. The data was collected at room temperature to ensure that structural O-H groups were retained. The structure was solved using the  $P1a1$  space group (unique axis b setting), as this was required to fit some significant split peaks. As discussed later, at higher temperatures these splittings disappear, accompanied by the loss of other minor peaks, indicating a shift to higher symmetry as O-D/O-H groups leave the structure in the form of water, and oxygen vacancies return.

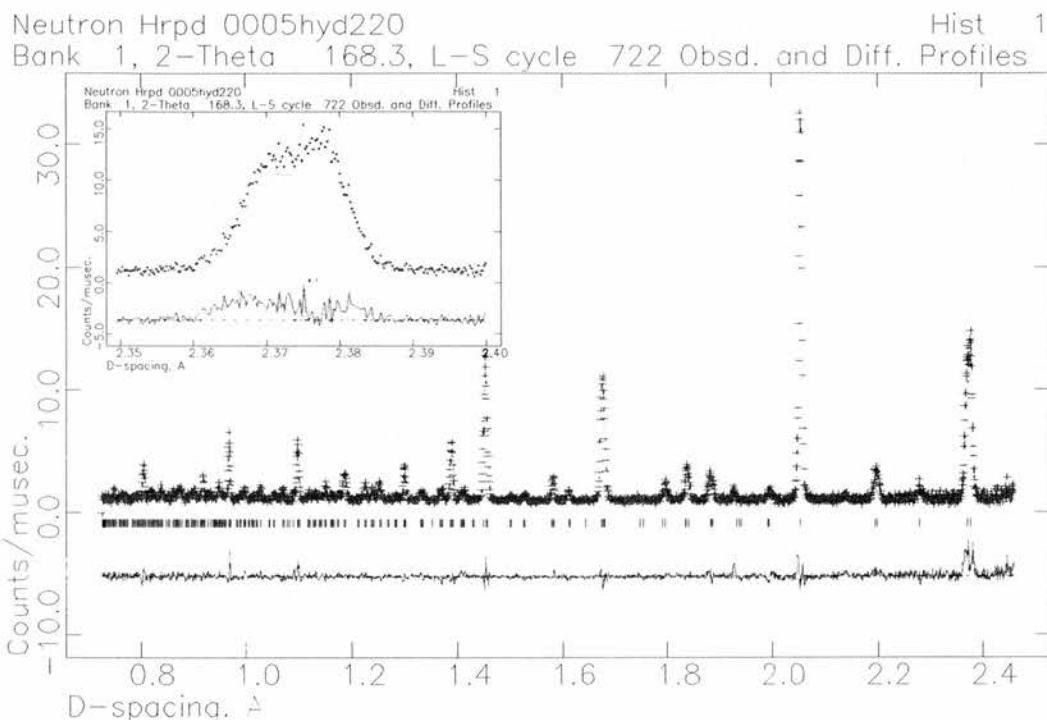


**Figure 5-11: Observed, calculated and difference profiles for  $\text{Sr}_3\text{CaZr}_{0.5}\text{Ta}_{1.5}\text{O}_{8.75-y}(\text{OH})_{2y}$  ( $y \approx 0.1375$ ) as a result of Rietveld Refinement using GSAS. P1a1 space group:  $\chi^2 = 1.979$ ,  $wR_p = 11.56\%$ ,  $R_p = 10.38\%$ . The inset shows the fit to the 220, 202, -202 split peak.**

The unit cell of the 2.5 MPa steam treated sample of  $\text{Sr}_3\text{CaZr}_{0.5}\text{Ta}_{1.5}\text{O}_{8.75}$  at  $25^\circ\text{C}$  was found to best fit a monoclinic  $\approx 2a_p \times \approx \sqrt{2}a_p \times \approx \sqrt{2}a_p$  unit cell in the space group P1a1 with  $a = 8.22030(6) \text{ \AA}$ ,  $b = 5.80047(9) \text{ \AA}$ ,  $c = 5.82668(5) \text{ \AA}$  and  $\beta = 89.973(1)^\circ$  (Figure 5-11). The unit cell volume is  $277.826(2) \text{ \AA}^3$ . A slight deviation from tetragonal  $2a_p \times \sqrt{2}a_p \times \sqrt{2}a_p$  symmetry is picked up by the neutron refinement, this symmetry reduction arising as a result of the distortions on the oxide sub-lattice due to the filling of vacancies with water from the hydration procedure.  $\text{Sr}_3\text{CaZr}_{0.5}\text{Ta}_{1.5}\text{O}_{8.75-x}(\text{OH})_{2x}$  is found to exhibit a  $\sqrt{2}a \times \sqrt{2}a \times 2a$  type tetragonal unit cell by X-ray diffraction studies. Neutron diffraction, however, has revealed that the symmetry is in fact lower, and the

unit cell is actually a distorted tetragonal, or monoclinic unit cell. However, with the space group P1a1, as it designated a unique axis b (cell choice 3 of Pc space group, No.7) and the angle  $\beta$  ( $< 90^\circ$ ) is between the a and c axes, the distortion is viewed as a  $[\approx 2a \times \approx \sqrt{2}a \times \approx \sqrt{2}a]$  type unit cell (i.e. a mere interchange of axes).

The inset in Figure 5-11 shows the (220) peak ( $\text{AO}_3$  ccp layers in the  $2a_p \times \sqrt{2}a_p \times \sqrt{2}a_p$  cell), which is clearly split. As shown for  $\text{Sr}_3\text{Ca}_{1+x}\text{Nb}_{2-x}\text{O}_{9-\delta} + \text{D}_2\text{O}$ , in Chapter Three, this peak is very sensitive to the level of hydration or percentage of  $\text{O}^{2-}$  vacancies filled.

Name	x	y	z	$U_{\text{ISO}}$ (x 100)	Site Occ.
Sr1	0.25132	0.00597	0.01619	1.829	0.9732
Sr2	0.25021	0.49764	0.47993	1.829	1.0669
Ca1	0.00514	0.50227	-0.00381	0.303	0.3451
Zr1	0.00514	0.50227	-0.00381	0.303	0.1948
Ta1	0.00514	0.50227	-0.00381	0.303	0.5282
Ca2	0.00594	0.00079	0.49789	0.866	0.3375
Zr2	0.00594	0.00079	0.49789	0.866	0.1708
Ta2	0.00594	0.00079	0.49789	0.866	0.5042
O1	0.44444	0.72153	0.33602	0.884	1.0313
O2	0.29569	0.57778	-0.02742	4.470	0.6078
O3	0.95072	0.20855	0.77969	0.917	1.0946
O4	0.53976	0.26045	0.72715	0.793	1.0785
O5	0.00774	0.73096	0.24672	1.912	1.2363
O6	0.75241	0.94966	0.54539	3.489	1.0669
H	0.05964	0.88874	0.67554	1.000	0.2300

**Table 5-4: Refined atomic positions, temperature factors, and fractional occupancies for  $\text{Sr}_3\text{CaZr}_{0.5}\text{Ta}_{1.5}\text{O}_{8.75-y}(\text{OH})_{2y}$  ( $y \approx 0.1375$ ). All positions are 2a with a multiplicity of 2 and site symmetry of 1.**

Table 5-4 shows the atomic positions for  $\text{Sr}_3\text{CaZr}_{0.5}\text{Ta}_{1.5}\text{O}_{8.75-y}(\text{OH})_{2y}$  ( $y \approx 0.1375$ ) at room temperature. The B-site cation occupancies closely match the compositional ratios. There is also evidence of some remaining  $\text{O}^{2-}$  vacancies with a slight occupancy deficiency on one site, that of O2 labelled in Table 5-4. Distinguishing Zr from Ta in a neutron diffraction experiment can be difficult because of their similar scattering factors, but good agreement with site occupancy and stoichiometry was achieved. The very close values in site occupancies for both B-sites is indicative of B-site disorder at room temperature, with a random distribution of Ca, Zr and Ta. There seems to be an equal distribution of Ca on both sites. Using the refined site occupancies, the stoichiometry is found to be  $\text{Sr}_{3.065}\text{Ca}_{1.024}\text{Zr}_{0.548}\text{Ta}_{1.549}\text{O}_{9.173}\text{H}_{0.345}$  (or  $\text{Sr}_{3.065}\text{Ca}_{1.024}\text{Zr}_{0.548}\text{Ta}_{1.549}\text{O}_9(\text{OH})_{0.345}$ ) whereas the oxygen content calculated from TGA water loss results was  $\text{Sr}_3\text{CaZr}_{0.5}\text{Ta}_{1.5}\text{O}_{8.625}(\text{OH})_{0.275}$ . The higher oxygen content revealed by the neutron diffraction results suggest that extra species containing oxygen, *as well as H<sub>2</sub>O*, may be incorporated within the structure due to high pressure steam treatments. This ties in well with the discovery that some  $\text{CO}_2$  is released from the sample above  $700^\circ\text{C}$  when hydrothermally pre-treated, as discussed in Chapter Four.

Fourier difference maps were used to discover a position for hydrogen atoms, and from bond distance calculations they were located at a distance of about  $0.9 \text{ \AA}$  from an oxygen position, essentially forming O-H groups. This will be discussed later. Table below lists the average bond lengths found:

<b>Atom Types</b>	<b>Average Bond Distance (Å)</b>
B1-B2	4.095(4)
B1-B1	4.110(9)
B2-O4	2.038(7)
B2-O5	2.137(7)
B2-O6	2.084(9)
B1-O2	2.423(1)
B1-O3	2.181(9)
B1-O4	2.115(2)
B1-O5	1.949(5)
Sr1-Sr1	4.110(6)
Sr2-Sr1	3.944(6)
O4-H2	0.930(6)

**Table 5-5: Average bond lengths from Rietveld refinement for  $\text{Sr}_3\text{CaZr}_{0.5}\text{Ta}_{1.5}\text{O}_{8.75-y}(\text{OH})_{2y}$  ( $y \approx 0.1375$ ) at 25°C. B1 and B2 denote the two  $\text{CaZr}_{0.5}\text{Ta}_{1.5}$  positions.**

5.3.4. The change in structure with temperature for  $\text{Sr}_3\text{CaZr}_{0.5}\text{Ta}_{1.5}\text{O}_{8.75} + \text{D}_2\text{O}$

Multi-temperature neutron diffraction data was also obtained on the Polaris instrument for a deuterated  $\text{Sr}_3\text{CaZr}_{0.5}\text{Ta}_{1.5}\text{O}_{8.75}$  sample. As is evident from Figure 5-12, some peaks, (indicated by an asterisk (\*)) disappear by 500°C, but others persist beyond this temperature, and only fully diminish by 1000°C, (indicated by an open circle (°)). This clearly suggests that there are two distinct changes in symmetry as the sample is heated. According to the hkl indices of the peaks that disappear for dry samples (by 600 and up to 1000°C), the following sequence of space group transformations can be proposed:

P1a1 Monoclinic (25°C) → P2/a Monoclinic (200°C) → Pmmn Orthorhombic (600°C)  
 → P4<sub>2</sub>/nmc Tetragonal (>600 to 800°C) → I4/mmm Tetragonal (>800°C) → Fm-3m  
 Cubic (1000°C)

Indeed, this corresponds to a transition from a *monoclinic* ( $\approx 2a_p \times \approx \sqrt{2}a_p \times \approx \sqrt{2}a_p, \beta \neq 90^\circ$ ) type unit cell to *orthorhombic* ( $\approx 2a_p \times \approx \sqrt{2}a_p \times \approx \sqrt{2}a_p, \beta = 90^\circ$ ) to *tetragonal* ( $2a_p \times \sqrt{2}a_p \times \sqrt{2}a_p$ ) through to *cubic* ( $2a_p \times 2a_p \times 2a_p$ ).

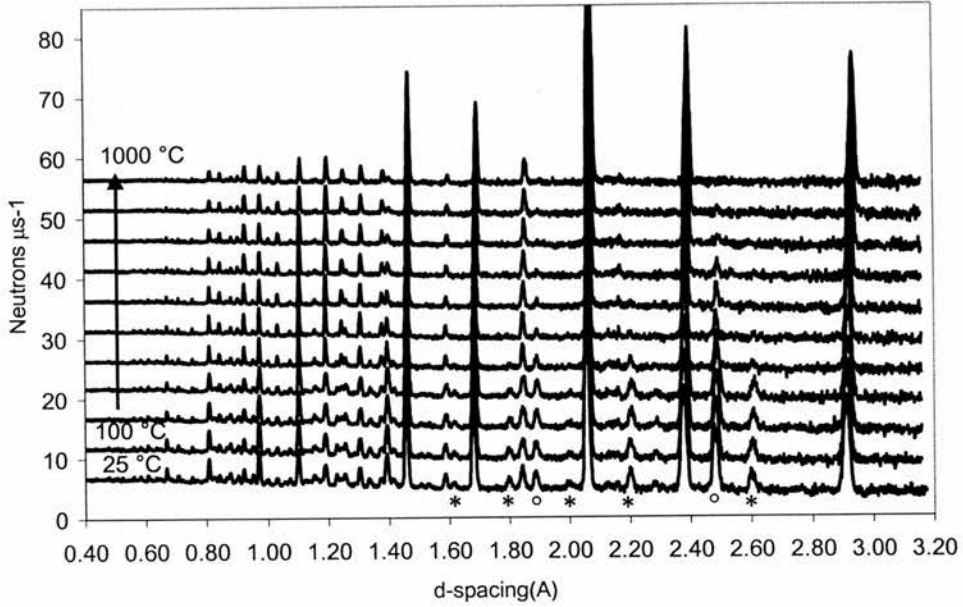


**Figure 5-12: Multi-temperature Neutron Diffraction patterns for  $\text{Sr}_3\text{CaZr}_{0.5}\text{Ta}_{1.5}\text{O}_{8.75-y}(\text{OD})_{2y}$  ( $y \approx 0.1375$ )**

Referring to Figure 5-12, a zoom in on the 220,202, -202 broad splitting centred at 2.375 Å at 25°C and from 100 to 1000°C, shows in more detail how the broad peak at low temperatures, forms a sharper single peak above 500°C (see Figure 5-13).

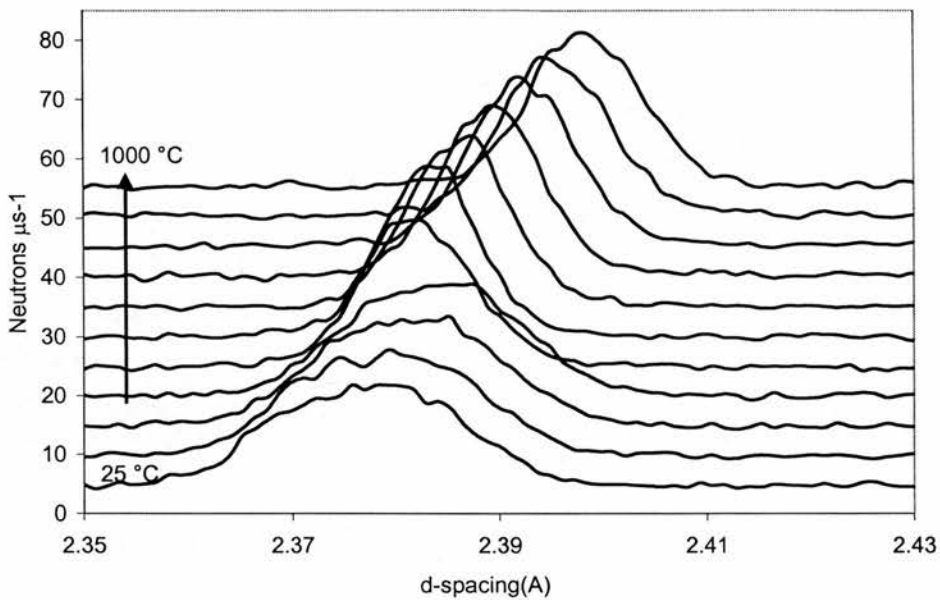


**Figure 5-13: Evolution of the 220,202,-202 splitting with temperature for  $\text{Sr}_3\text{CaZr}_{0.5}\text{Ta}_{1.5}\text{O}_{8.75-y}(\text{OD})_{2y}$  ( $y \approx 0.1375$ )**

Structureless whole pattern fitting (LeBail) [3] was used to elucidate the space group evolution with temperature using HRPD data. The space group sequence outlined above was tested at four different temperatures, 25°C (ambient conditions, hydrated), 200°C (hydrated), 600°C (dehydrated) and 1000°C. The proposed space group transformations with temperature seem very reasonable. Every peak at exhibits some minor asymmetry, which is a natural result of the pulse shape of the incoming neutron beam and will not be deliberated further here. Table 5-6 shows the expected ( $R_p$ ) and calculated weighted profile ( $wR_p$ ) agreement or  $R$ -factors as well as the “quality of fit”  $\chi^2$  values. A trend of expansion of the unit cell with temperature is also clearly evident, and these values remain similar even with different space groups, also indicating an accurate fit.

Temp (°C)	Space group	R <sub>p</sub> (%) (expected)	wR <sub>p</sub> (%) (calc)	χ <sup>2</sup>	Unit Cell Volume (Å <sup>3</sup> )
<b>25</b>	<b>P1a1</b>	<b>8.41</b>	<b>8.63</b>	<b>1.527</b>	<b>277.849(7)</b>
25	P 2/a	9.32	9.83	1.829	277.854(8)
25	P m m n	9.20	9.45	1.766	277.825(6)
200	P 1 a 1	7.71	8.88	1.703	279.628(5)
<b>200</b>	<b>P 2/a</b>	<b>7.85</b>	<b>9.07</b>	<b>1.676</b>	<b>279.611(7)</b>
200	P m m n	8.76	10.16	2.019	279.714(5)
<b>600</b>	<b>P m m n</b>	<b>8.87</b>	<b>12.19</b>	<b>2.456</b>	<b>282.020(9)</b>
600	P 4 <sub>2</sub> /n m c	10.21	16.82	2.795	282.021(8)
600	I 4/m m m	13.88	26.64	3.72	282.100(3)
<b>1000</b>	<b>P 4<sub>2</sub>/n m c</b>	<b>8.24</b>	<b>9.44</b>	<b>2.366</b>	<b>286.355(1)</b>
1000	I 4/m m m	9.09	10.98	2.376	286.213(3)
1000	F m -3 m	10.38	14.13	2.826	572.353(0)

**Table 5-6: LeBail structureless whole pattern fitting showing space group evolution with temperature. The bold figures show the logical choices.**

The peaks in a neutron diffraction pattern arise due to diffraction occurring at the *nuclei* of atoms. X-Ray diffraction however relies on the diffraction of incident radiation from the *electron clouds* of atomic planes. Neutron diffraction can be more sensitive to subtle distortions of the oxygen sublattice as the scattering factor for oxygen is on a par with that of most other metallic elements. Table 5-7 below gives the bound coherent scattering length values for the elements relevant to the present work.

Element	Neutron scattering factor (10 <sup>-15</sup> m)
Sr	7.02
Ca	4.70
Zr	7.16
Ta	6.91
O	5.803
H	-3.741
D	6.671

**Table 5-7: Neutron scattering lengths relevant for Sr<sub>3</sub>CaZr<sub>0.5</sub>Ta<sub>1.5</sub>O<sub>8.75</sub> [4]**

The scattering factors for X-rays, are however related to the number of electrons associated with a particular element or ion, and since oxygen has considerably less (eight) electrons compared to the heavy metals used to synthesise  $\text{Sr}_3\text{CaZr}_{0.5}\text{Ta}_{1.5}\text{O}_{8.75}$ , the influence of the oxygen sublattice (or slight distortions of it) on peak-splittings is less evident compared to neutron diffraction. The peaks due to oxygen planes are also much stronger in neutron diffraction patterns compared to X-ray patterns, for the reasons discussed previously. This is why neutron diffraction can be useful when subtle deviations in symmetry may be present which are due to oxygen ion displacements giving rise to octahedral distortions. The fact that protons are negative scatterers compared to deuterons (Table 5-7), also makes it easier to distinguish and locate O-H groups within the structure, and both deuterated and protonated samples are investigated here.

For  $\text{Sr}_3\text{CaZr}_{0.5}\text{Ta}_{1.5}\text{O}_{8.75} + \text{D}_2\text{O}$ , Figure 5-12, there is clear evidence for symmetry increase in going from a hydrated to a dry state. At low temperatures (100 to 500°C) the sample can be considered to be in a “hydrated state” whereby up to 60 % of oxygen ion vacancy positions are filled by  $\text{D}_2\text{O}$ . At 1000°C, the sample is under high vacuum conditions ( $10^{-5}$  to  $10^{-6}$  mbar), so it is possible to determine the symmetry *in situ* for a very dry sample. All incorporated  $\text{D}_2\text{O}$  is lost from the structure by this temperature.

#### 5.3.5. Structure modelling and proton positions

It was possible to build up a structural model from the refined atomic positions as a result of the Rietveld refinement. This was specifically acquired to highlight the high level of octahedral distortion present at room temperature, and also to show the possible

positions of the O-H groups in the structure (discussed later). Furthermore, as there are 2 distinct B-sites in this perovskite, the model also served as a visual aid to highlight the type of B-cation order present. Figure 5-14 and Figure 5-15 show two representations of the refined structural model for  $\text{Sr}_3\text{CaZr}_{0.5}\text{Ta}_{1.5}\text{O}_{8.75} + \text{H}_2\text{O}$ . The 1:1 ordering of B-sites is clearly evident in the bc plane. They can also be termed as alternating ab planes along the c-direction. Refinements of the B-cation site occupancies however, suggests a disordered distribution of Zr, Ta and Ca cations is present at low temperatures (Table 5-4).

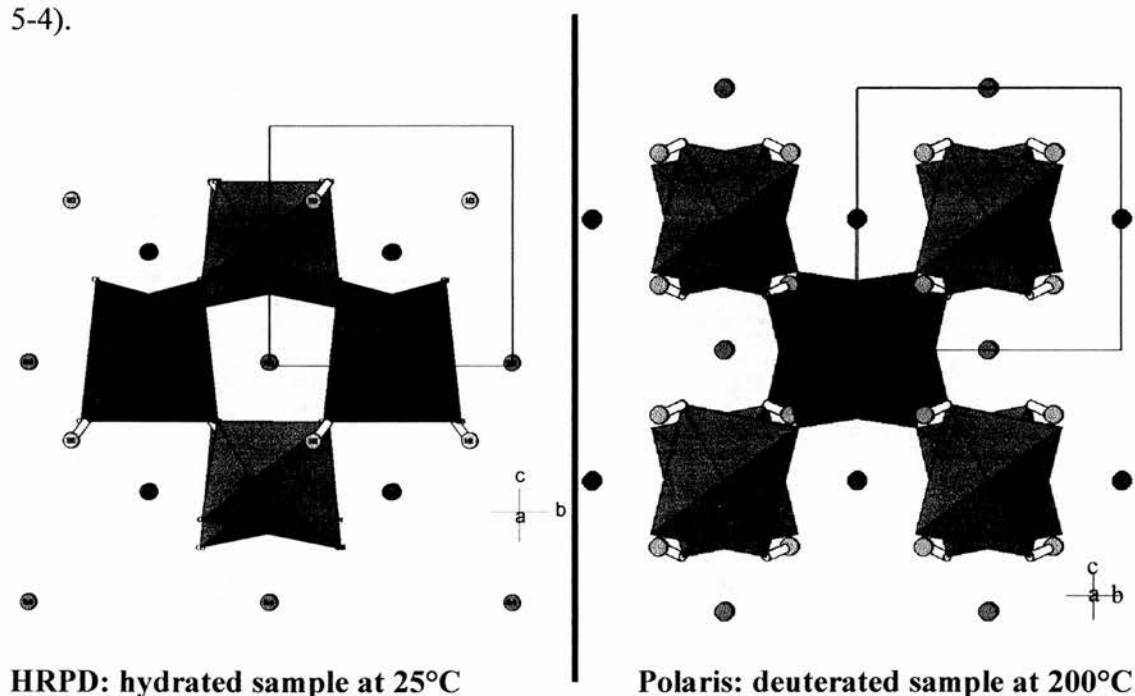


**Figure 5-14: Refined structural model of the bc plane of both bomb hydrated [left] and deuterated [right, (Section 5.3.4)]  $\text{Sr}_3\text{CaZr}_{0.5}\text{Ta}_{1.5}\text{O}_{8.75}$  measured on HRPD and Polaris. The unit cell axes are also shown. The located H and D positions are highlighted (although *all* of these positions may not be filled in practice).**

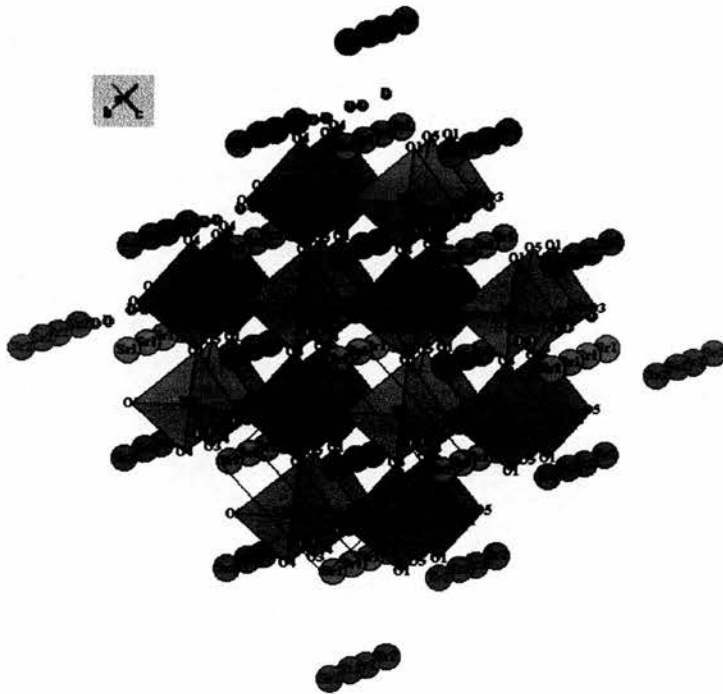


**Figure 5-15: Room temperature structure model of  $\text{Sr}_3\text{CaZr}_{0.5}\text{Ta}_{1.5}\text{O}_{8.75} (\text{D}_2\text{O})$  measured on HRPD. The two B-sites are shown in blue and red.**

A Fourier difference map revealed volumes of “unfitted density” in the structure, and can be attributed to the existence of hydrogen atoms (which diffuse as protons) close to the atomic positions of some oxygens. These exist as O-H groups, which have filled an oxygen ion vacancy position as a result of sample hydration. The procedure would then involve the introduction of hydrogen atoms into the atomic position listing of the Rietveld data input at the calculated positions of this negative (nuclear) density, in order to obtain a better quality of fit the subsequent round of refinement cycles.

It can be seen from the picture of the “closest-fit” refined structure in Figure 5-15 ( $\chi^2 = 1.987$ ), that “O-H” groups present in the structure, can significantly distort the oxygen-ion framework, and also give rise to substantial  $\text{BO}_6$  octahedral tilt. It has been shown that the disorder (and hence the splitting of the peak centred at  $2.375 \text{ \AA}$ ) will reduce, as

water is lost from the structure (all structural H<sub>2</sub>O is lost by 600°C). Another structure change occurs between 600 and 1000°C, as TGA evidence suggests that oxygen (molecular or atomic) and CO<sub>2</sub> are lost from the structure.

The accurate location of protons/O-H groups in perovskite oxides has also very recently been investigated for BaCe<sub>0.9</sub>Y<sub>0.1</sub>O<sub>2.95</sub> [5], which was cooled to 4.2 K to freeze out lattice vibrations and proton diffusion. It was reported that an O-H bond distance of 0.93 Å is present. In this work, refinement of room temperature neutron diffraction data has revealed a possible O-H distance of about 0.9 Å. This is a result of the fact that difference Fourier density maps of hydrated Sr<sub>3</sub>CaZr<sub>0.5</sub>Ta<sub>1.5</sub>O<sub>8.75</sub> showed small volumes of negative unfitted density in 3-D space at positions near to oxygen positions. These positions have been initially ascribed to hydrogen, and the refinement was continued until the hydrogen position remained consistent and stable. It is possible that the second position proposed for H is not realistic as the O-H distance is almost 1.4 Å. The typical bond length for O-H is usually 1.02 to 1.22 Å [6]. It often turns out to be the case in Fourier maps, that an *alternative* missing atom position is the result of noise misfit around existing heavier atoms than the one in question (hydrogen). TGA-MS results have also indicated that a small percentage of oxygen vacancy positions may in fact be occupied by an oxygen species (peroxide/superoxide or molecular CO<sub>2</sub>).

As an aid to clearer visualisation of where the proposed missing hydrogens may be in the structure, a 3-dimensional VRML (Virtual Reality Modelling Language) Fourier map was generated (Figure 5-16). The resultant image reveals small elongated “cages” around some oxygen positions, indicative of the existence of O-H groups. There is also some noise present. The generation of a 3-D VRML map with the lowest level of noise while maintaining the information on the missing atoms, required the adjustment and

modification of the contour levels, i.e. the sensitivity of the calculation to nuclear density. A detailed account of this procedure is outlined in the Collaborative Computational Project No. 14 (CCP14) documentation [7]

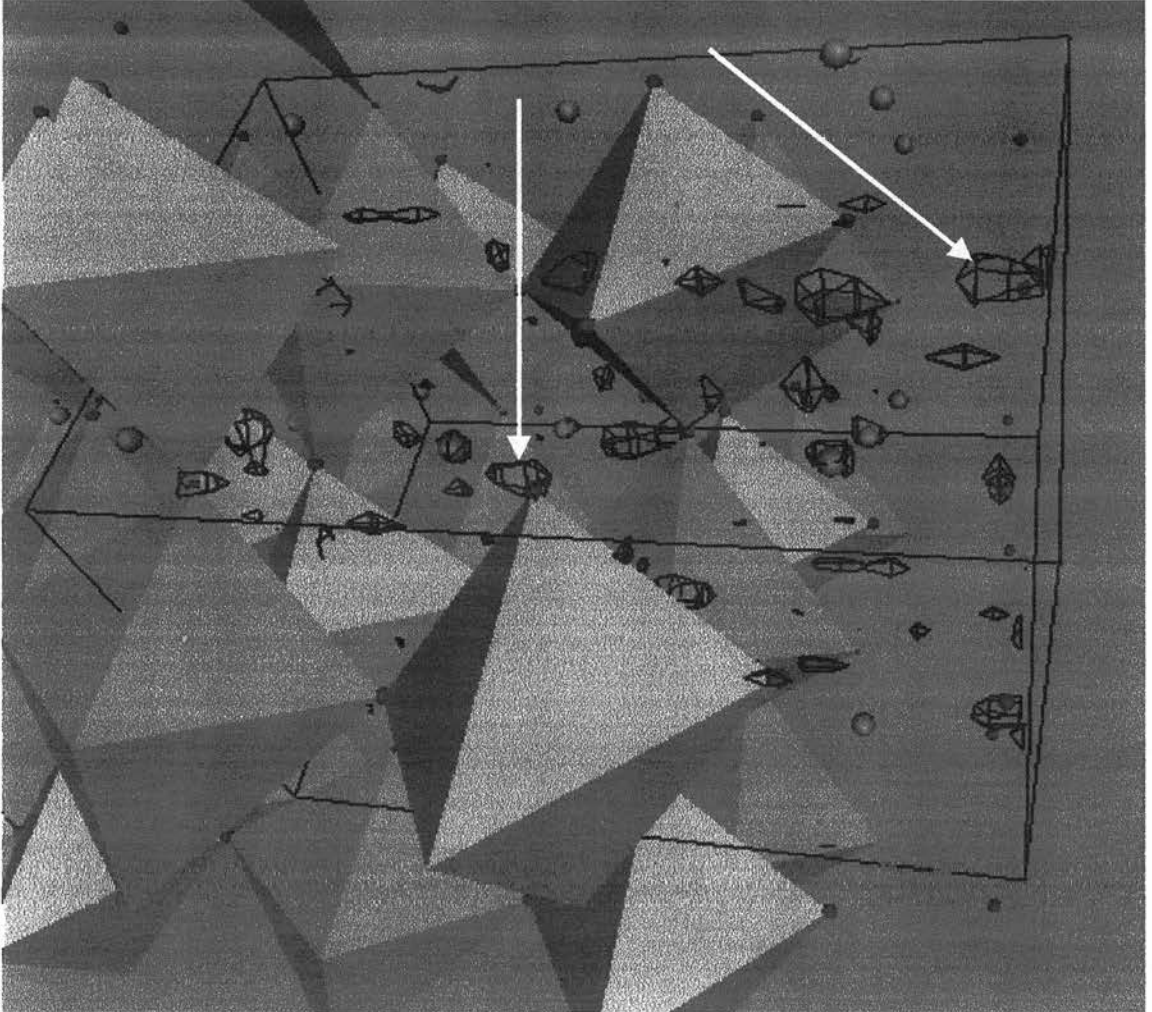


**Figure 5-16: 3D VRML Fourier Difference Map for  $\text{Sr}_3\text{CaZr}_{0.5}\text{Ta}_{1.5}\text{O}_{8.75} + \text{H}_2\text{O}$ . The white arrows point to the missing nuclear density zones where O-H groups are located. The missing hydrogen is inserted into the structural model in GSAS for further refinement.**

5.3.6. Structural data for  $\text{Sr}_3\text{CaZr}_{0.5}\text{Ta}_{1.5}\text{O}_{8.75-y}(\text{OD})_{2y}$  ( $y \approx 0.1375$ )

The structure of deuterated  $\text{Sr}_3\text{CaZr}_{0.5}\text{Ta}_{1.5}\text{O}_{8.75}$  was also investigated, and a Fourier difference map was also generated, however in this case, a small region of “positive density” was missing next to some oxygen positions. This position was ascribed to deuterium, which has formed O-D groups within the structure. Deuterium was inserted at the “missing” positions, and the data was further refined to locate one deuterium position. The data was collected at 200°C on Polaris so that all the incorporated  $\text{D}_2\text{O}$  was still retained. The unit cell was found to be:

$a = 8.22618(32) \text{ \AA}$  ;  $b = 5.8375(4) \text{ \AA}$  ;  $c = 5.82396(33) \text{ \AA}$  ;  $\beta = 90.249(4)^\circ$  ; Cell volume =  $279.665(26) \text{ \AA}^3$ . This volume is 0.65 % larger compared to  $\text{Sr}_3\text{CaZr}_{0.5}\text{Ta}_{1.5}\text{O}_{8.75-y}(\text{OH})_{2y}$  at the same temperature. The space group used was P2/a.  $\chi^2 = 2.4$ ;  $wR_p$  (expected) = 8.071 %;  $R_p$  (calculated) = 7.800 %. Structural parameters are set out below.

Name	x	y	z	UIISO(x100)	Site Sym	SiteOcc.
Sr1	0.250000	0.500000	0.000000	3.15	2(010)	1.0000
Sr2	0.250000	0.000000	0.500000	2.67	2(010)	1.0000
Ca1	0.000000	0.000000	0.000000	2.14	-1	0.3175
Zr1	0.000000	0.000000	0.000000	2.50	-1	0.1659
Ta1	0.000000	0.000000	0.000000	1.52	-1	0.4996
Ca2	0.000000	0.500000	0.500000	1.14	-1	0.3118
Zr2	0.000000	0.500000	0.500000	2.47	-1	0.1666
Ta2	0.000000	0.500000	0.500000	2.50	-1	0.5000
O1	0.250000	0.000000	0.000000	3.05	2(010)	0.5690
O2	0.250000	0.500000	0.500000	3.54	2(010)	0.9204
O3	0.033523	0.341812	0.209570	2.98	1	1.0000
O4	0.541555	0.224082	0.297054	1.97	1	1.0000
D1	0.062869	0.746488	0.757142	2.20	1	0.4683

**Table 5-8: Refined atomic positions for  $\text{Sr}_3\text{CaZr}_{0.5}\text{Ta}_{1.5}\text{O}_{8.75-y}(\text{OD})_{2y}$  at 200°C using P2/a. All site multiplicities are 2 except O3,O4 and D1 which are 4.**

<b>Atom Types</b>	<b>Average Bond Distance (Å)</b>
B1-B2	4.122(8)
B1-B1	4.113(6)
B2-O4	2.027(6)
B2-O3	1.947(7)
B2-O2	2.056(8)
B1-O4	2.194(5)
B1-O3	2.354(5)
B1-O1	2.056(8)
Sr2-B2	3.570(5)
Sr2-B1	3.557(9)
Sr1-Sr1	4.113(5)
Sr2-Sr1	4.122(8)
O4-D1	0.966(1)

**Table 5-9: Average bond lengths from Rietveld refinement for  $\text{Sr}_3\text{CaZr}_{0.5}\text{Ta}_{1.5}\text{O}_{8.75-y}(\text{OD})_{2y}$  ( $y \approx 0.1375$ ) at 200°C. B1 and B2 denote the two  $\text{CaZr}_{0.5}\text{Ta}_{1.5}$  positions.**

5.3.7. Multiple temperature neutron diffraction for  $\text{Sr}_3\text{CaZrTaO}_{8.5-y}(\text{OD})_{2y}$

The parent phase,  $\text{Sr}_3\text{CaZrTaO}_{8.5}$  was also deuterated and investigated by neutron diffraction at various temperatures on the Polaris instrument. The diffraction patterns on Polaris are generally of higher intensity than HRPD, however a higher background and poorer peak resolution is to be expected.

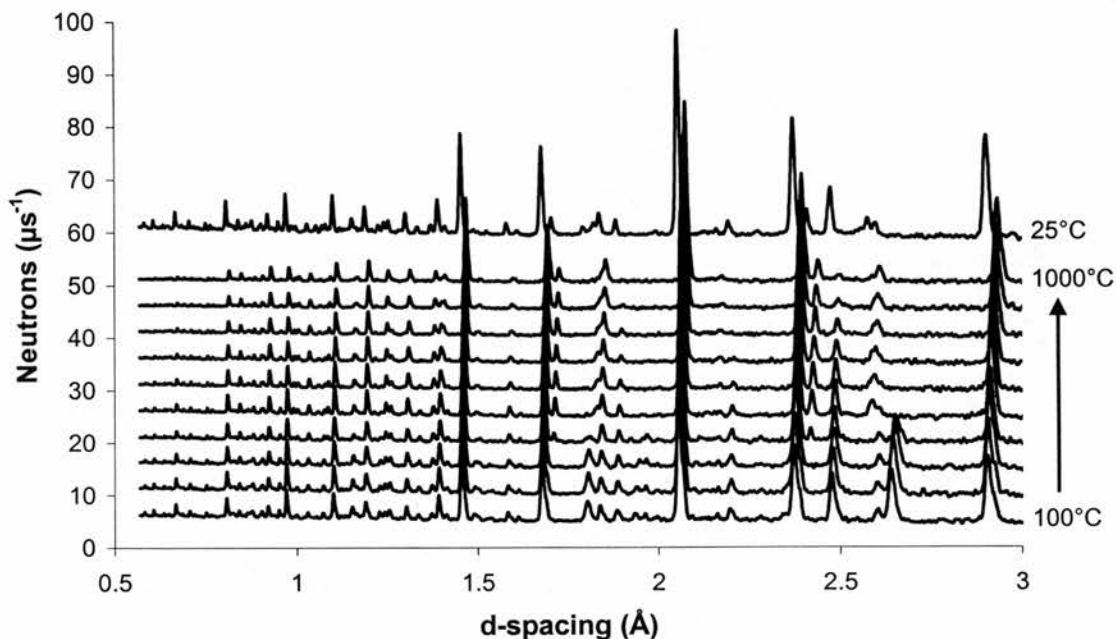


**Figure 5-17: Multiple temperature neutron diffraction patterns for  $\text{Sr}_3\text{CaZrTaO}_{8.5-y}(\text{OD})_{2y}$**

Figure 5-17 above shows that there is also a similar increase in symmetry with temperature for the related phase  $\text{Sr}_3\text{CaZrTaO}_{8.5-y}(\text{OD})_{2y}$ . Again, some peaks persist only up to  $500^\circ\text{C}$ , as some  $\text{D}_2\text{O}$  is still retained in the structure, although some other smaller peaks remain only to finally fade by  $1000^\circ\text{C}$ , as seen for  $\text{Sr}_3\text{CaZr}_{0.5}\text{Ta}_{1.5}\text{O}_{8.75-y}(\text{OD})_{2y}$ . The top scan reveals that a reversion to lower symmetry may be occurring when the sample is cooled back to room temperature, as it appears that some small peaks return.

Close examination also reveals the onset of the *appearance* of some extra peaks beginning in the range of  $400$  to  $600^\circ\text{C}$  along with the *diminishing* of others with at this temperature, implying that the structural changes occurring may be more complicated. A possible explanation may be that as the water is lost in this temperature range, an increase in symmetry with a loss of some peaks is accompanied by the appearance of *ordering* peaks. This composition may be more susceptible to cation ordering at higher

temperatures due to the equal ratio of B-cations. Further work needs to be done to determine the symmetry changes which are associated with each temperature for  $\text{Sr}_3\text{CaZrTaO}_{8.5-y}(\text{OD})_{2y}$ , however from initial investigations, it seems that the space group changes would be similar to those found for  $\text{Sr}_3\text{CaZr}_{0.5}\text{Ta}_{1.5}\text{O}_{8.75-y}(\text{OD})_{2y}$  as discussed previously.

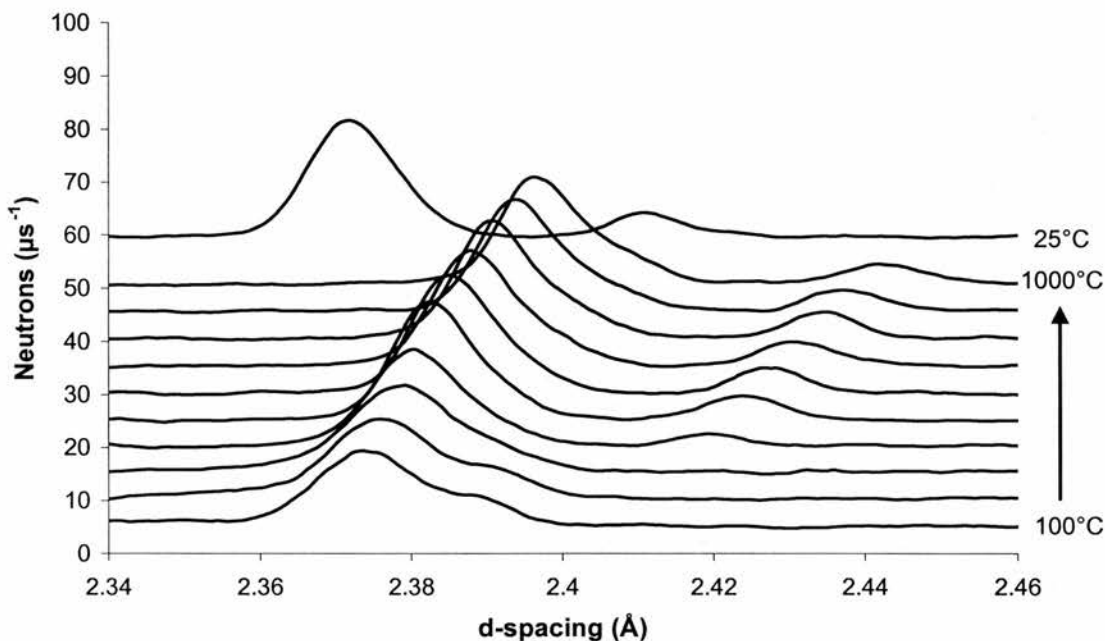


**Figure 5-18: A zoom in on the evolution of the 220,202 doublet evident at 100°C for  $\text{Sr}_3\text{CaZrTaO}_{8.5-y}(\text{OD})_{2y}$ . The pattern of the final cooled sample is shown at the top.**

Figure 5-18 above clearly shows how the 220,202 (equivalent to  $111_p$ ) split peak merges to form a singlet by 500°C. The emergence of an extra peak from 2.42 to 2.44 Å after the onset of  $\text{D}_2\text{O}$  loss (above 400°C) is also evident, implying a more complicated structural change with temperature compared to  $\text{Sr}_3\text{CaZr}_{0.5}\text{Ta}_{1.5}\text{O}_{8.75-y}(\text{OD})_{2y}$ , and is possibly due to the onset of ordering on the B-site sublattice as structural O-D groups are lost, giving rise to a supercell.

### 5.3.8. High Resolution TEM Studies of (vacuum treated) phase, $\text{Sr}_3\text{CaZr}_{0.5}\text{Ta}_{1.5}\text{O}_{8.75}$

To confirm the type of perovskite unit cell variation (doubled, tripled, etc) for the  $\text{Sr}_3\text{CaZr}_{0.5}\text{Ta}_{1.5}\text{O}_{8.75}$  composition, transmission electron microscopy was used to identify the remnant single primitive unit cell ( $a_p$ ) and the doubled cell ( $2a_p$ ). Similar confirmations were obtained for the  $\sqrt{2}a_p$  cell side.

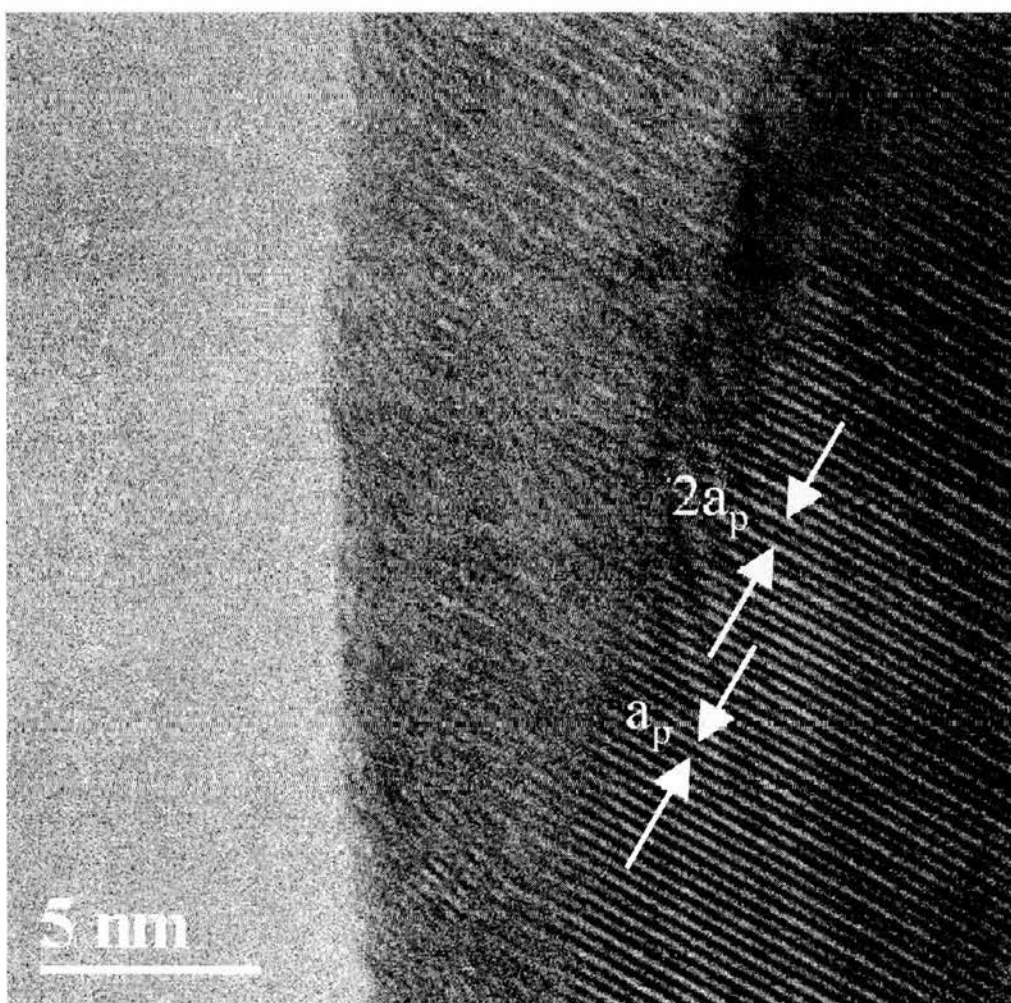


**Figure 5-19: High Resolution TEM image of the edge of a vacuum degassed (1000°C) sample of  $\text{Sr}_3\text{CaZr}_{0.5}\text{Ta}_{1.5}\text{O}_{8.75}$ . The view is perpendicular to the c-axis.**

Figure 5-19 shows the HRTEM image looking perpendicular to the doubled  $a_p$  axis. Bright and less bright alternating fringes can clearly be seen. The distance  $a_p$  of the primitive unit cell (about 4.1 Å) is between bright and less bright fringes, the doubled side ( $2a_p \approx 8.2$  Å) is the distance between the brighter ones. This again, is further evidence for the  $2a_p \times \sqrt{2}a_p \times \sqrt{2}a_p$  tetragonal/monoclinic type unit cell for  $\text{Sr}_3\text{CaZr}_{0.5}\text{Ta}_{1.5}\text{O}_{8.75}$ .

#### 5.4 Summary

New complex triple perovskites of formulae  $\text{Sr}_3\text{CaZr}_{0.5}\text{Ta}_{1.5}\text{O}_{8.75}$  and  $\text{Sr}_3\text{CaZrTaO}_{8.5}$  have been synthesised and their structure examined by multiple temperature Neutron and X-Ray diffraction. Structure refinement from neutron data of a hydrothermally ( $\text{H}_2\text{O}$  or  $\text{D}_2\text{O}$ ) treated sample of  $\text{Sr}_3\text{CaZr}_{0.5}\text{Ta}_{1.5}\text{O}_{8.75}$  reveals a distorted perovskite unit cell with monoclinic distortion, space group  $P1a1$  with  $a = 8.22030(6)$  Å,  $b = 5.80047(9)$  Å,  $c = 5.82668(5)$  Å and  $\beta = 89.973(1)^\circ$ . Difference Fourier maps have been examined and the probable positions of OH (or OD) groups on the  $\text{BO}_{6-x}$  sub-lattice ascertained. Even though there are 2 B-site positions available, it appears that (at least at room temperature), a random distribution of Ca, Zr and Ta centred octahedra may be prevail throughout the structure.

The novel distorted perovskite phases,  $\text{Sr}_3\text{CaZr}_{0.5}\text{Ta}_{1.5}\text{O}_{8.75}$  and  $\text{Sr}_3\text{CaZrTaO}_{8.5}$  along with the literature-established phase  $\text{Sr}_3\text{Ca}_{1.18}\text{Nb}_{1.82}\text{O}_{8.73}$  (Chapter Three) have all been shown to exhibit significant distortions from cubic/tetragonal symmetry when hydrated/deuterated at elevated temperatures and/or pressures. A distortion towards monoclinic symmetry at lower temperatures cannot be ignored, as the influence of O-H

group incorporation into the  $O^{2-}$  vacancies (of the dry state), is required by necessity for proton conduction to occur at intermediate temperatures (350-500°C). There is also some evidence that cation ordering may accompany water loss for the parent phase  $Sr_3CaZrTaO_{8.5}$ . The aim here is to highlight the fact that these symmetry changes have generally been overlooked in the related literature on these types of complex perovskite proton conductors, an important issue when these materials are heated to the operating temperature of an electrochemical device such as a fuel cell.

## 5.5 References

- [1] F. A. Kröger, H.J. Vink, "Relations between the concentrations of imperfections in crystalline solids", in *Solid State Physics*, vol. 3, F. Seitz and D. Turnbull (eds.), Academic Press Inc, New York (1956)
- [2] N.Peng. J.T.S. Irvine, A.G. Fitzgerald, *J. Mater. Chem.*, 1998, **8** (4), 1033-1038
- [3] A. LeBail, in *Microstructure Analysis by Diffraction*, edited by H. Bunge, J. Fiala and R. L. Snyder, IUCr/Oxford University Press (1988)
- [4] <http://www.ncnr.nist.gov/resources/n-lengths/>
- [5] K.S. Knight, *Solid State Ionics*, **127** (2000) 43-48
- [6] A.R West, in "Solid State Chemistry", John Wiley and Sons (1992) p.711
- [7] <http://www.ccp14.ac.uk/solution/gsas/vrmlviewing/index.html>

Chapter Six

Electrical Characterisation of  $\text{Sr}_3\text{CaZr}_{0.5}\text{Ta}_{1.5}\text{O}_{8.75}$  and  
 $\text{Sr}_3\text{CaZrTaO}_{8.5}$

“I think it's tragic that scientific advances have caused many people to imagine that they know it all, and that God is irrelevant or nonexistent. The fact is that everything we learn reveals more things that we do not understand.”

---*Donald E. Knuth*  
(on Proverbs 3:16)

## 6 Electrical Characterisation of $\text{Sr}_3\text{CaZr}_{0.5}\text{Ta}_{1.5}\text{O}_{8.75}$ and $\text{Sr}_3\text{CaZrTaO}_{8.5}$

### 6.1 2-Terminal (A.C. Impedance) Conductivity Studies

#### 6.1.1 Introduction

Certain doped perovskite oxides of the formula  $\text{AB}_{1-x}\text{X}_x\text{O}_{3-\delta}$ , have been shown to exhibit high protonic conduction in wet hydrogen atmospheres [1], and a wide range of possible applications such as sensors, fuel-cells and hydrogen pumps, has led to vigorous research in this area since the early eighties. Important early examples are doped  $\text{BaCeO}_3$  and  $\text{SrCeO}_3$ . The introduction of trivalent ions ( $\text{Gd}^{3+}$ ) to the B-site of the stoichiometric compound  $\text{BaCeO}_3$  creates vacant oxygen sites, or, when in oxidising atmospheres, creates electronic holes [2].

Subsequent exposure of these materials to humid atmospheres is presumed to lead to the incorporation of protons by the filling of some oxygen-ion vacancies and in Kröger-Vink notation [3], this can be denoted by:



$$K_3 = [\text{OH}^{\bullet}_{\text{o}}]^2 / ([\text{V}''_{\text{o}}]p\text{H}_2\text{O}) \quad \text{Equation 6-2}$$

These materials do have some limitations, including poor stability in certain atmospheres (with disintegration under  $\text{CO}_2/\text{H}_2\text{O}$ ), some electronic conductivity, and a tendency for oxide ion conductivity at high temperatures. Doped  $\text{BaZrO}_3$  is more stable under  $\text{CO}_2$  but exhibits lower protonic conductivity [7].

For the application of proton conducting solid oxides as electrolytes for the next generation of SOFCs, it is a requirement that the total conductivity of the material be as high as possible, while the resistance of the grain boundary component is kept at a minimum [4]. A.c. Impedance Spectroscopy is a useful tool in separating these bulk and grain boundary contributions to the overall conductivity of an electroceramic material [5].

### 6.1.2 Equivalent circuit fitting

Equivalent circuit fitting can aid in simulating (modelling) the resistive, capacitive, inductive and possible constant phase element components associated with the a.c. impedance response of an ionic conductor. Due to the depression of the arcs (circle centre is below the x-axis), the use of pure capacitors is not sufficient to model the response, so a more sophisticated model with frequency dependent elements such as a constant phase element (described in Chapter Two) is used.

It is clear from all ac impedance measurements performed that the bulk arc (first response) is only evident at relatively low temperatures ( $< 200^{\circ}\text{C}$ ), and can therefore only be clearly extracted from the overall resistance contributions at these temperatures. The equivalent circuit fitting results correspond very well with the capacitance and resistance values obtained by fitting semicircles to the different arcs.

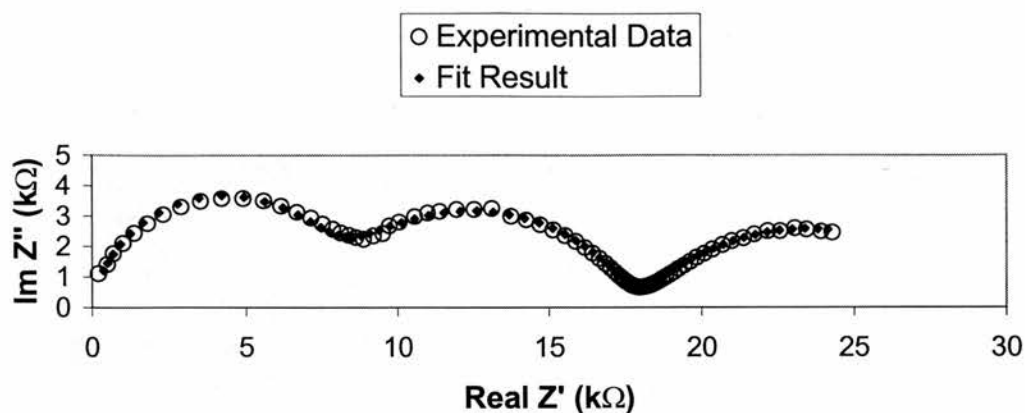


**Figure 6-1: Experimental data and equivalent circuit fit for  $\text{Sr}_3\text{CaZrTaO}_{8.5}$  in  $\text{H}_2\text{O}$  saturated 5%  $\text{H}_2/\text{Ar}$  flow at  $238^\circ\text{C}$ .**

The level of depression of each semicircle is represented as a  $\tan$  of the angle  $\chi$  (or  $\alpha$ ) as outlined in Chapter Two. Each CPE also has its own associated capacitance values. The low value for  $\tan \chi$  of  $< 1$  (the depression angle relationships are described in Chapter Two) for the CPE used to fit the double layer response suggests that it can be considered a diffusion element associated with the diffusion of protons at the electrode surface. The Warburg diffusion element has a  $\tan \chi$  value of 1 ( $45^\circ$  slope) and is independent of frequency.

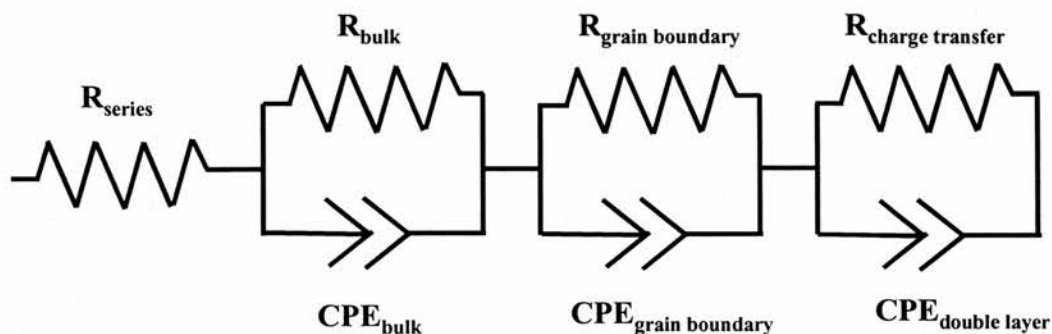


**Figure 6-2: Equivalent circuit used for the fit to the experimental data as shown in Figure 6-1**

These values are in good accord with the generally associated values for the bulk, grain boundary, and electrode responses for a solid electrolyte outlined in Table 2-1. Even though the visual fit is very good in Figure 6-1, the errors in the calculated capacitance values (Table 6-1) are attributed to the fact that there is some significant overlap of each response. This could be due to the fact that there may be an uneven distribution of particle sizes. Careful sieving of the powders before pellet compaction and sintering may help overcome this problem.

A good fit is obtained for the data at 238°C for  $\text{Sr}_3\text{CaZr}_{0.5}\text{Ta}_{1.5}\text{O}_{8.75}$  in wet 5%  $\text{H}_2/\text{Ar}$  using the circuit described above. A series resistance is used to account for the internal resistance of any connecting wires, and this is fixed at 1  $\Omega$  for the purposes of the least squares fitting routine (EquivCrt in ZView, Scribner and Associates). The individual circuit element values are shown in Table 6-1 below:

Element	Value ( $\Omega$ , F)	Error ( $\Omega$ , F)	Error (%)
$R_{\text{series}}$	1 $\Omega$	n/a	n/a
$R_{\text{bulk}}$	7505 $\Omega$	145.07 $\Omega$	1.93
$CPE_{\text{bulk}}$ (C)	$9.11 \times 10^{-11}$ F	$8.53 \times 10^{-12}$ F	9.36
$CPE_{\text{bulk}}$ ( $\tan \chi$ )	0.919	0.0061	0.66
$R_{\text{grain boundary}}$	10296 $\Omega$	253.23 $\Omega$	2.46
$CPE_{\text{grain boundary}}$ (C)	$6.62 \times 10^{-8}$ F	$1.11 \times 10^{-8}$ F	16.74
$CPE_{\text{grain boundary}}$ ( $\tan \chi$ )	0.678	0.018	2.61
$R_{\text{charge transfer}}$	11356 $\Omega$	1495.3 $\Omega$	13.17
$CPE_{\text{double layer}}$ (C)	$9.30 \times 10^{-5}$ F	$7.28 \times 10^{-6}$ F	7.83
$CPE_{\text{double layer}}$ ( $\tan \chi$ )	0.540	0.043	8.05

**Table 6-1: Equivalent circuit element values for the fitting results as per Figure 6-1 and Figure 6-2**

Although the equivalent circuit model gives a very good fit to the observed data, the important resistance values obtained by a more simple analysis of the Nyquist plots assuming Debye-type behaviour did not differ significantly from those obtained by equivalent circuit analysis. As the major sources of error relate to instrumental factors such as frequency limitations and voltage range steps, the simpler analysis was more generally used.

### 6.1.3 Nyquist ( $Z''$ versus $Z'$ ) plots for $\text{Sr}_3\text{CaZr}_{0.5}\text{Ta}_{1.5}\text{O}_{8.75}$

To illustrate the typical form of the response (plotted on the real-complex impedance plane), Figures 6-3 and 6-4 below show the results for  $\text{Sr}_3\text{CaZr}_{0.5}\text{Ta}_{1.5}\text{O}_{8.75}$  in a wet 5% at low temperatures (149-258°C). Over this temperature range the bulk (Figure 6-3), grain boundary (Figure 6-4), and electrochemical (Figure 6-4) responses can clearly be distinguished. The initial points of the bulk arcs all coincide at one point. This small resistance value corresponds to the ohmic resistance of the connecting wires from the Frequency Response Analyser. The beginning of the grain boundary arcs of course do not coincide because the bulk arcs (x-axis intercept) decrease with increasing temperature (i.e the conductivity increases). The high frequency intersection points of these arcs with the  $Z'$  axis were used as resistance values to create an Arrhenius plot similar to that in Figure 6-6. In general for these phases, above 220°C, the bulk arc is difficult to discern, and by 260°C, it has moved to frequency ranges above 6 MHz, which are beyond the capabilities of the Solartron 1260 Analyser. Figure 6-4 presents impedance data where only the grain boundary and electrochemical responses can be clearly seen.

The individual impedance responses at 284°C and 184°C in wet hydrogen are shown in Figure 6-5, showing three distinct elements: bulk, grain boundary, and electrode responses. Table 6-2 shows values for the capacitances of the three responses evident in the Nyquist plot at 184°C. The frequency of the applied signal is shown for some points. The sample resistance is considerably higher at the lower temperature (184°C), being over six times larger than that at 284°C.

At these temperatures, the oxygen ion vacancies which would exist in the dry state are filled by O-H groups due to water incorporation from the wet gas atmosphere. It is likely that the conductivity at these temperatures is almost entirely due to proton hopping between oxygen ions. The phase is stable in this reducing atmosphere and is most susceptible to water uptake in the temperature range 25°C to 500°C, although an enhancement in the conductivity at temperatures over 600°C has been verified, on increasing the  $p_{\text{H}_2\text{O}}$  of the gas stream. This will be discussed later, when the influence of a drying or hydrating atmosphere with time is investigated.

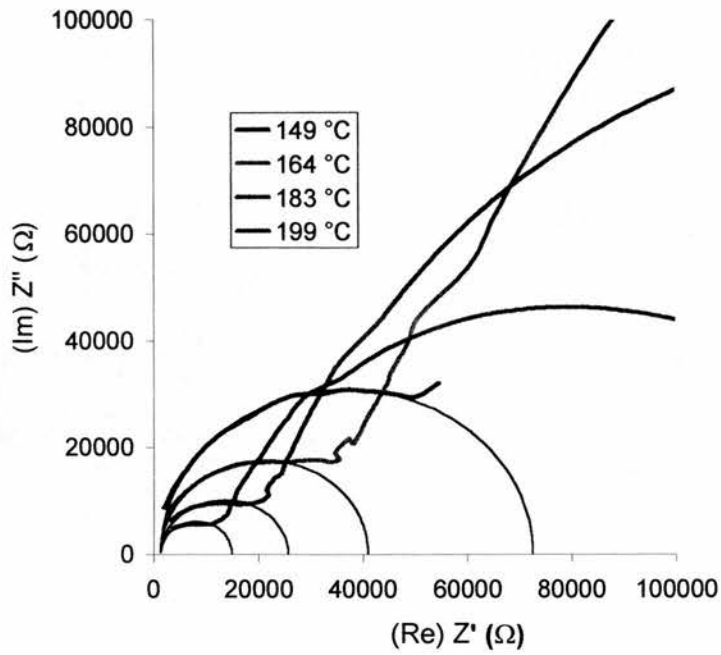


**Figure 6-3: Complex plane (Nyquist) plots for  $\text{Sr}_3\text{CaZr}_{0.5}\text{Ta}_{1.5}\text{O}_{8.75}$  in wet 5%  $\text{H}_2/\text{Ar}$ . The bulk arcs are outlined.**

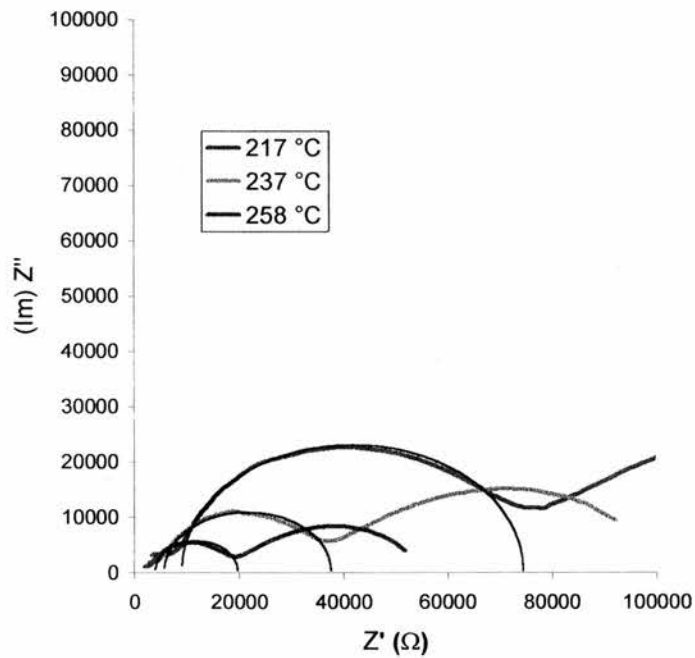


**Figure 6-4: Complex plane (Nyquist) plots for  $\text{Sr}_3\text{CaZr}_{0.5}\text{Ta}_{1.5}\text{O}_{8.75}$  in wet 5%  $\text{H}_2/\text{Ar}$ . The grain boundary arcs are outlined.**

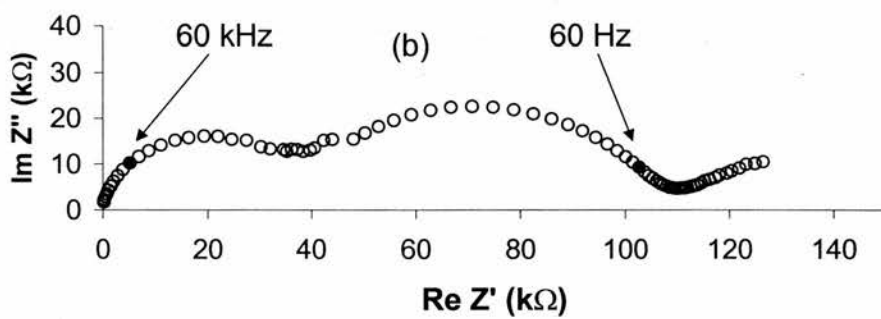
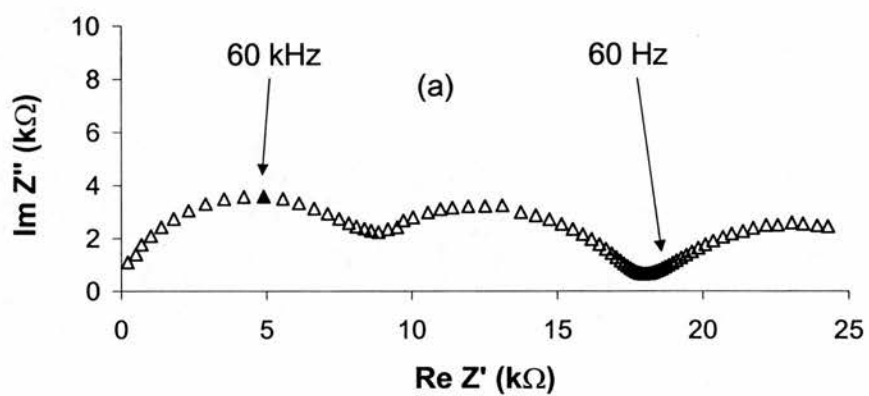


Figure 6-5: Complex versus real impedance plane plot for  $\text{Sr}_3\text{CaZr}_{0.5}\text{Ta}_{1.5}\text{O}_{8.75}$  in wet 5%  $\text{H}_2/\text{Ar}$  flow at (a) 284°C and (b) 184°C

<b>Impedance Response</b>	<b>Capacitance at 184°C</b>	<b>Frequency Range (Hz)</b>
Bulk	$2.3359(7) \times 10^{-12} \text{ F cm}^{-1}$	$1 \times 10^6$ to $6.3 \times 10^4$
Grain Boundary	$1.2138(3) \times 10^{-9} \text{ F cm}^{-1}$	$6.3 \times 10^4$ to 50
Electrode	$2.0233(7) \times 10^{-7} \text{ F cm}^{-1}$	50 to 0.1

**Table 6-2: Capacitance values for the 3 Impedance Responses evident in Figure 6-5(b)**

#### 6.1.4 The total conductivity of $\text{Sr}_3\text{CaZr}_{0.5}\text{Ta}_{1.5}\text{O}_{8.75}$

The conductivity of  $\text{Sr}_3\text{CaZr}_{0.5}\text{Ta}_{1.5}\text{O}_{8.75}$  was examined in the temperature range 100°C to 900°C in two atmospheres with differing levels of hydration. The incoming 5%  $\text{H}_2/\text{Ar}$  was either pre-bubbled through distilled water to moisten the gas stream ( $\approx 3 \text{ kPa}$  vapour pressure) or through concentrated  $\text{H}_2\text{SO}_4$  to remove as much water as possible, giving  $< 10 \text{ Pa}$   $\text{H}_2\text{O}$  vapour. A comparison of the overall ceramic conductivity, i.e. the grain + grain boundary contributions, of  $\text{Sr}_3\text{CaZr}_{0.5}\text{Ta}_{1.5}\text{O}_{8.75}$  in dry and wet atmospheres is presented in Figure 6-6, showing that the presence of water vapour increases the conductivity, and therefore indicates the presence of protonic conduction.

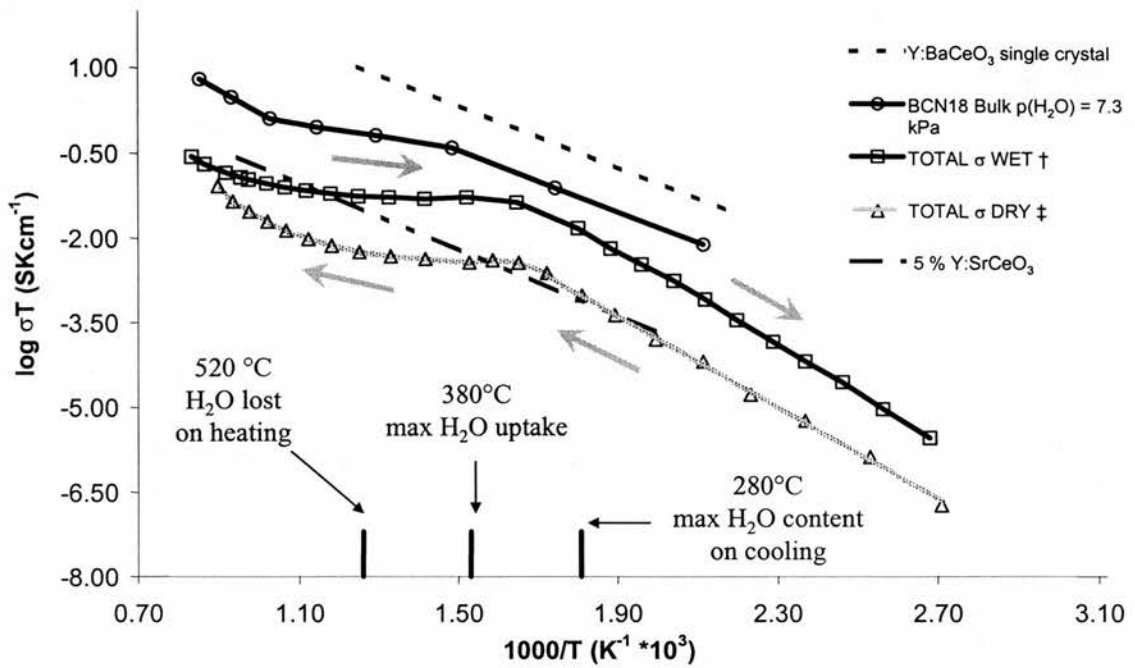


**Figure 6-6: Total conductivity for pre-dried  $\text{Sr}_3\text{CaZr}_{0.5}\text{Ta}_{1.5}\text{O}_{8.75}$  heated in dry atmosphere [ $\ddagger$  ( $5\% \text{H}_2/\text{Ar}$ ,  $< 0.01\% \text{H}_2\text{O}$ )], and then cooled in wet atmosphere [ $\dagger$  ( $4\% \text{H}_2\text{O}$ ,  $4\% \text{H}_2$ ,  $92\% \text{Ar}$ )]**

Figure 6-6 shows the total conductivity (bulk + grain boundary) dependence for a vacuum treated sample as the temperature was raised from room temperature in a dried  $5\% \text{H}_2/\text{Ar}$  stream to  $840^\circ\text{C}$ , and then cooled from  $840^\circ\text{C}$  to room temperature in a wet  $5\% \text{H}_2/\text{Ar}$  stream. Since relatively little water vapour was present in the dry gas flow during the initial heating to  $840^\circ\text{C}$ , the result is substantially lower conductivity and an apparent activation energy (for the total conductivity) approaching  $1 \text{ eV}$  from  $700$  to  $900^\circ\text{C}$  in the dry atmosphere.

There is a difference, between the wet and the dry situations, of more than one order of magnitude in the conductivity of the sample for temperatures below  $500^\circ\text{C}$ . Water from the moist gas can enter the structure, by filling oxide ion vacancies with O-H groups, engendering protonic conduction. The relatively constant value of the conductivity (from  $380^\circ\text{C}$  to  $520^\circ\text{C}$  in Figure 6-6) can be ascribed to a combination of the increase in

thermal activation and mobility of the protonic charge carriers, as well as the decrease in their concentration due to water loss [6]. This would result in a decrease in the value of  $K_3$  (Equation 6-2). When the sample is cooled from 840°C to room temperature in a wet atmosphere, at 300°C and below, the sample is fully hydrated, and proton conduction dominates over n-type or oxygen ion conduction. The presence of structural O-H groups enables a dominating protonic conduction in the bulk at lower temperatures, but the conductivity reaches a plateau when the water is lost from the structure on heating (greater than 500°C).

Also in Figure 6-6, the total (bulk plus grain boundary) conductivities of  $\text{Sr}_3\text{CaZr}_{0.5}\text{Ta}_{1.5}\text{O}_{8.75}$  (in wet and dry atmospheres) are compared to Y-doped  $\text{BaCeO}_3$  single crystal [7], 5% Y: $\text{SrCeO}_3$  [8] and  $\text{Ba}_3\text{Ca}_{1.18}\text{Nb}_{1.82}\text{O}_{8.73}$  (BCN18) [9].

#### 6.1.5 The bulk and grain boundary conductivities of $\text{Sr}_3\text{CaZr}_{0.5}\text{Ta}_{1.5}\text{O}_{8.75}$

Figure 6-7 shows the Arrhenius behaviours of the bulk and grain boundary components at lower temperatures. At higher temperatures the bulk response moves to higher frequencies and is thus not discernible. The hydrating atmosphere enhances the conductivity in both the grain interior and the grain boundaries. The highest conductivity is evident in the bulk of the grains, when the sample is exposed to a wet gas atmosphere.

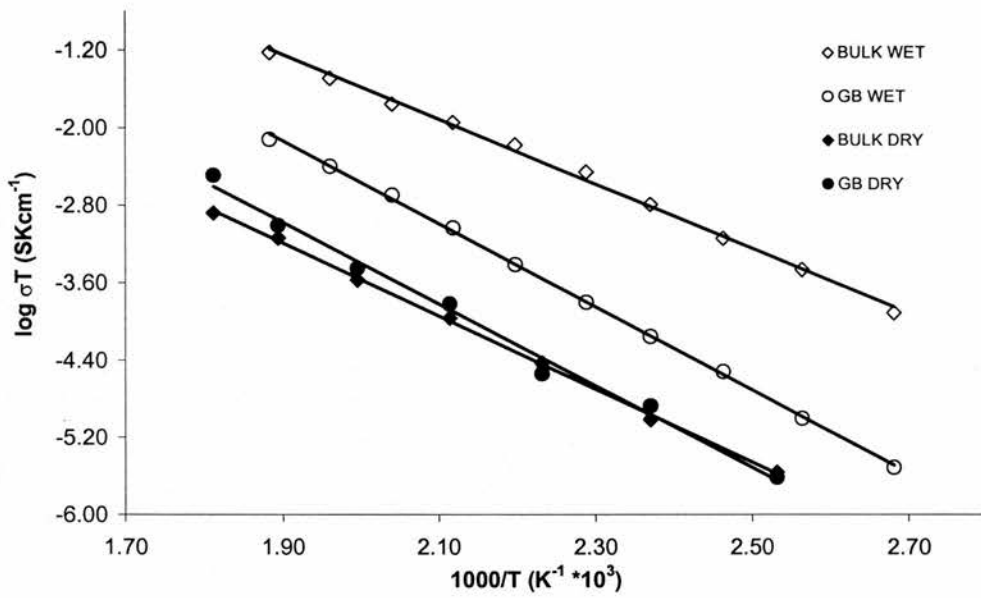


**Figure 6-7: Bulk and Grain Boundary (GB) Arrhenius Plots for  $\text{Sr}_3\text{CaZr}_{0.5}\text{Ta}_{1.5}\text{O}_{8.75}$  in wet and dry atmospheres**

The bulk (grain interior) and grain boundary conductivities of  $\text{Sr}_3\text{CaZr}_{0.5}\text{Ta}_{1.5}\text{O}_{8.75}$  were found to be  $4.64 \times 10^{-4} \text{ S cm}^{-1}$  and  $7.04 \times 10^{-5} \text{ S cm}^{-1}$  respectively at  $300^\circ\text{C}$  (in wet 5%  $\text{H}_2/\text{Ar}$ ) with activation energies of  $E_a(\text{bulk}) = 0.66 \text{ eV}$  and  $E_a(\text{gb}) = 0.85 \text{ eV}$ . This is an improvement over  $\text{BaCe}_{0.7}\text{Zr}_{0.2}\text{Gd}_{0.1}\text{O}_{2.95}$  (bulk  $\sigma = 6.95 \times 10^{-5} \text{ S cm}^{-1}$  at  $300^\circ\text{C}$ ), recently proposed as a suitable candidate (sufficiently high chemical stability and proton conductivity) for fuel cell electrolyte applications in SOFCs [10]. 5% Nd-doped  $\text{BaCeO}_3$  has a total proton conductivity of  $2.64 \times 10^{-4} \text{ S cm}^{-1}$  at  $300^\circ\text{C}$  [11], while  $\text{Sr}_3\text{Ca}_{1.18}\text{Nb}_{1.82}\text{O}_{8.73}$  has a reported total of  $1.5 \times 10^{-4} \text{ S cm}^{-1}$  at the same temperature [12]. The bulk and grain boundary conductivities of a sample pre-treated in vacuum at  $1000^\circ\text{C}$  for 6 hours and measured in-situ in a dried 5%  $\text{H}_2/\text{Ar}$  gas flow were found to be  $\sigma_{\text{bulk}} = 4.75 \times 10^{-6} \text{ S cm}^{-1}$  ( $E_a = 0.75 \text{ eV}$ ) and  $\sigma_{\text{gb}} = 7.01 \times 10^{-6} \text{ S cm}^{-1}$  ( $E_a = 0.84 \text{ eV}$ ) at  $300^\circ\text{C}$

Figure 6-8 shows that the resistance of the sample is quite high, and hence the conductivity much lower ( $\approx 10^{-8} \text{ S cm}^{-1}$ ) when the sample is pre-dried (vacuum treated at  $1000^\circ\text{C}$ ) and also when the gas flow over the sample is kept dry (pre-bubbled through  $\text{H}_2\text{SO}_4$ ). Data at lower frequencies was unclear, as the resistance approached too high a value for the impedance analyser to measure accurately. This resulted in data scatter from 300 Hz to 0.1 Hz at this temperature ( $181^\circ\text{C}$ ), and this data was cut from the plot. Also, only the bulk arc is evident due to this low-frequency scatter, even though one expects the bulk, grain boundary and electrochemical responses to be evident at these lower temperatures. They are of course evident when the sample is exposed to a hydrating 5%  $\text{H}_2/\text{Ar}$  atmosphere, as seen previously in Figure 6-5.

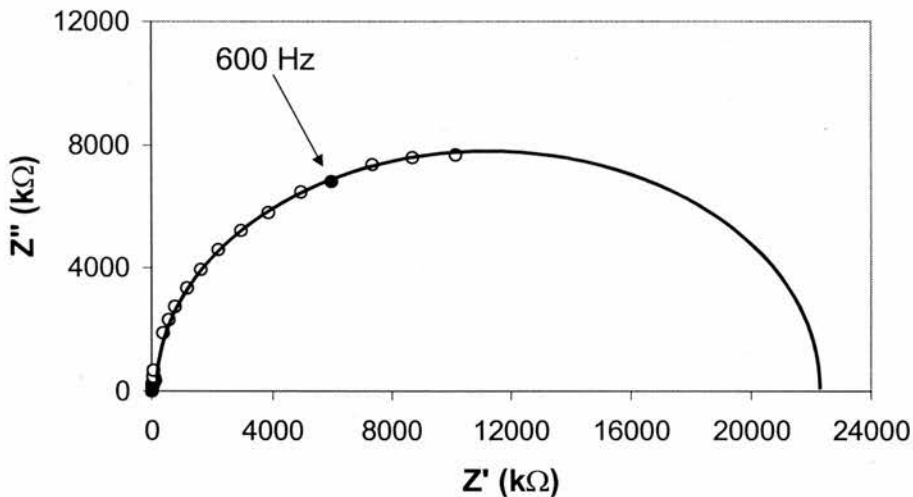


**Figure 6-8: Complex impedance plane plot for vacuum treated  $\text{Sr}_3\text{CaZr}_{0.5}\text{Ta}_{1.5}\text{O}_{8.75}$  in a dry 5%  $\text{H}_2/\text{Ar}$  atmosphere at  $181^\circ\text{C}$**

It is clear, however, from all a.c. impedance measurements performed that at temperatures greater than  $500^\circ\text{C}$ , only the highest intercept of the total (bulk + grain

boundary) response is discernible. The grain boundary arc (second response) is only evident at relatively low temperatures ( $< 300^{\circ}\text{C}$ ), and can therefore only be clearly extracted from the sum of the resistance contributions at these temperatures, as the end of the bulk arc is needed to extract the grain boundary resistance. At higher temperatures, the bulk response dominates the total resistance while the grain boundary arc diminishes, lying hidden beneath the bulk response.

#### 6.1.6 The influence of wet and dry atmospheres over time

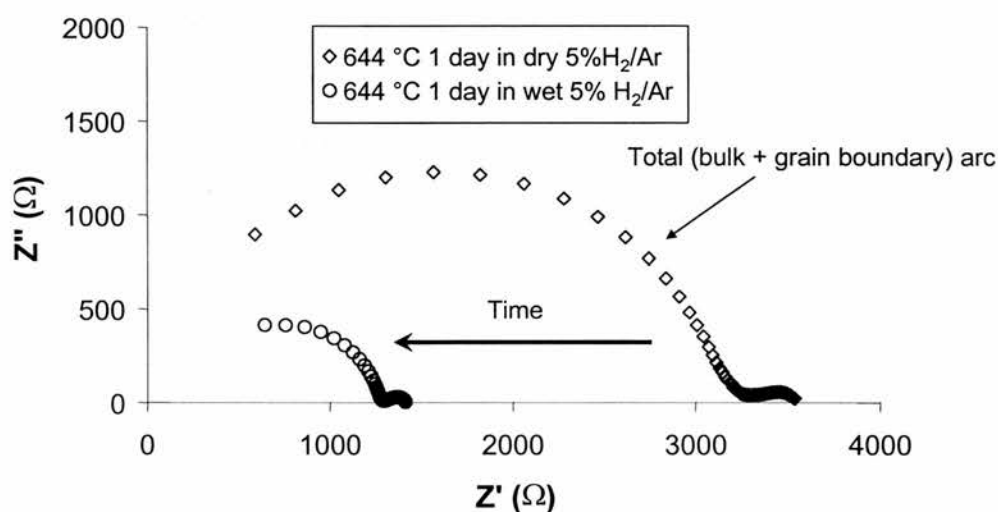


**Figure 6-9: Influence of a hydrating atmosphere (5%  $\text{H}_2/\text{Ar}$  bubbled through distilled  $\text{H}_2\text{O}$ ) on the resistance of a  $\text{Sr}_3\text{CaZr}_{0.5}\text{Ta}_{1.5}\text{O}_{8.75}$  sample at  $644^{\circ}\text{C}$**

Figure 6-9 above shows that the total resistance of the sample is reduced from about  $3250 \Omega$  to about  $1250 \Omega$  when a wet 5%  $\text{H}_2/\text{Ar}$  atmosphere is provided (flowing over the sample) after a drying stage in-situ for 1 day at  $644^{\circ}\text{C}$ . However, since the conductivity of the sample is improved upon exposure to wet hydrogen even above

650°C, some structural water (as O-H groups) must still be present.

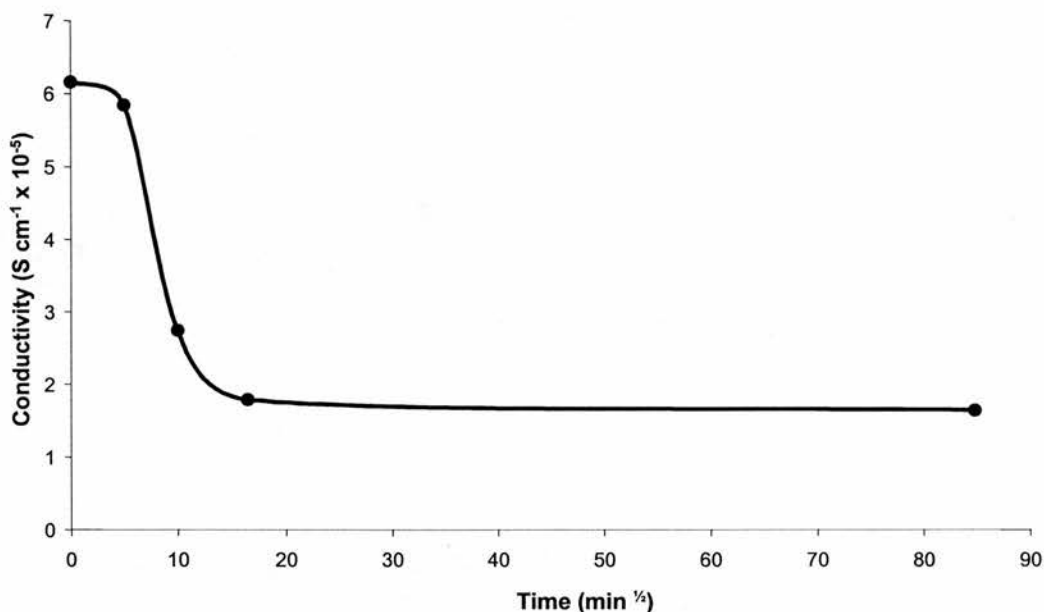


**Figure 6-10: Conductivity of hydrated  $\text{Sr}_3\text{CaZr}_{0.5}\text{Ta}_{1.5}\text{O}_{8.75}$  at 440°C as a function of time in dry atmosphere (5%  $\text{H}_2/\text{Ar}$ , < 0.01 %  $\text{H}_2\text{O}$ )**

Figure 6-10 shows how the conductivity of hydrated  $\text{Sr}_3\text{CaZr}_{0.5}\text{Ta}_{1.5}\text{O}_{8.75}$  at 440°C changes over time when the gas flow is changed from wet to dry at time  $\approx 0$ . Since the drop in conductivity is quite sharp when the water vapour supply is cut-off, and observations are made over almost 5 days, a square-root time axis was used to help illustrate the time dependence. The estimated half life of the drying process (water/proton loss) is 72 minutes, the time taken for the conductivity to decrease to half its value when the gas stream is dried (bubbled through conc.  $\text{H}_2\text{SO}_4$ , giving < 0.01%  $\text{H}_2\text{O}$  in the flow).

### 6.1.7 Discussion

$\text{Sr}_3\text{CaZr}_{0.5}\text{Ta}_{1.5}\text{O}_{8.75}$ , is a member of a new series of ordered perovskites and shows promise as a proton conducting solid oxide for electrochemical device applications. Opportunities exist to optimise the conductivity by varying the amount of 4+ cation or incorporating a shift in stoichiometry on the B-site sublattice. Wet hydrogen/argon atmospheres enhance the conductivity of this material, indicating the presence of protonic conduction. There may be more than one exclusive mechanism of protonic conduction present over the temperature range 100 to 1000°C, as crystallographically incorporated water begins to leave the structure above 400°C, and is totally lost at 600°C, even though protonic conduction still seems to exist above 600°C.

The differences between the conductivities in wet and dry atmospheres confirm significant protonic conductivity in the sample when exposed to a water-saturated gas stream. If the conductivity present was n-type, the expectation would be an increased conductivity in dry, more reducing atmospheres, but this is not the case. Referring to Figure 6-6, at low temperatures (less than 380°C), there is protonic conductivity in both wet and dry atmospheres, which is seen to increase with temperature, and is significantly greater when the sample is hydrated. At mid-range temperatures (380-600°C), the conductivity remains constant due to the loss of structural protons (in both “dry” and wet gas streams). At high temperatures (greater than 600°C), both dry and wet Arrhenius-type behaviours begin to coincide. In the dry atmosphere, oxygen-ion conduction may dominate at higher temperatures, and in the wet atmosphere, the pronounced curvature in the Arrhenius-type behaviour indicates a gradual change from mixed (oxygen-ion and protonic) conduction to that of dominating oxygen-ion

conduction as temperature increases. It seems that an identical linear Arrhenius behaviour may become evident for both wet and dry atmospheres at temperatures in excess of 1000°C). Further work is ongoing in order to confirm the nature of the mobile species; these include permeation and concentration cell measurements.

## **6.2 D.c. 4-terminal conductivity versus $pO_2$ for $Sr_3CaZrTaO_{8.5}$**

### 6.2.1 Results and discussion

The conductivity of an as-prepared porous (70 % dense) pellet (13mm diameter, 2.2 mm thick) was measured as a function of the partial pressure of oxygen ( $pO_2$ ) in a wet atmosphere. Two temperatures were chosen, 515°C (close to the highest temperature that  $H_2O$  remains incorporated within the lattice) and 887°C (all  $H_2O$  is lost from the structure), according to water loss investigations for this sample, and samples of similar composition using the TGA technique as described in Chapter Four.

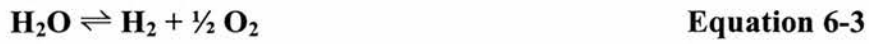
The sample was first equilibrated in wet 5%  $H_2/Ar$  ( $\approx 3$  kPa  $H_2O$ ) at 515°C and the conductivity reached a stable value of  $4.46 \times 10^{-4}$  S  $cm^{-1}$ . The atmosphere was then changed to dry air and the conductivity slowly decreased to  $7.08 \times 10^{-6}$  S  $cm^{-1}$ . A similar experiment was performed at 887°C, but there was very little difference between conductivity values in wet  $H_2$  and dry air at this temperature. The conductivity in fact increased slightly from  $6.31 \times 10^{-5}$  S  $cm^{-1}$  to  $1 \times 10^{-4}$  S  $cm^{-1}$  on going from wet hydrogen to dry air at 887°C.

Temperature (°C)	Conductivity (S cm <sup>-1</sup> )	pO <sub>2</sub> (atm)	Atmosphere
515	4.46 x 10 <sup>-4</sup>	3.16 x 10 <sup>-28</sup>	wet 5% H <sub>2</sub> /Ar
<i>*515</i>	<i>*1.27 x 10<sup>-4</sup></i>	<i>*≈ 10<sup>-28</sup></i>	<i>*wet 5% H<sub>2</sub>/Ar</i>
515	7.08 x 10 <sup>-6</sup>	0.21	dry air
<i>*515</i>	<i>*2.26 x 10<sup>-6</sup></i>	<i>*≈ 10<sup>-30</sup></i>	<i>*dry 5% H<sub>2</sub>/Ar</i>
887	3.31 x 10 <sup>-5</sup>	1 x 10 <sup>-18</sup>	wet 5% H <sub>2</sub> /Ar
<i>*887</i>	<i>*2.73 x 10<sup>-5</sup></i>	<i>*≈ 10<sup>-18</sup></i>	<i>*wet 5% H<sub>2</sub>/Ar</i>
887	1 x 10 <sup>-4</sup>	0.21	dry air
<i>*887</i>	<i>*5.44 x 10<sup>-5</sup></i>	<i>*≈ 10<sup>-20</sup></i>	<i>*dry 5% H<sub>2</sub>/Ar</i>

**Table 6-3: Conductivity as a function of pO<sub>2</sub>, temperature, and supplied atmosphere. \*2-terminal a.c. results for Sr<sub>3</sub>CaZr<sub>0.5</sub>Ta<sub>1.5</sub>O<sub>8.75</sub> from Figure 6-6. Estimated values for pO<sub>2</sub> are given.**

These results indicate that at 515°C, the conductivity is dominated by the water content of the atmosphere and hence is assumed to be largely protonic. At 887°C however, there seems to be little evidence of a protonic contribution to the conductivity, and rather seems to be largely oxide ionic with perhaps a small p-type contribution in air. The a.c. conductivity results at 887°C and 515°C for Sr<sub>3</sub>CaZr<sub>0.5</sub>Ta<sub>1.5</sub>O<sub>8.75</sub> in wet and dry 5% H<sub>2</sub>/Ar are also given in Table 6-3 in italics. They are in good agreement with the d.c. results for Sr<sub>3</sub>CaZrTaO<sub>8.5</sub>, and slightly higher values for this composition are to be expected with a higher number of oxide ion vacancies available. The fact that the conductivities in “dry” air are slightly higher than in dry 5% H<sub>2</sub>/Ar may be due to the fact that the 5% H<sub>2</sub>/Ar gas was bubbled through conc. H<sub>2</sub>SO<sub>4</sub> (< 0.01 % H<sub>2</sub>O), whereas the air atmosphere was not pre-dried and may contain slightly more moisture.

The lowest  $pO_2$  achievable with 5%  $H_2/Ar$  in this experiment at  $887^\circ C$  was  $1 \times 10^{-18}$  atm, while at  $515^\circ C$ ,  $1 \times 10^{-28}$  atm could be reached. The reason why a lower  $pO_2$  is attainable at lower temperatures is as follows:

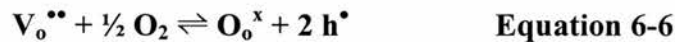


$$\text{with } K_p = \frac{p_{H_2} \cdot p_{O_2}^{1/2}}{p_{H_2O}}, \text{ with } p_{H_2O} \gg p_{O_2} \quad \text{Equation 6-4}$$

$$\text{And } \Delta G = -RT \ln K_p \quad \text{Equation 6-5}$$

So that as  $T \uparrow$ ,  $K_p \downarrow$ , therefore  $pO_2 \downarrow$ .

These conductivity measurements indicate that a move to oxide ion or perhaps mixed oxide-ion/p-type hole ( $h^\bullet$ ) conduction may be occurring at these higher temperatures, especially in dry air (high  $pO_2$ ) according to the equation:



where  $V_o^{\bullet\bullet}$  denotes an oxygen ion vacancy.

### 6.3 Summary

The conductivity of  $Sr_3CaZr_{0.5}Ta_{1.5}O_{8.75}$  has been examined under both wet and dry conditions and the influence of water vapour is shown to increase the conductivity at intermediate and low temperatures. The behaviour of the conductivity over time as the gas stream was changed from wet to dry or vice-versa was also investigated. These results provide good evidence that the conductivity is almost entirely due to protons at

temperatures < 500°C, and that the presence of a proton supply in the form of water enhances the conductivity.

The conductivity of  $\text{Sr}_3\text{CaZrTaO}_{8.5}$  was also investigated as a function of  $p\text{O}_2$  in a hydrating atmosphere. No significant n-type conduction is evident at intermediate temperatures and the conductivity does not increase when the temperature is increased to 887°C. Some hole or oxygen ion conduction may be present at higher temperatures. The dominant conducting species at 515°C is most likely protonic.

#### 6.4 References

- [1] H. Iwahara, T. Esaka, H. Uchida, N. Maeda, *Solid State Ionics* **3/4** 359 (1981)
- [2] S.M. Haile, D.L. West, J. Campbell, *J. Mater. Res.*, **13** 6 (1998) 1576-1595
- [3] F.A. Kröger and H.J. Vink, in "Solid State Physics" (F. Seitz and D. Turnbull, Eds.), p. 307 (1956)
- [4] J. Fleig, *Solid State Ionics* **131** (2000) 117
- [5] J.R. Macdonald (ed.), "Impedance Spectroscopy" (1987) John Wiley and Sons (publishers)
- [6] N. Bonanos, *Solid State Ionics* **53-56** (1992) 967-974
- [7] K.D. Kreuer, *Solid State Ionics* **97** (1997) 1-15
- [8] H. Maekawa, N. Kashii, J.I. Kawamura, Y. Hinatsu, *Solid State Ionics* **122** (1999) 231-236
- [9] B. Groß, St. Marion, R. Hempelmann, D. Grambole, F. Hermann, *Solid State Ionics* **109** (1998) 19
- [10] K.H. Ryu, S.M. Haile, G. Staneff, S. Jamindar, FETC Publications (US DOE) Conference Proceedings "Joint Fuel Cell Technology Review" (Aug 1999)
- [11] J.F. Liu, A.S. Nowick, *Solid State Ionics* **50** (1992) 131
- [12] A.S. Nowick, Y. Du, *Solid State Ionics* **77** (1995) 137-146

## Chapter Seven

### Hydrogen Titanates as Potential Proton Conducting Fuel Cell Electrolytes

"In science it often happens that scientists say, 'You know, that's a really good argument; my position is mistaken,' and then they actually change their minds and you never hear that old view from them again.

They really do it. It doesn't happen as often as it should, because scientists are human and change is sometimes painful. But it happens every day. I cannot recall the last time something like that happened in politics or religion."

---*Carl Sagan*

## 7 Hydrogen Titanates as Potential Proton Conducting Fuel Cell

### Electrolytes

#### 7.1 Introduction

A viable low to mid temperature proton conducting solid oxide fuel cell electrolyte, which would operate at temperatures of 200 to 500°C, is a tantalising prospect. Recent work has concentrated on ceramic perovskite materials such as Gd doped BaCeO<sub>3</sub> [1] and Sr<sub>3</sub>Ca<sub>1.18</sub>Nb<sub>1.82</sub>O<sub>9-δ</sub> [2], which can exhibit proton conductivities as high as 10<sup>-3</sup> S cm<sup>-1</sup> at 300°C. If conductivity could be further enhanced by 1 or 2 orders of magnitude then a very attractive technological material would have been achieved. The present work focuses on some hydrogen titanate materials derived from their respective lithium analogues, which are known to be good Li<sup>+</sup> ion conductors at temperatures around 300°C.

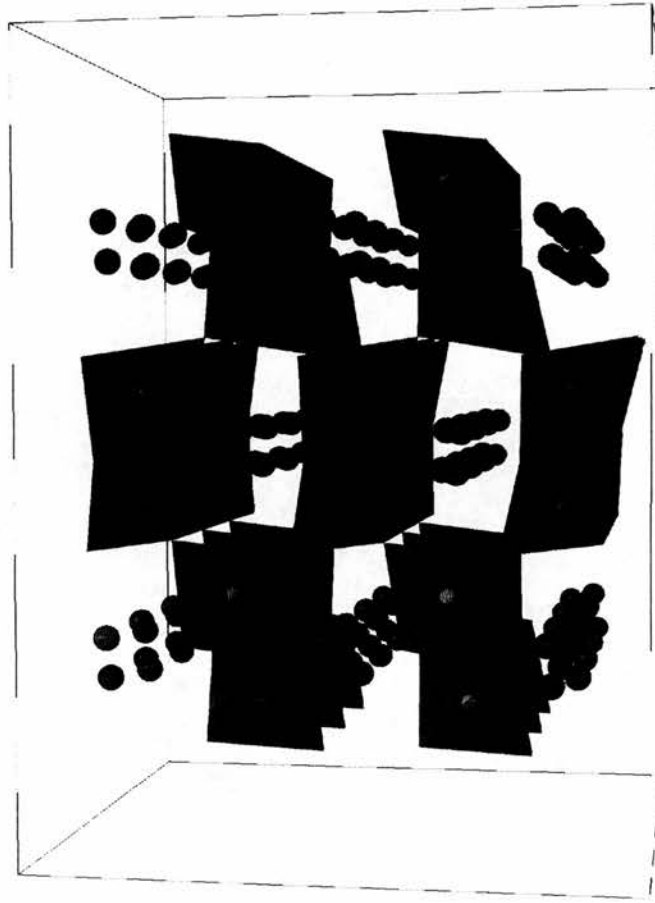


**Figure 7-1: Crystal structure of a typical ramsdellite lithium titanate, comprising (Ti,Li)O<sub>6</sub> framework with Li occupying channel sites [4]. As channel sites are split, maximum occupancy is 50% for these sites. It is anticipated that in H<sub>2</sub>Ti<sub>3</sub>O<sub>7</sub> the structure is closely related.**

Li<sub>2</sub>Ti<sub>3</sub>O<sub>7</sub> with the ramsdellite structure is known to be a fast Li-ion conductor with a conductivity of  $4.6 \times 10^{-4} \text{ S cm}^{-1}$  at 300°C [3]. A solid solution series has also recently been discovered linking the Li<sub>2</sub>Ti<sub>3</sub>O<sub>7</sub> and LiTi<sub>2</sub>O<sub>4</sub> ramsdellite phases, namely that of Li<sub>1+x</sub>Ti<sub>2-2x</sub>O<sub>4</sub> ( $0 \leq x \leq 0.143$ ), where Li<sub>2</sub>Ti<sub>3</sub>O<sub>7</sub> can be written as Li<sub>1.143</sub>Ti<sub>1.714</sub>O<sub>4</sub> [4]. The ramsdellite structure consists of edge-shared MO<sub>6</sub> chains, which form a one-dimensional tunnel structure, Figure 7-1. In LiTi<sub>2</sub>O<sub>4</sub> all the metal cation sites in the MO<sub>6</sub> framework are occupied by Ti, with Li occupying the channel sites. In Li<sub>2</sub>Ti<sub>3</sub>O<sub>7</sub>,

however, 14% of the framework sites are occupied by Li and effectively 14% of the channel sites are vacant.  $\text{H}_2\text{Ti}_3\text{O}_7$  has recently been prepared by ion exchange from  $\text{Li}_2\text{Ti}_3\text{O}_7$  and it is believed that it may have a similar structure to the Li analogue [5].  $\text{Li}_2\text{Ti}_3\text{O}_7$  was used as a basis for  $\text{Li}^+/\text{H}^+$  exchange to give the hydrogen titanate analogue,  $\text{H}_2\text{Ti}_3\text{O}_7$  [5] and its conducting properties investigated.

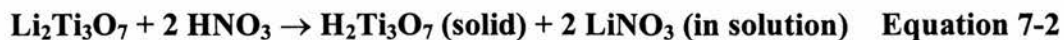
## 7.2 Experimental

The synthesis of  $\text{Li}_2\text{Ti}_3\text{O}_7$  involves solid-state mixing/grinding of  $\text{Li}_2\text{CO}_3$  (Aldrich), and rutile  $\text{TiO}_2$  (Aldrich), according to the following reaction:



The reactants were predried at  $300^\circ\text{C}$  for at least 6 hours. After drying, they were immediately weighed out in the appropriate ratios according to Equation 7-1, and ground under acetone for approximately 30 min under acetone using an agate pestle and mortar. The mixture was then transferred to an alumina crucible and fired at  $750^\circ\text{C}$  overnight to remove  $\text{CO}_2$ . This resultant mixture was pelletised in a 13 mm die at 2-3 tonnes and then refired for 3 days at  $1050^\circ\text{C}$  in a muffle furnace to form (on quenching to room temperature in air) the ramsdellite phase  $\text{Li}_2\text{Ti}_3\text{O}_7$ .

The proton exchanged analogue,  $\text{H}_2\text{Ti}_3\text{O}_7$  was prepared by refluxing 1 g of finely powdered  $\text{Li}_2\text{Ti}_3\text{O}_7$  with 50 ml of a 5 M  $\text{HNO}_3$  solution at  $135\text{-}140^\circ\text{C}$  for 12 hours according to the following reaction:



The white powder was then filtered, washed with 10 x 10 ml aliquots of cold distilled water and ethanol (50/50 v/v) and then suction filtered in air.

X-ray diffraction was carried out using a Stoe StadiP Transmission X-Ray Diffractometer, with  $\text{CuK}\alpha_1$  radiation. The unit cells of these materials were initially indexed using the Stoe computer program LATREF [6], and the recent Werner least squares refinement module of the 1999 Stoe Software. Thermal analysis (DTA/TGA) to determine water loss was performed using a TA instruments 2960 connected to a PC. These measurements were carried in a flow of  $\text{N}_2$  gas with a flow rate of 75 ml/min.

Solid State Magic Angle Spinning Nuclear Magnetic Resonance (SS-MAS-NMR) was carried out using a Bruker MSL-500 MHz NMR Spectrometer. A DOTY probe was used for  $^6\text{Li}$  (resonant frequency at 73.599 MHz) and  $^7\text{Li}$  (194.366 MHz) nuclei, while a Bruker probe was used for  $^1\text{H}$  (500.13 MHz). Spinning rates were in the range 4 – 7 kHz.

Impedance measurements were made using a Solartron 1260 frequency response analyser, connected to a PC, using Zplot and Zview impedance software (Scribner and Associates). Horizontally mounted sealed quartz jigs were used to contain the sample in a controlled gas environment in a tubular furnace arrangement. Sample preparation involved uniaxial pressing (2-3 tonnes) of the powders in a 13 mm die press, to obtain cylindrical pellets about 0.2 cm in height. Sintering or heating of  $\text{H}_2\text{Ti}_3\text{O}_7$  at temperatures above  $290^\circ\text{C}$  was not attempted due to the likely risk of losing water, and

therefore protons from the system (see TGA Analysis). This is one of the crucial difficulties in dealing with this material. The pellets were then painted on each face with platinum ink (Engelhard) and left to dry at 140°C. Thin strips of Au foil were attached to the Pt coated faces with Au paste (Engelhard).

## 7.3 Results

### 7.3.1 X-Ray Diffraction studies

X-ray diffraction data was carried out using a Stoe StadiP Transmission X-Ray Diffractometer and peak refinement analysis revealed  $\text{Li}_2\text{Ti}_3\text{O}_7$  to have an orthorhombic unit cell in the Pnma space group,  $a = 9.5337(5)$ ,  $b = 2.9407(1)$ ,  $c = 5.0081(4)$ . After  $\text{H}^+$  exchange on the lithium sites, XRD diffraction analysis indicated that the sample was still a single phase ramsdellite. The hydrogen titanate had a similar orthorhombic cell with  $a = 9.739(2)$ ,  $b = 2.9410(6)$ ,  $c = 4.725(2)$ , with a total change in unit cell volume (shrinkage) on proton exchange of about 3.62 %. This is expected when taking into account the relative sizes of the proton and lithium ion. These changes in unit cell parameter indicate a significant change in the channel cross-section. The powder patterns of  $\text{Li}_2\text{Ti}_3\text{O}_7$  and  $\text{H}_2\text{Ti}_3\text{O}_7$  are compared in Figure 7-2.

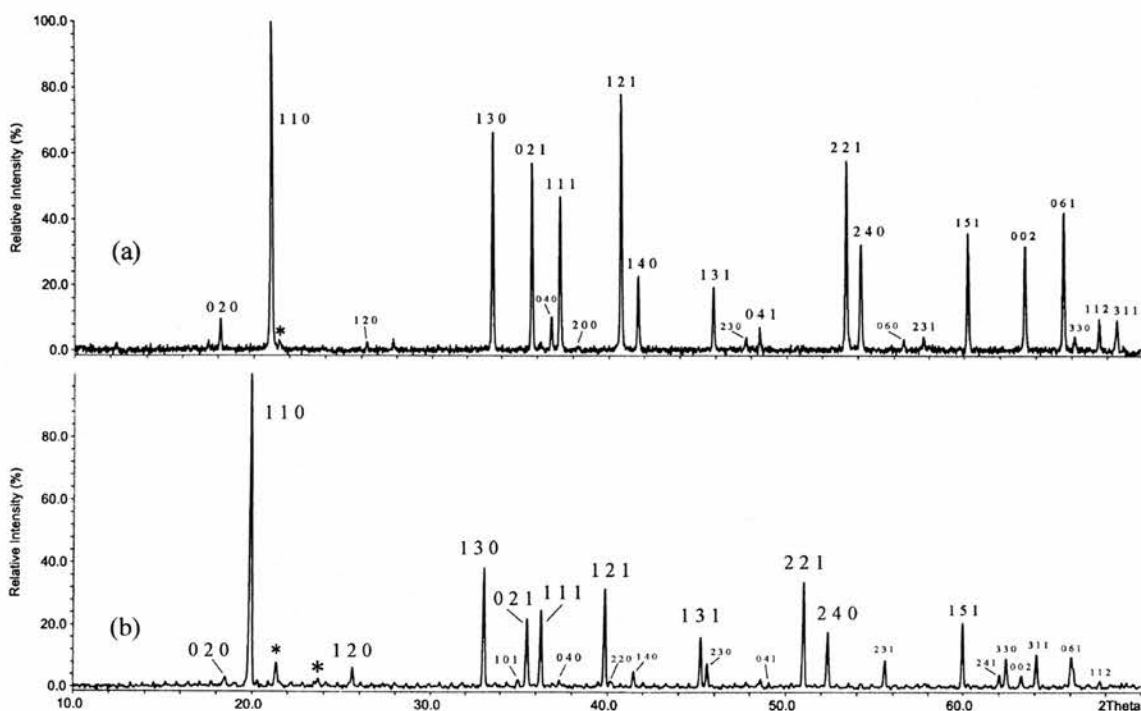


**Figure 7-2 : Powder X-ray diffraction patterns of (a)  $\text{Li}_2\text{Ti}_3\text{O}_7$  and (b)  $\text{H}_2\text{Ti}_3\text{O}_7$  ramsdellites. \*represents peak from petroleum jelly**

#### 7.4 Solid-State Magic Angle Spinning NMR studies

For  $\text{Li}_2\text{Ti}_3\text{O}_7$ ,  $^6\text{Li}$ -MAS-NMR studies at room temperature exhibited only one single sharp peak of approx. 200 Hz basewidth. In this case, it seems clear that the Li channel and framework sites must have very similar chemical shifts. Lithium in solids is known to show only a small range of chemical shifts as evident in the difficulty in distinguishing the Li sites in  $\text{Li}_4\text{Ti}_5\text{O}_{12}$  [7]. After  $\text{Li}^+/\text{H}^+$  exchange  $^6\text{Li}$ -MAS-NMR showed no signal confirming the loss of lithium. Proton MAS-NMR of the resulting  $\text{H}_2\text{Ti}_3\text{O}_7$ , Figure 7-3, showed 2 overlapping (but resolvable) peaks, integrating to 55% and 45%. So for the hydrogen analogue MAS-NMR, the difference in chemical shifts between the different cation sites is significant compared to the linewidth. The

measured shifts of the two lines were +6.0 and +8.0 ppm, relative to TMS (tetramethylsilane)

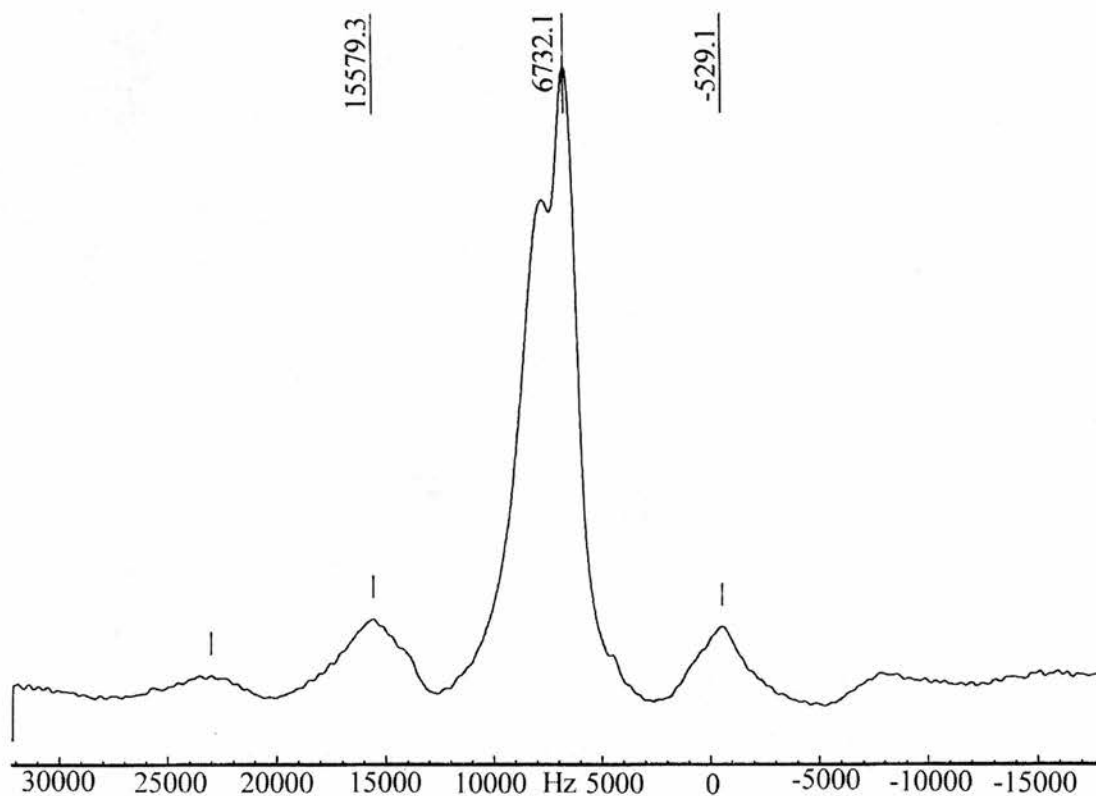


**Figure 7-3:  $^1\text{H}$  MASNMR of  $\text{H}_2\text{Ti}_3\text{O}_7$ . The central double peak reveals that there are two distinct proton sites in the lattice. Spinning side-bands are present.**

## 7.5 Thermogravimetric analysis of ramsdellite $\text{H}_2\text{Ti}_3\text{O}_7$

Our thermal analysis investigations of  $\text{H}_2\text{Ti}_3\text{O}_7$  are in accord with those previously reported by LeBail [5]. On heating, a broad exotherm is observed at  $237^\circ\text{C}$  and then a sharp exotherm associated with the onset of decomposition is observed at  $290^\circ\text{C}$ , Figure 7-4. The observed mass loss corresponds within experimental error ( $\pm 0.1\%$ ) to that expected for the decomposition of  $\text{H}_2\text{Ti}_3\text{O}_7$  to  $\text{TiO}_2$ , 6.99%. Previous work [5] has suggested that the broad exotherm at  $237^\circ\text{C}$  relates to a structural modification of the  $\text{H}_2\text{Ti}_3\text{O}_7$ , although its composition remains constant, electrical measurements are reported from below this temperature only.

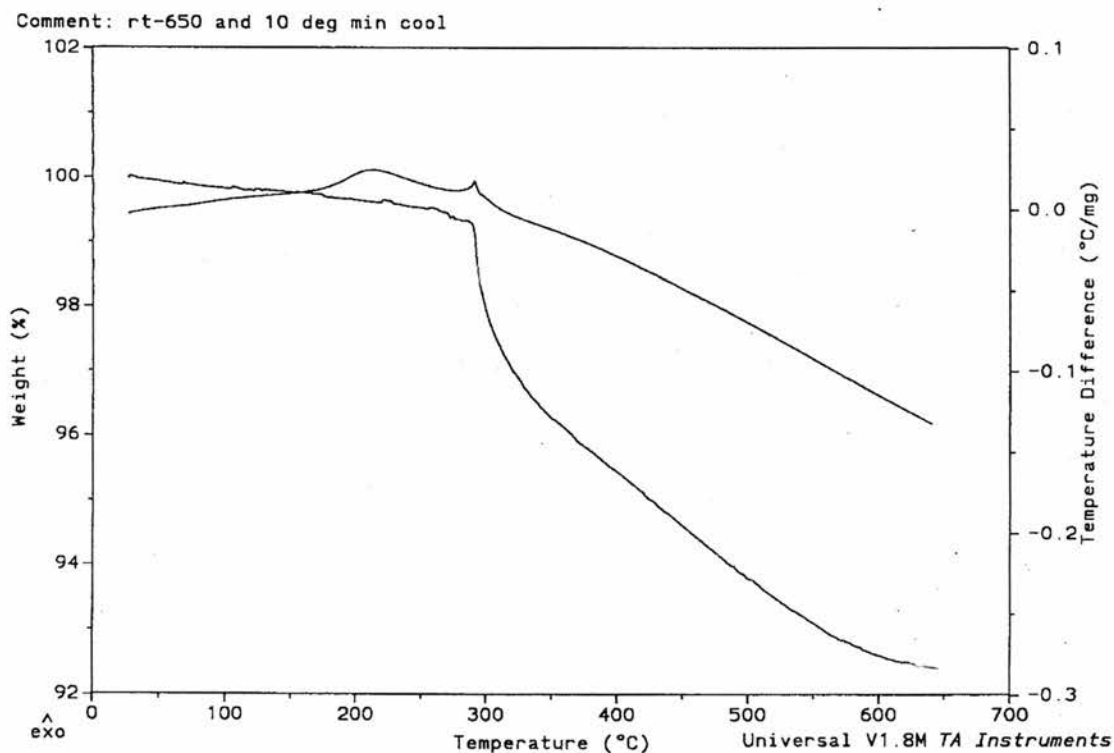


**Figure 7-4 : TGA and DTA traces for  $\text{H}_2\text{Ti}_3\text{O}_7$  decomposition, heating at  $10^\circ\text{C min}^{-1}$  from ambient to  $650^\circ\text{C}$**

## 7.6 A.c. impedance spectroscopy studies of the conductivity

A.c. impedance spectra were taken on  $\text{H}_2\text{Ti}_3\text{O}_7$  under a wet-air gas flow with a Solartron 1260 Frequency Response Analyser in the range 1 MHz to 0.1 Hz, using platinum paste as electrodes on each face of the 13mm sample pellet. Maximum sample densities achievable were approximately 70% theoretical. The conductivity of this compound was examined in the temperature range 140 °C to 233 °C. The impedance plane response at 185°C is shown in Figure 7-5; this shows two elements, a constriction grain boundary [8] ("neck") element and at higher frequencies the grain interior response. A third grain boundary element was also observed at higher temperatures.

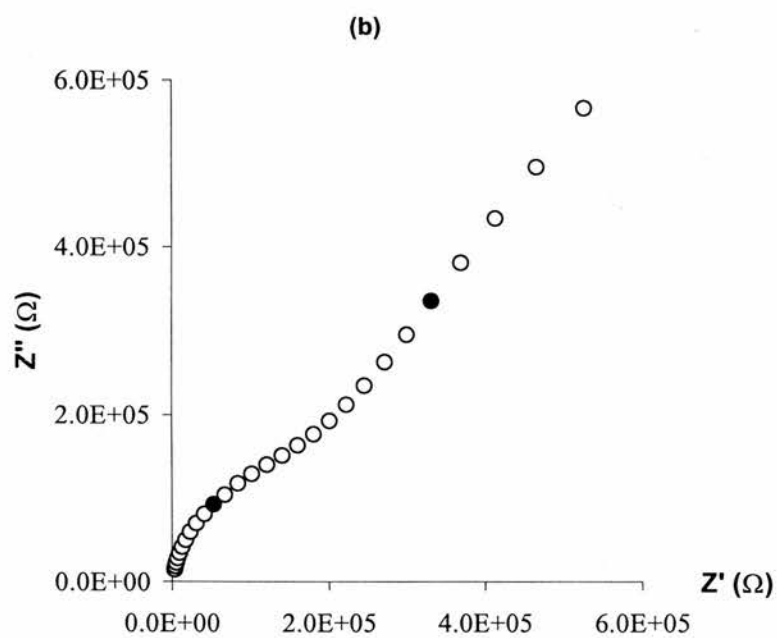
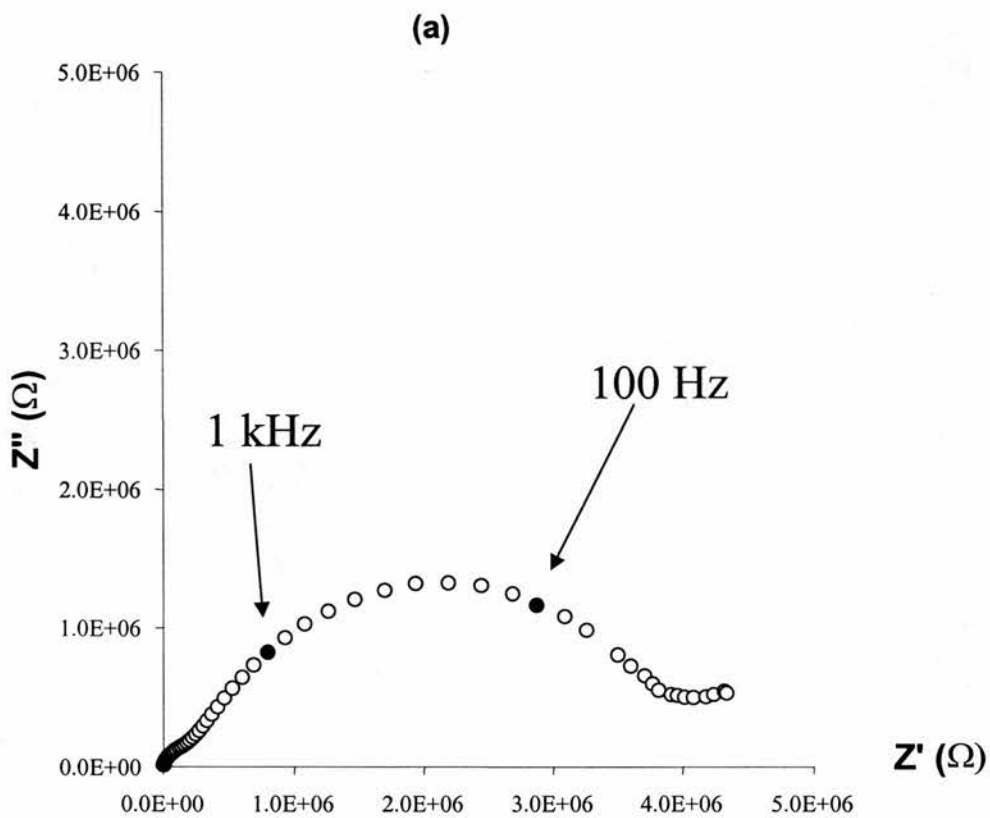


**Figure 7-5: Nyquist plots of  $H_2Ti_3O_7$  at  $185^\circ C$  in wet air flow. (a) Main Constriction Grain Boundary response clearly evident. (b) Rescaling reveals the bulk response at high frequency.**

Capacitance values associated with these responses are presented in Table 7-1 and these confirm the bulk, constriction and grain boundary component assignments [9].

<b>Impedance Response</b>	<b>Geometric Capacitance Value (F cm<sup>-1</sup>)</b>
Bulk	$7.1 \times 10^{-12}$
Constriction Grain Boundary	$4.1 \times 10^{-11}$
* Grain Boundary	$3.6 \times 10^{-9}$

**Table 7-1 : Main A.C. Impedance responses and Capacitances (inclusive of sample geometry correction) obtained for H<sub>2</sub>Ti<sub>3</sub>O<sub>7</sub>. \* GB response only discernible over ~220°C**

The bulk response conductivity was found to be  $2.7 \times 10^{-6} \text{ S cm}^{-1}$  at  $200 \text{ }^{\circ}\text{C}$ , with an activation energy of  $0.95 \text{ eV}$  in the temperature range studied. The “constriction” grain boundary conductivity was found to be  $6.3 \times 10^{-8} \text{ S cm}^{-1}$  at  $200 \text{ }^{\circ}\text{C}$  with an activation energy of  $0.71 \text{ eV}$  in the same temperature range, both demonstrated linear Arrhenius conductivity dependencies, Figure 7-6.

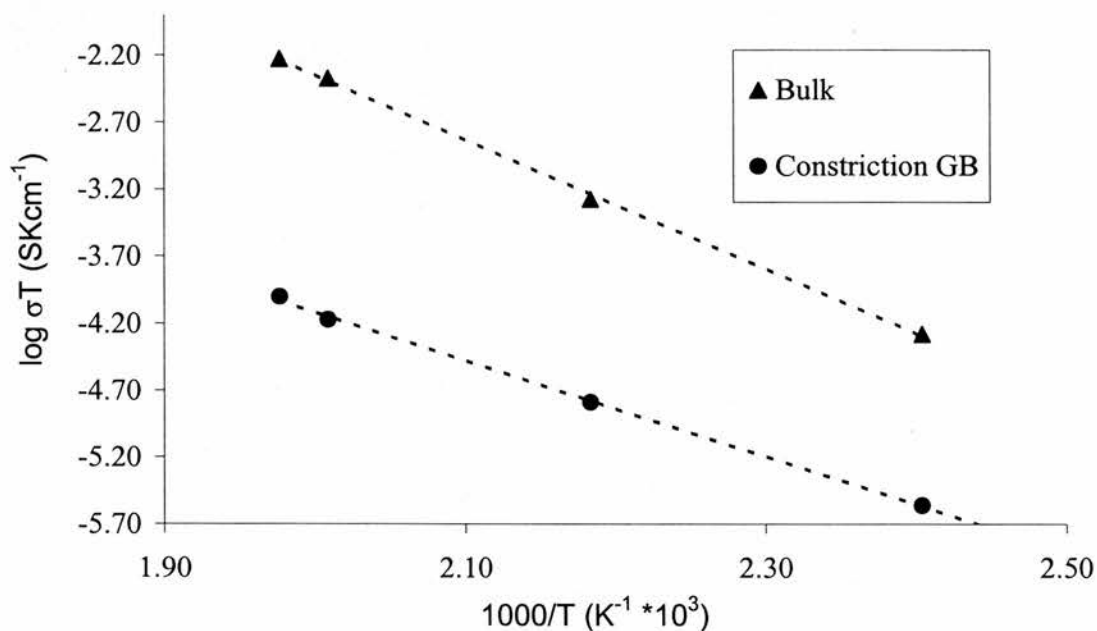


**Figure 7-6 : Bulk and Constriction Grain Boundary Conductivity Arrhenius plot for  $\text{H}_2\text{Ti}_3\text{O}_7$**

## 7.7 Discussion

The major problem with this material is its poor stability at higher temperatures, so direct sintering is not possible. The volume change associated with proton exchange means that sintered  $\text{Li}_2\text{Ti}_3\text{O}_7$  compacts disintegrate on exchange, so indirect sintering is also not possible. Future work will target other compositions with the ramsdellite structure that exhibit better stability for the protonated form or a smaller degree of structural change on proton exchange.

The conductivity observed for  $\text{H}_2\text{Ti}_3\text{O}_7$  is considerably higher than would be expected for defect electronic conductivity in oxidising atmospheres for a lithium titanate; it therefore seems highly likely that conduction is due to proton transport. Due to the stability problems, it is impossible to sinter this material, so definitive confirmation by techniques such as concentration cell measurements will not be possible. The proton conductivity does seem to be intrinsic, so changing of water vapour concentration in the atmosphere would not dramatically change its properties, until the phase degrades. The protonic conductivity of ramsdellite  $\text{H}_2\text{Ti}_3\text{O}_7$  appears to be about 1 order of magnitude lower than the lithium ion conductivity of ramsdellite  $\text{Li}_2\text{Ti}_3\text{O}_7$  and also compares unfavourably with the best perovskite protonic conductors, Table 7-2. The activation energy for proton migration in  $\text{H}_2\text{Ti}_3\text{O}_7$  (0.95 eV) also seems to be much higher than that for lithium migration in  $\text{Li}_2\text{Ti}_3\text{O}_7$  (0.46 eV), indicating that the protons are more strongly bound to the oxide lattice in  $\text{H}_2\text{Ti}_3\text{O}_7$  than lithium in  $\text{Li}_2\text{Ti}_3\text{O}_7$ . The activation energy is also much higher than for perovskite proton conductors. This may relate to a fairly large O-O separation in this ramsdellite.

Material	Conducting Ion	Bulk $\sigma$ (S cm <sup>-1</sup> )	Temp (°C)	Reference
H <sub>2</sub> Ti <sub>3</sub> O <sub>7</sub>	H <sup>+</sup>	2.66 x 10 <sup>-6</sup>	200	This work
Li <sub>2</sub> Ti <sub>3</sub> O <sub>7</sub>	Li <sup>+</sup>	2.84 x 10 <sup>-5</sup>	200	[3]
BaCe <sub>0.85</sub> Gd <sub>0.15</sub> O <sub>3-<math>\delta</math></sub>	H <sup>+</sup>	8.0 x 10 <sup>-4</sup>	200	[1]
Sr <sub>3</sub> Ca <sub>1.18</sub> Nb <sub>1.82</sub> O <sub>9-<math>\delta</math></sub>	H <sup>+</sup>	2.0 x 10 <sup>-4</sup>	200	[2]

**Table 7-2 : Comparative conductivity values for some known ionic conductors**

## 7.8 Summary

This work examines the possibility of using hydrogen titanate materials, which may exhibit appreciable protonic conductivity at low temperatures (100-500°C), as electrolytes in the next generation of Solid Oxide Fuel Cells. The ramsdellite lithium titanate phase, Li<sub>2</sub>Ti<sub>3</sub>O<sub>7</sub> was used as a basis for H<sup>+</sup> exchange to form H<sub>2</sub>Ti<sub>3</sub>O<sub>7</sub>. The ramsdellite structure of this compound was confirmed by X-ray diffraction and its composition confirmed by thermogravimetric analysis Magic angle spinning solid state NMR showed that the protons occupied at least two sites in the ramsdellite structure, in accord with the proposed H<sub>2</sub>Ti<sub>3</sub>O<sub>7</sub> formula. The conductivity of compressed compacts of this compound was measured and the bulk value extracted. The measured conductivity of H<sub>2</sub>Ti<sub>3</sub>O<sub>7</sub> was 2.66 x 10<sup>-6</sup> S cm<sup>-1</sup> at 200°C, about 1 order of magnitude lower than the Li-analogue Li<sub>2</sub>Ti<sub>3</sub>O<sub>7</sub>, and 2 orders of magnitude lower than the best perovskite ceramic proton conductors at this temperature.

## 7.9 References

- [1] D.A. Stevenson, N.Jiang, R.M. Buchanan, F.E.G. Henn, *Solid State Ionics*, **62** (1993) 279
- [2] A.S. Nowick, Y. Du, *Solid State Ionics*, **77** (1995) 137
- [3] J.B. Boyce, J.C. Mikkelsen Jr., *Solid State Comm.*, **31** (1979) 741
- [4] R.K.B. Gover, J.T.S. Irvine, *J. Solid State Chem*, **141** (1998) 365
- [5] A. Le Bail, J.L. Fourquet, *Mat. Res. Bull.*, **27** (1992) 75
- [6] "Stoe StadiP User Guide," Stoe Automated Diffractometer Systems for powder and single crystal diffractometry, Darmstadt, 1987
- [7] M. Dalton, D.P. Tunstall, J. Todd et al, *J. Phys. Condens. Mat.* **6** (1995) 8859
- [8] P.G. Bruce, A.R. West, *J. Electrochem. Soc.* **130** (1983) 662
- [9] J.T.S. Irvine, D.C. Sinclair and A.R. West, *Adv. Mater.*, **2** (1990) 132.

## Chapter Eight

### Conclusion

"Find something you love doing and stick with it. Find people who support you in what you love doing and stick with them. Do not engage in too much self-doubt...and never get too arrogant. You don't need as much as you want of anything, but you need enough to make you feel you've succeeded."

---*Greg Bear*

## 8 Conclusion

Successful initial structural and thermal characterisation of single phases in the  $\text{Sr}_3\text{Ca}_{1+x}\text{Nb}_{2-x}\text{O}_{9-(3x/2)}$  (SCN) system were performed. These phases were used as a basis for creating a new phase that would be stable in such reducing atmospheres as would likely be present in an SOFC, and yet would less likely exhibit electronic conduction as a result of cation reduction and electron release. A similar or increased level of oxygen ion vacancies was also desirable so that significant water uptake would be possible.

The new system of general formula  $\text{Sr}_3\text{Ca}_{1+x}\text{Zr}_{(1-y)-x/2}\text{Ta}_{(1+y)-x/2}\text{O}_{8.5-[(5x-2y)/4]}$  (SCZT) was devised to meet these criteria. Specifically, the composition  $\text{Sr}_3\text{CaZr}_{0.5}\text{Ta}_{1.5}\text{O}_{8.75}$  and the parent phase  $\text{Sr}_3\text{CaZrTaO}_{8.5}$  were produced single phase by the solid state method and investigated, thermogravimetrically, electrically, and structurally.

The level of water uptake/loss in the SCZT system has been shown to be in accordance with SCN18 and with other complex perovskite systems, whereby approximately 60 % of the oxygen ion vacancies can be filled by hydration treatments. Detailed thermogravimetric-mass spectroscopic measurements have also revealed that some  $\text{CO}_2$  uptake occurs when SCZT phases are hydrothermally treated. This  $\text{CO}_2$  is 100 % reduced to CO under 5 %  $\text{H}_2/\text{Ar}$  atmospheres. Some evidence for incorporated “free-radical” oxygen species due to high pressure treatments with  $\text{KClO}_4$  has also been discussed. These investigations show that this system also has interesting capability of incorporating molecular species at the vacant oxygen ion positions.

The conductivity of  $\text{Sr}_3\text{CaZr}_{0.5}\text{Ta}_{1.5}\text{O}_{8.75}$  was also investigated to show that this material behaves as a proton conductor, by 2-terminal a.c. and 4-terminal d.c. measurements. A

new design of 2-terminal jig was constructed to ensure reliable contacts with the sample electrodes. The conductivity below 550°C is assumed to be almost entirely protonic and is found to be  $4.6 \times 10^{-4}$  and  $5.6 \times 10^{-4}$  S cm<sup>-1</sup> at 300 and 500°C respectively. Experiments have also shown how the conductivity of SCZT is improved by 2 orders of magnitude when exposed to moist 5 % H<sub>2</sub>/Ar atmospheres. Parallel work on these materials has verified successful operation as an SOFC electrolyte, and although a thick (1.5 mm) disc was used, the opportunities for improvement using sol-gel synthesis and thin layer deposition techniques to improve power density are very promising and work is being continued to achieve this.

Structural work revealed that the unit cells of these phases has shown that a  $\sqrt{2}a_p \times \sqrt{2}a_p \times 2a_p$  type unit cell is present, with distortion to monoclinic symmetry exhibited in the hydrated room temperature phase Sr<sub>3</sub>CaZr<sub>0.5</sub>Ta<sub>1.5</sub>O<sub>8.6125</sub>(OH)<sub>0.275</sub>. High resolution variable temperature neutron diffraction techniques were used to clarify subtle structural change with temperature. A change to higher tetragonal symmetry was only found to be present in the dehydrated phase at 1000°C. A similar change from orthorhombic to cubic was observed for SCN18. Although the hydrated SCZT system exhibits a higher degree of unit cell distortion compared to SCN18, this work has shown that these changes in symmetry with temperature have generally been overlooked in the relevant literature.

Ramsdellite H<sub>2</sub>Ti<sub>3</sub>O<sub>7</sub> was also investigated as a potentially useful proton conducting oxide, however the protonic conductivity proved to be much lower than expected, as the lithium ion is quite mobile in the Li<sub>2</sub>Ti<sub>3</sub>O<sub>7</sub> precursor. This result is explained in terms of the nature of the H<sup>+</sup> versus Li<sup>+</sup> environment. The hopping distance for the proton is too

large across the channels of the ramsdellite structure, resulting in a high activation energy for proton conduction.

In summary overall, single-phase novel perovskite oxides were successfully synthesised and characterised in detail by various techniques, and been shown to exhibit appreciable proton conductivity and stability for SOFC electrolyte applications.